Investigation of the Role of Iron-Sulfur Clusters in Polymerase Alpha Primase

By

Lauren Elizabeth Salay

Dissertation

Submitted to the Faculty of the

Graduate School of Vanderbilt University

in partial fulfillment of the requirements

for the degree of

DOCTOR OF PHILOSOPHY

in

Chemical and Physical Biology

December 12, 2020

Nashville, Tennessee

Approved:

Katherine L. Friedman, Ph.D.

Walter J. Chazin, Ph.D.

Brandt F. Eichman, Ph.D.

David Cortez, Ph.D.

James M. Dewar, Ph.D.

To my family,

my constant cheerleaders.

ACKNOWLEDGEMENTS

During times of change, I am always reminded of the song “For Good” by Stephen Schwartz in the musical *Wicked*:

> “I’ve heard it said that people come into our lives for a reason, bringing something we must learn. And we are led to those who help us most to grow, if we let them and we help them in return. I don’t know if I believe that’s true, but I know I’m who I am today because I knew you.”

Reflecting on my time in graduate school and on my personal development, I am awed by and incredibly grateful to the people who have enriched my life by being mentors, collaborators, colleagues, friends, and family. Each one is unbelievably special and I will forever value them and what they have taught me. They have truly changed me for the better, for good.

I first want to acknowledge my mentors. Professor Walter Chazin, thank you. Your mentorship, advice, and support mean the world to me. You truly are an inspiration. I value your kindness, patience, understanding, determination, and forthrightness. I joke that joining your lab was the best choice I have made in my life so far. But, it’s not really a joke. You are the perfect mentor for an imperfect mentee, especially one who, when asked what I want to do with my life, simply replies “science”. I love that you are so passionate about science. You always encouraged me to think and explore and speak up. You gave me room to grow and become an independent scientist. I am particularly grateful for the environment you foster in the lab, where mistakes are fine as long as you learn from them, and everybody is a work in progress and can contribute to our community in a meaningful way.

To my committee, Professors Kathy Friedman, Brandt Eichman, Dave Cortez, and James Dewar, thank you for your guidance. Speaking with you is always inspiring and only encourages me more to ask more question and be more passionate about my project.

Professor Friedman, I am grateful that I was able to collaborate closely with you and that you listened to my crazy hypotheses about priming in yeast and made them better. It’s inspiring

that you have so many responsibilities but still found time for science, family, mentoring, caring for your students, and chatting with me about both science and life. You have such a big heart and I always felt that I could ask your advice on anything and get an honest and fair opinion. Thank you for letting me work in your lab and thank you for being a fantastic role model for all women in science.

Professor Eichman, I somehow always entered your office in a state of despair over failed experiments and terrible sequencing gels but left feeling like everything was going to be alright. I love that you somehow know all the literature and can engage in a discussion about detailed priming mechanisms at any time. I will always appreciate your advice and perspectives.

Professor Cortez, I am inspired by your depth of knowledge and your passion for all things DNA repair. I am so grateful for your input, especially on my half-baked ideas that, with your advice, became full, testable hypotheses. I always enjoy hearing your thoughts on a paper or experiment because I always learn something. You caused me to want to pursue DNA replication/repair as a dissertation project and I will forever be grateful.

Professor Dewar, thank you for joining my committee partway through my candidacy. I love that I can just pop by to chat about science. I enjoy speaking with you because you are so knowledgeable and creative with experiments. Talking with you always made me feel like science is doable and that I could speak up and be taken seriously. Your respect and encouragement really made a difference in how I see my scientific career.

To my collaborator, Professor Jackie Barton, thank you for being invested in the primase project. I am so grateful that you and your lab are the other half of this project. I also appreciate your optimism. Speaking with you over the phone about experiments was really refreshing, specifically during times when nothing was working. Thank you for letting me come to your lab to learn about anaerobic environments, electrochemistry, and really cool Ruthenium complexes.

I would also like to acknowledge my mentors from my previous life as a mere high school/undergraduate student. Lee Ann Zobbe, thank you for your help in training the Worthless

Creature. You taught me the value of hard work and discipline, how to fail (and fall) gracefully, and that the competition result is not as important as the improvements you made. Mrs. Glick, thank you for always indulging me when I asked you to look up random animal/plant facts in your chemistry and biology classes. Thank you for normalizing curiosity, women in science, and knowledge as worthy pursuit. Madame Geisinger, thanks for your encouragement and support. You gave me an opportunity to “see” the world and discover other cultures through your French classes. For that, I will always be grateful.

Professor Cheira Belguellaoui, thank you for opening my mind and encouraging me to follow my passions. Your classes were my refuge when I was exhausted by science classes and they have had a huge impact on how I see the world. I am genuinely honored to know you and still incorporate French into my life, keeping in mind that if I want something, I have to actively seek it.

To Professors Henning Schneider and Sharon Crary, thank you for encouraging my burgeoning love for research. I would have chosen a different path if it weren’t for my experiences in your labs. Professor Schneider, I will always remember the awe I felt when you showed me zebrafish that had labeled serotonin receptors under a fluorescent microscope. Professor Crary, I loved working in your lab. Thank you for allowing me the freedom to explore and make mistakes. I am also grateful that you shared your love for global health and science communication. From you, I learned so much about social responsibility and how we can use science to make the world a better place.

To my lab mentors, Professor Matt Thompson, Dr. Ben Gilston, and Dr. Aaron Ehlinger, thank you for your training, mentorship, and guidance. I learned so much about the technical aspects of many facets of structural biology.

To the summer students, rotation students, and mentees, Dr. Huiqing Chen, Andy Dorfeuille, Durbis Castillo Pazos, Katherine Amidon, Jessica Hill, Kateryna Nabukhotna, and

Caley Gullett, thank you for your patience and support. You have taught me as much as I taught you. I loved sharing science with you and will be forever grateful.

To my colleagues and friends, Dr. Marilyn Holt, Dr. Liz O'Brien, Dr. Esther Epum, Dr. Aoshu Zhong, Dr. Kausar Raza, Dr. Amanda Erwin, Dr. Anais Naretto, Dr. Johnathan Dorival, Dr. Elwood Mullins, Johnny Cordoba, Dr. Alex Blee, Dr. Swati Balakrishnan, Kevin Pereira, Dr. Aslin Rodriguez, Dr. Nina Bozhanova, Kateryna LeMeur, Simone Harrison, Noel Maxwell, Frank Hu, and Dr. Megan May thank you for your support and encouragement. Each person on this list has acted as a sounding board, someone to vent to, someone with whom to share sorrows and joys, experimental failures and successes, and someone I can ask for help with no expectations of repayment or pettiness. These are true friends and have all contributed meaningfully to my research, well-being, and sanity.

To my chosen family, Renee Bockting, Madeline Leclair, and Lisa Pankewitz, you are truly sisters from another mister. Your encouragement and unconditional support have really made it possible for me to follow my passions, with no regard for anyone else's expectations. Thank you for encouraging me to live my life the way I want to.

To my biological family, I love you more than you can imagine. Mom and Dad, thank you for encouraging me to do what I want, even if it was not the easiest path. Thank you for always answering my phone calls and for being my number one fans. Thank you for trying to understand why I love science even if it is boring to you. To my sisters, Rachel and Chelsea, thank you for always being there for me. It will always be us against the world. To my grandparents, I love you so much and I am so grateful for your support over the years.

TABLE OF CONTENTS

LIST OF TABLES

LIST OF FIGURES

Figure Page

CHAPTER 1

INTRODUCTION[1]

Introduction

DNA replication is fundamental to the maintenance and propagation of life. All three kingdoms of life use a common, semiconservative mechanism to replicate DNA. During replication, the process of daughter strand synthesis starts with the unwinding of duplex DNA by helicases, which enables complementary copies of each strand to be synthesized by DNA polymerases. The junction between the parental duplex DNA and the unwound single stranded templates is termed the replication fork. The coordinated action of a substantial number of proteins at the replication fork is required in order to maintain orderly and accurate replication (Figure 1.1).

Early studies with the SV40 T antigen model system and recent studies of *in vitro* reconstitution of the eukaryotic replisome have clearly shown that polymerase α – primase (pol-prim) is required for both leading and lagging strand synthesis [1]. At the time of its discovery, pol-prim was termed polymerase α (pol α) and thought to be the only eukaryotic polymerase, responsible for all of replication [2]. Subsequent studies revealed that polymerase δ (pol δ) was also a major replicative polymerase, and importantly, that it had proofreading 3' to 5' exonuclease activity, a feature lacking in pol α [3]. *In vitro* pol-prim primer extension assays performed with activated calf thymus DNA indicated that pol α was not as processive as pol δ [4]. However, pol δ was unable to function on naked DNA in the absence of pol-prim, nor could it extend efficiently from an RNA primer; it required a DNA primer to function. Reconstitution of

[1] Portions of this chapter are in press in the Encyclopedia of Biological Chemistry, 2020: Salay, L.E. Cordoba, J.C. Chazin, W.J., "DNA polymerase alpha-primase: biochemical and structural mechanisms".

replication machinery *in vitro* with the SV40 T antigen system as well as studies of yeast mutator phenotypes led to the proposal that pol-prim generates the primer for proofreading polymerases [5, 6]. Subsequently, it was shown that pol δ performs strand displacement synthesis during Okazaki fragment maturation [7-9].

It is now well established that eukaryotes have three primary replicative polymerases (pols), pol α-primase, pol δ, and pol ε, which together perform the bulk of daughter strand synthesis. Polymerases δ and ε are processive polymerases that are able to proofread their products, generating accurate daughter strands. However, neither of them can function without having a ~30 nt complementary 'primer' strand already in place. It is the task of DNA pol α – primase (pol-prim) to generate the primer. DNA primase is critical to the process because it is the only replicative polymerase capable of initiating oligonucleotide synthesis on the ssDNA template, i.e. with no primer [2]. Pol-prim does not have the ability to proofread its products and

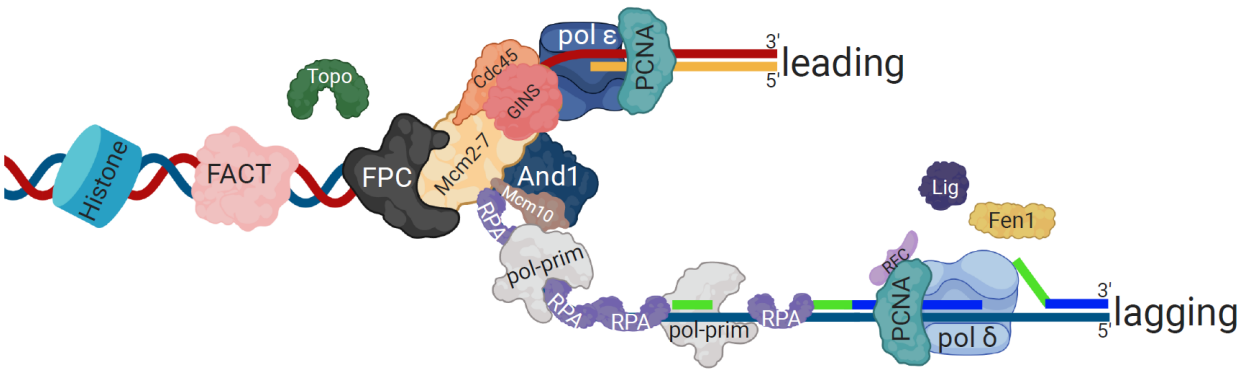

Figure 1.1: Schematic diagram of the replication fork showing key proteins. Duplex DNA is wrapped in histones, which are remodeled by the FACT complex ahead of the replication fork. At the replication fork, the fork protection complex (FPC- claspin, timeless, tipin) aids in stabilizing the replisome. Topoisomerase 2 (Top2) relieves topological stress due to histone movement and duplex unwinding. Mcm2-7, GINS, and Cdc45 form the CMG helicase, which unwinds duplex DNA. The single stranded DNA (ssDNA) binding protein Replication Protein A (RPA) coats the newly unwound ssDNA. This is particularly important on the lagging strand, where the daughter strand is synthesized discontinuously. And1 and Mcm10 interact with the helicase and aid in recruiting pol-prim to the replication fork. Pol-prim synthesizes a ~30 nt RNA-DNA primer (green) before handing off to the processive polymerases δ and ε for bulk synthesis of the DNA. Pol ε functions primarily on the leading strand, generating a continuous daughter strand (orange). Pol δ functions primarily on the lagging strand, elongating the primer synthesized by pol prim and generating Okazaki fragments of ~200 nts in eukaryotes. Pol δ is loaded onto the DNA via the clamp loader replication factor C (RFC) and the processivity clamp proliferating cell nuclear antigen (PCNA). Pol δ can perform strand displacement synthesis, replacing the primer synthesized by pol-prim. The displaced primer is removed by the Fen1 nuclease and ligated to the rest of the newly synthesized DNA by DNA Ligase (Lig), generating a continuous daughter strand.

consequently, has a relatively high error rate of 1 in 10^4 to 10^5 nts, consistent with it producing a relatively small primer before the substrate is handed-off to the replicative polymerases δ and ε. Pol-prim, pol δ, and pol ε all synthesize complementary strands in the same 5'-3' direction. Since the two strands of ssDNA emerging from a helicase have opposing polarities, pol-prim is particularly important on the lagging strand, as synthesis occurs discontinuously in blocks and requires thousands of primer initiation events.

Within the complex, multi-protein DNA replication machinery (Figure 1.1), pol-prim primarily interacts with the replisome via the scaffolding factor And1 (Ctf4) [10, 11] and Mcm10 [12, 13], a nuclear chaperone that stimulates helicase progression. There is also evidence that pol-prim associates with Tipin, part of the replication pausing complex, and GINS, which promotes pol-prim activity and is thought to aid in the stabilization of pol-prim during replication [14-16]. Other proteins that directly interact with pol-prim at the replication fork include replication protein A (RPA) and replication factor C (RFC) [17-20]. It is believed that these interactions mediate pol-prim recruitment to the replisome and aid in handoff to other polymerases.

The roles of pol prim subunits in priming

Pol-prim is comprised of two different polymerases, primase and pol α, whose activities are distinct but tightly coordinated. Primase is a DNA dependent RNA polymerase that initiates daughter strand synthesis by generating the initial primer of 7-12 ribonucleotides. This initial RNA primer is transferred to pol α, which extends the primer by ~20 deoxyribonucleotides. The chimeric primer is then handed off to one of the processive polymerases for further extension. While the primer generated by pol-prim is absolutely essential to replication, the majority of the primer is not ultimately incorporated into the genome; chimeric RNA-DNA primers are processed by the combined action of pol δ, Fen1, and DNA ligase during Okazaki fragment maturation (Figure 1.1) [21].

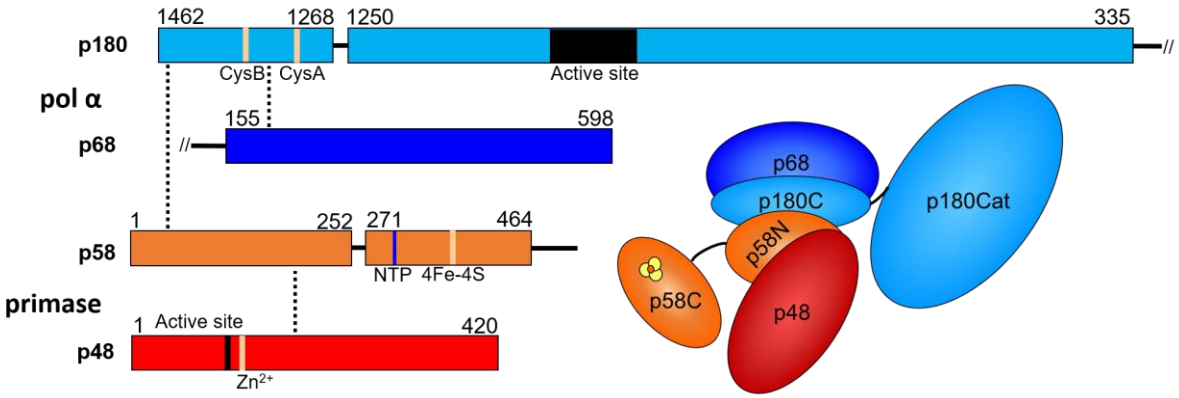

Figure 1.2: Domain structure, key binding sites, and organization of DNA polymerase α - primase. Residue numbers are indicated for each globular domain. Dashed lines identify regions mediating interactions between subunits. Solid horizontal lines indicate disordered/flexible linkers and domains. The two active sites are designated by black bars. Metal/Fe-S cluster binding sites are indicated by vertical coral lines. The location of the NTP binding site in p58C is identified by a vertical blue line. The lower right image is a schematic diagram of the architecture of the heterotetramer.

Primase and pol α each contain a catalytic and a regulatory subunit. In primase, the catalytic subunit p48 (also commonly called p49, PriS, and Pri1) is constitutively bound to the regulatory subunit p58 (also termed PriL, and Pri2) through its N-terminal domain (p58N) (Figure 1.2). Pol α consists of a catalytic subunit p180 (Pol1) and a regulatory subunit p68 (also called p70, B subunit, and Pol12). The C-terminal domain of p180 (p180C) is a critical interaction center linking to both p58 and p68. All four subunits of pol-prim are necessary for priming in cells [22]. However, the primase and pol α subunits can be generated independently, which enables their *in vitro* biochemical activities to be characterized. These studies have been useful for dissecting the action of pol-prim and defining the respective roles of its four subunits. The isolated primase catalytic subunit p48 is able to generate complementary RNA strands in the presence of single-stranded DNA, ribonucleotides, and divalent metal cations (typically Mn^{2+} or Mg^{2+}), albeit inefficiently [23, 24]. It uses the common two-metal mechanism to synthesize these primers. In the presence of p58, p48 synthesizes primers more efficiently. p58N functions as a scaffold and is tightly bound to p48. The p58 C-terminal domain (p58C) is flexibly tethered to p58N, and aids in initiation of primer synthesis. It is essential for generating primers of appropriate length (7-12 nts), i.e. is responsible for primer length 'counting' [24].

The catalytic subunit of pol α contains three functional domains: p180N, p180cat, and p180C. The disordered p180N is key for interactions with other replisome components. Beyond this, it is unclear if p180N has additional functional roles; in most *in vitro* studies, p180N is truncated to improve solubility[25]. The p180cat is the catalytic domain of pol α. It is highly conserved among eukaryotes and adopts the same fold as the pol δ and pol ε [26]. This domain in isolation elongates RNA or DNA primers with deoxyribonucleotides [27]. In the cell, elongation of the initial RNA primer with deoxyribonucleotides is limited to ~20 nucleotides; the processivity of this domain *in vitro* is still under debate [26, 27]. The p180cat domain is flexibly tethered to the p180C domain, which in turn associates tightly with p58N and the pol α regulatory subunit p68. p68 stabilizes the p180C domain and is important for proper targeting of pol-prim to the nucleus during the cell cycle [28]. The p68 subunit has been shown to be essential for association of pol-prim with the SV40 T-antigen helicase [29]. It also interacts with additional replisome factors in eukaryotic systems, notably human And1. Interestingly, human and yeast pol-prim utilize different subunits to interact with other replisome factors. For example, although p68 strongly interacts with And1, it is p180 that mediates the interaction with the yeast And1 homolog Ctf4 [10, 11]. Hence, there is more divergence among the eukaryotic pol-prims than the field initially anticipated.

Although its activities have been mapped to specific domains, as will be described in more detail below, biochemical studies with the full pol-prim heterotetramer show that pol α affects primase activity [25, 30-32]. Moreover, pol-prim has been shown to carry out lagging strand synthesis in the absence of other polymerases [1, 33]. Such observations make evident that although studies with isolated primase and pol α are insightful, a complete understanding of how pol-prim functions will only be possible by including data from analysis of the full pol-prim heterotetramer.

Table 1.1: Three-dimensional structures of eukaryotic pol-prim				
Subunit(s)	**Entry ID**	**Organism**	**Ligand(s)**	**Citation**
p48	4LIK	human	-	[35]
	4LIL	human	UTP, Mn(II)	
	4LIM	yeast	-	
	6RB4	human	-	[37]
	6R4S	human	ATP	
	6R4T	human	vidarabine triphosphate	
	6R4U	human	fludarabine triphosphate	
	6R5E	human	2F-ATP	
	6R5D	human	dATP	
p48-p58N	4BPU	human	-	[36]
	4BPW	human	UTP	
	4BPX	human	p180 peptide	
p58C	3L9Q[a]	human	-	[73]
	3LGB	yeast	-	[72]
	3Q36	human	-	[71]
	5F0Q	human	RNA/DNA, Mg(II)	[38]
	5F0S	human	RNA/DNA, Mn(II)	
	6DI6[b]	yeast	-	[77]
	6DHW	human	-	[86]
p48-p58	4RR2	human	-	[34]
p68-p180C	3FLO	yeast	Zn(II)	[42]
	4Y97	human	Zn(II)	[43]
p180cat	4FVM[c]	yeast	-	[26]
	4FXD	yeast	RNA/DNA	
	4FYD	yeast	RNA/DNA, dGTP	
	4Q5V	human	RNA/DNA, aphidicolin	[41]
	5IUD	human	DNA/DNA	[40]
	4QCL	human	RNA/DNA, dCTP	[39]
	6AS7	human	DNA/DNA, dCTP	
Tetramer	1618[d]	yeast	-	[44]
	5EXR	human	-	[38]

[a] related PDBs: 5DQO, 5I7M
[b] related PDBs: 6DI2, 6DTV, 6DTZ, 6DU0
[c] related PDB: 4B08
[d] EMDB entry

Three-dimensional structures of polymerase α – primase

Structural characterization of pol-prim has been extensive over the past decade using x-ray crystallography and a “divide and conquer” strategy. High-resolution 3D structures have been determined for each of the globular domains of pol-prim alone and/or as well as part of larger multi-domain complexes. A number of crystal structures have been determined in complex with model RNA and DNA substrates (Table 1.1). In addition to high-resolution crystal structures, negative-stain EM studies of yeast pol-prim have been published, yielding both a low-resolution shape reconstruction and two-dimensional class averages that showed significant interdomain flexibility. Taken together the data thus far provide highly detailed information on the structural characteristics of each domain, the interfaces between subunits, and insights into the catalytical mechanisms of RNA and DNA primer synthesis. Nevertheless, there remains a significant gap in knowledge of the structural mechanisms of how the pol-prim machinery functions due to the limited number of structures of the full pol-prim tetramer.

Structures of primase

The primase p48/p58 heterodimer contains three globular domains: one that covers the large majority of p48 and two others in p58 (p58N, p58C), which are tethered by a ~20-residue linker (Figure 1.3A) [34]. The p48 domain in eukaryotes adopts a characteristic archeo-eurkaryotic primase fold, in which a conserved mixed helix-sheet region forms the core around a typical aspartate-divalent metal active site (Figure 1.3B). Several crystal structures have been determined with different combinations of NTP’s and catalytic metals (PDBID 4BPW, 4LIL, 6R4S) [35-37]. Incoming NTPs are stabilized in the active site by key contacts between the negatively charged phosphate groups of the NTP and positively charged Arg and Lys side-chains of p48. The catalytic divalent metals (Mg^{2+} or Mn^{2+}) are ligated by three key Asp residues (Figure 1.3B). Human and yeast primase have a helical accessory subdomain that diverges in both sequence and structure from archaeal primases [35, 36]. A zinc motif is located at the

interface of the core and accessory regions, neighboring the catalytic center. The interface with p58N is on the opposite side of the Zn^{2+} binding module (Figure 1.3B).

The p58N domain serves as a critical scaffold mediating contact between primase and the p180 subunit of pol α. The domain consists of a mixed sheet-helix subdomain that serves as the interaction platform with p48 and a primarily helical subdomain that interacts with p180C. p58N is unstable in the absence of p48 and is tightly bound to it with an interface of ~1600 $Å^2$ of predominantly hydrophobic surface (Figure 1.3A). In eukaryotes, p58N is tethered to the unique p58C domain by a ~20 residue flexible linker. p58C is a compact helical domain with a 4Fe-4S cluster that is buried within the protein (Figure 1.3C). The domain has a nucleotide binding site within a highly basic groove. A structure of p58C bound to a product substrate has been determined, showing the key interactions with the 5' terminal triphosphate of the RNA primer

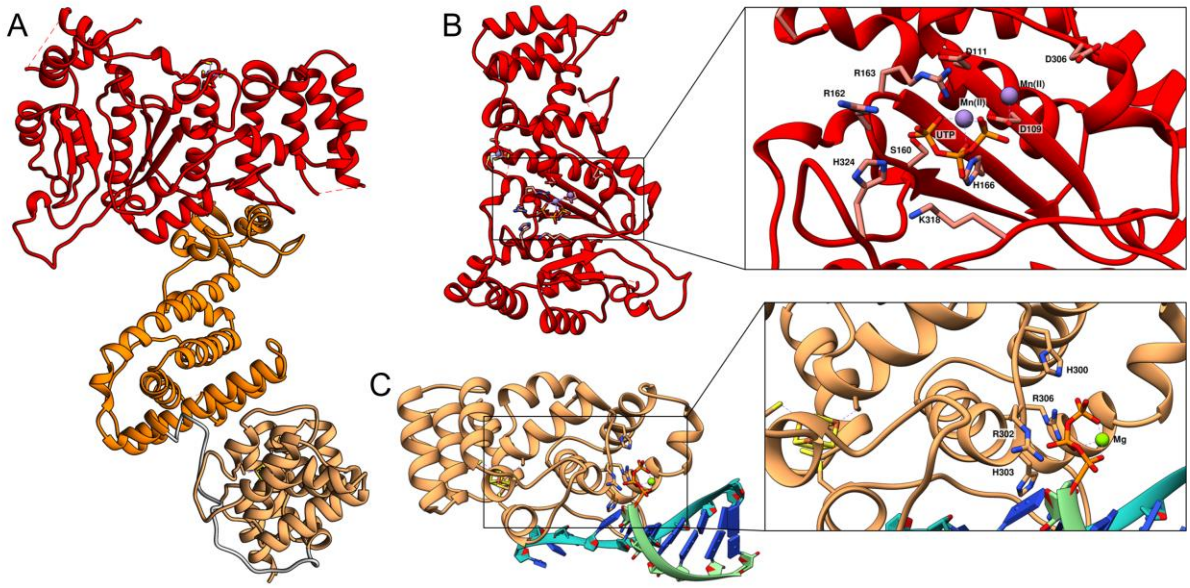

Figure 1.3: X-ray crystal structures of human DNA primase. A) Primase in an open configuration (PDBID 4RR2). The p48 core domain (red) is tightly bound to p58N (orange), whereas p58C (coral) is tethered to the p48/p58N platform by a flexible linker (gray). B) The isolated p48 core domain with Mn(II) and UTP co-factors (PDBID 4LIL). The inset shows a zoomed-in view of the active site with metals depicted as purple spheres, the triphosphate of a UTP molecule (orange and red) in stick representation, and labels for key residues stabilizing the co-factors. C) The isolated p58C domain in complex with an RNA/DNA duplex substrate (PDBID 5F0Q). The inset shows a zoomed-in view of the 4Fe-4S cluster (yellow and orange) and the RNA-DNA duplex and nucleotide binding sites. A Mg^{2+} ion is depicted as a green sphere, the 5’ triphosphate (orange and red) in stick representation, the RNA in green ribbon, the DNA in teal ribbon, and labels for key residues stabilizing the RNA/DNA duplex and co-factors. Dashed lines are drawn for segments of the protein that are not visible in the structure.

strand of a RNA/DNA duplex (Figure 1.3C) [38]. This interaction, in coordination with the linker to p58N may serve to restrict the length of the emergent RNA primer and terminate RNA primer synthesis (Figure 1.3A).

A crystal structure has been determined of the full-length primase in an 'open' configuration in which the p58C domain is located far from the p48 active site (Figure 1.3A). It is highly unlikely that this is an active configuration for primase. Rather primase must occupy a 'closed' configuration to generate the initial dinucleotide with the p58C template and nucleotide binding sites positioned close to the p48 active site. Such a change in configuration is presumably enabled by the flexible linker tethering p58C to p58N.

Structures of pol α

The pol α heteromdimer contains three globular domains: the p180 large central catalytic (p180cat) and C-terminal (p180C) domains, and a central core domain in p68 (Figures 1.4, 1.5). The two domains in p180 are tethered by a ~20 residue flexible linker. As a consequence, p180cat is structurally independent from the rest of the pol-prim complex. In addition to the structurally characterized globular domains, significant N-terminal disordered domains exist for both p68 and p180 (Figure 1.2). These domains function as interaction sites for binding to other replication factors.

Crystal structures of p180cat revealed a classic B-family polymerase hand fold, consisting of an active site located in the palm domain, a fingers domain responsible for binding incoming nucleotides, a thumb domain that grasps the duplex, and an inactive exonuclease domain (Figure 4A). Structures of p180cat have been determined in complex with several different model primer substrates, including RNA/DNA and DNA/DNA duplexes (Table 1.1) [26, 39-41]. These structures provide insight into primer length counting by pol α, although no conclusive mechanism has been determined to date.

No crystal structures have been determined for the isolated p68 and p180C domains, but there are several of their complex (Figure 1.4B, Table 1.1) [42, 43]. They show a compact slab-like structure in which the helical p180C domain forms a saddle shape that abuts the triangular p68 globular domain. The interaction between the two domains is stabilized by a large interface that occludes ~4500 $Å^2$ and is mediated by a number of polar and hydrophobic interactions. Two zinc motifs are observed on opposite sides of p180C (Figures 1.4B); as discussed below, these may serve to maintain the structural integrity of the domain and/or play a role in the regulation of primer synthesis.

Structures of the pol-prim tetramer

Though informative, structural data for individual domains and sub-complexes are not sufficient to define the mechanism and organization of pol-prim as it synthesizes chimeric RNA-DNA primers. The first step in this direction was a low-resolution negative stain EM structure of yeast pol-prim [44]. A bilobal structure was observed with significant inter-lobe flexibility evident from variability in the relative positioning of the two lobes in different 2D class averages. This

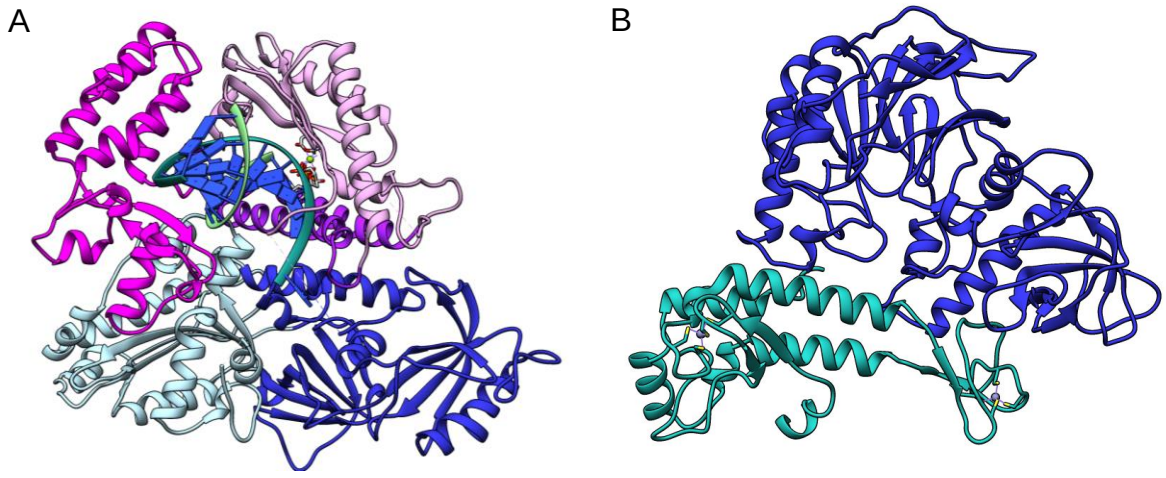

Figure 1.4: X-ray crystal structures of domain constructs of human polymerase α. A) The p180cat domain in complex with an RNA/DNA duplex (PDBID 4QCL). The subdomains are colored: thumb (magenta); palm (light purple); fingers (purple); exonuclease (light blue); N-terminal domain (dark blue). The hybrid RNA-DNA duplex is depicted with a ribbon backbone and blue bases. The RNA strand is illustrated by green ribbon and the template DNA strand is depicted by teal ribbon. B) The p68 core domain (blue) in complex with p180C (teal) (PDBID 4Y97). Dashed lines are drawn for segments of the protein that are not visible in the structure.

structure was informative despite its low resolution because it revealed the ability of pol-prim to undergo significant configurational rearrangements, which are commonly accepted as being essential to the coordination and regulation of primer synthesis across its two polymerase active sites.

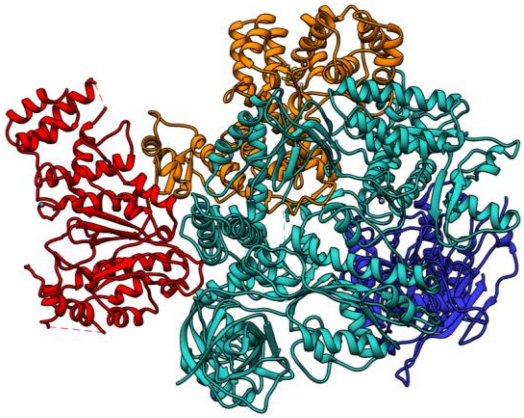

Figure 1.5: X-ray crystal structure of human polymerase α – primase. The structure is from PDBID 5EXR with different colors for each subunit: p48 (red); p58 (orange); p180 (teal); p68 (blue). Dashed lines are drawn for segments of the protein that are not visible in the structure.

More recently, a substantially higher resolution 3.6 Å crystal structure was determined for pol-prim in the absence of substrate or co-factors (Figure 1.5) [38]. This structure is especially valuable for visualizing the organization of the primary lobe of pol-prim containing the p48, p58N, p68 and p180C globular domains. However, the p180cat domain is seen to occupy an inactive configuration with the thumb domain splayed open. Overall, pol-prim structures have provided only limited insight into the mechanisms of generating a primer. In particular, they have yet to address where the flexibly tethered p180cat and p58C domains are located with respect to the p48/58N/p68/p180C platform at different points during primer synthesis. Clearly, there is an abundance of additional structural analysis required in order to understand how the dynamic pol-prim machinery is remodeled through the trajectory of generating the initial RNA primer, handing off RNA primed template, completing the synthesis of the RNA-DNA hybrid primer, and handing off to the processive polymerases δ and ε.

The unique 4Fe-4S clusters in eukaryotic pol-prim

Pol-prim makes extensive use of metals to carry out it functions. Like all polymerases, pol-prim utilizes divalent metals, typically Mg^{2+}, to catalyze the nucleotide polymerization reaction. Polymerases also bind Zn^{2+}, which serves to stabilize specific structural elements in and around DNA binding sites. Remarkably, over the past 15 years, an ever-increasing number of polymerases have also been shown to contain Fe-S clusters.

Iron-sulfur clusters are ancient, ubiquitous, and versatile protein cofactors that have many purported functions, including redox sensing, structural scaffolding, catalysis, and, most commonly, electron transport during respiration [45]. Fe-S clusters are found in a variety of different stoichiometries, the most common being 2Fe-2S and 4Fe-4S clusters. Though the cofactor itself is fairly simple, assembly and insertion of Fe-S clusters into proteins has a very high metabolic cost, requiring multiple, complex protein machineries [46].

In eukaryotes, there are multiple pathways for assembly and insertion of Fe-S clusters. These pathways involve the Iron Sulfur Cluster assembly (ISC) machinery in the mitochondria and the Cytosolic Iron-sulfur cluster Assembly (CIA) machinery in the cytosol [46, 47]. Though the genes encoding proteins for each set of machineries are nuclear, Fe-S cluster biogenesis depends on the mitochondria [47, 48]. In the mitochondria, the ISC pathway uses a cysteine desulfurase complex to generate sulfide ions and a mitochondrial iron importer, mitoferrin, and a still-unidentified iron sequestration protein, possibly frataxin, to generate raw materials for Fe-S assembly. The iron and sulfide ions are then transferred from their source complexes to scaffold proteins to generate a Fe-S cluster. This cluster can then be transferred to apoproteins via Fe-S cluster chaperone proteins. Alternatively, the complete Fe-S cluster can be transported out of the mitochondria via ABCB7 and targeted to apoproteins using CIA machinery [49].

The majority of nuclear and cytosolic proteins that contain Fe-S clusters are generated by the CIA pathway. It is known that the CIA machinery can use assembled Fe-S clusters

resulting from ISC assembly to target the appropriate apoproteins and facilitate Fe-S cluster insertion [50]. However, it has been recently discovered that the CIA machinery is involved in more than transferring Fe-S clusters to the proper apoproteins. In fact, the CIA machinery includes proteins that can sequester cytosolic iron, cytosolic scaffold proteins upon which Fe-S clusters can be assembled, and chaperones to facilitate Fe-S transfer. The source of sulfide is still under debate. Currently, it is hypothesized that a sulfide containing compound, named X-S, is generated by the ISC machinery in the mitochondria and exported for use by the CIA machinery [51]. Importantly, this tightly couples proper mitochondrial ISC function to all processes involving Fe-S cluster proteins, including polymerases involved in DNA replication [47, 48].

Fe-S clusters are electron rich and exist in multiple oxidation states. They are oxygen sensitive and can easily be destroyed through oxidation and nitrosylation. Their sensitivity to oxygen and the complexity of the cluster insertion machinery have historically hindered identification and characterization of Fe-S cluster-containing proteins [52-54]. In particular, the isolation of cluster-containing enzymes often requires an anaerobic environment as oxidative degradation occurs rapidly [55]. On the other hand, their volatility makes Fe-S clusters excellent sensors of oxidative stress and suggests why, on the whole, they are not well-suited for non-redox based cellular processes. Despite the instability of the cofactor and the potential for producing harmful radicals, a wide variety of polymerases and other proteins associated with DNA replication and repair contain Fe-S clusters.

Certain 4Fe-4S cluster-containing proteins have been proposed to engage in DNA charge transport (CT) [56-61]. DNA CT is defined here as the transport of electrons though the π-stacked bases between redox centers, such as 4Fe-4S clusters. This process is dependent on an intact nucleic acid duplex as even a slight perturbation in the integrity of the base pair stack, such as a mismatch or lesion, impairs the ability of nucleic acids to support electron transport [62]. The nucleic acid can thus serve as a conduit, allowing long-range manipulation of

the redox state of a 4Fe-4S cluster. The redox state has been observed to modulate the affinity of the protein for its nucleic acid substrate, with oxidized 4Fe-4S^{3+} proteins typically binding tightly and reduced 4Fe-4S^{2+} proteins binding more loosely to nucleic acid substrates [63].

DNA CT is now a well-accepted *in vitro* chemical phenomenon, but its functional relevance remains controversial [64, 65]. It has been hypothesized that DNA CT is used in DNA repair to signal between 4Fe-4S cluster containing proteins, such as XPD and MUTYH [45, 66-68]. In this model for signaling through DNA in DNA repair, a 4Fe-4S cluster in a repair protein is oxidized, allowing an electron to travel through an intact DNA duplex to reduce another 4Fe-4S cluster containing protein with a matched potential. The reduced protein then dissociates from the DNA diffuses away to search for damage in a new area [56]. As the identification and characterization of nucleic acid associated iron-sulfur cluster proteins increase, this hypothesis is being increasingly investigated as a method of coordinating replication, repair, and other nucleic acid transactions.

The unique p58C domain of DNA primase contains a 4Fe-4S cluster [69, 70]. The first indication of a cluster in p58C was the realization that even highly purified primase has a yellow-brown color. After discovery of the structural independence of p58C in limited proteolysis experiments on DNA primase, the domain was sub-cloned, purified and characterized by a range of biophysical and biochemical methods. It too had the yellow-brown color, which is characteristic of a 4Fe-4S cluster-containing proteins with a broad shoulder around 400-410 nm in the UV-vis spectrum. Electron paramagnetic resonance is sensitive to the exact nature of Fe-S clusters, and it revealed that p58C contains a high potential iron-sulfur protein (HIPIP)-like 4Fe-4S cluster [69, 70].

The identity of the cluster in p58C was subsequently confirmed by x-ray crystallography (PDBID 3LGB, 3L9Q, 3Q36) [71-73]. It is chelated by four conserved cysteines and is buried in the protein (Figure 1.6). Mutation of even a single cysteine is sufficient to inhibit primase function *in vitro* [70-72]. In yeast cells, mutations of the conserved cysteines cause a

temperature-dependent delay in S-phase or cell cycle arrest before S phase, indicating that the 4Fe-4S cluster is essential for proper initiation of daughter strand synthesis during replication [74].

Although the p58C 4Fe-4S cluster was identified over a decade ago, its precise role in priming is still ill-defined. The initial hypothesis was that the cluster plays a structural role, helping to maintain the architectural integrity of the essential p58 subunit (Figure 1.6) [71]. However, we, and others, argued that the metabolic cost of placing a cluster in the domain simply for structural stability is too high and rather, it must function in a regulatory role such as controlling the length of the primer.

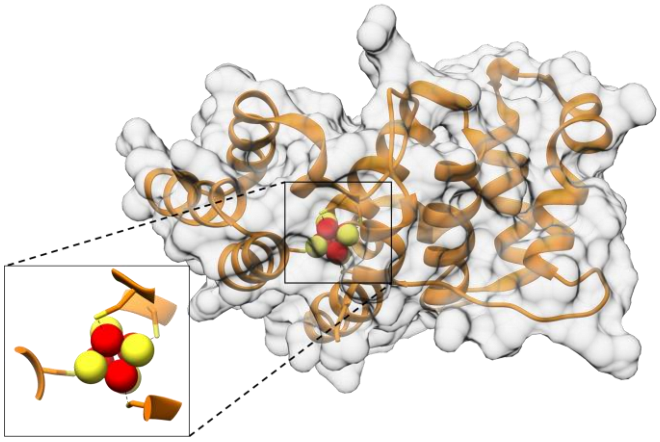

Figure 1.6: X-ray crystal structure of yeast p58C. The structure (PDBID 6DI6) is depicted in a both surface and ribbon representation to highlight the extent to which the 4Fe-4S cluster is buried in the protein matrix. The inset shows how the cluster is ligated with 4 Cys side chains, which are depicted with sticks. Each Cys residue interacts with one iron atom (short dotted lines, visible for on three of the residues). Iron atoms are shown as red spheres and sulfur atoms as yellow spheres.

One interesting alternate hypothesis is that the 4Fe-4S cluster in primase serves as a redox sensor at the replication fork, critical to maintaining redox homeostasis during replication. The purported mode of action would be that the cluster inhibits replication progression when the cell is under oxidative stress. Genetic experiments in budding yeast were performed in which the primase 4Fe-4S cluster was disrupted in combination with known superoxide dismutase mutations that lead to increased sensitivity to redox stress; the yeast grew poorly and had a major defect in replication initiation [74]. These observations are intriguing in light of the recent

discovery at the replication fork of peroxiredoxin2, a eukaryotic redox sensor that interacts with the pol-prim associated Tipin [75]. Further investigation of the role of pol-prim in response to oxidative stress will be of intense interest with respect to clarifying the role of the 4Fe-4S cluster in primase.

A critical insight into the p58C 4Fe-4S cluster was made in early 2107 when a report appeared demonstrating that the cluster is redox-active when bound to nucleic acid substrates and can engage in DNA CT [76]. An electrochemical approach was used to manipulate and monitor the redox state of the cluster, showing that charge can be transported through the protein and the duplex portion of the DNA substrate, and implicating the redox state of the cluster in governing the affinity for substrate. In particular, the data strongly implied that reduction of the Fe-S cluster promotes disengagement from the substrate. Subsequent studies showed that these redox-sensitive properties are conserved between yeast and human primase [77]. Moreover, mutations that abrogate charge transport cause defects in both initiation and termination of primer synthesis, and in one notable case, lethality in yeast [77, 78]. Further studies should clarify how and in what manner changes in the redox state of the primase 4Fe-4S cluster affects priming.

Primase is not the only polymerase that contains a 4Fe-4S cluster. In fact, with improved recombinant expression and purification methods, 4Fe-4S clusters have been identified in a number of family B polymerases, including pol α, pol δ, pol ε, and pol ζ. After discovery of the 4Fe-4S cluster in primase, clusters were proposed to exist in other polymerases [79]. The authors went on to show that mutations of Cys residues predicted to chelate the cluster in pol δ are synthetically lethal with mutations of the Fe-S cluster assembly machinery. The C-termini of the family B polymerases are structurally similar (Figure 1.7) and the observation of corresponding cysteine mutations that are synthetically lethal with mutations in Fe-S cluster machinery was also shown for pol α, pol ε, and pol ζ [79].

Interestingly, all four replicative polymerases (α, δ, ε and ζ) contain two sites that could chelate a cluster in their C-terminal domains: CysA and CysB. Electron paramagnetic resonance studies of isolated recombinant C-terminal domains showed that pol δ, pol ε, and pol ζ exhibit 4Fe-4S cluster signals and that these are associated with the CysB motif. The absence of a signal for pol α was attributed to the lability of the cluster in an aerobic environment and the very poor structural stability of the C-terminal domain of pol α in the absence of the p68 regulatory subunit.

A crystal structure of the p180C domain in complex with the p68 subunit was reported in 2015 (Figure 4B) [43]. In this structure, both the Cys-A and Cys-B sites contain Zn^{2+} ions. The authors noted that the domain can accommodate either a 4Fe-4S cluster or a Zn^{2+} ion, and that the presence of Zn^{2+} could be due to incorporation of spurious metals as a result of producing the sample by recombinant overexpression in *E. coli* [80]. The presence of oxygen-insensitive Mg^{2+} or Zn^{2+} in place of an Fe-S cluster has been observed for a number of Fe-S cluster-containing proteins [52, 54]. It is well-documented that Fe-S clusters are sensitive to oxygen and often require anaerobic purification and handling [53, 55]. Until the purification and characterization are carried out anaerobically, it is impossible to be certain whether the p180C domain of pol α does or does not contain a 4Fe-4S cluster.

Insights into the mechanism of polymerase α - primase

Biochemical studies of pol-prim *in vitro*, along with 3D structures, have been vital in generating knowledge of the mechanisms by which primase and pol α generate primers. The studies have been greatly enabled by the fact that these two enzymes maintain at least some of their biochemical functions when separated from each other. Moreover, even the isolated catalytic domains, p48 and p180cat, also retain some biochemical activity. Because pol-prim is a complex dual enzyme and the components are easier to produce and work with, the majority of *in vitro* investigations of priming mechanisms have been performed with either isolated primase, isolated p180cat, or soluble fragments of the pol-prim tetramer.

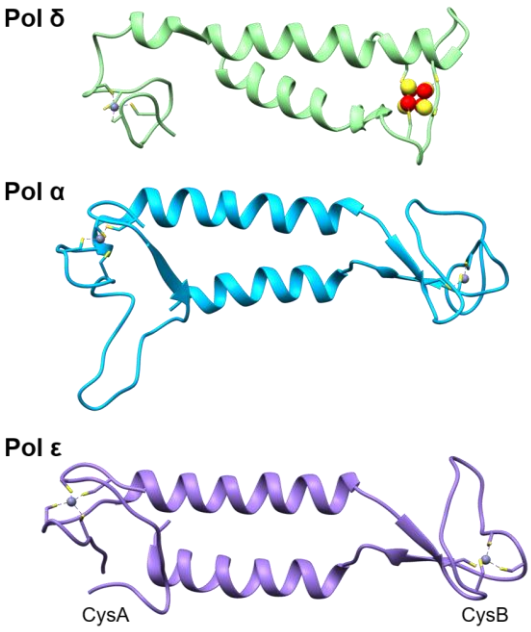

Figure 1.7: Comparison of the C-terminal domains of polymerase δ, polymerase α, and polymerase ε. The structures shown are from PDBID 6TNY, 5EXR, and 5VBN, respectively. Each CysA site has a Zn^{2+} ion (purple sphere) coordinated by 4 Cys side chains depicted as yellow sticks. The CysB site of pol δ contains a 4Fe-4S cluster ligated with 4 Cys side chains depicted as yellow sticks; red and yellow spheres are drawn for the Fe and S atoms, respectively. The CysB sites of pol α and pol ε are occupied by Zn^{2+} ions. Dashed lines are drawn for segments of the protein that are not visible in the structure.

The initial RNA priming step

DNA primase has been the object of intense investigation because it is the sole enzyme capable of initiating oligonucleotide synthesis on a DNA template without a primer and is therefore responsible for initiating daughter strand synthesis in replication. In addition, it has the curious property of synthesizing initial RNA primers of limited length (7-12 nts). These properties are fundamental to primase function and are observed for both the full pol-prim tetramer and the isolated primase heterodimer. Primase synthesizes the RNA primer in two steps: formation of the initial dinucleotide and extension from the dinucleotide (Figure 1.8, steps 1 and 2). Simultaneous binding of template DNA, nucleotides that are incorporated into the daughter

strand, and catalytic metals is required to generate the initial dinucleotide; this is the rate-limiting step in RNA priming. The subsequent elongation of the dinucleotide is much more rapid [81, 82].

RNA primer initiation

The primase active site was identified because the p48 subunit contains the catalytic residues conserved in eukaryotic primases. This was confirmed by mutagenesis studies in yeast cells [35, 83]. Interestingly, even though p48 contains the active site, its intrinsic affinity for single stranded and RNA primed templates is weak. Crosslinking experiments with photoactivatable nucleotides generated no observable template-p48 species, only modified p58 species [84]. Recently, electrophoretic mobility shift assays (EMSAs) revealed that the isolated p58C domain has a very similar affinity for an RNA-DNA junction substrate as the intact primase heterodimer [85]. These observations suggest that RNA priming requires both primase subunits.

Priming assays analyzing the *de novo* RNA synthesis activity of primase with mutations in p58C indicate that this domain has a key role in primer synthesis and counting; deletion of the domain impaired initiation of primer synthesis and completely abolished counting. Alanine scanning mutagenesis coupled with *de novo* RNA synthesis assays identified residues R302, R306, and K314 as essential for primer initiation and elongation[24]. The crystal structure of the p58C-product complex shows that R302 and R306 make strong contacts with the 5’ nucleotide (Figure 1.3C) [38]**.**

Taken together, these results confirm that both the p48 and the p58 subunits are required for priming, and suggest a mechanism by which dinucleotide synthesis occurs. The p58C domain binds the template DNA and the 5’ nucleotide, and p48 binds the 3’ nucleotide and provides the active site for polymerization of the two nucleotides complementary to the template. In this model, p58C must be positioned over the active site of p48 for initiation (generation of the first dinucleotide) to occur (Figure 1.8, step 1).

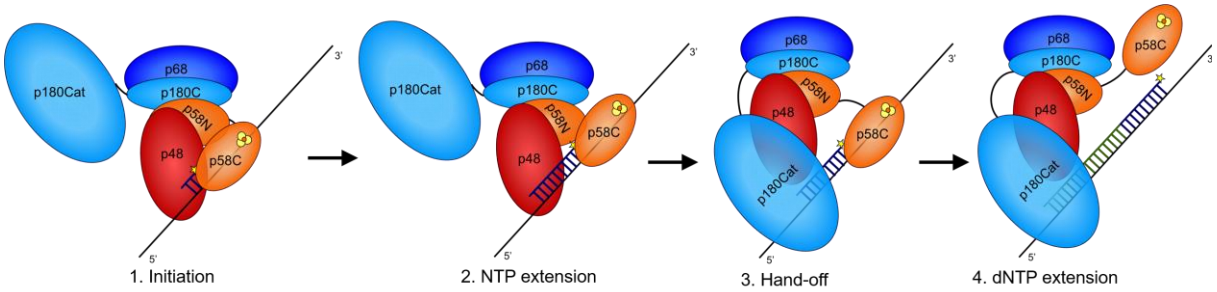

Figure 1.8: The four steps of primer synthesis by DNA polymerase α - primase. (1) Initiation: The first dinucleotide is formed when p58C swings into position over the p48 active site, binds the template DNA and the 5' nucleotide (star), as p48 binds catalytic metals and the 3' nucleotide. (2) NTP extension: p48 rapidly elongates the dinucleotide to 7-12 nts. p58C is thought to remain bound to the 5' nucleotide throughout. (3) Hand-off: exchange of the RNA primed template from the p48 active site to the p180cat active site. (4) dNTP extension: p180cat rapidly extends the RNA primer by an additional ~20 dNTPs (green).

Remarkably, despite the large number of crystal structures available, none show primase in this configuration (Table 1.1). This is a by-product of the inability to crystallize primase (or pol-prim) in complex with the template DNA and nucleotide co-factors required for initiation. The only available crystal structure of free primase occupies an open configuration with p58C extended far away from the p48 domain (Figure 3A) [34]. Hence, a significant reorganization, mediated by the flexible linker tethering p58C to the p48-p58N platform, would be required to attain the active configuration. We and others propose that the positioning of p58C is the rate limiting step of RNA primer initiation [78, 82]. However, direct evidence is lacking; structures of primase in the active configuration are required to convincingly determine the mechanism of RNA primer initiation.

RNA primer elongation and counting

Once the initial dinucleotide is formed, its extension to 7-12 nts is relatively rapid. However, generation of the primer length product is relatively inefficient overall. *De novo* RNA synthesis assays with isolated primase revealed that the most abundant product is a dinucleotide rather than primer length primers of ~7-12 nt [30, 31, 34, 82]. This indicates that once the dinucleotide is formed, the primase-template-dinucleotide complex more readily dissociates than extends on to a primer length product. The abundance of dinucleotide products

has been attributed to the low annealing temperature of the dinucleotide to the template. Support for this hypothesis was provided by a series of *de novo* RNA synthesis assays with isolated primase, which invariably produced many times more dinucleotide products for every primer-length product [24, 30, 82].

After extension to approximately 7-12 nucleotides, primase pauses and the substrate is handed off to pol α (Figure 1.8, step 3). In *de novo* RNA synthesis assays with isolated primase, a low level of primer multimers were observed, whose abundance increased over time [30, 34, 81, 82]. These were believed to arise because primase can either dissociate from the primer-length primer or re-engage the same or a different primer and extend it by another primer-length. However, it turns out that primer multimers are not generated in assays with the intact pol-prim [30, 31]. Hence, these multimers are viewed as artifacts of working with isolated primase *in vitro*.

The termination of elongation at only 7-12 nts is the most notable aspect of RNA priming. The mechanism by which primase is able to 'count' the primer length has been a subject of intense speculation, yet remains undefined. Based on the available data so far, the unique 4Fe-4S cluster-containing p58C domain appears to be the key to the ability of eukaryotic primases to count. Already in early studies using d*e novo* RNA synthesis assays, p58 deletion and missense mutations implicated the p58 subunit in counting [24].

Subsequent crystal structures, binding assays, and primer elongation assays by Tahirov and coworkers suggested that the interaction of p58C with the triphosphate of the 5' nucleotide is particularly important. One informative study revealed that primase preferentially extends, and counting is enhanced for, a primer that has a triphosphate on the 5' nucleotide relative to a primer that has a monophosphate on the 5' nucleotide [85]. These observations led to the proposal that the p58C domain remains bound to the triphosphate of the 5' nucleotide throughout primer synthesis. In this model, p58C and p48 interact with the primer and template DNA throughout elongation, moving apart as the primer elongates (Figure 1.8). This is an

attractive hypothesis as it is supported by data indicating p58 has a role in initiation, elongation, and counting. However, while elongation and counting are enhanced for primers with a triphosphate on the 5' nucleotide, primase does count properly when extending primers lacking the triphosphate on the 5' nucleotide [25, 76]. Moreover, studies from several other groups using a range of different techniques and pol-prim constructs report that the difference in affinity is minimal between substrates without or with a 5' triphosphate [86, 87]. Hence, the importance of the triphosphate on the 5' nucleotide remains an open controversy.

Over the years, three mechanisms for counting have been proposed. In all cases, the flexible tethering of p58C through the ~20 residue linker to the p48/p58N platform plays a major role. In the simplest model, the linker physically limits the distance between the active site in p48 and the template binding region of p58C, preventing primer extension beyond a defined primer length. However, *de novo* RNA synthesis assays with p58 mutants with different linker lengths had no apparent effect on the ability of primase to synthesize products of the appropriate length, suggesting that this hypothesis is not sufficient to describe how primase can count [34]. A refined version of this mechanism attributes counting to p58C remaining bound to the 5' nucleotide throughout the RNA priming step and encountering steric hindrance near the end of its catalytic cycle [38]. In this model, as the primer elongates, p58C moves away from the p48 active site until it is hindered from further movement by the p48-p58N platform. One issue with this model is that it is inconsistent with the generation of the primer length multimers that are observed in primer elongation assays.

The third proposed mechanism for counting includes the movement of p58C away from the active site of p48 as RNA primer grows, but also invokes a role for change in the redox state of the 4Fe-4S cluster in p58C [76, 77]. This novel concept is derived from the observation that p58C is more tightly associated with substrate when the 4Fe-4S cluster is oxidized, then when it is reduced. In this model, the cluster switches from oxidized to the reduced state after the primer reaches the 7-12 nt primer length, thereby driving disengagement of primase from the substrate.

In summary, although several strong hypotheses have been proposed, there is not yet a comprehensive explanation for how primase counts. While each of the three proposed mechanisms has some support, the dearth of relevant structures has inhibited understanding of not only the structural mechanism for primer length counting, but of the overall action of the primase subunits in generating the RNA primer.

The DNA extension step

The extension of the initial RNA primer is performed by pol α and involves two key steps: hand-off of the substrate from DNA primase to pol α, and synthesis of ~20 DNA nts. The term DNA polymerase α has a storied past as it was originally assigned to the first protein replicative polymerase activity identified. In fact, it was a number of years before the distinct active sites for the RNA and DNA synthesis activities were assigned and the full subunit structure was identified (Figure 2). The ability to isolate and study the pol α subunits has been critical to defining their specific functions in generating the RNA-DNA hybrid primer.

Because pol α adds only a finite number of nucleotides (~20) to the initial RNA primer before it hands off the substrate to the processive polymerases δ and ε, it appears to have the ability to count. However, unlike primase, counting is not a fundamental property of pol α. Initially, only limited extension was observed in RNA primer extension assays using the isolated p180cat and the oft-used poly dT template [26]. However, the substrate seems to be peculiar, a result of low processivity, because assays with random sequences or activated calf thymus DNA extend to the end of a variety of long templates [27, 31, 33, 88]. Hence, extension by pol α of the RNA primer by only ~20 nts must be attributed to other replisome factors.

Primase to pol α hand-off

Before pol α can act, the initial RNA primer must be handed-off from primase to pol α. Although absolutely essential, hand-off is very complicated and consequently, poorly understood. It requires not only transfer of the substrate but also reorganization of the pol-prim architecture (Figure 1.8). One thing that is clear is that termination of RNA priming by primase

and hand-off are tightly coupled. As noted above, *de novo* RNA synthesis and elongation assays show that the presence of pol α directly alters product distribution, at least part of which can be attributed directly to transfer of the substrate from the primase to the pol α active site [89]. In assays performed on full length pol-prim with aphidicolin blocking the pol α active site, higher levels of dinucleotide products and of primer multimers are generated with the inhibitor, similar to what is observed for isolated primase.

Only limited insights have been obtained about the structural basis for the transfer of the RNA primed template from primase to pol α. There is no doubt that a very substantial rearrangement of the pol-prim architecture must occur and that the flexible linkers between p58N and p58C, and between p180C and p180cat, are critically important. One model has been proposed based on available crystal structures [38]. In this model, movements of subunits during the catalytic cycle are proposed. However, since there are no pol-prim structures with co-factors and substrates along the trajectory of priming, such models remain purely speculative.

Considering the mechanism for hand-off at its most basic level, when the RNA primer reaches an adequate length either primase releases the substrate or the p180cat domain dislodges the substrate from primase. The simplest explanation would be that the affinity for the primed template of p180cat is higher than that of primase. For example, Tahirov and coworkers proposed that hand-off is a by-product of the intrinsic flexibility of the p58 and p180 linkers, and tighter binding of the RNA primed template by p180cat than primase [38, 85]. However, in an assay that monitors the efficiency of adding the first nucleotide by pol α, intact pol-prim was much more efficient than the system in which p180cat was added back in trans to the rest of the

pol-prim complex, even with p180cat in excess [44]. This suggests that p180cat is unable to simply take the primer from primase. What then is the driving force for hand-off?

In collaboration with the laboratory of J.K. Barton, we have proposed a mechanism in which 4Fe-4S cluster redox provides the unknown driving force. This model is based on the observation that altering the redox state of the 4Fe-4S cluster in p58C leads to an apparent

decrease in affinity of primase for substrate [76-78]. In this model, primase with an oxidized 4Fe-4S cluster binds template and initiates primer synthesis. As the primer nears 7-12 nts in length, the 4Fe-4S cluster is reduced, leading to dissociation of primase and allowing p180cat access to the primer. This would necessitate the presence of a redox active partner to drive the primase 4Fe-4S switch from an oxidized to a reduced state. Since other family B polymerases are thought to contain a 4Fe-4S cluster, they might fill this role. The still-controversial cluster in the p180C domain of pol α is the obvious first choice and is under investigation as the potential redox partner.

DNA primer extension

After hand-off of the RNA primed template, p180cat extends the primer strand by ~20 deoxy-ribonucleotides (Figure 1.8, step 4). p180cat functions as an independent unit due to its flexible tether to p180C, which enables it to be studied as an isolated domain. Like all DNA pols, pol α can only elongate from a primed template. However, pol α is biochemically unique in that it can elongate efficiently not only from a DNA duplex but also from the chimeric RNA-DNA duplexes generated by primase [40, 87]. Kinetic studies of the rate of nucleotide addition showed that p180cat extends DNA primers more efficiently than RNA primers, but the latter are elongated with higher processivity [39, 87]. Pol α can extend from as small as a 4 nt primer and a template of any length. However, it has maximum efficiency extending primers of ~9 nts, which matches well to the structural footprint of p180cat on a primed substrate [85, 90].

Pol α has been observed to elongate leading strand primers up to ~3 kilobases in recombinant replisome reconstitution assays [33]. However, in cells, it extends the RNA primer by a much more specific length. This apparent ability to generate primers of a defined length has led to a debate as to whether pol α has the inherent ability to count, like primase. A mechanism was proposed, which argued that as pol α extends an RNA primer, the shape of the primer changes from an A-form to a B-form duplex. In this model, the change in structure of the substrate causes the polymerase to stall as the active site struggles to accommodate the

changing duplex. An assay that showed limited processivity and polymerase stalling at ~30 nts on a poly(dT) template was used as support for this model [26]. However, follow-up studies from other groups suggested that the limited processivity and stalling was caused by secondary structure in the poly(dT) substrate and the choice of divalent metal ions in the primer elongation reaction. On a scrambled template, pol α extends primers without stalling [25, 27, 39]. Furthermore, recent studies with recombinant yeast pol-prim indicate that pol α is as processive as pol ε *in vitro* [33, 91-93]. This suggests that termination at ~20 nts in cells or cell extracts is not due to changes in substrate structure but rather the presence of other factors at the replication fork.

Termination and hand-off to pol δ and pol ε

During replication, the hand-off of the primed template from pol-prim to pol δ or pol ε is essential for faithful duplication of DNA, yet the mechanism(s) are still unknown and highly debated. An important role in primer termination by pol-prim for the polymerase clamp loader replication factor C (RFC) was established in experiments using synthetic DNA with calf thymus proteins and independently, using the SV40 model system [19, 88, 94, 95]. More recent studies of the reconstituted replication reaction with purified Cdc45, Mcm2-7, GINS, pol-prim, RFC and PCNA, in the absence of pol δ and pol ε, revealed that pol-prim will generate daughter strands of up to 3000 nts on the leading strand and hundreds of nts on the lagging strand. When the hand-off partners pol δ or pol ε were added to the reactions, synthesis of daughter strands by pol-prim was significantly curtailed [33]. This suggests that RFC is a contributing but not the sole factor limiting DNA synthesis by pol-prim.

In single molecule fluorescence experiments, pol-prim is seen to associate and dissociate multiple times with the replisome once a minimal threshold in concentration is surpassed [96]. The authors proposed that the repeated binding and unbinding facilitates polymerase hand-off, which led to the hypothesis that on the leading strand, as pol-prim encounters the CMG helicase, its dynamic association with the primed template facilitates hand-

off to pol ε. Given the greater complexity of the events on the lagging strand, no corresponding mechanistic model for hand-off to pol δ was proposed.

As proposed for hand-off from primase to pol α, 4Fe-4S cluster redox may also provide a mechanism for stimulating hand-off of the fully primed template from pol α to pol δ or pol ε. All three of these polymerases contain 4Fe-4S clusters [79, 80, 97], and the 4Fe-4S cluster in pol δ has been shown to be redox active and able to influence DNA synthesis *in vitro* [98]. Although corresponding studies of pol α and pol ε have yet to be reported, it is logical to assume their clusters function like those in primase and pol δ. If they do function similarly, it is conceivable that tuning of substrate affinity via changes in the redox state of the 4Fe-4S cluster could drive hand-off from pol α to pol δ or pol ε. As first proposed for primase, this would involve redox switching between 4Fe-4S cluster lower affinity reduced states to higher affinity oxidized states. Communication between the clusters through stacked bases in duplex regions of nascent daughter strands provides an intriguing solution for how the redox switching between polymerases occurs. Clearly, such a highly speculative model requires a substantial amount of supporting data and intensive testing before it can be accepted as a viable mechanism for hand-off.

Experimental Approaches[2]

The research in this dissertation primarily focuses on *in vitro* analysis of recombinant primase, the primase 4Fe-4S cluster domain, and a fragment of the pol-prim heterotetramer. Below, the most commonly used techniques in this dissertation are discussed, including UV-VIS absorption spectroscopy, circular dichroism spectroscopy, fluorescence polarization anisotropy, x-ray crystallography, and priming assays. Information about maintaining anaerobic environments is also discussed.

[2] Parts of this chapter was published as Holt ME, Salay LE, & Chazin WJ., A Polymerase with Potential: The Fe-S Cluster in Human DNA Primase. Methods Enzymol, 2017. 595:361-390.

UV-VIS absorption spectroscopy

Many biomolecules and transition metals absorb light at specific wavelengths. Absorption spectroscopy at these specific wavelengths provides a simple way to characterize and quantify biomolecules. Light in the ultraviolet (UV) and visible (VIS) regions are particularly useful. Biological samples typically contain various moieties that absorb light in the UV region. Notably, aromatic residues in protein molecules, such as tryptophan, tyrosine, and phenylalanine residues, and disulfide bonds absorb light around 280 nm. The peptide backbone of a protein absorbs light strongly at ~190 nm and weakly at ~215 nm. Absorbance at these wavelengths provides an alternate measurement if the protein contains very few aromatic residues. In nucleic acids, nucleobases strongly absorb at ~260 nm. In all cases, the contributions of the individual chromophores can vary based on its microenvironment [99].

The absorption (A) of the sample is related to the concentration (c), pathlength (l), and molar absorptivity (ε) of the sample. This relationship can be described by Equation 1, a representation of the Beer-Lambert Law.

$$A = \varepsilon c l \quad \text{(Equation 1)}$$

The molar absorptivity can be estimated by the number of moieties that contribute to the absorption. Thus, with the absorption, the pathlength, and the calculated molar absorptivity, the concentration of the analyte can be estimated.

Many analytes absorb light in the visible region. In particular, 4Fe-4S clusters exhibit a broad absorbance peak at 410 nm [100]. Measuring the absorbance at 410 nm can be used to estimate the concentration of 4Fe-4S cluster in the sample. Other analytes that absorb light in the visible include colored solutions, including those used in colorimetry, such as ferene. Ferene (3-(2-pyridy1)-5,6-bis(2-fury1)- l,2,4-triazine) is a sensitive and soluble chromogenic ligand that binds to Fe (II) with a stoichiometry of 3 ferene molecules to 1 Fe (II) molecule [101]. It is used to determine an accurate concentration of iron in a sample.

Typically, in colorimetric assays, a standard curve is generated by monitoring the absorbance of known concentrations of a sample at a reporter wavelength. Then, the concentration of the analyte is determined by comparing the absorbance of the unknown analyte to that of the standard.

Circular dichroism spectroscopy

Circular dichroism (CD) spectroscopy is a quick and relatively straightforward method to analyze secondary structure content (e.g., helices, beta sheets, random coil) and tertiary structure related to packing of aromatic side chains in a hydrophobic core of a protein molecule [102]. This technique uses the difference in left- and right-handed circularly-polarized light as it is passed through a sample. Backbone secondary structures and aromatic residues in proteins give rise to characteristic contributions to the CD spectrum in the range of 190–260 and 250–330 nm, respectively. This allows for the secondary structure content and packing of the hydrophobic core to be analyzed from CD spectra. The data are often used to compare mutants of a protein to assess if the mutations perturb the structure. The characteristic spectrum for

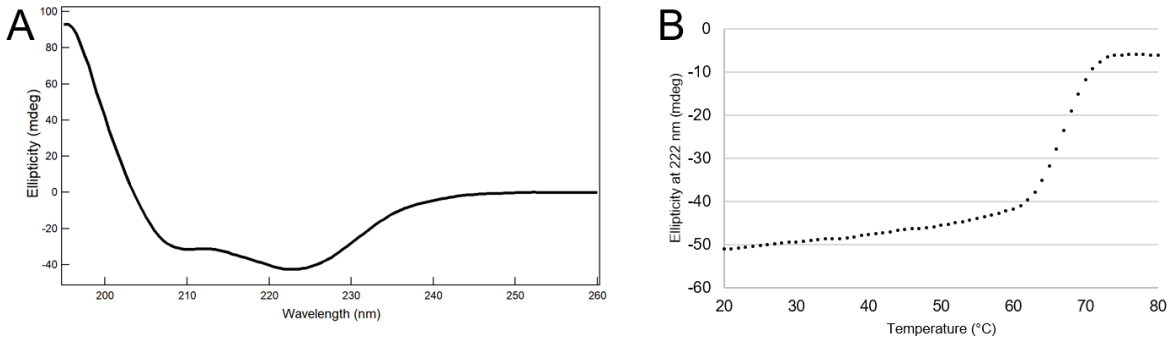

Figure 1.9: Example of CD analysis for the primase 4Fe-4S cluster domain. A.) CD spectrum of the domain from 190-260 nm. Note the characteristic local minima at 208 nm and 222 nm for proteins with high alpha helical content. B.) thermal denaturation curve for the same domain, monitored at 222 nm from 20-80 °C.

p58C is shown in Figure 1.9A. Nucleic acids can also be characterized using this method [103], though this will not be discussed during this dissertation.

Another useful application of CD spectroscopy is to track thermal or chemical denaturation and thereby monitor the stability of biomolecules [104, 105]. In this assay, heat or a denaturant (i.e. urea) is applied to the sample to promote denaturation. The ellipticity, and thus the secondary structure content, is monitored at a reporter wavelength as the sample denatures (Figure 1.9B). This approach is most frequently used to estimate the relative stability of a protein under different conditions or to compare denaturation midpoints of different variants.

Maintaining anaerobic environments

Proteins that contain iron-sulfur clusters are uniquely susceptible to oxidative degradation by atmospheric oxygen. In order to counteract this, many iron-sulfur cluster proteins must be manipulated in an anerobic environment. Anaerobic chambers can maintain an argon or nitrogen atmosphere with less than 5 ppm O_2. In order to generate this environment, silica coated palladium catalysts convert oxygen and hydrogen into water. The water molecule then adsorbs to the silica coat surface. Importantly, this chemical reaction generates heat. It is necessary to take measures to maintain a cold environment for optimal protein stability. Solid ice is not ideal for this environment as it can evaporate and affect the efficiency of the oxygen to water reaction. Icepacks and dry aluminum beads provide an adequate alternative to keep solutions and samples cool. This environment, coupled with deoxygenated buffers, allows for the characterization of iron-sulfur cluster proteins with a minimum of oxidative degradation.

Priming assays

Critical mechanistic insights into primase function have been obtained using two biochemical techniques: (1) *de novo* RNA synthesis (initiation) assays requiring synthesis without a primer; (2) elongation assays that extend from an existing primer. In a *de novo* RNA synthesis assay, primase is incubated with radiolabeled nucleotides, template DNA, and catalytic metals (Mg^{2+} or Mn^{2+}). The results are interpreted in terms of the total amount of products at different timepoints or by analyzing product length and product abundance over time. In an elongation assay, primase is incubated with radiolabeled nucleotides, template DNA

in complex with a primer, and catalytic metals (Mg^{2+} or Mn^{2+}). The results are interpreted by analyzing the amount and rate of extension to primer length products and the presence of multimers of primer length products. Modifications of these priming assays, specifically titrating important components, are easily performed and mechanistically informative.

In this dissertation, the results of initiation and elongation assays are analyzed after denaturing polyacrylamide gel electrophoresis (PAGE). This technique uses a gel matrix and an electric field to separate molecules by size. The gel can be visualized by phosphor imaging, where the gel-bound radiolabeled product emits energy that is absorbed by a phosphor layer. The phosphor layer has the property of photostimulable luminescence, where the energy can be stably absorbed and released as light by application of a laser. The intensity of the light is proportional to the amount of radiolabeled product in the gel, facilitating quantification of the products.

Fluorescence polarization anisotropy

Fluorescence is a phenomenon that results from excitation of a fluorophore. It occurs when light of a specific wavelength excites an electron in the fluorophore. The electron subsequently relaxes to its ground state and emits the excess energy as radiation. The wavelength of the emitted radiation is always at a lower wavelength than the wavelength used for excitation. It is particularly useful for labeling ligands, reactants and products for use in biophysical and biochemical assays.

One common method where fluorescence is used is a fluorescence polarization anisotropy assay. This is a method that can be used to quantify binding affinities in solution at equilibrium [106]. In a fluorescence polarization anisotropy assay, polarized light is applied to a sample containing a fluorescent probe attached to molecule. The difference in intensity between emitted parallel and perpendicular polarized light (anisotropy) is measured as a function of ligand concentration. The degree of anisotropy is proportional to the extent of binding at equilibrium. This arises because fluorescent molecules tumble in solution according to Brownian

motion. Upon interaction with a binding partner, the fluorescent probes tumble slower, as they are part of a larger complex. This information can be used to calculate the dissociation constant (K_D), which describes the propensity of the probe-ligand complex to dissociate. This approach is used extensively in this thesis to measure the DNA binding affinity of different pol-prim constructs and variants, run in a mode where DNA substrates are synthesized with a fluorophore and the fluorescence polarization is monitored as protein is added to the substrate.

X-ray Crystallography

X-ray crystallography is the most common method for determining three-dimensional structures of biomolecules at atomic resolution. This can be used for biomolecules, such as protein, DNA, RNA, etc, as well as small molecule compounds. In this dissertation, crystallization is used as a method to characterize protein structure (Figure 1.10).

X-rays are a form of electromagnetic radiation that typically have a wavelength of ~10 – 0.1 Å. Due to their size, x-rays are well-suited for examining atomic bonds. An atomic bond consists of overlapping electron clouds. These electron clouds scatter x-rays. The scattering of a single bond or even a single molecule is insufficient to observe. To overcome this, an array of regularly occurring molecules in a crystalline lattice is prepared, which amplifies scattering and creates a diffraction pattern. The diffraction pattern can be used to back-calculate the electron density, providing a three-dimensional model of the biomolecule [107, 108].

There are several methods used to obtain crystals. All involve allowing the molecule of interest to precipitate out of the solution in a very orderly way, i.e. crystallize, which creates an array of molecules that interact in regular pattern. This can be achieved by crowding molecules together in a way that predisposes orderly precipitation [109]. The most common method to induce this is termed vapor diffusion crystallization.

Vapor diffusion crystallization takes advantage of equilibrium in a closed system to encourage crystallization. A very pure sample of interest is mixed with a mother liquor to create a drop. The drop is placed in a closed system with the mother liquor, typically on a slide that

functions as a seal to a mother liquor-containing well. The drop and the mother liquor are allowed to equilibrate; water leaves the drop and enters the mother liquor, thereby concentrating the sample of interest, promoting crystallization.

The stability, purity, and concentration of the sample as well as the composition of the mother liquor are key to generating crystals in this way. Since crystallization depends on an ordered array of regularly-interacting molecules, disorder typically prevents this. It is important to remove as many disordered regions as possible and to verify that the sample is well folded and homogenous.

There are three steps to crystal generation: nucleation, growth, and growth cessation [109]. Nucleation occurs when the first biomolecules associate in a way that forms the crystal lattice of the protein. Additional protein molecules associate with the lattice in a regular pattern, causing crystal growth. Nucleation is typically considered the rate determining step [110]. Furthermore, the incorporation of mutations in a protein molecule can significantly impact the probability of nucleation, to the point where the protein will not crystallize without external intervention.

One common way to overcome this is to use a technique called micro-seeding [111]. In this technique, a crystal of a related protein is generated, usually a more stable mutant or the wild-type protein. This crystal is resuspended in mother liquor and crushed. Microscopic fragments of the crushed crystal are added to crystallization drops containing the mutant protein. These microscopic fragments function as a nucleation site for the protein of interest, a platform upon which molecules can associate in an orderly way. This circumvents the need for nucleation. The use of a different protein as a seed is not typically an issue in processing crystallography data. Due to the nature of crystallography, which requires many molecules in a crystalline lattice, the diffraction from the protein of interest drowns out the diffraction from the crushed crystal used as a seed.

After obtaining a crystal, it is necessary to collect x-ray diffraction data (Figure 1.10A, B). This is done by placing the crystal in an x-ray beam and measuring the scattered x-rays at various angles. The scattered x-rays have both an amplitude and a phase. Because multiple scattering events occur in a crystal, each scattered x-ray interacts with others, leading to constructive (in-phase) and destructive (out-of-phase) interference. The collected data are the sum of the scattered waves. The diffracted radiation has a different amplitude and relative phase from the contributing waves. Both the amplitude and the phase information are necessary to reconstruct the electron density of the scatterer. However, it is only possible to measure the intensity of the diffracted x-rays, which is proportional to the amplitude of the wave. The phase information is lost.

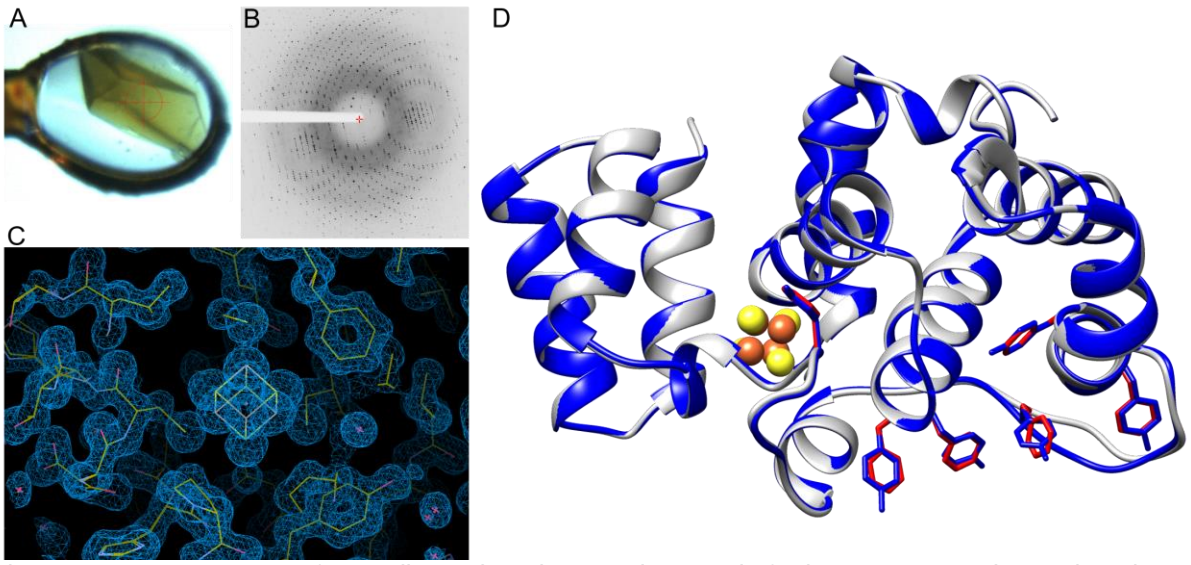

Figure 1.10: Components of crystallography. A) a protein crystal of primase 4Fe-4S cluster domain. B) a diffraction pattern of the protein crystal. C) electron density map and initial model. D) final model calculated from the density map (grey) superimposed on the wild-type protein (blue). Highlighted are the 4Fe-4S cluster (yellow and orange) and the mutations characterized by this crystallization experiment (shown in sticks and colored red).

There are several methods used to compensate for this lost information. One of the most common methods is molecular replacement [112, 113]. This method takes advantage of the library of structures for which the phases are known. Using a characterized model that is closely related to the molecule of interest, it is possible to approximate the locations of scatterers and

construct a theoretical diffraction pattern that matches the observed diffraction pattern. The phases are then approximated from the model and applied to the experimental data. Thus, an initial electron density map and model can be created (Figure 1.10C). The electron density map can be improved by improving the model in programs like *Coot* [114] and refining the data in programs like Refmac [115] or Phenix [116] In this dissertation, molecular replacement is the method primarily used to determine the phases for crystals of mutant primase 4Fe-4S cluster domain, with the wild-type protein serving as the initial model.

Typically, several iterative rounds of model building and refinement are necessary to generate a final model that best represents the electron density of the scatterer (Figure 1.10D). In this dissertation, these models are used to compare the structure of mutant proteins to the wild-type to analyze the effects of mutations on the atomic structure of the protein.

Closing Remarks

Pol-prim is a fascinating complex. Despite over fifty years of intense study, fundamental aspects about pol-prim remain enigmatic. How does handoff between the primase active site and the pol α active site occur? What is the purpose of the 4Fe-4S cluster in primase? Are the 4Fe-4S cluster in primase and the question of intramolecular primer handoff related? If not, what are the other possible roles of the 4Fe-4S cluster in primase? Do 4Fe-4S clusters play a larger role at the replication fork?

The research described in this dissertation seeks to understand the answers to some of these questions. In Chapter Two, the primase 4Fe-4S cluster domain (p58C) was discovered to be redox-active. The redox state of the 4Fe-4S cluster is shown to be associated with the ability to strongly or weakly associate with a nucleic acid substrate. Furthermore, the implications for priming activity and primer handoff are discussed. Finally, limitations of the study are addressed and commented upon. Chapter Three furthers the investigation of 4Fe-4S cluster redox by performing structural and functional characterization of the p58C domain in solution. This confirms that the results discussed in Chapter Two are not an artifact of and are intrinsic to the

p58C domain of primase. Chapter Four applies the knowledge gained from the previous chapters to investigate the redox-switching ability of the full primase heterodimer. Chapter Five uses the *Saccharomyces cerevisiae* model system to probe if the ability to engage in redox switching is conserved and, when disrupted, how this affects yeast cells. Chapter Six seeks to understand the difference between the efficiency of human and yeast p58C in redox switching and the role of intermediate residues mediating the redox switch. Chapter Seven pivots to show evidence that a 4Fe-4S cluster can exist in pol α and discusses the implications in regard to primase activity. Finally, Chapter 8 summarizes and discusses the results obtained from the research performed for this dissertation.

CHAPTER 2

THE [4FE4S] CLUSTER OF HUMAN DNA PRIMASE FUNCTIONS AS A REDOX SWITCH USING DNA CHARGE TRANSPORT[3]

Introduction

The ability of DNA to transport charge over long range represents an intriguing potential regulatory mechanism in biology. DNA charge transport (DNA CT) provides a rapid means of signaling among redox moieties coupled into the DNA duplex, as well as a mechanism to sense the integrity of DNA [56, 58, 61, 67, 117, 118]. Remarkably, [4Fe4S] clusters, inorganic cofactors often associated with biological redox chemistry [119, 120], are now being identified in proteins involved in DNA replication [34, 36, 69-73, 79, 121]. The eukaryotic DNA primase enzyme responsible for initiation of replication on single-stranded DNA, for example, is a [4Fe4S] cluster enzyme. The [4Fe4S] cluster in primase has been shown to be essential for activity [34, 36, 69-74, 121], but the role of this cofactor was unclear.

Rapid and accurate copying of genomic DNA in humans and other higher eukaryotes is the product of high fidelity, processive, replicative DNA polymerases [122-125]. While efficient, these enzymes are unable to initiate synthesis of the new complementary strand without a short primer on the single-stranded DNA (ssDNA) template. The task of initiating synthesis of the new DNA strand is the responsibility of a heterotetrameric complex of two specialized polymerases: DNA primase and DNA polymerase α (pol α), both of which were discovered to contain [4Fe4S] clusters [69, 70, 79]. Primase, a DNA-dependent RNA polymerase, generates an initial 8-12

[3] The contents of this chapter were published in O'Brien E, Holt ME, Thompson MK, Salay LE, Ehlinger AC, Chazin WJ, Barton JK. The [4Fe4S] Cluster of Human DNA Primase Functions as a Redox Switch using DNA Charge Transport. Science, 2017. 335 (6327) and in O'Brien, E; Holt, ME; Thompson, MK; Salay, LE; Ehlinger, AC; Chazin, WJ; Barton, JK; Response to Technical Comments on "The [4Fe4S] Cluster Functions as a Redox Switch in Human DNA Primase". Science, 2017. 357 (6348).

nucleotide RNA primer on ssDNA before handing the nascent primer-template off to pol α, which extends the primer by ~20 DNA bases before handoff to the more processive polymerases (δ and ε). X-ray crystal structures have been determined for all globular domains of primase and pol α as well as for the primase heterodimer and the heterotetrameric pol-α-primase (pol-prim) complex [26, 34-36, 38, 42, 71-73, 121]. However, limited structural data have been obtained about catalytically active conformations and architectural changes in the pol-prim tetramer as the primer is initiated, elongated first by primase then by pol α, and subsequently handed off to a processive polymerase. In particular, although the mechanism and structure of the catalytic subunit of primase have been extensively studied [33, 36, 121, 126], the chemistry behind primase transferring a nascent primer to pol α is poorly understood.

Eukaryotic primases are heterodimeric, composed of a catalytic subunit (p48) and a regulatory subunit (p58) [24, 127]. The regulatory subunit contains a C-terminal domain (p58C) that is unique to eukaryotes and contains the [4Fe4S] cluster cofactor required for efficient priming [70]. The biochemical evidence of the role for the [4Fe4S] cluster in primase, in addition to the high energetic cost [120] paid by cells to assemble and load this cofactor into an enzyme, argues for a functional rather than structural role for the cofactor [45].

Methods

Pro*tein Expression and Purification*.

Recombinant protein generation of p58C was performed by L.E. Salay. Recombinant protein generation of primase was performed by Dr. M.E. Holt. Recombinant WT and mutant p58C were expressed and purified as previously described [73]. For crystallization of the proteins, an extra affinity purification step was added before size exclusion chromatography. Both WT and mutant p58C were buffer exchanged into 20 mM HEPES (pH 7.2), 2 mM DTT and 200 mM NaCl. Each protein sample was then loaded onto a HiTrap® Heparin column and eluted with a gradient of 20 mM HEPES (pH 7.2), 2 mM DTT and 1 M NaCl. To express primase, full-length p48 and p58 in the pBG100 and multiple cloning site 2 of the pETDuet

vectors, respectively, were co-transformed into BL21 (RIL) D3 *E. coli*. The culture was grown in Terrific Broth at 37° C until it reached an O.D. of 0.5-0.8, at which point the growth was transferred to an 18° C incubator. This was allowed to continue growing until it reached an OD of 1-1.5, at which point protein expression was induced with 0.5 mM IPTG. The cells were harvested after expressing at 18° C for 20 hours. To purify primase, cells were lysed using a sonicator and spun at 50,000 rcf. Supernatant loaded onto a nickel column equilibrated in Buffer A (20 mM Tris, 300 mM NaCl, and 20 mM imidazole (pH 8.0). After washing with five column volumes of Buffer A, the primase was eluted with Buffer B (20 mM Tris, 300 mM NaCl, and 300 mM imidazole (pH 8.0). H3C protease was added to primase-containing fractions, and these were dialyzed in to Buffer A at 4° C overnight. Primase was separated from the cleaved 6xHis tag (and uncleaved protein) by repassing over the nickel column. This sample was further purified by carefully diluting to 150 mM NaCl, loading onto a HiTrap® Heparin column, and eluting with a gradient of 20 mM HEPES (pH 7.2), 3% glycerol, and 1 M NaCl. This was followed by size exclusion chromatography with a Superdex S200 column from GE Healthcare. Primase was eluted into a final storage buffer containing 20 mM HEPES, 150 mM NaCl, 3% glycerol, pH 7.2.

Site Directed Mutagenesis.

Site-directed mutagenesis for the p58C mutants was performed by L.E. Salay. Mutagenesis for the primase heterodimer was performed using the same protocol as described below by Dr. M.E. Holt. The Y309F, Y345F, and Y347F p58C mutants were created using a Q5 site directed mutagenesis kit from New England Biolabs. The following primers were supplied by Sigma Genosys to generate the mutant DNA plasmids. For Y309F, the forward primer was 5'-CCGAATGCAGTTTGGCCTATTTC-3' and reverse primers was 5'-CCTCCATGACGAAGATGG-3'. For Y345F, the forward primer was 5'-TGATAAAGGTTTCTCTTACAACATCC-3' and reverse primers was 5'-AACTTGTCTGGATCCATC-3'. For Y347F, the forward primer was 5'-

AGGTTACTCTTTCAACATCCGTC-3’ and reverse primers was 5’-TTATCAAACTTGTCTGGATCC-3’.

Oligonucleotide preparation.

All oligonucleotide preparation was performed by E. O’Brien. All standard or modified phosphoramidites and DNA synthesis reagents were purchased from Glen Research. Unmodified DNA and 2’-OMe RNA substrates used in electrochemical experiments or primase activity assays were purchased from Integrated DNA Technologies, Inc. DNA sequences for electrochemistry and primase activity assays are shown in Table 2.1. Thiol-modified DNA strands for electrochemistry were made on an Applied Biosystems 3400 DNA synthesizer, with a C6 S-S phosphoramidite incorporated at the 5’- terminus. Single-stranded DNA was purified using standard procedures as described previously [118]. High pressure liquid chromatography (HPLC) using a reverse-phase PLRP-S column (Agilent) was used, and oligonucleotide mass confirmed using MALDI-TOF Mass Spectrometry. Thiol-modified strands were reduced after the initial HPLC purification with 100mM dithiothreitol (Sigma) for 2-3 h in 50 mM Tris-HCl, pH 8.4, 50 mM NaCl. Reduced thiol-modified DNA was purified by size exclusion chromatography (Nap5 Sephadex G-25, GE Healthcare) and subsequent reverse-phase HPLC. Single-stranded oligonucleotides were then desalted using ethanol precipitation and stored in low salt buffer (5 mM Phosphate, pH 7.0, 50 mM NaCl). Duplex DNA for electrochemistry and duplex 2’-OMe RNA/DNA was prepared by quantification of the complementary single-stranded oligonucleotides by UV-Visible spectroscopy, followed by annealing at 90 °C. A mixture of equimolar complementary single-stranded DNA/2’-OMe RNA (50 μM) was prepared in low salt buffer. Thiol-modified duplex DNA substrates were then deoxygenated by bubbling argon gas through the solution for 90 s. Duplex DNA was annealed on a thermocycler (Beckman Instruments) by initial heating to 90 °C, followed by slow cooling to 4 °C over 90 minutes. DNA was quantified using absorbance at 260 nm, with extinction coefficients at 260 nm for DNA or 2’-

OMe RNA obtained using Integrated DNA Technologies online OligoAnalyzer tool. Single-stranded DNA substrates were quantified using UV-Visible spectroscopy and stored in low salt buffer at a stock concentration for activity assays.

Multiplexed Chip Fabrication.

Multiplexed electrode platforms were prepared by Dr. E. O'Brien using standard photolithography techniques, adapted from established protocols [118, 128, 129]. Nine 1 in. by 1 in. chips were patterned on 525 μm thick silicon wafers (SiliconQuest). A thermal oxide layer roughly 4000 Å thick was grown on the silicon wafers using a Tytan tube furnace (Tystar). S1813 photoresist (2 μm layer) was deposited onto the wafers for patterning of the chips before metal deposition. Electron beam evaporation (CHA Industries) was then used to deposit a 3nm titanium adhesion layer followed by a 100nm gold layer, without breaking vacuum between depositions. Metal lift-off using Remover PG (MicroChem) was performed overnight (10-12 h) at room temperature. Wafers were subsequently dried with a nitrogen gun and dehydrated at 140 °C for 10 minutes. A 3 μm layer of insulating SU-8 photoresist was deposited and patterned onto the wafer as described previously [118, 128, 129], with connective wires between contact pads on the edges of the chips and working electrodes in the center were covered but the contact pads and working electrodes left exposed. This ensured a fixed working electrode surface area of 2 mm^2. SU-8 photoresist was cured (150 °C, 15 minutes) and wafers cleaved into individual chips using a Dynatex Scriber/Breaker.

DNA Modified Electrode Assembly/Preparation.

Electrodes were assembled by E. O'Brien. Multiplexed chips were cleaned using sonication in acetone and isopropyl alcohol as described previously [118]. Chips were then dried using argon gas and ozone-cleaned for 15-20 minutes at 20 mW using a Uvo brand ozone cleaner. Clean chips were assembled onto polycarbonate holders with acrylic clamp and Buna-N rubber gasket according to previous protocols, with four quadrants in the chip separated by

fastened gasket and clamp [118]. Duplex DNA substrates, with a thiol modifier at the 5'- end, (25 μM) were deposited in a 20 uL volume onto each quadrant of the multiplex chip. Substrates incubated for 18-24 hours on the gold surface to allow formation of self-assembled DNA monolayer. DNA monolayers were washed with phosphate buffer (5mM phosphate, pH 7.0, 50mM NaCl, 5% glycerol) and subsequently backfilled with 1mM 6-mercaptohexanol (Sigma) in phosphate buffer for 45 minutes. Monolayers are then washed 10 times per quadrant with phosphate buffer and twice per quadrant with TBP buffer (5 mM phosphate, pH 7.0, 50 mM NaCl, 4 mM $MgCl_2$, 4 mM spermidine) to aid in formation of a monolayer with termini accessible for p58C binding. Assembled chips were transported into an anaerobic glove bag chamber (Coy Products) and washed 5 times per quadrant with p58C storage buffer (20 mM Tris-HCl, pH 7.2, 75 mM NaCl), which was previously deoxygenated by argon bubbling (approx. 1 hour per mL of buffer solution) and allowed to incubate at least 1-2 days in the chamber prior to the experiment. Initial cyclic voltammetry scans of the monolayers in p58C storage buffer were performed to ensure monolayer formation on each electrode. All washes were performed with 20 μL buffer volumes on each quadrant. Before scanning, a 200 μL volume was deposited over the chip surface, a bulk solution well for completion of a three-electrode circuit with an external reference and counter electrode.

Mutant Selection and Design.

Mutations in the p58C domain of human DNA primase were designed by Dr. M.E. Holt and Dr. M.K. Thompson based on previously determined structural data [73] and bioinformatics [72] compiled for conserved residues in this domain. Chimera software [130] was used to model the mutations in a 1.7 Å resolution structure of human p58C (PDB 3L9Q) [73]. Mutagenesis and measurement tools were used to model possible point mutations and approximate distances between residues/cofactors. The COSMIC database [131] was used to search for somatic

mutations of the primase large subunit (PRIM2 gene) in cancer. The point mutation Y345C was found and selected for charge transfer and activity assays.

Circular dichroism spectroscopy.

CD was performed by L.E. Salay. The WT and mutants of p58C were concentrated to 2 mg/mL and buffer exchanged into 10 mM potassium phosphate (pH 7.2). The far-UV CD spectrum over the range 190–260 nm was acquired at room temperature using a Jasco J-810 spectrophotometer. Each spectrum is the average of three scans acquired with a scanning rate of 0.5 nm/s.

Fluorescence anisotropy.

Fluorescence anisotropy analysis of p58C was performed by L.E. Salay. Fluorescence anisotropy analysis of primase was performed by Dr. M.E. Holt. The binding of DNA to wild-type and mutant p58C and primase was measured by monitoring the change (increase) in fluorescence anisotropy as protein was added to a solution containing 5'-FITC labeled DNA (see Table 2.1 for substrates).

Table 2.1. Electrochemistry, primase activity assay, and fluorescence anisotropy DNA substrates used.		
p58C Electrochemistry Substrates	Well-matched 5'-SH-GTCGTGCAACGTGTCTGCGC-3' 3'-CAGCACGTTGCACAGACGCGTAC-5'	Abasic Site 5'-SH-GTCGTGCAACGTGTCTGCGC-3' 3'-CAG_ACGTTGCACAGACGCGTAC-5'
Initiation Substrate	3'-AAAAAAAAAAAAAAAAAAAAAAAAATAAAGAGAGAGAGAGAGAGAAAAGA-5'	
Elongation Substrate	5'-$(T)_{15}(U)_{16}$-3'	
	3'-$(A)_{31}$TAAGAAAAGAGAGAGAGAGAGAGAAAAGA-5'	
p58C Fluorescence Anisotropy Substrate	3'-GAGAGTTT-5′	
	5'-[FITC]-TCTCTCTCTCAAA-3′	
Primase Fluorescence Anisotropy Substrate	5'-[FITC]-TTTTTTTTTTTTTTTTTTTTTTTTT-3'	

Table 2.1. Electrochemistry, primase activity assay, and fluorescence anisotropy DNA substrates used. Electrochemistry of p58C was performed on self-assembling monolayers of a 20-mer DNA duplex substrate with a 3-nt 5'- ssDNA overhang. A 50-nt ssDNA substrate with a single thymine base complementary to the α-32P radiolabeled ATP was used in the primase initiation assay comparing wild type and CT-deficient full-length enzyme. A 2'-OMe RNA-primed ss/dsDNA substrate, containing a 31- nucleotide duplex segment and a 29- nucleotide 5'-ssDNA overhang was used to assay elongation. The mismatched elongation assay was performed with a cytosine engineered into the substrate (red) to promote a mismatch in the elongated primer segment. U = 2'-OMe rU, SH = $-(CH_2)_6$-SH, Flc = FITC

The p58C DNA substrate was annealed using a buffer containing 20 mM MES (pH 6.5) and 75 mM NaCl. In each case, an increasing concentration of protein was added to a solution containing DNA substrate at a concentration of 50 nM (p58C) or 20 nM (primase). Polarized fluorescence intensities were measured using excitation and emission wavelengths of 485 nm and 520 nm using a SpectraMax M5 microplate reader (Molecular Devices).

X-ray crystallography.

X-ray crystallography was performed by L.E. Salay with input from Dr. M.K. Thompson. Crystals of Y347F p58C were grown by hanging drop vapor diffusion at 21 °C from a drop composed of equal volumes of 75 mg/ml protein in 20 mM TRIS (pH 7.2) and 75 mM NaCl and reservoir solution containing 100 mM Tris (pH 8.5), 300 mM Li_2SO_4 and 20% PEG 3350. Crystals of Y345F p58C were grown in 20 mM MES (pH 6.5) and 50 mM NaCl and reservoir

solution containing 100 mM Tris (pH 8.5) 150 mM Li_2SO_4 and 18% PEG 3350. Crystal growth was stimulated by streak seeding with WT. Prior to data collection, crystals were soaked in mother liquor containing 20% glycerol and flash frozen in liquid nitrogen.

X-ray data were collected at Sector 21 (Life Sciences Collaborative Access Team) of the Advanced Photon Source at Argonne National Laboratory. All data were processed by HKL2000 [132]. The Y347F crystals belong to the P3 space group and were twinned. The Y345F crystals were not twinned and belonged to the C2 space group. Prior to phasing, the twinned data set was de-twinned using the Detwin program of the CCP4 program suite [133] by applying the twin law, h,-h-k,-l. Phasing of the diffraction data was done by molecular replacement using PHASER [134] and PDB entry 3L9Q as the search model. Manual model building for the structure was performed using *Coot* model building software [114], and waters were placed with the *Coot* routine, Find Waters. The final model was obtained by iterative cycles of model building in *Coot* and structure refinement using Refmac5 in the CCP4 suite of programs [115]. The final model of Y347F was a dimer of dimers with four Y347F p58C subunits in the asymmetric unit. The final model of Y345F was a dimer with two Y345F subunits in the asymmetric unit.

All protein figures were prepared with Chimera [130]. Data collection and refinement statistics are given in Table 2.2.

Table 2.2: Data collections and refinement statistics for crystal structures of CT deficient mutants.

PDB	5I7M	5DQO
Mutant	Y345F	Y347F
Wavelength (Å)	0.97872	0.999
Resolution range (Å)	49.7 – 1.93 (1.96 - 1.93)	44.14 – 2.30 (2.36 – 2.30)
Space group	C2	P31
Unit cell (a, b, c Å; α, β, δ °)	109.9, 52.7 89.2; 90, 115.25, 90	60.40, 60.40, 246.73; 90 90 120
Total reflections	142467	167361
Unique reflections	35604	19561
Multiplicity	4.2 (4.0)	4.5 (2.9)
Completeness (%)	99.9 (99.8)	99.1 (89.6)
Mean I/sigma(I)	18.7 (2.1)	27.6 (2.1)
R-merge (%)	8.7 (58.4)	5.8 (49.3)
R-work	21.0	17.3
R-free	24.9	19.1
Number of		
protein residues	314	628
ligands	2	4
solvent	81	41
RMS(bonds)	0.02	0.02
RMS(angles)	2.11	1.91
Ramachandran favored (%)	99.0	90.0
Ramachandran allowed (%)	1.00	9.22
Ramachandran outliers (%)	0.00	0.78
Average B-factor (Å^2)	29.4	54.3
macromolecules	28.8	53.7
ligands	21.5	46.2
solvent	27.7	55.7

Statistics for the highest-resolution shell are shown in parentheses.

*Sample Preparation for Electrochemistry**.***

All sample preparation for electrochemistry was performed by Dr. E. O'Brien. Wild type and mutant p58C samples were stored prior to experiments in p58C storage buffer. Concentrations of [4Fe4S] cluster-containing p58C or mutants were measured using UV-Visible spectroscopy, by absorbance of the [4Fe4S] cluster at 410 nm (extinction coefficient = 17000 M^{-}

^{1} cm^{-1}) [135]. Aliquots of stock samples (45-90 µL) were deoxygenated using argon bubbling for 4-5 minutes. Samples were then transferred into the anaerobic chamber. Before deposition onto the gold electrode surface, p58C/mutant samples were diluted to a molar concentration of 16 µM [4Fe4S] p58C variant with previously deoxygenated p58C storage buffer. Samples were deposited onto multiplex chip quadrants in 20 µL volumes initially, with the remaining sample deposited in a well of bulk solution above the chip surface.

Wild Type/Mutant p58C Electrochemistry.

All electrochemistry was performed by Dr. E. O'Brien using a CHI620D potentiostat and 16-channel multiplexer (CH Instruments), in an anaerobic glove chamber. Multiplex gold electrodes were part of a three-electrode system with an external Ag/AgCl reference electrode (Bioanalytical Systems) and platinum counter electrode. Cyclic voltammetry scans were performed at 100 mV/s scan rates, over a potential range of +0.412 V to -0.288 V vs. NHE. Bulk electrolysis on DNA was performed at an applied potential of +0.412 V vs. NHE for all electrochemical oxidation reactions and -0.188 V vs. NHE for all electrochemical reduction reactions. The oxidizing potential was applied for 8.33 minutes for single oxidation reactions on a surface, and 5.83 minutes or 6.67 minutes for the iterative oxidation cycles of p58C variants. The reducing potential was applied for 8.33 minutes in all electrochemical reduction reactions. All bulk electrolysis and cyclic voltammetry were performed in previously deoxygenated p58C storage buffer (20 mM Tris, pH 7.2, 75 mM NaCl). Charge transfer (nC) in the cathodic peak of oxidized samples' CV scans was assessed using the area under the current wave of the reduction signal. All p58C variants were compared over three trials of oxidation at +0.412 V vs. NHE (two oxidation reactions after 500 s of applied potential, one reaction after 400 s of applied potential). The charge transfer in the bulk electrolysis curves was calculated as the area under the current curve plotted versus time for the bulk electrolysis reaction, as the current decays to a constant value. The percent recovery of bulk electrolysis charge in the CV peak after oxidation

was averaged over three trials for each variant; error bars represent the standard deviation of the average fraction of charge recovered.

Full-Length Wild Type/Mutant Primase Initiation and Elongation Assays.

All activity assays were performed by Dr. E. O'Brien in an anaerobic glove chamber (Coy Products) using deoxygenated buffer, protein, DNA substrates, and nucleotide triphosphates. All reagents were deoxygenated by argon gas bubbling after thawing from storage temperature immediately prior to assay. Buffer was deoxygenated by bubbling argon gas for several hours (approx. 1 hour per mL buffer) and subsequent incubation in the glove chamber atmosphere for at least 1-2 days prior to the assay. Initiation assays were performed using the 50-nt Initiation Substrate listed in Table 2.1. Elongation assays were performed with the Elongation Substrate in Table 2.1, in which a 2'-OMe RNA/DNA primer is annealed to a 60-nt ssDNA complement strand. Initiation assays (18 µL total volume) contained 250 nM ssDNA Initiation Substrate, 1 µM [α-^{32}P ATP] (Perkin Elmer), 112 µM [CTP] (Sigma), 188 µM [UTP] (Sigma), and 400 nM primase or primase variant, in 50 mM Tris-HCl, pH 8.0, 3 mM $MgCl_2$. Reactions were initiated by the addition of primase or primase variant enzyme and incubated anaerobically at 37°C. Aliquots (5.5 µL) were removed from the primase reactions after 5 minutes, 10 minutes, and 30 minutes of incubation for wild type/mutant comparison assays and after 30 minutes, 60 minutes, and 120 minutes for wild type primase well-matched and mismatched primer comparison assays. All samples were quenched by addition of an equal volume of 1% SDS (Sigma), 25 mM EDTA (Sigma) solution. Samples were then removed from the glove chamber after quenching and heat denatured at 70°C. Products were then purified by size exclusion, using mini Quick Spin Oligo columns (Roche Diagnostics) for wild type/mutant comparison assays and Micro-Bio Spin™ P-6 columns (BioRad Laboratories) for wild type well-matched/mismatched primer comparison assays. Radioactivity counts for products were measured using a LS5000TD scintillation counter (Beckman Instruments). Products were dried in vacuo, resuspended in 2 µL

loading dye (Xylene cyanol, bromophenol blue), and further annealed for 1 minute at 90°C before gel separation. Primase/mutant comparison elongation assays were performed under identical conditions, in the presence of 500 nM Well-Matched Elongation Substrate, 120 μM CTP (Sigma), 180 μM UTP (Sigma), and 1 μM α-^{32}P ATP (Perkin Elmer). The primase/variant concentrations used in elongation assays were 200 nM, 400 nM, 600 nM, or 800 nM. Primase assays for elongation in the presence of a mismatch were performed with 500 nM Well-Matched Elongation Substrate or Mismatched Elongation Substrate, 200 μM CTP (Sigma), 100 μM UTP (Sigma), and 1 μM α-^{32}P ATP (Perkin Elmer). Assays were performed anaerobically and quenched/purified in a manner identical to initiation assays.

Primase Assay Product Separation/Analysis.

Primase assay analysis was performed by Dr. E. O'Brien. All primase/primase variant assay products were separated by denaturing polyacrylamide gel electrophoresis (20% polyacrylamide). Separated products were visualized using phosphorimagery on a Typhoon FLA 9000 imager (GE Healthcare) and quantified using ImageQuant TL software. Products synthesized by different primase variants were directly compared using measured ^{32}P counts detected by software. Initiation and Elongation Substrates (Table 2.1) were designed to contain a single base complementary to the radiolabeled NTP, α-^{32}P ATP. Quantification could thus have a basis 1:1 product: radioactivity ratio, as the sole purine NTP and would be the strongly preferred site of initiation and an optimal 5'- elongation site [136, 137]. Product sizes were assigned by comparison with a 10/60 Oligo Length Standard (Integrated DNA Technologies). Single-stranded oligonucleotides in standard were labeled by incubation for 1 hour at 37°C with γ-^{32}P ATP (Perkin Elmer) and T4 polynucleotide kinase enzyme (Roche Diagnostics). Labeled standard was purified using size exclusion chromatography with mini Quick Spin Oligo columns (Roche Diagnostics). All product quantifications were averaged over three trials for

p48/p58Y345F and p48/p58Y345C and six trials for p48/p58. Error bars represent the standard deviation of average values obtained over these trials.

Results

DNA-Mediated Electrochemistry

To study the DNA-bound redox properties of enzymes with [4Fe4S] clusters, we employ DNA-mediated electrochemistry, a robust method for directly measuring DNA CT in the ground state [118, 128, 129] (Figure 2.1). An alkanethiol-terminated, annealed duplex DNA (dsDNA) substrate is deposited on a gold surface, facilitating covalent linkage of the DNA to the gold through the thiol moiety. The gold is passivated using β-mercaptohexanol and becomes the working electrode in a three-electrode cell, with an external Ag/AgCl reference electrode and a platinum counter electrode [118, 128, 129]. Charge transport through the stacked bases of dsDNA between the gold surface and a redox-active species bound at the distal end of the DNA can be measured using this platform under solution conditions. Cyclic voltammetry (CV) is employed to measure changes in current over a range of applied potentials. Earlier electrochemical studies of the base excision repair glycosylase Endonuclease III (EndoIII) using CV have shown that binding of the protein to the DNA polyanion shifts the redox potential of the [4Fe4S] cluster 200 mV negative to ~80 mV vs. NHE, into the physiological range of cellular potentials, activating the cluster for redox chemistry [58, 138]. Importantly, this potential shift corresponds thermodynamically to a 1000-fold increase in DNA binding affinity for the oxidized $[4Fe4S]^{3+}$ state of EndoIII relative to the reduced $[4Fe4S]^{2+}$ state.

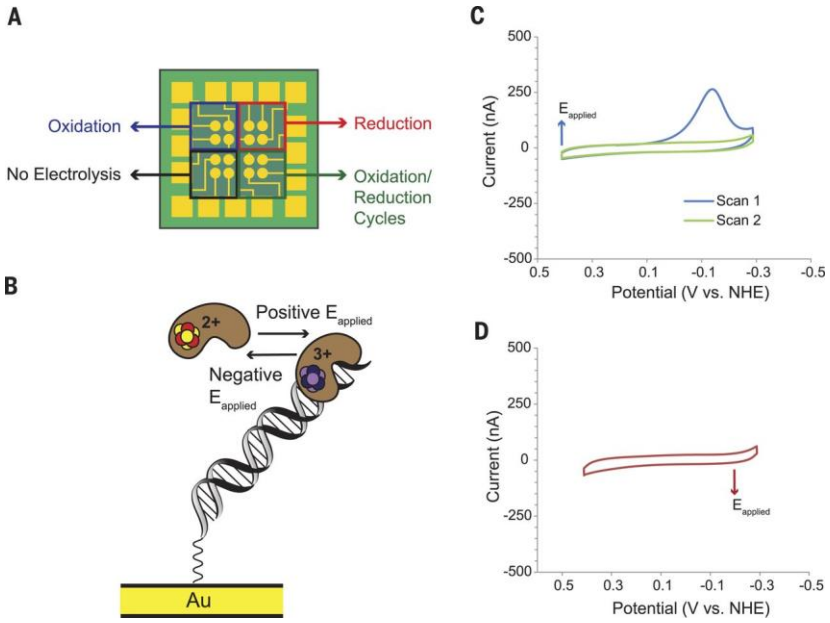

Figure 2.1: Oxidized $[4Fe4S]^{3+}$ and reduced $[4Fe4S]^{2+}$ p58C display different behavior on DNA-modified electrodes. A) Multiplex chip with 16 DNA-modified Au electrodes (circles at center). This platform facilitates direct comparison of oxidized, reduced, unaltered, and iteratively oxidized samples on four separate quadrants of a single surface. B) Depiction of the effects of electrochemical oxidation and reduction on p58C DNA binding and redox activity. C) Cyclic voltammetry (CV) of electrochemically oxidized p58C. After electrochemical conversion (applied potential $E_{applied}$ = 412 mV versus NHE) of the sample at the electrode/solution interface to the $[4Fe4S]^{3+}$ state, CV scans display a large cathodic peak only in the initial scan to negative, reducing potentials. D) CV of electrochemically reduced p58C. After electrochemical conversion ($E_{applied}$ = –188 mV versus NHE) of the sample to the $[4Fe4S]^{2+}$ state, CV scans show no electrochemical signal on DNA. Electrochemistry was performed on 16 mM p58C in 20mM Tris (pH 7.2) and 75 mM NaCl; CV scan rate was 100 mV/s using an Ag/AgCl reference electrode. Electrochemistry performed by Dr. E. O'Brien.

Oxidized and Reduced p58C Electrochemistry

The p58C domain of human DNA primase, independently of the rest of the enzyme, binds a primed template DNA with modest affinity (K_d = 5.6 ± 0.5μM) when initially present as isolated in the reduced, EPR-silent $[4Fe4S]^{2+}$ state [69, 70]. To investigate whether the p58C [4Fe4S] cluster oxidation state affects DNA binding, as observed in Endonuclease III, we used DNA electrochemistry. Experiments are carried out using a sixteen-electrode multiplexed chip, which allows for robust, reproducible, and internally consistent measurements of various conditions on a single surface (Figure 2.1A) [67, 118, 128, 129, 138]. Bulk electrolysis is used to convert a sample to a uniform redox state in this setup, and it is performed by passage of current through

the DNA at a constant applied potential. This technique facilitates the oxidation or reduction of the DNA-bound protein with a direct transfer of electrons through the DNA, eliminating the need for exogenous chemical oxidants or reductants that could damage the protein.

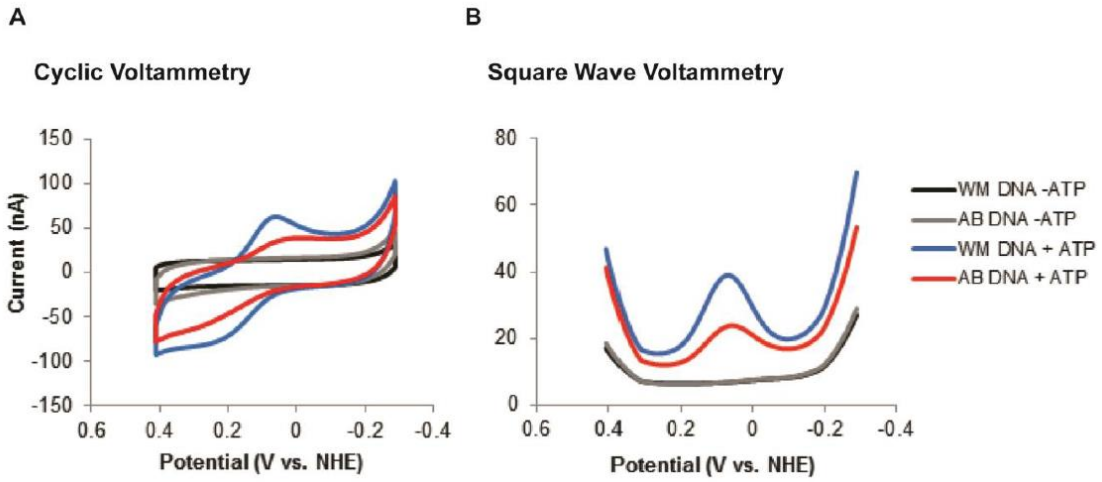

Figure 2.2: Charge transfer is DNA-mediated. Cyclic voltammetry A.) and Square Wave Voltammetry B.) signals of p58C bound to of well-matched (WM) DNA or DNA containing an abasic site (AB DNA) in the duplex segment, in the presence and absence of an NTP pool. The p58C domain displays a reversible redox signal centered at 140-150mV vs. NHE in the presence of ss/dsDNA and 500μM [ATP]. This suggests that the [4Fe4S] cluster in DNA primase is capable of undergoing reversible redox activity when the enzyme is in its active form, bound to DNA and NTPs. All electrochemistry was performed in anaerobic conditions with a Ag/AgCl reference, on 10μM [p58C] in 20mM Tris, pH 7.2, 75mM NaCl. Cyclic voltammetry scan rate: 100mV/s, square wave voltammetry scan frequency: 15 Hz. Electrochemistry performed by Dr. E. O'Brien.

For DNA electrochemistry on p58C, an alkane-thiol modified primed template DNA substrate (Table 2.1) was used. All experiments are performed in an anaerobic environment with deoxygenated reagents to prevent atmospheric cluster oxidation [139] and to ensure control of the redox state of the p58C samples on the electrode. As in earlier studies [58], we confirmed that p58C electrochemistry is DNA-mediated by observing a reversible p58C CV signal in the presence of ATP, which is attenuated when an intervening abasic site perturbs the base stacking of the duplex DNA substrate (Figure 2.2). Oxidized and reduced samples are generated and subsequently compared on a single surface using bulk electrolysis followed by CV scanning. By passing sufficient current through the DNA-modified electrode at an oxidizing

(412 mV vs. NHE) or reducing (-188 mV vs. NHE) potential, p58C is converted to the desired redox state (Figure 2.1B).

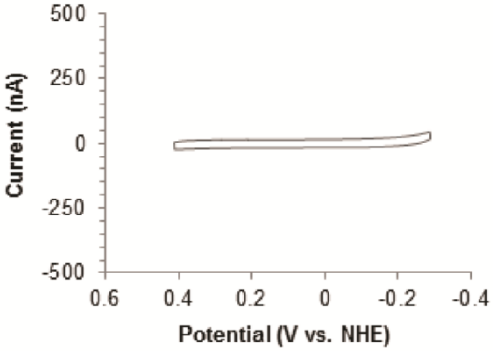

Figure 2.3: p58C does not produce a redox signal on ss/dsDNA in the absence of electrochemical alteration. CV performed in anaerobic conditions on 16μM p58C using a Ag/AgCl reference electrode, in 20mM Tris buffer, pH 7.2, 75mM NaCl. CV scans were conducted at a 100mV/s scan rate. Electrochemistry performed by Dr. E. O'Brien.

We observe no redox signal by CV for electrochemically unaltered p58C, indicating that the EPR-silent, $[4Fe4S]^{2+}$ protein obtained upon isolation [69, 70] is not electrochemically active on DNA (Figure 2.3). After oxidation by bulk electrolysis, however, a large cathodic peak between -130 and -140 mV vs. NHE appears in CV (100 mV/s scan rate) during the initial scan to negative potentials (Figure 2.1C). Importantly, the electrochemical signal through DNA is lost after scanning to reducing potentials. The signal observed in the CV scan to negative potential for the oxidized p58C sample corresponds to a reduction event, which we assign to the electron transfer reaction in which the tightly bound, electrochemically active $[4Fe4S]^{3+}$ p58C is converted to a more weakly associated, electrochemically inactive $[4Fe4S]^{2+}$ state. Consistent with this observation, CV after reduction displays no redox signal (Figure 2.1D), as observed initially for the native protein, which we attribute to the lower affinity for DNA of the $[4Fe4S]^{2+}$ state.

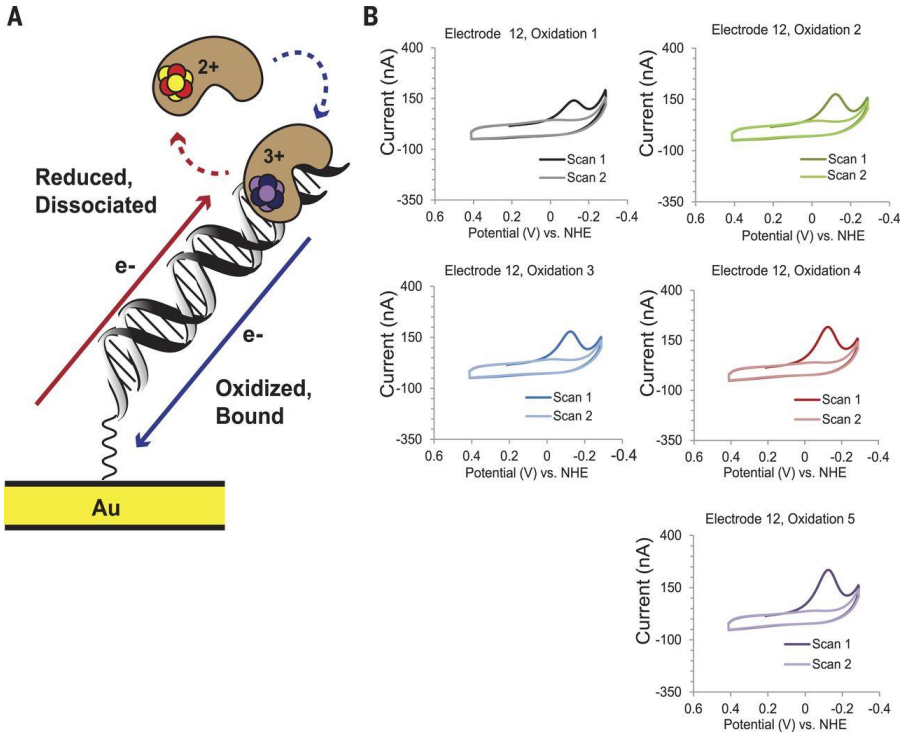

Figure 2.4: Iterative oxidation/reduction cycles of p58C on a single electrode surface. A) Depiction of the redox switch in p58C DNA binding. When oxidized, p58C is bound tightly to DNA. Reduction converts p58C to a weakly DNA-associated state. B) CV following five sequential oxidation reactions on one DNA-modified electrode of a multiplex chip. Electrolysis conditions ($E_{applied}$ = 412 mV versus NHE) are identical for each oxidation. A cathodic peak at –130 to –140 mV versus NHE is regenerated each time in the first CV scan after oxidation. The cathodic peak corresponds to a reduction of tightly bound, oxidized p58C to weakly associated p58C. Charge transfer values in the cathodic peaks for scans 1 to 5, in chronological order, are 65.4 nC, 112.4 nC, 116.4 nC, 151.1 nC, and 170.9 nC. Peak charge increases over trials because of increasing p58C at the solution/DNA interface. Electrochemistry was performed on 16 mM p58C in 20mM Tris (pH 7.2) and 75 mM NaCl; CV scan rate was 100 mV/s using an Ag/AgCl reference electrode. Electrochemistry performed by Dr. E. O'Brien.

To confirm assignment of the p58C redox signal, we employed iterative cycles of p58C electrochemical oxidation on a single electrode surface, followed each time by CV scanning (Figure 2.4). If scanning to negative potentials reduces the tightly bound $[4Fe4S]^{3+}$ p58C coupled to the DNA duplex for CT, to the weakly bound, uncoupled $[4Fe4S]^{2+}$ state, a second oxidation of the same sample should convert p58C again to the $[4Fe4S]^{3+}$ state and regenerate the CV signal as the protein rebinds tightly to the DNA. We performed five sequential bulk electrolysis reactions on a single electrode surface, followed each time by CV scanning (100 mV/s). We found each time that the p58C redox signal was not present after reduction during

CV. However, upon conversion from the reduced to the oxidized state, the CV signal was regenerated. During the initial scan after oxidation, a cathodic peak between -130 and -140mV vs. NHE (100mV/s scan rate) consistently appears (Figure 2.4). This reversible behavior suggests that the oxidation state of the [4Fe4S] cluster alters DNA binding by p58C; tighter DNA binding is associated with oxidation.

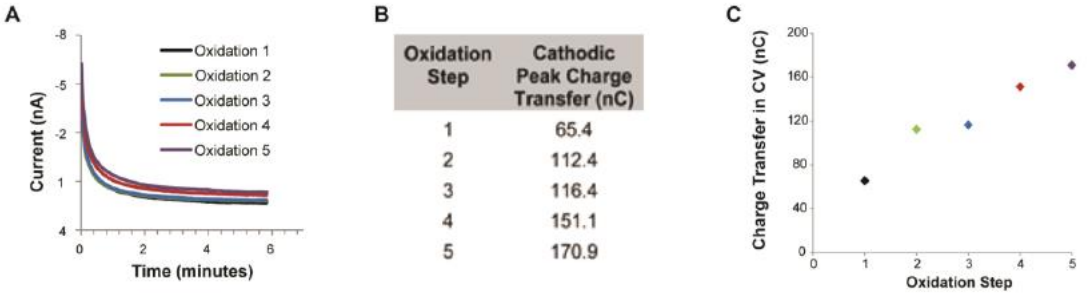

Oxidation Step	Cathodic Peak Charge Transfer (nC)
1	65.4
2	112.4
3	116.4
4	151.1
5	170.9

Figure 2.5: Charge transfer (nC) increases with iterative oxidation reactions. A.) Iterative oxidation reactions on a single DNA-modified multiplex electrode surface. Oxidation reactions of p58C indicate that charge passes, converting a reduced species to an oxidized species at an applied potential of +412mV vs. NHE. This shows that after reduction in CV, p58C can be oxidized again on a DNA-modified surface. B.) Charge transfer (nC) in the cathodic peak signal for each CV scan of the iteratively oxidized p58C sample. Charge transfer increases during iterative oxidations, due to more p58C available at the DNA/solution interface during later trials. C.) Plot of CV charge transfer for iterative oxidation steps. Charge transfer in CV peak increases over iterative scans, suggesting that electrochemical oxidation brings more p58C to the ss/dsDNA substrate. Electrochemistry performed on 16μM p58C in 20mM Tris, pH 7.2, 75mM NaCl. CV scans performed at 100mV/s scan rate. Electrochemistry performed by Dr. E. O'Brien.

Progressively larger CV signals appear with each iterative oxidation performed under identical electrolysis conditions (Figure 2.5). The change in CV signal under constant oxidation conditions suggests that oxidation brings more molecules of p58C to the DNA substrate on the electrode each time that electrolysis is performed. Previously oxidized p58C molecules, together with newly oxidized p58C generated during each electrolysis at 412 mV vs. NHE, appear in the CV signal obtained after each oxidation. Moreover, it is not feasible on our experimental timescale that two serial protein diffusion events, diffusion of previously oxidized p58C molecules away from the DNA, followed by diffusion of a new sample to the DNA replacing them, can occur. This evidence therefore strongly suggests that the redox switch in the oxidation state of the [4Fe4S] cluster modulates DNA binding and coupling of the [4Fe4S]

cluster into the DNA duplex for CT. The molecular basis for how oxidation controls this increase in DNA affinity is not known; progress to define this mechanism has been inhibited by the inability to produce sufficient quantities of uniformly oxidized, $[4Fe4S]^{3+}$ p58C, despite an extended and systematic survey of oxidizing agents and experimental conditions in an anaerobic environment.

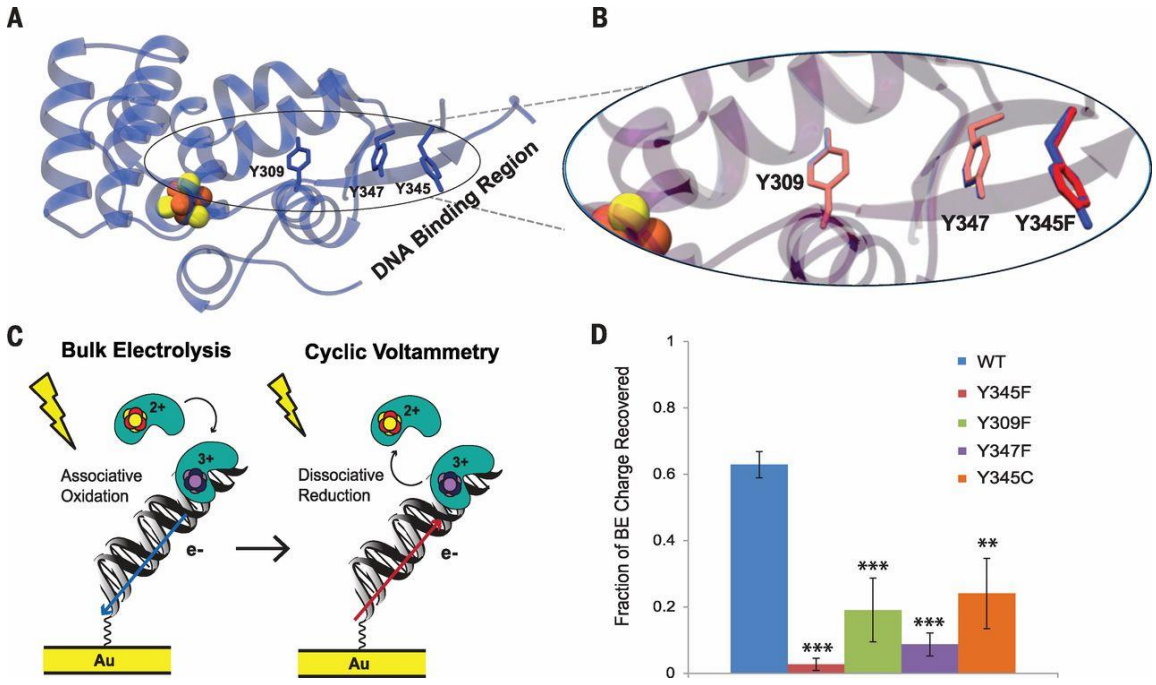

Figure 2.6: DNA-binding, charge transfer– deficient p58C mutants. A) Tyrosine residues conserved in the eukaryotic primase [4Fe4S] domain (Y309, Y345, and Y347 in H. sapiens, blue sticks) are located between the [4Fe4S] cluster (orange and yellow spheres) and DNA binding region. The DNA binding region, consisting of residues R302, R306, K314, and W327, is located ~20 to 30 Å from the cluster, necessitating electron transfer through the protein matrix for exchange of charge between the [4Fe4S] cofactor and bound DNA. B) Expanded region of the overlaid crystal structures of p58C (PDB 3L9Q, blue) and p58C Y345F (PDB 517M, red) demonstrates the minimal structural impact of the Y-F mutation; the residue in the mutant adopts the same orientation as the Tyr in wild-type p58C. All mutants bind DNA with approximately the same affinity as wild-type p58C. C) Depiction of redox reactions in electrochemical assays with wild-type and mutant p58C. Bulk electrolysis first oxidizes p58C and promotes tight DNA binding. CV then reduces the DNA-bound protein, converting it to the weakly associated, electrochemically inactive form. Both require the Tyr charge transfer pathway and must be accounted for when comparing charge transfer proficiency. D) Wild-type (WT) p58C recovers significantly more (63 ± 4%) bulk electrolysis charge than the mutants, which suggests that perturbation of the charge transfer pathway diminishes DNA-bound redox chemistry and consequently affects the redox switch. All bulk electrolysis reactions and CV scans were performed on 16 mM p58C/mutant in 20 mM Tris (pH 7.2) and 75 mM NaCl; CV scan rate was 100 mV/s using an Ag/AgCl reference electrode. Data are means ± SD of n = 3 scans per variant; **P < 0.001, ***P < 0.0005 (Student t test). Crystallography performed by L.E. Salay, electrochemistry experiments performed by Dr. E. O'Brien.

Charge Transfer Pathway through p58C

Iterative, electrochemically controlled oxidation and reduction cycles demonstrate the ability of p58C to switch between weak and tight DNA binding upon a change in the oxidation state of the [4Fe4S] cluster under the control of DNA-mediated CT through the DNA electrode. For this DNA-mediated redox switch reaction to occur, however, a tunneling pathway [140] through p58C is necessary to move charge the ~25 Å distance between the primed template DNA binding site and the [4Fe4S] cluster cofactor [38, 73]. Residues within p58C must therefore shuttle charge through the insulating protein matrix to mediate the DNA binding switch reaction. In order for the protein-mediated redox reactions to occur on a feasible timetable over these distances, it is critical that residues with a low ionization potential are present in the electron transfer pathway [140-142]. Tyrosine residues, whose aromatic rings can stabilize protein radicals, serve as redox mediators in a variety of proteins [143]. Moreover, conservation of tyrosine residues across p58C domains of eukaryotic primases suggests potential participants in such a CT pathway through the protein to the DNA interface. In all structures of human p58C, three conserved tyrosine residues (Y309, Y345, Y347) form a pathway from the cluster to the putative DNA binding surface (Figures 2.6). Given its low ionization energy of 8.5 eV in solution relative to 9.4 eV for phenylalanine [143] and an average of ~9.6 eV [140] for aliphatic residues, tyrosine is more readily able to mediate electron/hole transfer through proteins. This chain of tyrosines in p58C is within a feasible range for tunneling [140] and was thus viewed as a likely conduit to facilitate electron/hole hopping from the cluster to the DNA.

To test the proposed CT pathway, we designed and isolated three human p58C Y-F variants (Y309F, Y345F, Y347F), which were characterized in the same manner as the wild type protein. All three mutants are loaded with [4Fe4S] cluster to a similar degree as WT, as reflected in the UV-Visible absorbance 280 nm/410 nm ratio. To validate proper folding of the Y-F variants, circular dichroism was used to establish that the distribution of secondary structure is essentially identical to wild type (Figure 2.7).

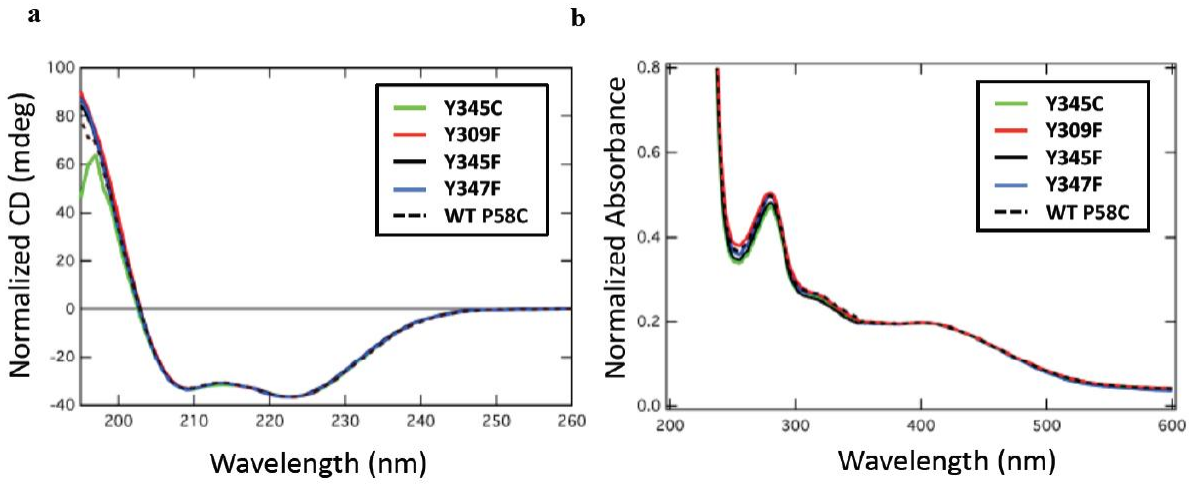

Figure 2.7: WT and mutant p58C biophysical characterization. A: circular dichroism (CD) spectroscopy of WT and mutant p58C indicate that the mutations do not perturb any of the elements of secondary structure. All spectra are normalized to WT at 222 nm. B: UV-Visible spectroscopy of WT and mutant p58C shows similar 280 nm /410 nm absorbance ratios, indicating similar degrees of [4Fe-4S] cluster cofactor loading in all variants. All spectra normalized to WT at 410 nm. CD spectroscopy and UV-VIS spectroscopy performed by L.E. Salay

We also determined an X-ray crystal structure of p58C Y345F (Table 2.2, Figure 2.8). The presence of the cluster in the mutant and the RMSD from the wild type protein of only 0.22 Å for the Y345F variant confirms that the structure is not perturbed. Critically, the crystal structure reveals that the F345 aromatic ring in the mutant adopts the same orientation as the Y345 ring in wild type p58C (Figure 2.8).

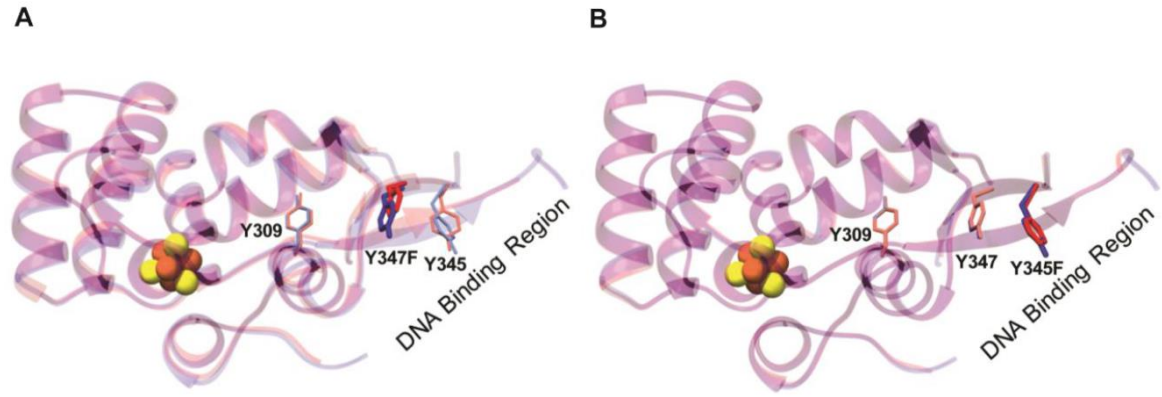

Figure 2.8: Structural comparison of WT and mutant p58C. A) Superposition of the WT p58C (PDB 3L9Q) and Y347F p58C (PDB 5DQO) structures. B) Superposition of the WT p58C (PDB 3L9Q) and Y345F p58C (PDB 517M) structures. In both panels, WT p58C is colored blue and the tyrosine to phenylalanine mutant is red. Crystallography performed by L.E. Salay

We also determined the X-ray crystal structure of the Y347F variant, with a similarly low RMSD (0.33 Å) relative to wild type p58C (Figure 2.8). DNA binding measurements using *in vitro* fluorescence anisotropy (Figure 2.9) under aerobic conditions demonstrate that the mutations do not significantly affect the binding of p58C to a DNA substrate. Since the structures and biochemical properties of the mutants are the same as WT p58C, but the electron/hole transfer properties of tyrosine and phenylalanine are different, these single-atom mutations provide a powerful means to investigate the importance of the CT pathway through p58C and its effect on the DNA-mediated redox switch in primase.

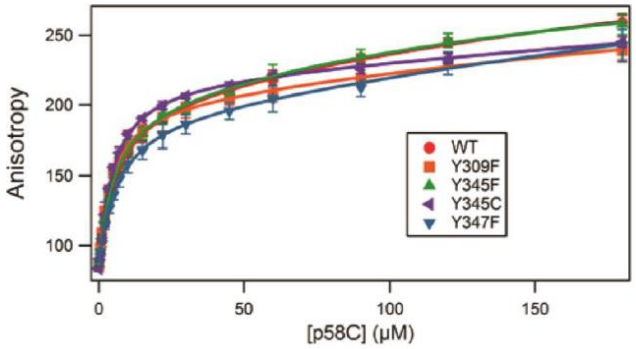

Dissociation constants for p58C

Construct	K_D (μM)
WT	5.5 ± 0.5
Y309F	4.1 ± 0.3
Y345C	4.6 ± 0.2
Y345F	4.9 ± 0.4
Y347F	4.1 ± 0.4

Figure 2.9: DNA binding for WT and mutant p58C. WT and mutant p58C domains have similar DNA binding affinities with low micromolar dissociation constants. Affinities were measured in aerobic conditions by fluorescence anisotropy of FITC-labeled DNA substrates in 20 mM MES, pH 6.5, 50 mM NaCl. Background was subtracted from anisotropy values prior to plotting. K_D values are mean ± SD over n=3 measurements for each variant. Fluorescence anisotropy performed by L. E. Salay

Anaerobic electrochemical characterization was performed on all three Y-F variants (Figure 2.10). Oxidation and reduction using bulk electrolysis, followed by redox cycling during CV scanning (Figure 2.10, 2.11), were performed on an identical multiplex chip surface as for wild type p58C (Figure 2.3).

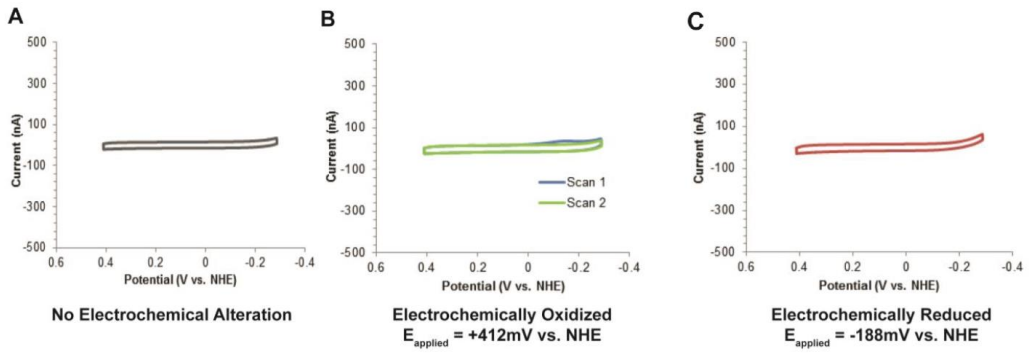

Figure 2.10: CV scans of p58C Y345F. A) Electrochemically unaltered p58C tyrosine mutants display no electrochemical signal on DNA. B) Electrochemically oxidized p58C tyrosine mutants display a cathodic peak between -150mV and -160mV vs. NHE after oxidation at an applied potential of +412mV vs. NHE; the peak signal is smaller than that observed for wild type. C) Tyrosine mutants of p58C display no redox signal on DNA after electrochemical reduction at an applied potential of -188mV vs. NHE. All scans performed on 16μM p58C variant, in 20mM Tris, pH 7.2, 75mM NaCl, at a 100mV/s scan rate. p58C Y345F is shown as a representative example of the mutants. Electrochemistry performed by Dr. E. O'Brien.

Though the general DNA-mediated electrochemical behavior of the mutants is the same as for the WT protein, it was observed that all three mutants are charge transfer-deficient compared to WT p58C. As a control that the phenomena we observed are not unique to Y-F substitution, we also assayed p58C Y345C, a somatic mutation discovered in a gastric tumor [131]. Oxidation of each mutant produces a cathodic peak at potentials similar to wild type in CV scanning after electrolysis, with a much smaller signal height and a slightly positive shift in average cathodic peak potential (Figure 2.12), both of which suggest that the charge transfer pathway facilitating conversion from the native reduced, $[4Fe4S]^{2+}$ state to the oxidized, $[4Fe4S]^{3+}$ state is attenuated with mutation.

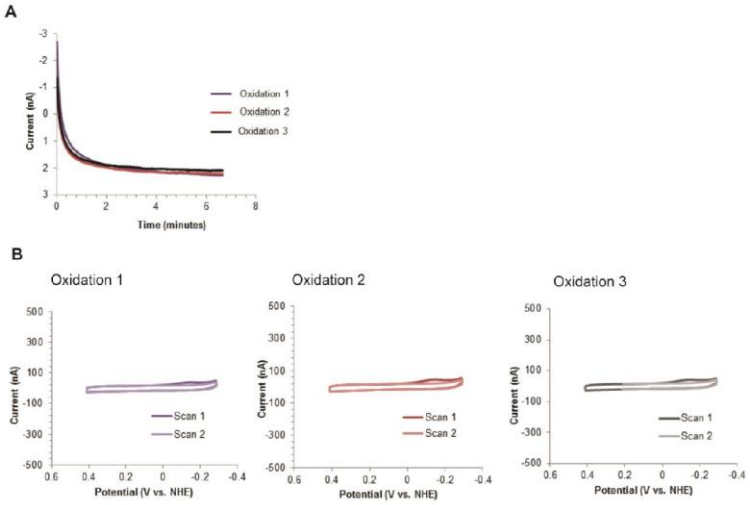

Figure 2.11: Iterative Oxidations, followed by CV scans, of p58C Y345F on a single electrode surface. A) Three bulk electrolysis reactions at an applied potential of +412mV vs. NHE were performed in immediate succession on a single electrode surface. B) CV scans after each successive oxidation. Charge transfer in the cathodic peak was 4.1nC, 5.3nC, and 6.3nC during oxidations 1, 2, and 3, respectively. The mutant p58C thus shows the same general trend as WT but transfers less charge in bulk electrolysis and subsequent CV on the DNA-modified surface. All scans performed on 16μM p58C variant, in 20mM Tris, pH 7.2, 75mM NaCl, at a 100mV/s scan rate. p58C Y345F is shown as a representative example of the mutants. Electrochemistry performed by Dr. E. O'Brien.

Although perturbation of the CT pathway in p58C can be observed on DNA-modified electrodes, the rate-limiting step, tunneling of charge through the alkanethiol linker [128] appending the DNA to the gold surface, obscures a measurable difference in rate between wild type and mutant p58C redox switch pathways; the similar scan rate dependence of WT and mutant p58C cathodic peak potentials (Figure 2.13) demonstrates that charge transfer through the 6-carbon alkanethiol linker is still rate limiting on this platform. Nonetheless, redox proficiency of WT and mutant p58C may be compared using charge transfer values over a fixed time in bulk electrolysis and CV.

Conversion of the reduced $[4Fe4S]^{2+}$ p58C to the oxidized $[4Fe4S]^{3+}$ p58C in bulk electrolysis, and subsequent conversion of the oxidized $[4Fe4S]^{3+}$ p58C to the reduced $[4Fe4S]^{2+}$ p58C in CV, *both* require electron transfer through the protein, between bound duplex DNA and the [4Fe4S] cluster. If a pathway through conserved tyrosines mediates the redox switch, then less charge transfer in bulk electrolysis and CV should occur for the mutants.

Diminished charge transfer through p58C during bulk electrolysis necessarily results in less oxidized mutant p58C being tightly bound to the DNA before CV scanning. This alone could produce the smaller CV signals observed. These signals, however, could also be diminished by the perturbed pathway impeding cluster oxidation in bulk electrolysis as well as reduction in CV. To assess whether charge transfer deficiency is additive for the mutants over both electrolysis and CV, we compare the percent of initial electrolysis charge observed in the CV signal for WT

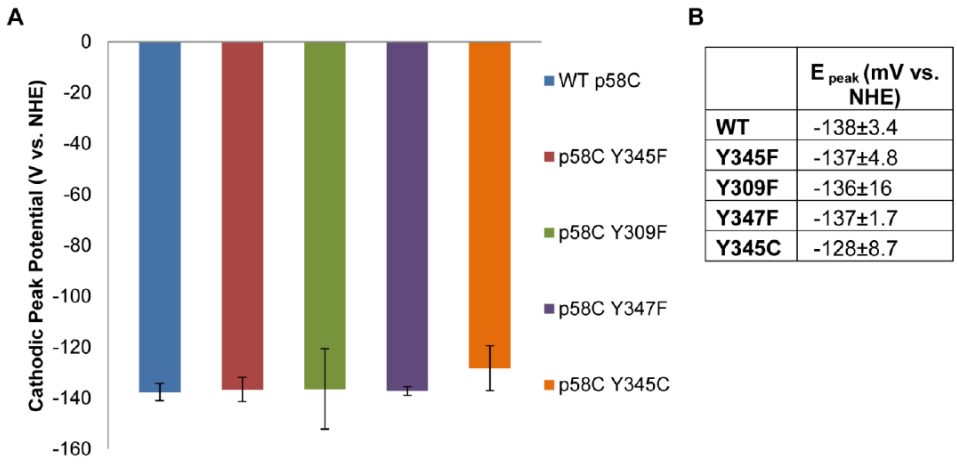

	E_{peak} (mV vs. NHE)
WT	-138±3.4
Y345F	-137±4.8
Y309F	-136±16
Y347F	-137±1.7
Y345C	-128±8.7

Figure 2.12: Change in potential value for cathodic peak after p58C oxidation, WT and tyrosine mutants of p58C. Potential measurements from three CV trials after p58C electrochemical oxidation show that the WT potential is more negative on average, but the difference between WT and mutant p58C cannot be determined to a significant degree outside the margin of error. This suggests that the mutants are more likely to be in the reduced [4Fe4S]2+ state than the WT protein with an intact charge transfer pathway, as expected. Potential values are reported as mean ± SD over n= 5 trials. Electrochemistry performed by Dr. E. O'Brien.

and mutant p58C. Wild type p58C recovers an average 63±4% of electrolysis charge in the CV peak, whereas the mutants recover an average of 24±11% (Y345C), 19±10% (Y309F), 9±4% (Y347F), and 3±2% (Y345F) of this charge under the same conditions (Figure 2.6D). The larger recovery percentage measured for p58C Y345C may be due to transiently formed cysteine-thiyl radicals participating in a CT pathway through the protein with neighboring tyrosine residues [144-146], partially retaining redox switching capability. These attenuations are on the order of magnitude expected from the positive shift in cathodic peak potential [58]. Thus, the mutants are significantly CT-deficient by this comparison, demonstrating that all three conserved tyrosine

residues aid in shuttling charge between the [4Fe4S] cluster and bound DNA.

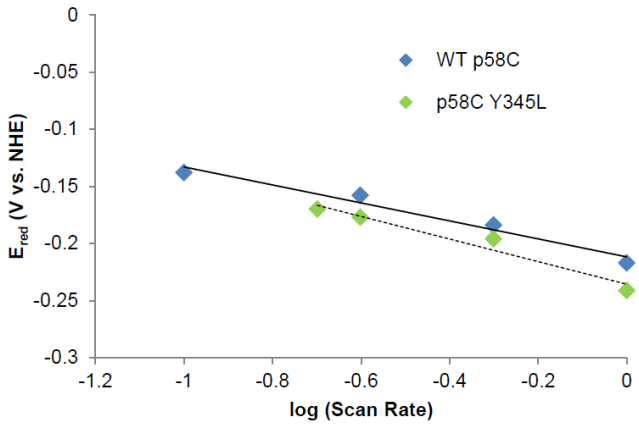

Figure 2.13: Scan rate dependence of cathodic peak potential in p58C CV signal after electrochemical oxidation. The peak potential varies with the log of the scan rate for WT p58C (blue points, solid line) and for p58C Y345L (green points, dashed line), as is expected for an irreversible signal in CV. The similar linear relationships of the potential and log of the scan rate for these two relationships demonstrate that the rate-determining step in generating this CV signal is tunneling through the alkanethiol linker tethering the DNA substrate to the gold electrode surface. Electrochemistry performed by Dr. E. O'Brien.

Redox Switch Required for Initiation but not Elongation

In order to investigate the connection between the DNA-dependent redox switch in p58C and priming activity, we assayed *in vitro* initiation and elongation activity of the full-length primase heterodimer and variants containing p58Y345F and p58Y345C mutations (Figure 2.14). Anaerobic nucleotide incorporation assays were performed to test primase activity, measuring incorporation of α-^{32}P labeled ATP on ssDNA for initiation and 2'-OMe RNA-primed DNA for elongation. Anaerobic conditions for these assays are necessary when measuring the effect of the redox switch on priming because atmospheric oxygen can oxidize the cluster when the protein is not bound to DNA. In the absence of oxygen, the switch mediated by a pathway of conserved tyrosine residues is thus the sole means through which to convert the enzyme from its native $[4Fe4S]^{2+}$ state to its tightly bound, CT-active $[4Fe4S]^{3+}$ state. We additionally note that in our assays, primase cannot truncate its products by handing them off to pol α; instead, we

observe a mixture of short primers and fully elongated ‘primer-multimer’ length products (Figure 2.14) [82, 147].

To characterize initiation, we used a 50-nt ssDNA substrate (Table 2.1) containing exactly one complementary base for the radiolabeled nucleotide triphosphate, α-^{32}P ATP. We found that WT primase has much higher overall initiation activity than both mutants tested, including the single-atom p48/p58Y345F variant (Figure 2.14).

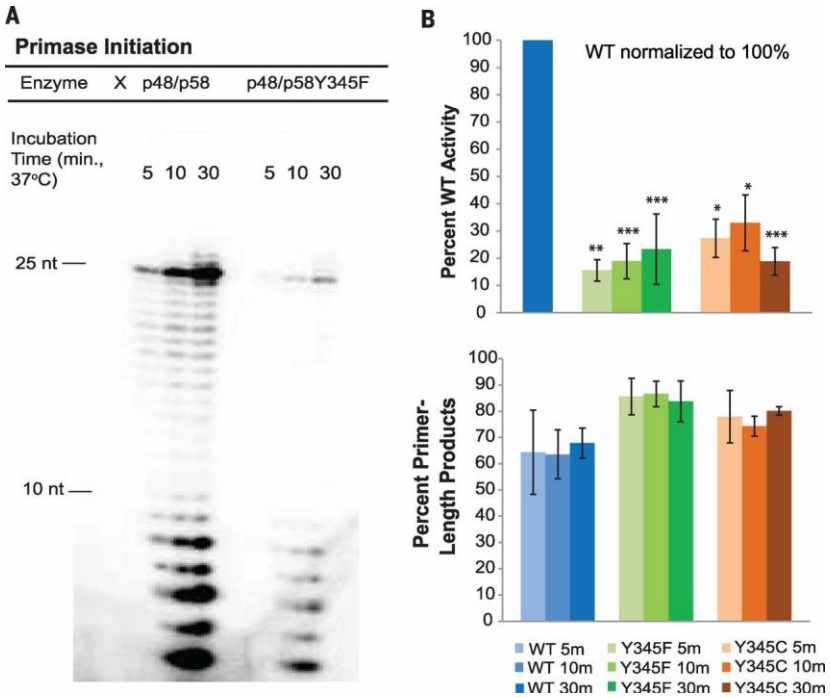

Figure 2.14: Initiation activity of primase and CT-deficient primase mutants A) Gel separation of products for wildtype p48/p58 and p48/p58 Y345F reactions on ssDNA. The wild-type enzyme is significantly more active on ssDNA than either mutant. B) Quantified products for wild-type p48/p58, p48/p58 Y345F, and p48/p58 Y345C initiation assays. Top: Mutants synthesize 15 to 35% of wild-type products on average. Bottom: Mutant primase synthesizes shorter products on average. Primer-length products are defined as products 7 to 10 nt in length. Initiation assays were performed anaerobically with 250 nM ssDNA, 1 mM [α-^{32}P] ATP, 112 mM CTP, 188 mM UTP, 400 nM enzyme in 50 mM Tris (pH 8.0), and 3 mM $MgCl_2$ at 37°C. Data are means ± SD of n ≥ 3 trials; *P < 0.005, **P < 0.001, ***P < 0.0005 (Student t test). Biochemistry performed by Dr. E. O’Brien.

CT-deficient primase mutants are significantly less active on ssDNA, synthesizing only 15-35% of the WT initiation products over multiple trials. Compared to WT primase, a larger portion of the products synthesized by the mutants is < 10 nucleotides in length, suggesting that the rate-determining initiation step in product synthesis is inhibited for mutants deficient in the redox

switch. The significant difference in initiation activity for the WT and CT-deficient mutant primase enzymes suggests that a redox switch changing the oxidation state of the [4Fe4S] cluster in p58C is crucial for the reaction to begin primer synthesis. Additionally, the difference in activity on ssDNA caused by a very subtle mutation in the CT pathway suggests that charge migration from bound DNA to the [4Fe4S] cofactor, through the insulating protein matrix of p58C, plays a significant role in mediating the rate-determining primase activation step on genomic template DNA, prior to the presence of duplex RNA/DNA.

We next tested the effect of a perturbation in the CT pathway through p58C on primase elongation. Primase can perform *de novo* primer synthesis on ssDNA, as well as elongation of an exogenous RNA primer on a duplex RNA/DNA substrate, *in vitro* [44, 69, 121]. The enzyme binds ssDNA more tightly than duplex segments [72], and this substrate preference leads to a mixture of products from both elongation of the exogenous primer and initiation on the ssDNA segment of the primed substrate. We designed a primed substrate for anaerobic elongation assays with WT and CT-deficient primase (Table 2.1); a 31-nt 2'-OMe RNA/DNA primer was annealed to a 60-nt DNA complement strand so that the primed substrate would contain a 31-nt RNA/DNA duplex sequence and a 29-nt 5'-ssDNA overhang. As expected, we observe a mixture of *de novo* initiation and primer elongation on these substrates with WT and mutant primase. We find that WT primase synthesizes more short, primer-length products through initiation on the ssDNA overhang and more truncated exogenous primers (Figure 2.15), slightly larger than 30-nt in length, while the CT-deficient mutant primase enzymes fully elongate the primer to 60-nt (Figure 2.15).

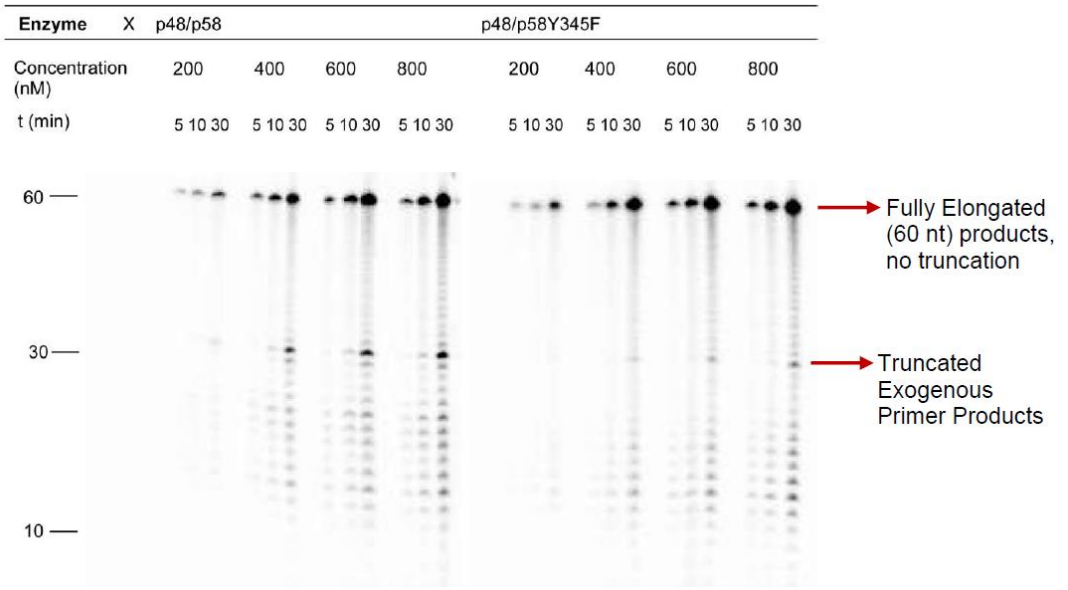

Figure 2.15: Gel separation of products for elongation reactions with increasing concentrations of p48/p58 and p48/p58Y345F on 2'-OMe RNA-primed DNA. WT primase, which has an efficient redox switching pathway between bound DNA and the [4Fe4S] cluster, synthesizes slightly more truncated products on average. The CT pathway through the protein is important for the redox switch, but it does not appear to be the sole mediator of primase product truncation. Elongation assays were performed anaerobically, with 500nM primed DNA, 1 μM α-^{32}P ATP, 120 μM CTP, 180 μM UTP, 200-800 nM enzyme in 50 mM Tris, pH 8.0, 3 mM $MgCl_2$, at 37 °C. Biochemistry performed by Dr. E. O'Brien.

To examine the effect of additional copies of primase on the proportion of truncated versus fully elongated products formed, we repeated the experiment over a range of enzyme concentrations (200-800 nM). We had previously documented redox signaling using DNA CT between DNA repair proteins with [4Fe4S] clusters by atomic force microscopy [56, 61, 67], even using repair protein partners from different organisms. Hence, we hypothesized here that redox signaling between primases through DNA CT could lead to the product truncation we observe. Since DNA CT can occur through RNA/DNA duplexes [148, 149], a redox-proficient partner for primase *in vitro* (i.e. another primase molecule), provides a means for the enzyme to change redox state, thus truncate synthesis and hand off the primer-template. Within the cell, the partner for primase handoff would presumably be DNA polymerase α, which also contains a [4Fe4S] cluster, rather than a second copy of primase. For these elongation assays, the products isolated were all at least 20 bp long, which is easily large enough for two copies of primase to bind simultaneously

on the duplex, based on modeling from structural data [38, 73, 126, 150], and be coupled into the duplex segment electronically. Quantification of products reveals that CT-proficient WT primase truncates products to a greater degree than the mutants, but the differences are small, especially between the WT and Y345F variants (Figure 2.16).

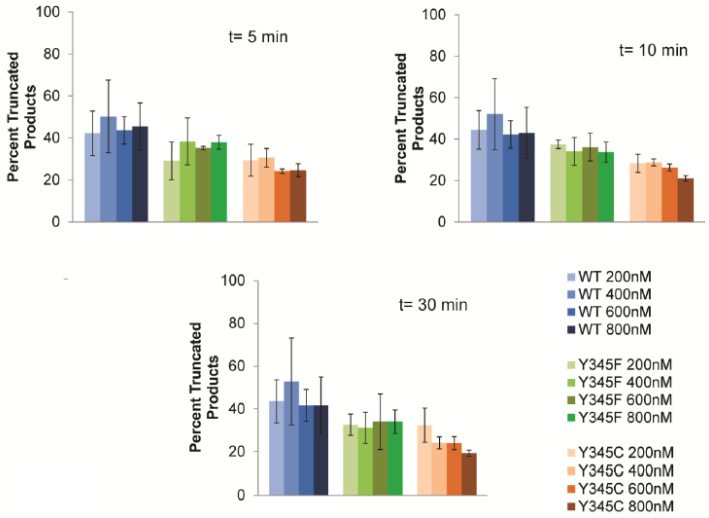

Figure 2.16: Quantification of elongation assays with WT and CT-deficient variants Percent of primase products truncated by WT and CT-deficient variants at 5, 10, and 30 minutes of incubation at 37°C, under anaerobic conditions. Primase mutants are identified by the mutation in the p58C domain. WT and mutant primase elongation activity at t= 5 minutes (top left), t= 10 minutes (top right), and t= 30 minutes (bottom left) of incubation. Legend is shown on the bottom right. All measurements are mean ± SD for n= 3 trials.

This effect is not as striking as the difference seen between WT and mutant primase initiation activity, but the assay does underscore that CT proficiency is not critical to nucleotide polymerization in primase. Fully elongated, 60-nt products are synthesized by WT and mutant primase (Figure 2.16) to the same degree, within the margin of error.

DNA Charge Transport Regulates Truncation and Handoff

We next examined whether primase product truncation could be gated by DNA CT through the growing product duplex. This experiment provides a means to model substrate handoff by primase to pol α the product duplex can mediate CT for the redox switch in protein binding and enable primer handoff, in this case between primase molecules (Figure 2.1). We

designed and prepared an exogenously primed substrate nearly identical to the substrate used in the WT/mutant comparison assay; the only difference was a single cytosine base engineered into the 5'-ssDNA overhang. The new elongation substrate (Table 2.1), under conditions promoting synthesis of a primer containing a destabilizing C:C mismatch, should abrogate the CT signaling pathway through the RNA/DNA duplex and thus inhibit truncation of products by primase if DNA CT mediates the handoff. As anticipated, we observe that WT primase truncates significantly more products (Figure 2.17) when the synthesized primer is well-matched than when the primer contains a single-base mismatch.

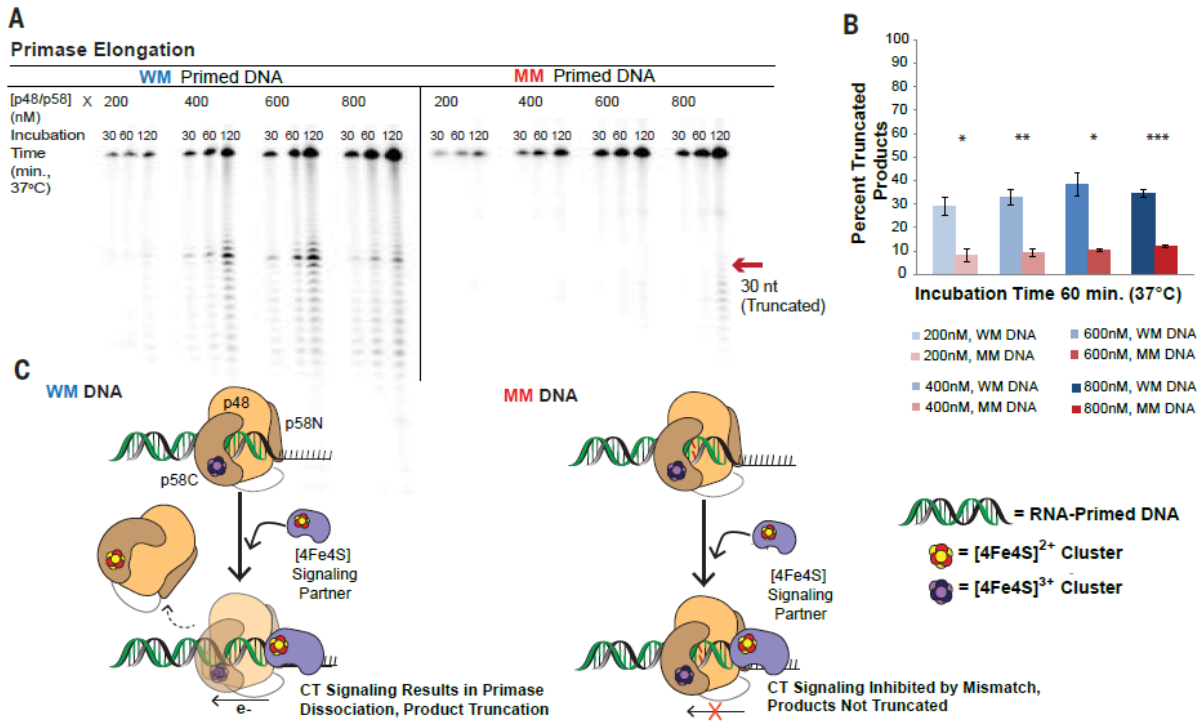

Figure 2.17: A Mismatch in the Nascent Primer Inhibits Primase Truncation**.** A) Gel separation of elongation products on a 2'-OMe RNA- primed DNA substrate, when a well-matched (WM) or mismatched (MM) primer is synthesized by WT p48/p58. B) Average percent truncated products after 60 minutes of incubation at 37°C. WT primase synthesizes significantly more truncated products with a WM primer than a MM primer. C) Scheme illustrating the observed products in the mismatched primer elongation experiment. When p58C is in contact with the RNA/DNA primer, primase can signal another DNA-bound [4Fe4S] enzyme through a WM primer and dissociate from the template, truncating products. (bottom left) DNA CT is inhibited with a MM primer, precluding redox signaling and primer truncation. Elongation assays were performed anaerobically, with 500nM primed DNA, 1 μM α-^{32}P ATP, 200 μM CTP, 100 μM UTP, 200-800 nM p48/p58 in 50 mM Tris, pH 8.0, 3 mM $MgCl_2$, at 37 °C. Quantifications shown are mean ± SD of n = 3 trials, * = 0.001<p<0.005, ** = 0.001<p<0.0005, *** = p<0.0005, student's t-test. Biochemistry performed by Dr. E. O'Brien.

This effect persists in anaerobic well-matched and mismatched primer elongation assays over a course of 30 to 120 minutes; we observe this effect over all concentrations of primase assayed (200 nM-800 nM) (Figure 2.18).

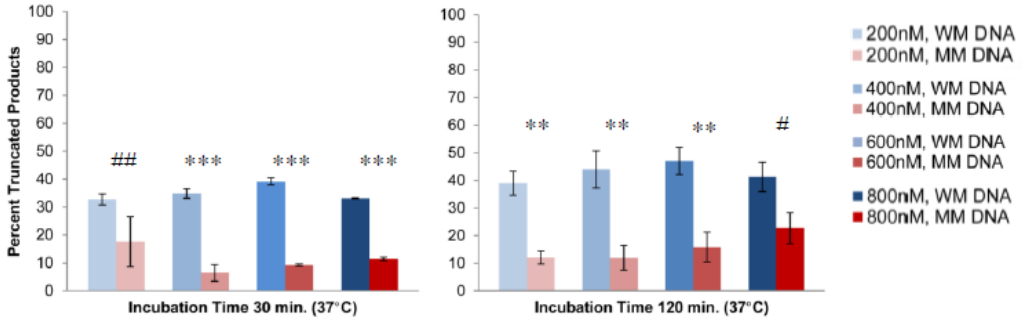

Figure 2.18: Quantification of well-matched and mismatched elongation assays. Percentage of WT primase truncated products for a) t = 30 minutes (left) and b) t = 120 minutes (right). Similar to the 60-minute time point (incubation at 37°C), these plots suggest that CT-proficient primase synthesizes significantly more truncated products on well-matched, primed DNA than in the presence of a single base mismatch within the RNA primer. When primase cannot participate in DNA CT, it favors product elongation to primer-multimer length, at all concentrations of CT-proficient primase assayed. Mean ±SD values are plotted for n= 3 trials, # = 0.025<p<0.01, ## = 0.005<p<0.01, ** = 0.001<p<0.0005, *** = p<0.0005 (student's t-test).

The striking difference in average percentage of truncated products (29-39% with a well-matched primer, 9-12% with a mismatched primer at t= 60 minutes) demonstrates that primase uses DNA CT as a means to modulate DNA binding through changing the redox state of its [4Fe4S] cluster.

Discussion

Implications for Primase Function in Replication

Our initiation and elongation assays together suggest that DNA primase initiation and product truncation are both dependent on a redox switch changing the oxidation state of the [4Fe4S] cluster in p58C. The redox switch first activates primase to tightly bind DNA, initiating primer synthesis. DNA CT through the nascent RNA/DNA primer then mediates primase truncation. On the basis of the available structural and biochemical data [26, 35, 36, 38, 42, 69, 70, 72, 73], we propose a model for priming that incorporates this redox switch (Figure 2.19).

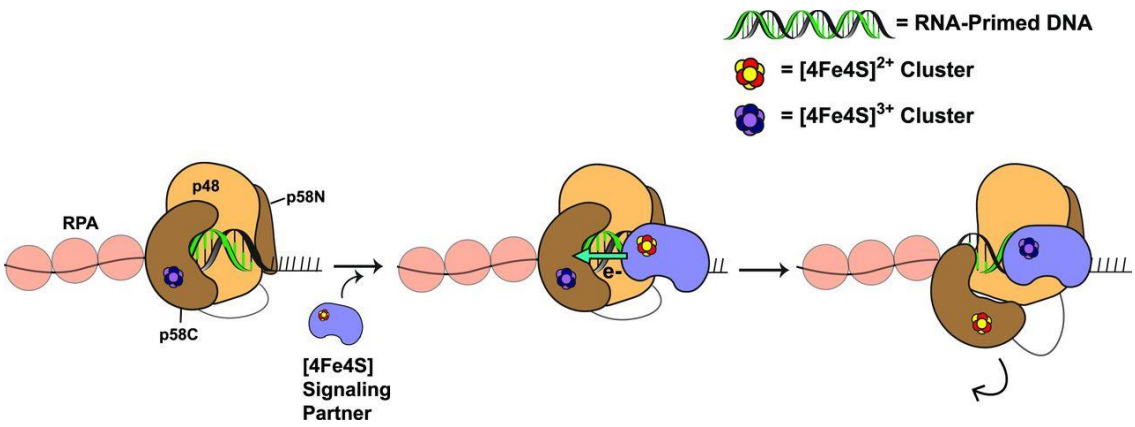

Figure 2.19: Proposed Mechanism of Primer Handoff Driven by DNA Charge Transport Chemistry. DNA primase elongates an RNA primer (green) to 8-12 nt length with both p48 and p58C contacting the nascent RNA/DNA duplex (left). When the nascent primer is large enough, another [4Fe4S] enzyme (purple), which we hypothesize to be DNA polymerase α *in vivo*, participates in DNA-mediated signaling through the primer-template duplex (middle). This promotes dissociation of p58C through reduction of the cluster from the $[4Fe4S]^{3+}$ state to the $[4Fe4S]^{2+}$ state; the next [4Fe4S] enzyme is then tightly bound and can continue elongation of the primer-template (right).

As DNA primase elongates the RNA primer to 8-12 nt length, a second [4Fe4S] enzyme, DNA polymerase α, comes into contact with the exposed nascent RNA/DNA helix[26] and associates with the primer-template so that its cluster is able to serve as a redox donor/acceptor through primed DNA. A DNA-mediated redox event can then occur, promoting p58C dissociation from the duplex and pol α binding. Since most polymerases bind to their duplex DNA substrates with modest affinity, as we show is the case for primase, pol α is unlikely to effectively *take* the primed substrate from primase. DNA-mediated signaling, which modulates polymerase binding affinity through a change in the redox state of the [4Fe4S] cluster, would thus provide the key driver for efficient primer handoff.

We propose that DNA-mediated CT drives signaling between the [4Fe4S] cluster cofactors in DNA primase and DNA polymerase α, facilitating rapid handoff of the RNA/DNA primer. Synthesis of a short primer to initiate replication must occur repeatedly on the lagging strand of the replication fork. DNA CT occurs on a timescale [151, 152] that could plausibly mediate this handoff; electron hopping through the protein matrix conversely occurs approximately 6 orders of magnitude more slowly [141, 142] and would not likely be the sole

mediator of primase/polymerase α redox signaling between [4Fe4S] centers. A major and likely rate-limiting conformational change for DNA polymerase α binding to DNA has been modeled on a timescale of 100-150 ns using molecular dynamics [26]. DNA-mediated redox signaling between primase and pol α to promote primase dissociation and primer-template transfer is thus a feasible redox mechanism for the proposed critical step for the primase-to-polymerase α transfer of the primer-template.

Our results support the proposal that the [4Fe4S] cluster in p58C serves as a redox switch governing binding, and therefore initiation and primer length counting, in the first step of replication. We show that oxidation of the $[4Fe4S]^{2+}$ cluster in human DNA primase to the $[4Fe4S]^{3+}$ state facilitates DNA binding by the p58C domain. We demonstrate an electrochemically controlled redox signal for p58C on DNA, dependent on the effective concentration of p58C at the DNA/solution interface, establishing a reversible redox switch. Conserved tyrosine residues in p58C on a pathway between the cluster and DNA mediate the redox reaction, affecting the [4Fe4S] cluster oxidation state and, consequently, DNA association of p58C. Moreover, primase initiation and termination activity, but notably not elongation activity or DNA binding, are compromised in these CT-deficient tyrosine mutants. The p58C domain has been proposed to contact ssDNA in the rate-determining primer initiation step [36, 72, 121], and to play a role in the ability of the enzyme to count the length of the primer and signal for the arrest of further synthesis coupled with hand-off of the initial primed substrate to pol α [71].

The recent discovery of [4Fe4S] cluster cofactors in each of the B-family replication-associated polymerases α, ε, δ, and ζ [79] is intriguing; combined with our results, this discovery suggests that redox reactions could be driving the DNA-binding switches generally necessary for polymerase handoffs. Moreover, studies similar to the work of Liu and Huang [74] investigating primase [4Fe4S] cluster sensitivity to oxidative stress may further illuminate how this chemistry relates to eukaryotic replication activity in different cellular redox environments. Could the redox switch for primase binding to DNA be part of a larger, DNA-mediated electron

transfer relay coordinating the association, transfer, and dissociation steps of replication? Our results illustrate a chemical role for the [4Fe4S] cluster as a DNA-binding redox switch and point towards a new mechanism for coordinating activity within the dynamic replication fork.

Response to Technical Comments

Baranovskiy et al. and Pellegrini argue that, based on structural data, the path for charge transfer through the [4Fe4S] domain of primase is not feasible. Our manuscript presents electrochemical data directly showing charge transport through DNA to the [4Fe4S] cluster of a primase p58C construct and a reversible switch in the DNA-bound signal with oxidation/reduction, which is inhibited by mutation of three tyrosine residues. Although the dispositions of tyrosines differ in different constructs, all are within range for microsecond electron transfer.

Our study [76] provides electrochemical and biochemical data for human DNA primase, supporting a proposal that [4Fe4S] cluster redox chemistry and DNA charge transport play a role in the binding and termination of the polymerase activity of primase. We describe (i) electrochemical experiments on DNA-modified electrodes demonstrating that the p58C domain of DNA primase exhibits tighter binding with the [4Fe4S] cluster in the 3+ state compared to the 2+ state, (ii) mutagenesis experiments showing that when any of three tyrosine residues are mutated to phenylalanine, the ability to carry out the redox reaction on the cluster electrochemically is inhibited, and that charge transfer-deficient mutants exhibit reduced ability to initiate priming, and (iii) primer elongation and termination assays with native full-length primase showing that the introduction of a mismatch into the growing primer inhibits termination, which is consistent with the regulation of primase termination by mismatch-sensitive DNA-mediated charge transport. These data support our proposal that electron transfer between clusters in primase and polymerase α mediated by the growing DNA/RNA duplex, contributes to handoff of the substrate between the two enzymes.

We emphasize that all electrochemistry and corresponding control experiments were performed on the truncated p58C construct, which contains the [4Fe4S] cluster, and all activity assays and corresponding control experiments were performed on the full-length p48/p58 enzyme. Neither Baranovskiy et al. [153] nor Pellegrini [154] directly dispute the electrochemical observations of charge transport through the DNA substrate to the [4Fe-4S] cluster of our p58 construct, nor do they dispute its inhibition by mutation of each of the three relevant tyrosine residues. Rather, they question the path for electron transfer through primase on the basis of differences in structures of p58C, the primase domain containing the [4Fe4S] cluster [71-73]. The structure of human p58C [73] from which we identify conserved tyrosine residues participating in a charge transfer pathway contains residues 318 to 360 folded in a β-hairpin arrangement. Other structures of human [71] and yeast [72] p58C show these residues in an α-helical arrangement and show that conserved tyrosines (Y309, Y345, and Y347 for the human protein) in the charge transport pathway through the protein are spaced and oriented differently in different structures. However, both Comments misinterpret the requirements for charge transport mediated by tyrosines in a protein. Charge transfer through protein, which is only weakly dependent on orientation, can occur over distances up to 15 Å on our proposed time scale and is most accurately estimated from the distances between tyrosine centroids [142]. In fact, regardless of the differences in structures, the tyrosine centroids in all human and yeast p58C structures are within feasible range for microsecond electron transfer through the protein matrix.

In addition to differences in crystallization conditions, our human p58C construct differs in sequence from that of Baranovskiy et al.; our p58C construct corresponds to residues 272 to 464 from the human protein, whereas the residues on the N terminus of our construct—essentially positions 269, 270, and 271—are left from the His tag used to purify the protein. Tahirov uses a different truncation, including more residues on the N terminus but fewer on the C terminus (266 to 456). Our p58C construct was used for the electrochemistry and

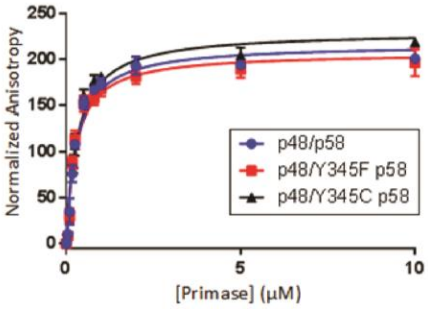

Dissociation Constants for p48/p58

Construct	K_D (μM)
p48/p58	0.30±0.03
p48/p58Y345F	0.28±0.04
p48/p58Y345C	0.32±0.04

Figure 2.20: DNA binding for WT and mutant primase. WT and mutant primase have similar DNA binding affinities with high nanomolar dissociation constants. Affinities were measured by fluorescence anisotropy of FITC-labeled DNA substrates in the presence of atmospheric oxygen in 20 mM HEPES, pH 7.5, and 75 mM NaCl. Background was subtracted from anisotropy values prior to plotting. K_D values are mean ± SD over n=3 measurements for each variant. Fluorescence anisotropy performed by Dr. M. E. Holt.

crystallography, but for all biochemical assays, we used the full human primase (no mutations).

The Comments also raise concerns over our interpretation of data obtained for a Y345F primase mutant, which results in reduced electron transfer efficiency. The argument is based primarily on the assignment of a hydrogen bond between Y345 and the triphosphate group at the 5’ end of the DNA/RNA substrate in a crystal structure [38]. We find it puzzling that elimination of only one of more than 15 hydrogen bonds between p58C and the substrate is proposed as an explanation for the dramatic change in biochemical activity that we observe. In fact, binding assays comparing the full, wild-type primase enzyme and the Y345F primase variant using a DNA substrate show no detectable differences, as expected (Figure 2.20). Furthermore, the placement of the Y345 side chain in the structure, which lies at the center of their claim, may be more ambiguous than previously implied [38]. Retrieving the coordinate files and electron density maps for the structures (5F0Q), we observe a very poor fit for this residue. High B factors for this residue relative to most other residues call into question whether the assigned hydrogen bond has high enough occupancy to substantiate the argument. Moreover, we have now carried out parallel biochemical experiments comparing primer synthesis of wildtype full primase and the charge transfer–deficient Y309F variant of full p48/p58 primase on single-stranded DNA (Figure 2.21).

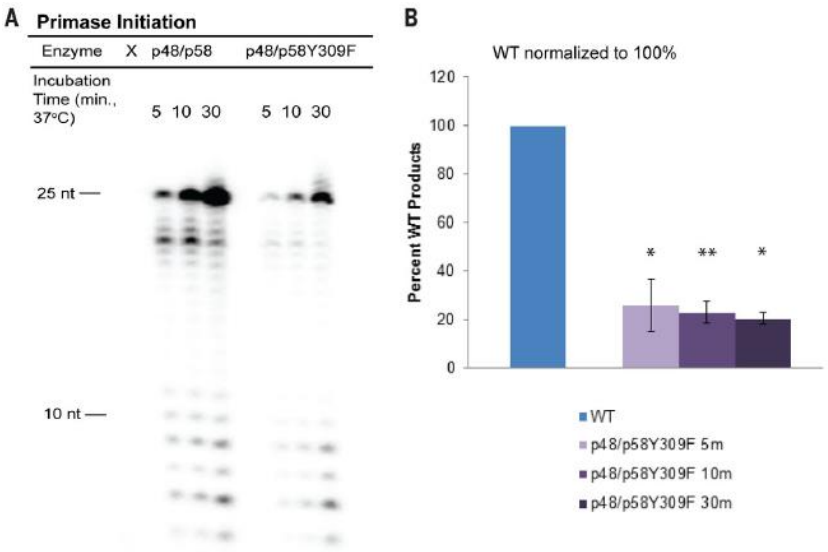

Figure 2.21: Wild-type (WT) p48/p58 versus p48/p58Y309F activity on ssDNA. A) Gel separation of products for primase initiation assay comparing WT and charge transfer–deficient primase. B) Product quantifications for p48/p58Y309F, with WT primase (p48/p58) products normalized to one. alues shown are the mean of n = 3 trials; error bars represent standard deviation. *, 0.001 ≤ P < 0.005; **, P < 0.001; Student's t test. All activity assays were performed under anaerobic conditions. Reactions contained 400 nM primase variant, 250 nM ssDNA, 188 mM uridine triphosphate (UTP), 112 mM cytidine triphosphate (CTP), 1 mM α-^{32}P adenosine triphosphate (ATP) in 50 mM Tris, pH 8.0, 3 mM $MgCl_2$.

Here, too, we observe significant inhibition of initiation in the mutant, just as we observed with the Y345F and Y345C primase variants. Thus, mutation of another tyrosine in the charge transfer pathway, one not interacting with any substrates, also inhibits initiation. Hence, inhibition of initiation is the result of inhibition of the redox switch.

Baranovskiy et al. criticize our choice of substrate for the electrochemical studies of p58C. Primase interacts with a range of DNA structures [73], enabling us to create a substrate that productively binds primase and satisfies the technical criteria needed for DNA-mediated electrochemistry. Our substrates were designed for the primary objectives of the experiment: (i) to assess the ability of p58C to participate in DNA charge transport and (ii) to examine the differential effects of [4Fe4S] cluster oxidation state. The binding affinity of p58C for the substrate should therefore not be particularly strong, so that any changes in affinity between oxidized $[4Fe4S]^{3+}$ and reduced $[4Fe4S]^{2+}$ protein can be detected. A substrate similar to the

construct containing a 3′ single-stranded DNA (ssDNA) overhang and 5′-triphosphate, which Baranovskiy et al. [85] observe p58C binds tightly, would obscure the observation of differences between the two redox states on the electrode. Moreover, as it contains a 5′-ssDNA overhang, our electrochemistry substrate is similar to the primed ends encountered by polymerase enzymes in cells.

Baranovskiy et al. additionally suggest that a mismatch in the nascent primer inhibits initiation, but not truncation in the assay with a primed template substrate. On both well-matched and mismatched substrates, we observe a mixture of initiation and elongation products because primase binds to both ssDNA and primed DNA portions of the substrate [76]. Primase initiation products (7 to 29 nucleotides) are synthesized on the ssDNA template used to generate a mismatched primer. Baranovskiy et al. also criticize our assignment of the oxidized $[4Fe4S]^{3+}$ species generated electrochemically. However, we show directly using cyclic voltammetry, as seen in Figures 2.1, 2.2, and 2.4 of [76], that we generate the oxidized $[4Fe4S]^{3+}$ product. The cathodic peaks in Figure 2.1 and Figure 2.4 [76] furthermore show the reduction of an oxidized species on the DNA-modified electrode. Additionally, chemical oxidants with potentials similar to the potential applied to p58C can oxidize human p58C to the $[4Fe4S]^{3+}$ state, as demonstrated by electron paramagnetic resonance spectroscopy [70], supporting our assignment of the $[4Fe4S]^{3+}$ species. We were not able to perform binding affinity measurements with the electrochemically oxidized p58C because the oxidized protein is unstable over the long periods of time required for the measurement.

Finally, Baranovskiy et al. criticize our performing *in vitro* priming assays under anaerobic conditions that they argue do not correspond to the cellular environment. Anaerobic conditions were used to ensure that we had full control over the redox state of the [4Fe4S] cluster, which can be oxidized in the presence of air [53]. In fact, controls performed under aerobic conditions gave similar results overall, although with greater scatter and lower precision.

Overall, the positioning of tyrosines 309, 345, and 347 in both structures of human p58C, irrespective of local conformation, suggests a feasible pathway for electron transfer through the [4Fe4S] protein. The electrochemical experiments with p58C variants, and the biochemical activity assays with corresponding full primase variants, illuminate the electron transfer chemistry performed by the primase [4Fe4S] cluster and the effect of this chemistry on DNA binding. Primer elongation assays with well-matched and mismatched template strands, moreover, demonstrate the regulatory role of DNA charge transport in termination. Thus, the concerns raised do not abrogate either our experimental observations of redox chemistry performed by the [4Fe4S] cluster or the proposal of a role for the redox chemistry, coupled to DNA charge transport, in regulating the activity of human DNA primase.

CHAPTER 3

FUNCTIONAL AND STRUCTURAL SIMILARITY OF HUMAN DNA PRIMASE 4FE-4S CLUSTER DOMAIN CONSTRUCTS[4]

Introduction

DNA synthesis at the replication fork begins with the formation of 8-12 nucleotide (nt) RNA primers on the single-stranded DNA template [155, 156]. In eukaryotes, primers are generated by the heterotetrameric DNA polymerase α-primase (pol-prim) complex, which possesses two enzymatic activities in two distinct active sites [81, 82, 157]. Primase, a DNA-dependent RNA polymerase, generates the initial hybrid RNA-DNA primed substrate, which is then handed off to DNA polymerase α (pol α) to extend the initial primer by approximately twenty DNA nts. The extended primed substrates are in turn handed off to the processive polymerases ε and δ, which synthesize the bulk of nascent DNA on the leading and lagging strands, respectively [158-160].

Human DNA primase is composed of catalytic (p48) and regulatory (p58) subunits. The regulatory subunit has a C-terminal domain (p58C) that is unique to higher eukaryotes and contains a [4Fe4S] cluster [69, 70, 161]. This domain regulates the catalytic efficiency of primase, a function attributed to the ability to bind nucleotides, DNA template, and primed substrate [24, 25, 38, 69-73, 84, 159]. We have recently proposed that [4Fe4S] redox control of DNA binding affinity may serve as a mechanism to drive handoff of the RNA primed template from the primase to the pol α subunits of human pol-prim [76]. Skepticism about some of the reported results have been expressed and debated [153, 154, 162], much of which was related to differences in crystal structures obtained from p58C constructs with different N-termini [163].

[4] This chapter was published as Holt ME, Salay LE, O'Brien E, Barton, JK, Chazin WJ., Functional and structural similarity of human DNA primase [4Fe4S] cluster domain constructs, PLoS One, 2018.

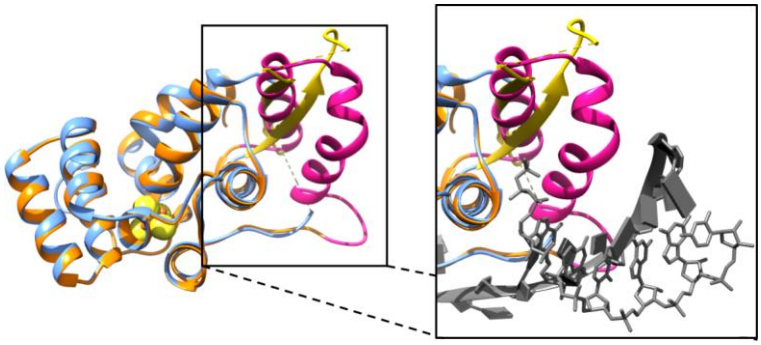

Figure 3.1: Comparison of the structures of p58C$_{272-464}$ and p58C$_{266-456}$. (A) Best-fit superposition over all backbone atoms of the crystal structures of the p58C$_{272-464}$ (PDB ID: 3L9Q) and p58C$_{266-456}$ (PDB ID: 5F0S) constructs. The substrate in the p58C$_{266-456}$ structure is removed for clarity. Inset: Best-fit superposition over all backbone atoms of the DNA binding region with the primed substrate shown in the p58C$_{266-456}$ structure. p58C$_{266-456}$ is colored orange, p58C$_{272-464}$ blue, and the RNA-primed DNA substrate in grey (RNA in sticks, DNA in slabs). In the inset, Leu318-His351 are colored yellow in the p58C$_{272-464}$ structure and pink in the p58C$_{266-456}$ structure. Connectivity between residues where electron density is missing is indicated by dashed lines.

The p58C domain of human primase has been crystallized under two different conditions and these have generated structures that have the same global fold but localized differences in secondary structures [71, 73]. Figure 3.2 shows a best-fit superposition of the high-resolution X-ray crystal structures of the two p58C$_{272-464}$ and p58C$_{266-456}$ constructs. The two structures are clearly very similar except for residues Leu318-His351, which are positioned near the DNA binding site. In the crystal structure of p58C$_{272-464}$, these residues occupy a β-sheet-like structure that is stabilized by cross-strand interactions with another molecule in the unit cell [73]. In addition, a disulfide cross-link is formed during crystallization between the Cys449 residues of adjacent p58C molecules. In contrast, when p58C$_{266-456}$ was crystallized under a different set of conditions, this β-type interaction is not observed and instead these residues occupy a helical hairpin [71]. It has been proposed that Ile271 is critical for stabilizing this helical motif and therefore the absence of this residue explains why p58C$_{266-456}$ has a different structure [153, 154].

Many of the concerns about our work were attributed to the fact that the structural differences between the two p58C constructs occurred in a region that contains residues interacting with DNA substrates. However, it is well known that differences between crystal

structures arise when crystals are formed under different crystallization conditions. In order to resolve any controversy and directly address the concerns raised about our findings, we report here a comprehensive set of studies of a $p58C_{266-464}$ construct. Comparisons of the crystal structure of this construct are made to previously reported crystal structures. In addition, the structure was analyzed in solution by circular dichroism and NMR, along with assays of DNA binding affinities and electrochemical properties. These results show that the structure of Leu318-His351 varies in accord with crystallization conditions, whereas the structure in solution and biochemical properties of different p58C constructs are effectively the same.

Methods

$p58C_{266-464}$ construct generation

The $p58C_{266-464}$ construct was created by Dr. M.E. Holt with a Q5 site-directed mutagenesis kit from New England Biolabs, using the $p58C_{272-464}$ construct plasmid [73] as the template, 5'- GGCAAGATTTCCTTAGATCAGATTGATTTGCTTTCTACC - 3' for the forward primer, and 5' – CACATTTCCGGGCCCCTGGAACAGAAC - 3' for the reverse primer. 10 ng of $p58C_{272-464}$ plasmid was used in the exponential amplification, which was completed as described in the Q5 Site-Directed Mutagenesis Kit manual (New England Biolabs), except that the final extension time was extended to 5 minutes. The KLD reaction was also completed as described in the manual, except that 4 µL of PCR product was used in the reaction and the incubation time was increased to 20 minutes. 10 µL of the KLD reaction product was transformed into XL1-Blue cells. DNA was extracted from individual colonies with a Qiagen QIAprep Spin Miniprep Kit. Appropriate insertion of residues 266-271 was confirmed through plasmid sequencing (GENEWIZ, LLC).

Protein expression and purification

p58C constructs were expressed and purified as previously described [76, 163] by L.E. Salay and Dr. M.E. Holt. In short, plasmid DNA was transformed into BL21 (DE3) cells (Novagen) and cultured in Terrific Broth media at 37 °C to an OD_{600} of 0.6-0.8, when flasks were

moved to a 21 °C incubator with shaking. After 30 minutes, ferric citrate and ammonium ferrous citrate were added to a final concentration of 0.1 mg/mL, and isopropyl 1-thio-β-D-galactopyranoside was added to a final concentration of 0.5 mM. Protein was expressed at 21 °C overnight. The same growth protocol was used to generate ^{15}N-labeled p58C, except that cells were cultured in M9 media supplemented with ^{15}N-labled ammonium chloride (Cambridge Isotopes) and expressed overnight at 25 °C. The same purification scheme was used for both unlabeled and ^{15}N-labeled protein [163]. In short, protein was first purified by nickel affinity chromatography (Amersham Biosciences). The 6xHis tag was cleaved with H3C protease and the protein was dialyzed into a low-imidazole buffer [76, 163]. The protein was repassed over the nickel column to remove the H3C protease and uncleaved protein. A heparin column was used as the final purification step to remove residual contaminants [76, 163].

Crystallization and structure determination

Crystallization was performed by Dr. M.E. Holt. Data collection, processing, model building and refinement was performed by L.E. Salay. The structure of $p58C_{266-464}$ was determined as previously described for $p58C_{272-464}$ [73, 163]. $p58C_{266-464}$ crystals were grown by hanging drop vapor diffusion at 16 °C from a drop composed of equal volumes of 50 mg/ml protein in 20 mM MES (pH 6.5) and 75 mM NaCl and reservoir solution containing 100 mM Tris (pH 8.5), 400 mM Li_2SO_4 and 18% (v/v) PEG 3350. Prior to data collection, crystals were transferred to a drop containing 100 mM Tris (pH 8.5), 400 mM Li_2SO_4,18% (v/v) PEG 3350, and 20% (v/v) glycerol for five seconds. The crystals were looped and flash frozen in liquid nitrogen. X-ray data were collected at beamline 21ID-D (Life Sciences Collaborative Access Team) of the Advanced Photon Source at Argonne National Laboratory at 11.5 kEV. All data were processed by HKL2000 [132].

Table 3.1. Crystallographic data collection and refinement statistics

Data collection	
Space Group	C2
Cell Dimensions	
a, b, c (Å)	110.19, 52.56, 88.77
α, β, γ (°)	90, 115.08, 90
Temperature (K)	100
Wavelength (Å)	1.08
Resolution (Å)	50.00-2.01 (2.08-2.01)
Unique Reflections	27193
R_{meas} (%)	0.14 (0.79)
$I/\sigma I$	10.06 (2.12)
Completeness (%)	88.6 (84.4)
Redundancy	3.6 (3.3)
Refinement	
Resolution (Å)	50.00-2.01 (2.08-2.01)
No. reflections	27153
R_{work}/R_{free}	0.18/0.21 (0.23/0.24)
No. molecules/ASU	2
No. atoms	2872
Protein	2689
Ligand/ion	41
Water	52
B-factors	
Mean	39.1
Protein	38.7
Ligand/ion	66.9
R.m.s. deviations	
Bond lengths (Å)	0.003
Bond angles (°)	0.62
Ramachandran	
Favored	308 (99.4%)
Allowed	2 (0.6%)
Disallowed	0 (0%)

Values in parentheses are for the highest-resolution shell.

The structure was determined using molecular replacement (PHASER-MR) with PDB entry 3L9Q, residues 274-316 and 360-457, as the search model. Manual model building for the

structure was performed using *Coot* model building software, and waters were placed with the *Coot* routine, Find Waters [114]. The final model was obtained by iterative cycles of model building in *Coot* and structure refinement using Phenix.refine in the Phenix suite of programs [116, 164]. Structures were superimposed and RMSD calculated in Chimera with the Matchmaker algorithm [165]. Programs used for structure determination and refinement were accessed through SBGrid [166]. Statistics for data collection and refinement are shown in Table 3.1.

Circular dichroism (CD) spectroscopy

CD spectroscopy was performed by Dr. M.E. Holt. Samples were buffer exchanged into 20 mM K_2HPO_4 (pH 7.2) and diluted to a concentration of 0.3 mg/mL. The far-UV CD spectrum over the range 190–260 nm was acquired at room temperature using a Jasco J-810 spectrophotometer. Each spectrum is the average of three scans acquired with a scanning rate of 50 nm/min and data pitch of 1 nm. Prior to generating the overlay in Graphpad Prism 7, the $p58C_{266\text{-}464}$ spectrum was scaled to the $p58C_{272\text{-}464}$ spectrum by averaging the values of the $CD_{208}(p58C_{272\text{-}464})/CD_{208}(p58C_{266\text{-}464})$ and $CD_{222}(p58C_{272\text{-}464})/CD_{222}(p58C_{266\text{-}464})$ ratios to generate a scaling factor (~0.86), then multiplying the entire $p58C_{266\text{-}464}$ spectrum by this scaling factor.

NMR spectroscopy

NMR spectroscopy was performed by Dr. M.E. Holt. Spectra were acquired using a Bruker AV-III 800 MHz spectrometer equipped with a CPTCI single-gradient cryoprobe. ^{15}N-enriched p58C constructs at a concentration of 200 µM were prepared in a buffer containing 20 mM MES (pH 6.5), 50 mM NaCl, 2 mM DTT, and 5% (v/v) D_2O. Two-dimensional ^{15}N-^{1}H heteronuclear single quantum coherence (HSQC) spectra were acquired at 25 °C with 2,048 and 128 points in the ^{1}H and ^{15}N dimensions, respectively. 64 scans were recorded in the direct (^{1}H) dimension for each point sampled in the indirect (^{15}N) dimension. Data were processed by Topspin (Bruker) and analyzed with Sparky (University of California).

RNA primer generation

RNA primer generation was performed by Dr. M.E. Holt. Triphosphorylated RNA primer was transcribed with T7 RNA polymerase [167] and purified on a 25% TBE-polyacrylamide gel supplemented with 8 M urea according to standard methods. Dried RNA pellet was resuspended in RNAse-free H_2O and aliquoted prior to further purification. RNAs used for binding assays were HPLC purified on a Luna 5 µM C18(2) 100 Å 250X4.6 mm column (Phenomenex). Buffer A: 0.1 M ammonium formate; Buffer B: acetonitrile; flow rate: 1.5 mL/min. Purification program: 1-5% Buffer B over three minutes, 5-8% Buffer B over 22 minutes, then 80% Buffer B for five minutes. RNA typically eluted around 11 minutes. HPLC-purified RNA was further validated with mass spectrometry, which confirmed that a product of the expected mass had been generated.

Substrate binding assays

Microscale thermophoresis measurements were performed by Dr. M.E. Holt. Initial fluorescence intensity was measured with a Monolith NT.115 series microscale thermophoresis (MST) instrument (NanoTemper) at 25 °C. Cy5-labeled 18 nt DNA template was purchased from Sigma-Aldrich. A 1.1:1 ratio of 8 nt RNA and this DNA template was annealed in annealing buffer (20 mM MES (pH 7.0), 75 mM NaCl), resulting in a 25 µM stock of annealed, primed substrate. This stock was diluted to 100 nM with MST buffer (20 mM MES (pH 6.5), 50 mM NaCl, 2 mM DTT, 0.05% Tween). This primed substrate was mixed with p58C and allowed to incubate in the dark at room temperature for 15 min. Samples with a final substrate concentration of 50 nM were then loaded into MO-K003 Monolith NT.115 hydrophobic capillaries (NanoTemper) and fluorescence was measured at 20% LED and 40% MST power. Final K_D values were calculated using the one-site total binding equation in GraphPad Prism 7. Titrations were completed after running an SD test to ensure that the concentration-dependent changes in fluorescence intensity were due to protein binding [168].

MST RNA primer: 5’-PPP-GGCUCGGA-3’

MST DNA template: 5’-Cy5-AAACTCCGAGCCAACATA-3’

Fluorescence anisotropy (FA) measurements were taken by L.E. Salay. FA was measured with a SpectraMax M5 microplate reader (Molecular Devices). A 6FAM-labeled 22 nt DNA template was purchased from Sigma-Aldrich. A 1.1:1 ratio of 12 nt RNA and this DNA template was annealed in annealing buffer (20 mM MES (pH 7.0), 75 mM NaCl), resulting in a 25 µM stock of annealed, primed substrate. The stock was diluted to 800 nM with DNA binding buffer (20 mM MES (pH 6.5), 50 mM NaCl, 2 mM DTT). This primed substrate was mixed with p58C and allowed to incubate in the dark at room temperature for 15 min. Samples with a final substrate concentration of 50 nM were then loaded into a 384-well plate and polarized fluorescence intensities were measured using excitation and emission wavelengths of 485 nm and 520 nm. For the fluorescein control, 25 nM fluorescein (Sigma Aldrich) was dissolved in DNA binding buffer containing 0.016% DMSO, mixed with p58C, and allowed to incubate in the dark at room temperature for 15 min prior determining fluorescence anisotropy in the same way as for the p58C-DNA titrations. For this control, 25 nM fluorescein was used to match the intensity of the probe in the fluorescence anisotropy substrate binding assay. Three replicates were collected for each titration. Final K_D values were calculated using the one-site specific binding equation in GraphPad Prism 7; prior to using this equation, each binding curve was normalized by subtracting the fluorescence anisotropy value of the zero point from each point on the curve. K_D values are reported as the mean ± standard deviation of three measurements for each variant.

FA RNA primer: 5’-PPP-GGACCTCCAGGA-3’

FA DNA template: 5’-6FAM-AAACTCCTGGAGGTCCAACATA-3’

Sample preparation for electrochemistry

Electrochemistry was performed by Dr. E. O’Brien. Multiplexed chips were fabricated as described previously [76]. p58C construct samples were stored prior to experiments in p58C

storage buffer (20 mM Tris (pH 7.2), 75 mM NaCl). All p58C constructs were buffer exchanged into HEPES electrochemistry buffer (20 mM HEPES (pH 7.2), 75 mM NaCl) using Amicon ultra centrifugal filters (0.5 mL, 3 kDa MWCO) (Millipore Sigma). Protein was applied to the filter in volumes of 90-140 µL and centrifuged for 15 minutes at 14000 x g at 4 °C. After centrifugation, 400 µL of HEPES electrochemistry buffer was applied to the filter and centrifuged at 14000 x g for 20 minutes. This was repeated four times to exchange p58C samples into HEPES electrochemistry buffer. After buffer exchange and recovery of sample by centrifugation (2 minutes, 1000 x g), concentrations of [4Fe4S] cluster-containing p58C or mutants were measured by using UV-Visible spectroscopy to monitor the absorbance of the [4Fe4S] cluster at 410 nm (extinction coefficient = 17000 M^{-1} cm^{-1}) [63, 76]. Recovered samples (approx. 100-150 µL in volume) were deoxygenated for 2-3 minutes with argon. Samples were then transferred into the anaerobic chamber (Coy Laboratory products). Prior to deposition onto the gold electrode surface, $p58C_{266-464}$ samples were diluted with previously deoxygenated HEPES electrochemistry buffer to a molar concentration of 40µM [4Fe4S] p58C. Samples were initially deposited onto multiplex chip quadrants in 20 µL volumes and the remaining sample deposited in a well of bulk solution above the chip surface, to a final volume of 200-300 µL.

p58C construct electrochemistry

Electrochemistry was performed by Dr. E. O'Brien. All electrochemistry was performed using a CHI620D potentiostat and 16-channel multiplexer (CH Instruments) in an anaerobic glove chamber. Multiplex gold electrodes were part of a three-electrode system with an external Ag/AgCl reference electrode (Bioanalytical Systems) and platinum counter electrode. Cyclic voltammetry scans were performed at a scan rate of 100 mV/s over a potential range of +0.412 V to -0.288 V vs. NHE or +0.512 V to -0.188 V vs NHE. Bulk electrolysis on DNA was performed at an applied potential of +0.512 V vs. NHE for all electrochemical oxidation reactions. The oxidizing potential was applied for at least 8.33 minutes for single oxidation reactions on a

surface, and 6.67 minutes for the iterative oxidation cycles of p58C variants. The reducing potential was applied for 8.33 minutes in all electrochemical reduction reactions. All bulk electrolysis and cyclic voltammetry were performed in previously deoxygenated p58C electrochemistry buffer (20 mM HEPES (pH 7.2), 75 mM NaCl). Charge transfer (nC) in the cathodic peak of oxidized samples CV scans was assessed using the area under the current wave of the reduction signal. Charge transfer was measured for oxidized samples using CHI software, assessing the area under the reductive peak in CV after electrochemical oxidation. NTP-dependence of electrochemical signals was measured by pipetting a small volume (1-3 µL) of a 0.1 M ATP stock solution into each quadrant of the multiplexed chip setup. Samples were added by quadrant, as physical barriers in the setup prevent diffusion of NTPs between electrode quadrants. After the volume of ATP stock was deposited onto the electrode quadrant, resulting in a 2.5 mM or 5 mM concentration of ATP in the quadrant, CV scans were measured (100 mV/s scan rate). Charge transfer was assessed using CHI software; charge values were determined by calculation of the area under the reductive and oxidative peak curves. Midpoint potentials of NTP-dependent redox signals were assessed using the peak selection function in CHI software.

Results

p58C can be crystallized in different conformations

To test if the differences between the $p58C_{266-456}$ and $p58C_{272-464}$ structures were a by-product of the differences in sequence, we produced, purified, and crystallized a p58C construct containing residues 266-464 in the conditions used to crystallize $p58C_{272-464}$ [73, 76]. These crystals diffracted to 1.6 Å and the data were phased using molecular replacement with the structure of $p58C_{272-464}$ (3L9Q). To avoid phase bias, residues 315-360 were excluded when defining the search model. With these residues omitted, density for residues in extended conformation that together formed a beta-type interaction were clearly evident in the $p58C_{266-464}$

2Fo-Fc map (Figure 3.2).

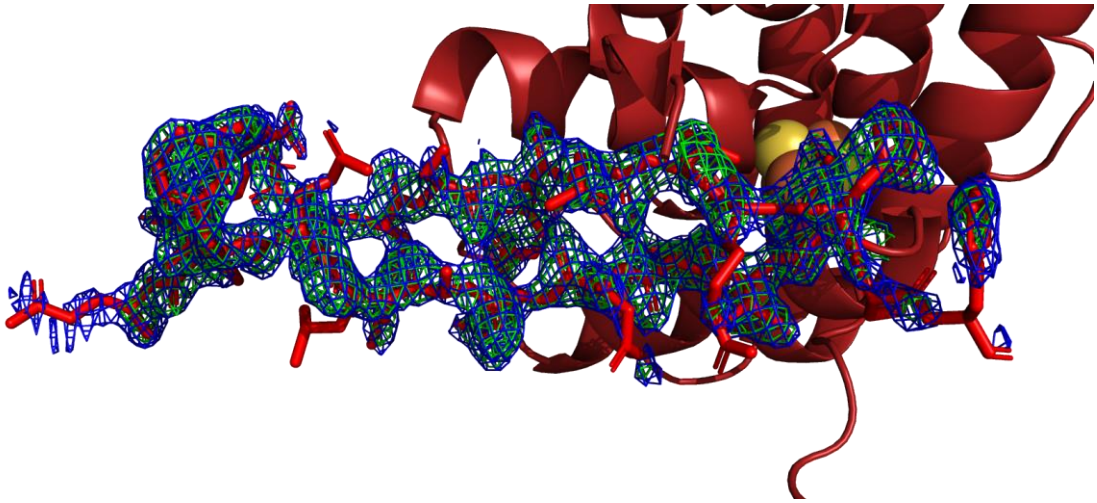

Figure 3.2: Electron density maps revealing β-sheet-like conformation for residues Leu318-His351. The ribbon diagram of the structure with Leu318-His351 displayed in stick representation is docked into the starting electron density map around the β-sheet-like region. Blue mesh represents the $2F_o$-F_c map contoured at 1 σ, Green mesh represents the F_o-F_c map, contoured at 3 σ. Figure made in Pymol using the isomesh command. Crystallography performed by L. E. Salay

This region was re-built manually in *Coot*, and the final structure was refined to 2.01 Å resolution. As previously observed for $p58C_{272-464}$ under these conditions, crystallized as a dimer, with a disulfide cross-link between the two Cys449 residues and several stabilizing interactions between symmetry-related molecules (Figure 3.3). In $p58C_{266-464}$, residues 330-340 and 353-360 in chain A and 330-345 and 353-359 in chain B are missing due to disorder.

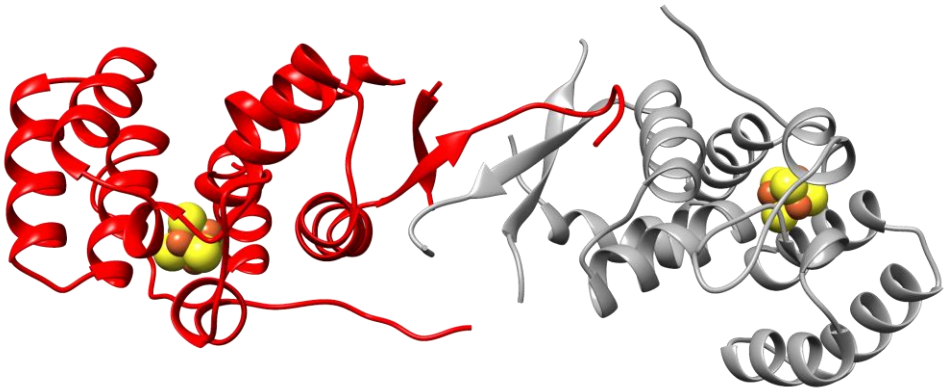

Figure 3.3: Interaction with a symmetry related molecule. The beta sheet-like region of $p58C_{266-464}$ (red) is stabilized by interactions with the beta sheet-like region of an adjacent symmetry-related molecule (grey). Crystallography performed by L. E. Salay

Disordered residues in the same regions are observed in the structure of p58C$_{272-464}$. A best-fit superposition of the two structures reveals they are very similar (Figure 3.4), with a backbone RMSD of only 0.23 Å. This finding shows that the differences in residues Leu318-His351 evident from comparing the previous p58C structures [71-73] are not intrinsic to the differences in the N-termini of the constructs but rather to differences in the crystallization conditions.

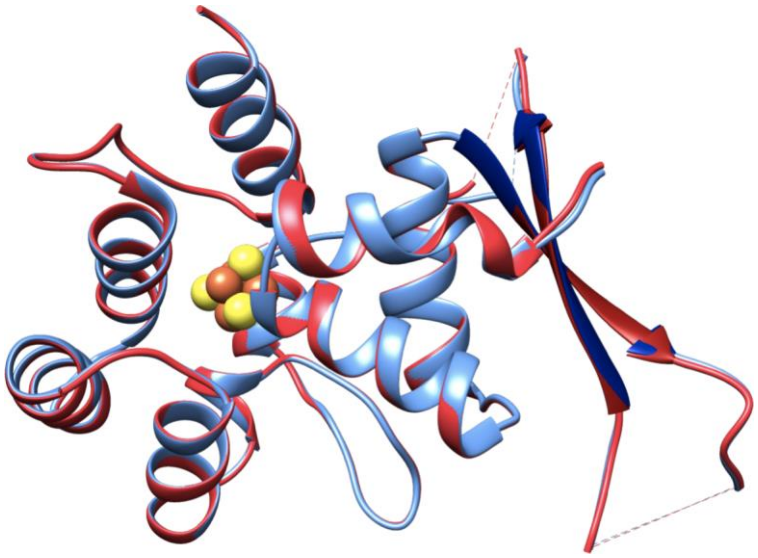

Figure 3.4: Comparison of the X-ray crystal structures of p58C$_{266-464}$ and p58C$_{272-464}$ obtained from crystals grown under identical conditions. Ribbon diagrams of the best-fit superposition over all backbone atoms of p58C$_{272-464}$ (blue) and p58C$_{266-464}$ (red) crystal structures. Residues Leu318-His351 are colored dark blue in the p58C$_{272-464}$ structure and dark red in the p58C$_{266-464}$ structure. Connectivity between residues where electron density is missing is indicated by dashed lines. The [4Fe4S] clusters are shown as the cluster of yellow and orange spheres. Crystallography performed by L. E. Salay

CD and NMR show p58C$_{272-464}$ and p58C$_{266-464}$ are structurally similar in solution

Because the differences in the X-ray crystal structures can be attributed to differences in the crystallization conditions, we used CD and NMR spectroscopy to determine if there are significant structural differences between p58C$_{272-464}$ and p58C$_{266-464}$ in solution. The CD spectra of p58C$_{272-464}$ and p58C$_{266-464}$ acquired under identical conditions were very similar (Figure 3.5), showing that the two constructs contain the same distribution of secondary structure [102]. To further investigate the structures of these constructs, ^{15}N-^{1}H HSQC spectra were collected for

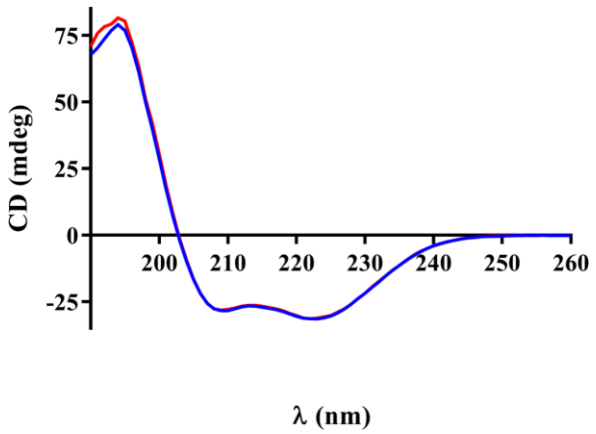

Figure 3.5: The p58C$_{272-464}$ and p58C$_{266-464}$ constructs have the same distribution of secondary structures in solution. CD spectra p58C$_{272-464}$ (blue) and p58C$_{266-464}$ (red) were collected at room temperature for a solution containing 0.3 mg/mL of protein in a buffer containing 20 mM K_2HPO_4 (pH 7.0). CD spectroscopy performed by Dr. M. E. Holt.

^{15}N-enriched p58C$_{272-464}$ and p58C$_{266-464}$. Figure 3.6 shows an overlay of HSQC spectra acquired under identical conditions for p58C$_{272-464}$ and p58C$_{266-464}$. These match well with previously published spectra [70, 73], indicating that both constructs are well-folded. There are a number of chemical shift perturbations between the two spectra, consistent with the presence of six additional N-terminal residues. Overall, the distribution of peaks is very similar in the two spectra, indicating that the overall tertiary structure of p58C$_{272-464}$ and p58C$_{266-464}$ are the same.

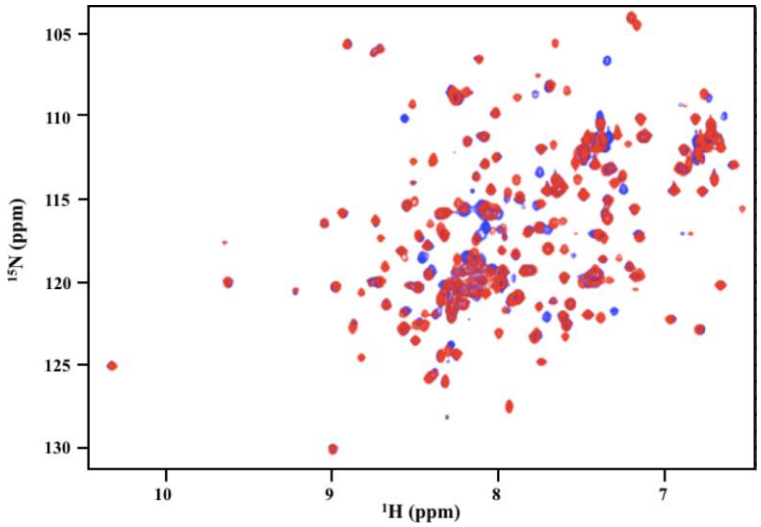

Figure 3.6: The tertiary structures of p58C$_{272-464}$ and p58C$_{266-464}$ constructs are similar in solution. ^{15}N-^{1}H HSQC NMR spectra of p58C$_{272-464}$ (blue) and p58C$_{266-464}$ (red) were acquired at 25 °C on a Bruker AV-III spectrometer operating at 800 MHz. The samples contained 200 µM protein in a buffer containing 20 mM MES (pH 6.5), 50 mM NaCl, 2 mM DTT, and 5% $^{2}H_2O$. NMR performed by Dr. M. E. Holt.

Sequence-specific assignments could provide insight into the nature of the differences in the NMR spectra. However, the presence of the paramagnetic [4Fe4S] cluster causes extreme line broadening due to rapid relaxation of spatially proximate residues, greatly complicating efforts to obtain resonance assignments [169]. Despite the absence of assignments, because the NMR spectra are so similar, and the CD spectra are virtually identical, we can conclude that there are no substantial differences in the structures of $p58C_{272-464}$ and $p58C_{266-464}$ in solution.

The $p58C_{272-464}$ and $p58C_{266-464}$ constructs have the same affinity for a primed template

Having established that the structures of $p58C_{272-464}$ and $p58C_{266-464}$ are essentially the same, it is important to determine if the two constructs are functionally equivalent. Since DNA binding is an essential property for p58C function, we turned to a fluorescence assays to compare the DNA binding properties of the two constructs. We first used a fluorescence intensity-based assay with an RNA-primed DNA substrate composed of a Cy5-labelled 18 nt DNA template strand annealed with a complementary 5'-triphosphorylated 8 nt RNA primer, corresponding to a high affinity product produced by primase [85]. The affinities of $p58C_{272-464}$ and $p58C_{266-464}$ for this substrate were measured by monitoring initial fluorescence intensity (FI) changes as p58C was titrated into a fluorescently-labelled substrate (Figure 3.6). Fitting these data to a single site binding equation returned dissociation constants (K_D) within statistical error: 2.7 ± 0.3 µM and 3.4 ± 0.5 µM for $p58C_{272-464}$ and $p58C_{266-464}$, respectively.

Because the fluorescence intensity-based assay is measuring fluorescence quenching, it is conceivable that this assay could be sensing direct interaction with the probe. While a standard SD test had been run to ensure that signal change was due to interaction of protein with substrate [168], we turned to a fluorescence anisotropy assay to further rule out the possibility of direct probe binding. For this assay, an RNA-primed DNA substrate was used composed of a 6FAM-labelled 22 nt DNA template strand annealed with a complementary 5'-triphosphorylated 12 nt RNA primer. We used the longer template to place the probe further away from the RNA-DNA hybrid region and minimize probe quenching. The K_D values of $3.6 \pm$

0.1 µM and 2.1 ± 0.1 µM obtained by FPA for p58C$_{272-464}$ and p58C$_{266-464}$, respectively are very similar to those obtained by the fluorescence intensity assay (Figure 3.7).

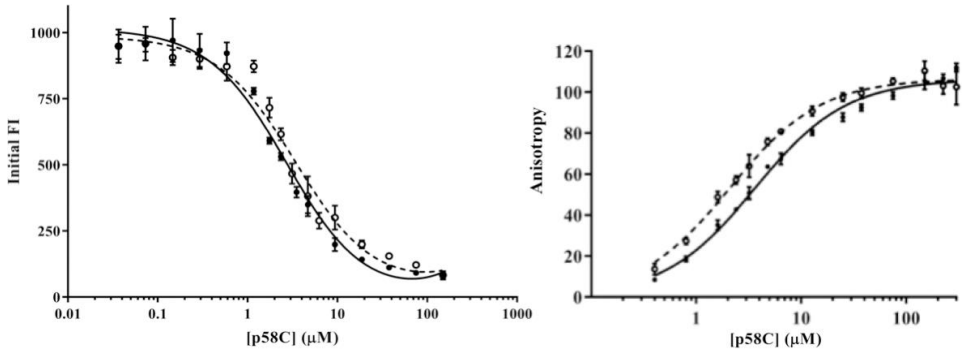

Figure 3.7: The two p58C constructs bind a RNA-primed substrate with the same affinity. Left: The p58C$_{272-464}$ (filled circle, solid line) and p58C$_{266-464}$ (open circle, dashed line) proteins were titrated into Cy5-labeled substrate in a buffer containing 20 mM MES (pH 6.5), 50 mM NaCl, 2 mM DTT, and 0.05% Tween. FI was measured at 25 °C. RNA: 5'-GGCUCGGA-3'; DNA: 5'-Cy5-AAACTCCGAGCCAACATA-3'. MST was performed by Dr. M.E. Holt. Right: The p58C$_{272-464}$ (filled circle, solid line) and p58C$_{266-464}$ (open circle, dashed line) proteins were titrated into 6FAM-labeled substrate in a buffer containing 20 mM MES (pH 6.5), 50 mM NaCl, and 2 mM DTT. Fluorescence anisotropy was measured at 25 °C. RNA: 5'-GGACCTCCAGGA-3'; DNA: 5'-6FAM-AAACTCCTGGAGGTCCAACATA-3'. Fluorescence anisotropy was performed by L. E. Salay. For both panels, error bars represent the standard deviation of three replicates.

Additionally, we conducted titrations of each p58C construct into fluorescein over the range of p58C concentrations utilized in these assays (Figure 3.8).

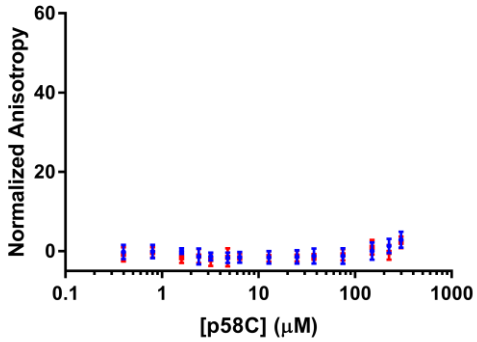

Figure 3.8. Titration of p58C$_{266-464}$ and p58C$_{272-464}$ into fluorescein. p58C$_{272-464}$ (blue circles) and p58C$_{266-464}$ (red squares) proteins were titrated into 25 nM fluorescein in a buffer containing 20 mM MES (pH 6.5), 50 mM NaCl, 2 mM DTT, and 0.016% DMSO. Fluorescence anisotropy was measured at 25 °C. Before plotting on the graph, these data were normalized by subtracting the fluorescence anisotropy value at [p58C] = 0 µM for each titration point. Error bars represent standard deviation. Fluorescence anisotropy was performed by L. E. Salay.

These control experiments revealed no apparent change in fluorescence anisotropy, indicating

that the observed binding interaction is caused by interactions between p58C and the DNA substrate, rather than between p58C and the probe. The narrow range (2.1 - 3.7 μM) and average values (3.2 μM and 2.8 μM, respectively) of K_D for the two constructs measured by the two approaches indicate there is no functionally significant difference in the DNA binding properties of these two constructs.

The p58C$_{272-464}$ and p58C$_{266-464}$ constructs have similar electrochemical properties

The [4Fe4S] cluster in p58C$_{272-464}$ was previously shown to function as a redox switch regulating DNA binding and signaling activity [76]. The oxidized, $[4Fe4S]^{3+}$ form of this protein was DNA-bound and redox-active; the reduced $[4F\text{-}e4S]^{2+}$ form was loosely associated with DNA and exhibited no DNA-mediated electrochemical signal in a cyclic voltammetry scan. To test whether the same redox switching function was present in p58C$_{266-464}$, we characterized this construct using DNA electrochemistry. Using the multiplexed, DNA-modified Au electrode platform shown in S3 Figure, we assessed the redox behavior of p58C$_{266-464}$ on a 20-nt duplex DNA substrate with a 3-nt, 5'-ssDNA overhang [76]. Electrochemical experiments were performed in anaerobic conditions to prevent nonspecific degradation of the cluster by atmospheric oxygen [53]. Electrochemically unaltered p58C$_{266-464}$, which is predominantly present in the $[4Fe4S]^{2+}$ oxidation state, displays no redox signal on DNA, as observed with p58C$_{272-464}$. However, upon electrochemical oxidation to the $[4Fe4S]^{3+}$ state by bulk electrolysis at an applied potential of 512 mV vs. NHE, CV scans of p58C$_{266-464}$ display a large reductive peak near -140 mV vs. NHE. As observed for p58C$_{272-464}$, this peak disappears after one scan to negative reducing potentials (Figure 3.9).

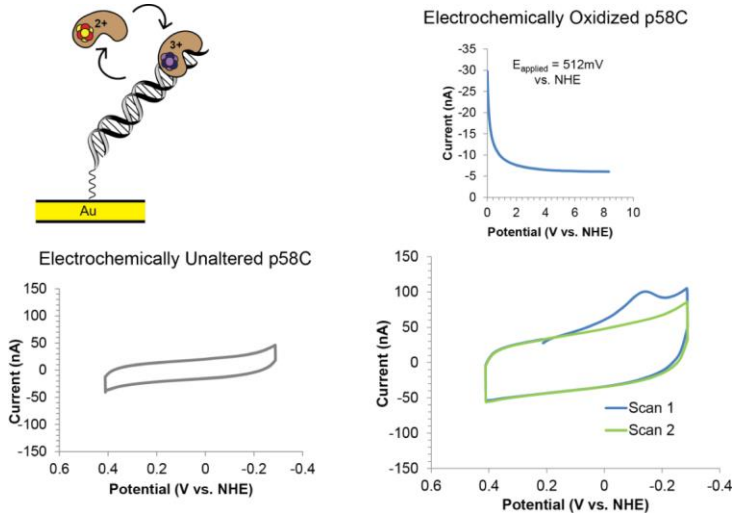

Figure 3.9: p58C$_{266-464}$ participates in redox switching on DNA. The cartoon (top left) depicts p58C DNA binding and redox switching on an Au electrode. (Bottom left) CV scan of electrochemically unaltered p58C$_{266-464}$. (Right) bulk oxidation (above) of p58C$_{266-464}$ and subsequent CV scans (below). This construct displays similar electrochemical behavior to p58C$_{272-464}$. All electrochemistry was performed in anaerobic conditions with 40 µM [4Fe4S] p58C$_{266-464}$ in 20 mM HEPES (pH 7.2), 75 mM NaCl. CV was performed at 100 mV/s scan rate. Electrochemistry was performed by Dr. E. O'Brien

We next tested if the [4Fe4S] cluster of p58C$_{266-464}$ functions as a redox switch and found that this construct can cycle between the tightly bound, redox-active [4Fe4S]$^{3+}$ state, and the loosely associated [4Fe4S]$^{2+}$ state. The p58C$_{266-464}$ construct also displays a robust, reversible, NTP-dependent signal (Figure 3.10) centered at 142 ± 12 mV vs. NHE on a DNA electrode.

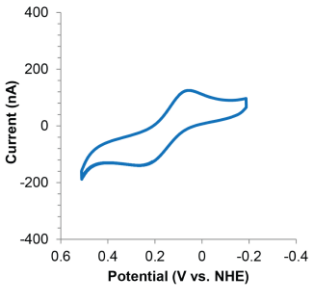

Figure 3.10: p58$_{256-464}$ Electrochemistry with 2.5 mM ATP. Upon addition of 2.5 mM ATP, a reversible redox signal generally appears in CV scans. The signal in the presence of 2.5 mM ATP was centered at an average midpoint potential measured near 142 ± 12 mV vs. NHE. The signal was observed at physiologically relevant redox potential, with a magnitude on the order of 10^2 nC charge transport. All scans were performed under anaerobic conditions on 40 µM [4Fe4S] p58C in 20 mM HEPES (pH 7.2), 75mM NaCl, at 100mV/s scan rate (CV) or 15 Hz (SQWV). Electrochemistry performed by Dr. E. O'Brien.

This is very similar to the signal observed for p58C$_{272-464}$ in the presence of DNA and NTPs, the

two necessary substrates for primase activity. Together, these data suggest that the two human p58C constructs, $p58C_{272-464}$ and $p58C_{266-464}$ have the same redox switching ability; the electrochemical function of the [4Fe4S] cofactor is consistent in both proteins.

Discussion

It has been proposed that differences in the structures of residues Leu318-His351 in the crystal structures of $p58C_{266-456}$ and $p58C_{272-464}$ are due to the difference in their N-termini [153, 154]. It has been hypothesized that Ile271 provides critical hydrophobic interactions stabilizing the helical hairpin in the $p58C_{266-456}$ crystal structure and that the absence of this residue leads to misfolding of Leu318-His351 in $p58C_{272-464}$ and formation of β-strands in the $p58C_{272-464}$ crystal structure. As these differences in structure are in the DNA-binding region of p58C, it is plausible to suggest that this may have significant functional repercussions. However, by determining the crystal structure of a new $p58C_{266-464}$ construct with the same extended N-terminal sequence as the $p58C_{266-456}$ construct, we demonstrated that the differences in the previously reported structures were not due to the difference in sequence, but rather to differences in the crystallization conditions.

Analysis of the $p58C_{266-464}$ and $p58C_{272-464}$ crystal structures reveals that substantial crystal lattice packing interactions stabilize this region in both structures. Specifically, Leu318-Gln329 are seen to interact extensively with the same region in the adjacent molecule in the lattice. The backbone atoms between the adjacent molecules in these regions show extensive hydrogen bonding, stabilizing the beta-like structure. In addition, on both sides of this extended interaction, Phe326 completes a hydrophobic pocket in the adjacent molecule, providing an additional anchor between the two molecules. In the structure of the $p58C_{266-456}$ crystallized under different conditions, a series of stabilizing interactions involve Leu318-His351, but none of these are formed between adjacent molecules in the crystal lattice. A number of crystal contacts in this lattice are found in loop regions and the interfaces of hydrophobic helices. The differences between the crystal contacts in these two models can be attributed to differences in

crystallization conditions, most notably the very high concentration of p58C (50 mg/mL) used originally for $p58C_{272-464}$ [163] and now for $p58C_{266-464}$. It is conceivable that at high concentration p58C forms dimers over time promoting the difference in crystal lattice and this in turn presumably facilitates formation of the inter-molecular Cys449 disulfide.

Crystallization contacts stabilizing alternate conformations of proteins is a well-demonstrated phenomenon [170]. Detailed comparative analysis of crystal structures, structural data obtained in solution, and simulations, has revealed a number of cases in which packing interactions affect backbone and side chain conformations, and even cases of alternate folds [171-173]. The addition of p58C to this group provides additional support for the importance of considering crystallization contacts between adjacent molecules in the crystal lattice when analyzing conformational changes of proteins crystallized with co-factors and ligands.

To further establish the structural equivalence of the p58C constructs, we turned to structural characterization in solution. Both CD and NMR (Figures 3.5, 3.6), showed that the absence or presence of residues Gly266-Ile271 has no significant impact on structure in solution. DNA binding and cyclic voltammetry assays (Figures 3.7, 3.10, and 3.11) showed that $p58C_{272-464}$ and $p58C_{266-464}$ have effectively the same biochemical properties. The evidence that the DNA binding region of p58C is capable of adapting to different crystallization conditions is consistent with the need for p58C to bind substrates sequence non-specifically, a property often associated with structural plasticity in sequence non-specific DNA binding domains (e.g. [174]). This raises the question: does the structure of p58C change upon DNA binding? At the time of this writing, a structure with bound DNA substrate is available only for the construct with the helical motif [38]. This structure and the corresponding structure without DNA bound show there are only subtle changes in side chains in required to bind the substrate [38, 71]. As far as we can tell by comparing structures, there is no reason to think the alternate conformation of residues 318-351 precludes DNA binding. However, at a more fundamental level, as the conformation of these residues in solution is not known, it is not possible to make any definitive

statement at this time. Further solution-state structural characterization of primase in complex with NTPs and primed substrates will be required to establish if there is a functional role for structural plasticity in the template-binding region of p58C.

We note that the approximately 3 μM dissociation constants we observe are similar to those previously reported using fluorescence anisotropy [76], but significantly higher than those reported for $p58C_{266-456}$ binding to a similar substrate measured using an electrophoretic mobility shift assay (EMSA) [85]. Molecular oxygen is known to be generated while running a polyacrylamide gel, which may cause redox-active proteins to become oxidized over the course of an EMSA [63]. As p58C is proposed to bind substrates more tightly when oxidized, we suggest that the EMSA measurements may report the affinity of primarily oxidized p58C, whereas the fluorescence-based measurements report the affinity of the directly purified p58C, which is primarily reduced [70, 76]. While it would be fascinating to directly assess the binding affinity of oxidized p58C for DNA substrate by performing fluorescence anisotropy using oxidized protein, it is not possible to perform these experiments due to the instability of the chemically oxidized cluster. Use of chemical oxidants cause degradation of the cluster and precipitation of the protein, as does extended exposure to atmospheric oxygen. The oxidized protein can be generated electrochemically, however, the lifetime of the oxidized state is not sufficiently long to make a reliable direct measurement of DNA binding affinity by any traditional method. However, regardless of the differences in the K_D values measured in solution and with EMSAs, our data show the DNA binding affinities of $p58C_{272-464}$ and $p58C_{266-464}$ are effectively the same, indicating that the shorter construct functions normally.

In summary, we have shown that the absence or presence of residues Gly266-Ile271 does not lead to any significant differences in the structure and biochemical properties of the p58C domain of human DNA primase. Beyond addressing the concerns raised about our initial studies, these data strengthen the support for our proposal that the [4Fe4S] cluster serves as a

redox switch that modulates the DNA binding affinity of p58C, setting the stage to further asses the role this switch plays in the priming function of human DNA primase.

CHAPTER 4

SUBSTRATE BINDING REGULATES REDOX SIGNALING IN HUMAN DNA PRIMASE[5]

Introduction

Dynamic, coordinated DNA replication in eukaryotic cells must efficiently duplicate genomes on the scale of 10^6−10^9 base pairs with error rates of approximately 10^{-9} mismatches per replication cycle[175]. The enzyme responsible for initiating daughter strand synthesis in eukaryotes is a heterodimeric DNA-dependent RNA polymerase, DNA primase [122-125, 156]. Primase is a heterodimer containing an RNA polymerase subunit, p48, and a regulatory subunit, p58 [34, 36, 72, 73]. Primase exists in complex with the heterodimeric DNA polymerase α (pol-prim), which functions to generate the RNA−DNA primer required for the bulk of genome duplication by processive DNA polymerases ε and δ [44, 81, 82, 122-124, 156]. Primase binds the ssDNA template, along with two nucleotide triphosphates (NTPs) and two catalytic metals, to synthesize the first dinucleotide (nt). After dinucleotide synthesis, primase rapidly elongates the primer to appropriate length (8−14 nts), before handing the primer off to polymerase α. Polymerase α then adds 10−20 deoxynucleotide triphosphates (dNTPs) downstream of the initial RNA primer before handing off the substrate to one of the processive DNA polymerases to complete genome duplication.

All eukaryotic replicative polymerases, as well as the translesion synthesis B-family polymerase ζ, are reported to contain [4Fe4S] clusters [69, 70, 79], which are metabolically expensive cofactors associated with biological redox chemistry [120, 176]. The clusters in both

[5] Parts of this section were published as O'Brien E, Holt ME, Salay LE, Barton, JK, Chazin WJ., Substrate Binding Regulates Redox Signaling in Human DNA Primase. J. Am. Chem. Soc., 2018, 140 (49), pp 17153–17162.

DNA polymerase δ [98] and the [4Fe4S] domain of primase, p58C [76], can be oxidized and reduced when bound to DNA through DNA-mediated charge transport (DNA CT).

DNA CT is a long-range, rapid, and mismatch-sensitive biochemical process [129, 177, 178], making it interesting to consider as a regulatory mechanism for replication. Moreover, experiments support the application of this chemistry in locating oxidative lesions *in vitro* and in cells [56, 67, 138] by DNA repair enzymes containing [4Fe4S] clusters.

The p58C domain of human and yeast DNA primase has been demonstrated electrochemically to undergo DNA-mediated redox switching between an oxidized, $[4Fe4S]^{3+}$ state and a resting, $[4Fe4S]^{2+}$ redox state [76, 77]. The oxidized $[4Fe4S]^{3+}$ p58C is tightly bound to DNA, whereas the reduced $[4Fe4S]^{2+}$ p58C is only loosely bound to DNA. A similar switch is evident in the base excision repair protein, Endonuclease III, which contains a [4Fe4S] cluster; here binding to the DNA polyanion shifts the $[4Fe4S]^{3+/2+}$ redox potential so that the oxidized $[4Fe4S]^{3+}$ form binds DNA 500- fold more tightly than the $[4Fe4S]^{2+}$ form [58, 63]. This redox switch in p58C appears to regulate primase activity and primer product distribution, yet the electrochemical behavior of the full primase enzyme, relative to that of p58C, has yet to be reported. Since both the catalytic subunit (p48) and the regulatory subunit containing the [4Fe4S] cluster (p58) of primase are required for binding of DNA and NTPs to initiate primer synthesis [24, 34-36, 72, 73], the electrochemical behavior of the complete p48/p58 heterodimer is likely an important element of the mechanism driving primer synthesis.

The p48 and p58C domains must be positioned near one another during priming, so that both can contact the template DNA; however, the DNA binding interfaces of p48 and p58C are separated by approximately 60 Å in the crystal structure of free primase [34]. These structural data suggest that primase must undergo a significant configurational rearrangement when binding DNA and NTPs, specifically a subunit realignment to position p58C over the p48 active site to begin primer synthesis. Beyond configurational rearrangement, moreover, the electrostatic environment of the [4Fe4S] cluster cofactor in primase is likely changed

dramatically by the binding of the anionic DNA and NTP substrates, as it is for Endonuclease III. Because electrostatic environment is a major factor in shifting the redox potential of [4Fe4S] cluster cofactors [179], it is reasonable to consider that binding of DNA and NTPs may change the redox behavior of the full-length p48/p58 primase enzyme. Characterization of both the electrostatic effect of DNA and NTP binding on primase [4Fe4S] cluster redox behavior and the configurational rearrangement of primase upon substrate binding, which positions the RNA polymerase and [4Fe4S] domains near the DNA, close to one another, is crucial for understanding the biochemical factors coordinating primase activity, which eventually culminates with primer termination and handoff to polymerase α.

Here we use DNA electrochemistry to investigate the electrostatic effects of DNA/NTP binding on primase redox activity. We find that full-length human primase displays a small amount of redox signaling upon electrochemical oxidation in the presence of DNA, though oxidation in the presence of DNA alone is a more dramatic redox switch for the isolated p58C domain [76]. When bound to both DNA and NTPs, however, p48/p58 displays robust, semi-reversible redox activity. Binding of anionic substrates changes the electrostatic environment of the primase [4Fe4S] cluster, shifting the potential into signaling range with other [4Fe4S] enzymes. Moreover, alignment of p58C over the active site of p48 should also alter the electrostatic field of the cluster. Preloading p48/p58 with NTPs, additionally, enhances catalytic activity on an exogenously primed substrate. In addition to the shift in electrostatic environment of the cluster, preloading NTPs should promote formation of the active primase initiation complex, with p58C and p48 proximal to the DNA template and NTPs bound in both the 3′ and 5′ sites.

Thus, the redox switch driven by the primase [4Fe4S] cluster is activated upon DNA and NTP binding, and combined with changes in configuration, regulates multistep RNA synthesis.

Methods

Protein Expression and Purification.

Full-length primase was expressed and purified by Dr. M.E. Holt and L.E. Salay as described previously [163]. In short, plasmid DNA was transformed into BL21RIL (DE3) cells (Novagen), and cultured at 37 °C to an OD_{600} of 0.6, when flasks were transferred to an 18 °C incubator with shaking. After 30 min, protein expression was induced through addition of isopropyl 1-thio-β-D-galactopyranoside to a final concentration of 5 mM. Media was also supplemented at this time with ferric citrate and ammonium ferrous citrate to a final concentration of 0.1 mg/mL. The primase subunits were expressed at 18 °C for 18 h prior to harvesting and freezing at −80 °C. After lysis, primase was first purified by nickel affinity chromatography (Amersham Biosciences). The 6xHis tag on p48 was the cleaved with H3C protease and primase dialyzed into a low-imidazole buffer. Primase was then repassed over the nickel column to remove the H3C protease and uncleaved protein. A heparin column was used to remove residual contaminants before passing over a Sephadex S200 sizing column to remove aggregates and buffer exchanged into electrochemistry storage buffer: 20 mM TRIS, pH 7.2, 150 mM NaCl, 5% glycerol.

Oligonucleotide Preparation.

Oligonucleotides were prepared by Dr. E. O'Brien. All standard or modified phosphoramidites and DNA synthesis reagents were purchased from Glen Research. Unmodified DNA oligonucleotides for electrochemical experiments were purchased from Integrated DNA Technologies, Inc. Thiol-modified DNA strands for electrochemistry were made on an Applied Biosystems 3400 DNA synthesizer, with a C6 S−S phosphoramidite incorporated at the 5′-terminus. Single-stranded DNA was purified using standard procedures as described previously [118, 128]. High pressure liquid chromatography (HPLC) using a reverse-phase PLRP-S column (Agilent) was used, and oligonucleotide mass confirmed using MALDI-TOF mass spectrometry. Thiolmodified strands were reduced after the initial HPLC purification with

100 mM dithiothreitol (Sigma) for 2−3 h in 50 mM Tris−HCl, pH 8.4, 50 mM NaCl. Reduced thiol-modified DNA was purified by size exclusion chromatography (Nap5 Sephadex G-25, GE Healthcare) and subsequent reverse-phase HPLC. Single-stranded oligonucleotides were then desalted using ethanol precipitation and stored in low salt buffer (5 mM Phosphate, pH 7.0, 50 mM NaCl). Duplex DNA for electrochemistry was prepared by quantification of the complementary single-stranded oligonucleotides by UV−visible spectroscopy, followed by annealing at 90 °C. A mixture of equimolar complementary single-stranded DNA (50 μM) was prepared in low salt buffer. Thiol-modified duplex DNA substrates were then deoxygenated by bubbling argon gas through the solution for 90− 180 s. Duplex DNA was annealed on a thermocycler (Beckman Instruments) by initial heating to 90 °C, followed by slow cooling to 4 °C over 90 min. DNA was quantified using absorbance at 260 nm, with extinction coefficients at 260 nm for DNA obtained using Integrated DNA Technologies online OligoAnalyzer tool. Single-stranded DNA substrates were quantified using UV−visible spectroscopy and stored in low salt buffer at a stock concentration for activity assays.

Multiplexed Chip Fabrication.

Multiplexed electrode platforms were prepared using standard photolithography techniques, adapted from established protocols [118, 128, 129]. Nine 1 in. by 1 in. chips were patterned on 525 μm thick silicon wafers (SiliconQuest). A thermal oxide layer roughly 4000 Å thick was grown on the silicon wafers using a Tytan tube furnace (Tystar). S1813 photoresist (2 μm layer) was deposited onto the wafers for patterning of the chips before metal deposition. Electron beam evaporation (CHA Industries) was then used to deposit a 3 nm titanium adhesion layer followed by a 100 nm gold layer, without breaking vacuum between depositions. Metal lift-off using Remover PG (MicroChem) was performed overnight (10−12 h) at ambient temperature. Wafers were subsequently dried with a nitrogen gun and dehydrated at 140 °C for 10 min. A 3 μm layer of insulating SU-8 photoresist was deposited and patterned onto the wafer

as described previously [118, 128, 129], with connective wires between contact pads on the edges of the chips and working electrodes in the center were covered but the contact pads and working electrodes left exposed. This ensured a fixed working electrode surface area of 2 mm^2. SU-8 photoresist was cured (150 °C, 15 min) and wafers cleaved into individual chips using a Dynatex Scriber/Breaker or broken manually after scoring with a diamond tip scriber.

DNA-Modified Electrode Assembly/Preparation.

Electrodes were prepared by Dr. E. O'Brien. Multiplexed chips were cleaned using sonication in acetone and isopropyl alcohol as described previously [118]. Chips were then dried thoroughly using argon gas and ozone-cleaned for 20 min at 20 mW using a Uvo brand ozone cleaner. Clean chips were assembled onto polycarbonate holders with acrylic clamp and Buna-N rubber gasket according to previous protocols, with four quadrants in the chip separated by fastened gasket and clamp.34 Duplex DNA substrates, with a thiol modifier at the 5′ end, (25 μM) were deposited in a 20 μL volume onto each quadrant of the multiplex chip. Substrates incubated for 18−24 h on the gold surface to allow formation of self-assembled DNA monolayer. DNA monolayers were washed with phosphate buffer (5 mM phosphate, pH 7.0, 50 mM NaCl, 5% glycerol) and subsequently backfilled with 1 mM 6-mercaptohexanol (Sigma) in phosphate buffer for 45 min. Monolayers are then washed 10 times per quadrant with phosphate buffer and twice per quadrant with TBP buffer (5 mM phosphate, pH 7.0, 50 mM NaCl, 4 mM MgCl2, 4 mM spermidine) to aid in formation of a monolayer with termini accessible for p58C binding. Assembled chips were transported into an anaerobic chamber (Coy Products) and washed 5 times per quadrant with p58C buffer (20 mM HEPES, pH 7.2, 75 mM NaCl), which was previously deoxygenated by argon bubbling (at least 1 s/μL of solution) and allowed to incubate at least 1−2 days in the chamber prior to the experiment. Initial cyclic voltammetry scans of the monolayers in p58C buffer were performed to ensure monolayer formation on each electrode. All washes were performed with 20 μL buffer volumes on each quadrant. Before scanning, a

200 µL volume was deposited over the chip surface, a bulk solution well for completion of a three-electrode circuit with an external reference and counter electrode.

Sample Preparation for Electrochemistry.

Samples were prepared by Dr. E. O'Brien. Samples were stored prior to experiments in p48/p58 storage buffer (20 mM Tris, pH 7.2, 150 mM NaCl, 5% glycerol). All p48/p58 samples were transferred to HEPES electrochemistry buffer (20 mM HEPES, pH 7.2, 150 mM NaCl, 5% glycerol) using Amicon ultra centrifugal filters (0.5 mL, 3 kDa MWCO) (Millipore Sigma). Catalytic metals were not included in the electrochemistry buffer so as to prevent NTP polymerization during electrochemistry experiments. Protein was applied in a 90−140 µL volume to the filter and centrifuged for 15 min at 14000g at 4 °C. After centrifugation, 400 µL of HEPES electrochemistry buffer was applied to the filter and centrifuged at 14000g for 20 min. This procedure was repeated four times to exchange the p48/p58 protein into HEPES electrochemistry buffer. After buffer exchange and recovery of sample by centrifugation (2 min, 1000g), the concentration of [4Fe4S] cluster-containing protein and loading of the [4Fe4S] cluster were assessed using UV−visible spectroscopy, by absorbance of the [4Fe4S] cluster at 410 nm (extinction coefficient = 17 000 M^{-1} cm^{-1}) [135]. Recovered samples (approximately 100−150 µL volume) were deoxygenated for 2−3 min with argon. Samples were then transferred into the anaerobic chamber (Coy Laboratory products). Before deposition onto the gold electrode surface, p48/p58 samples were diluted to a molar concentration of 5 µM or 7.5 µM [4Fe4S] p48/p58 with previously deoxygenated HEPES electrochemistry buffer. Samples were deposited onto multiplex chip quadrants in 20 µL volumes initially, with the remaining sample deposited in a well of bulk solution above the chip surface, to a final volume of 200−300 µL.

Wild Type Human p48/p58 Electrochemistry.

All electrochemistry was performed by Dr. E. O'Brien using a CHI620D potentiostat and 16- channel multiplexer (CH Instruments), in an anaerobic glove chamber. Multiplex gold

electrodes were part of a three-electrode system with an external Ag/AgCl reference electrode (Bioanalytical Systems) and platinum counter electrode. Cyclic voltammetry scans were performed at 100 mV/s scan rates, over a potential range of +0.412 to −0.288 V vs NHE or +512 to −188 mV vs NHE. Bulk electrolysis on DNA was performed at an applied potential of +0.512 V vs NHE for all electrochemical oxidation reactions and −0.188 V vs NHE for all electrochemical reduction reactions. The oxidizing potential was applied for at least 8.33 min for single oxidation reactions on a surface. The reducing potential was applied for 8.33 min in all electrochemical reduction reactions. All bulk electrolysis and cyclic voltammetry was performed in previously deoxygenated p48/p58 storage buffer (20 mM HEPES, pH 7.2, 150 mM NaCl, 5% glycerol). Charge transfer (nC) in the cathodic peak of CV scans for oxidized samples was assessed using the area under the current wave of the reduction signal. Charge transfer was measured for oxidized samples using CHI software, assessing the area under the reductive peak in CV after electrochemical oxidation. Yields for bulk electrolysis were assessed by subtracting the total charge reported in coulombs from the product of the electrolysis time (s) and the final current value (A). NTP-dependence of electrochemical signals were measured by pipetting a small volume (1−3 μL) of 0.1 M ATP stock solution into each quadrant of the multiplexed chip setup. Samples were added by quadrant, as physical barriers in the setup prevent diffusion of NTPs between electrode quadrants. After the volume of ATP stock was deposited onto the electrode quadrant, resulting in a 3.3 mM concentration of ATP in the quadrant, CV scans were measured (100 mV/s scan rate). Charge transfer was assessed using CHI software; charge values were determined by calculation of the area under the reductive and oxidative peak curves. Midpoint potentials of NTP-dependent redox signals were assessed using the peak selection function in CHI software.

Primase Preincubation Initiation Assays.

Priming assays were performed by Dr. E. O'Brien. All primase assays were performed anaerobically, with deoxygenated buffers and reagents. Primase was preincubated at ambient

temperature, either in a stock alone, with the DNA, or with the NTPs used in the reaction. The preincubation conditions were 30 min at ambient temperature; only DNA or NTPs, not both substrates at once, were incubated with each sample of primase. The α-^{32}P ATP was initially dried (2.5 µL of 12 µM, eventually diluted to 30 µL) in vacuo overnight the day preceding the reactions. The ^{32}P ATP-containing tubes were then brought into the anaerobic chamber, along with concentrated stocks of the unlabeled NTPs, CTP and UTP, and the single-stranded 50-nt initiation substrate, shown in Table 4.1.

Table 4.1: DNA substrates used for electrochemistry and DNA primase activity assays.	
p58C Electrochemistry Substrate (Well-Matched)	5'-SH-GTCGTGCAACGTGTCTGCGC-3' 3'-CAGCACGTTGCACAGACGCGTAC-5'
p58C Electrochemistry Substrate (Abasic Site)	5'-SH-GTCGTGCAACGTGTCTGCGC-3' 3'-CAG_ACGTTGCACAGACGCGTAC-5'
Initiation Substrate	3'-AAAAAAAAAAAAAAAAAAAAAAAAATAAAGAGAGAGAGAGAGAGAAAAGA-5'
Elongation Substrate	5'-$(T)_{15}$($\underline{U}$)$_{16}$-3' 3'-$(A)_{31}$TAAGAAAAGAGAGAGAGAGAGAAAAGA-5'

Table 4.1: DNA substrates used for electrochemistry and DNA primase activity assays. Electrochemistry of p48/p58 and p48/p58 was performed on self-assembling monolayers of a 36-mer DNA duplex substrate with a 9-nt 5'- ssDNA overhang. A 50-nt ssDNA substrate with a single thymine base complementary to the α-32P radiolabeled ATP was used in the primase initiation assay comparing wild type and CT-deficient full-length enzyme. A 2'-OMe RNA-primed ss/dsDNA substrate, containing a 31- nucleotide duplex segment and a 29- nucleotide 5'-ssDNA overhang was used to assay elongation. U = 2'-OMe rU, SH = -$(CH_2)_6$-SH.

Preincubation mixtures consisted of the following: protein-only preincubation samples contained 800 nM p48/p58 in primase activity buffer (50 mM Tris, pH 8.0, 5 mM $MgCl_2$), paired with a sample of 500 nM ssDNA and 376 µM UTP, 224 µM CTP, and 2 µM α-^{32}P ATP in activity buffer; DNA/protein preincubation samples contained 800 nM p48/p58 and 500 nM ssDNA and were paired with a sample containing 376 µM UTP, 224 µM CTP, and 2 µM α-32P ATP in primase activity buffer; NTP and protein preincubation tubes consisted of a sample containing 800 nM p48/p58 with 376 µM UTP, 224 µM CTP, and 2 µM α-32P ATP and paired with a sample containing 500 nM ssDNA, all in the Tris activity buffer. These samples were all

incubated anaerobically for 30 min at ambient temperature. The volume of reagents in each of the initial two tubes was 15 μL for each reaction, making a total reaction of 30 μL when combined and incubated at 37 °C. The final reaction conditions were 400 nM [4Fe4S] p48/p58, 112 μM CTP, 188 μM UTP, 1 μM α-^{32}P ATP, 250 nM ssDNA in 50 mM Tris, pH 8.0, 5 mM $MgCl_2$. The primase reactions were incubated for 1, 3, 5, 10, and 30 min at 37 °C in anaerobic conditions, and then quenched by an equal volume per 5.5 μL reaction aliquot of 1% SDS, 25 mM EDTA quenching solution to stop the reaction. Reactions, when quenched, were then transported out of the anaerobic chamber and heat-denatured for 10 min at 70 °C, aerobically. Finally, to remove the excess free ^{32}P-labeled nucleotide, the samples were each passed through spin columns (Mini Quick Spin Oligo Columns, Roche) according to manufacturer's protocols, to separate unincorporated radioactivity from small products made during primase initiation (7−10 nt). Samples were then scintillation-counted and dried overnight in vacuo. The samples were then separated using 20% polyacrylamide gel electrophoresis (denaturing gel). Gels were warmed at 1700−2000 V (90 W) for approximately 1.5 h before loading samples. Samples were resuspended after drying in 2 μL of formamide loading dye, vortexed, centrifuged, and heated at 90 °C for 1 min. They were then loaded onto the gel and run at ∼2000 V (90 W) for 3.5 h. Gels were then exposed to a phosphor screen (GE Healthcare) for 14 h and imaged on a Typhoon 9000 Phosphorimager (GE Healthcare). Products were quantified using ImageQuant TL software; reported numbers are mean ± SD values for n = 3 trials.

Preincubation Reactions: Elongation.

Priming assays were performed by Dr. E. O'Brien. For primase elongation reactions, preincubation, reaction, and purification conditions were generally similar to those of initiation assays. Reagents were prepared in essentially the same manner as for initiation. 2.5 μL of 12 μM α-^{32}P ATP was dried in vacuo overnight for each elongation reaction, then transported into the anaerobic chamber. Preincubation mixtures were prepared similarly to those used in initiation assays; two 15 μL fractions of reagents in various combinations were prepared for

each reaction and allowed to incubate in the anaerobic chamber for 30 min at ambient temperature before being mixed and reacted at 37 °C. The primase only preincubation samples consisted of 800 nM p48/p58 and a paired sample of 1 μM dsRNA/DNA and 360 μM UTP, 240 μM CTP, and 2 μM α-^{32}P ATP all in primase activity buffer; DNA/ protein preincubation samples consisted of 800 nM p48/p58 and 1 μM dsRNA/DNA and a paired sample of 360 μM UTP, 240 μM CTP, and 2 μM α-32P ATP all in primase activity buffer; NTP/ primase preincubation samples contained 800 nM p48/p58 with 360 μM UTP, 240 μM CTP, and 2 μM α-32P ATP and a paired sample of 1 μM dsRNA/DNA, all in primase activity buffer. The final reaction conditions, consequently, were 400 nM p48/p58, 120 μM CTP, 180 μM UTP, 1 μM α-32P ATP and 500 nM 2′-OMe RNA-primed DNA in 50 mM Tris, pH 8.0, 5 mM MgCl2. After preincubation and mixing for reaction, each primase assay was incubated anaerobically at 37 °C and aliquots of the reaction chemically quenched at 1, 3, 5, 10, and 30 min of reaction time. The chemical quencher for each 5.5 μL aliquot of reaction was an equal volume of 1% SDS, 25 mM EDTA, administered anaerobically. Reactions were further aerobically heat-denatured at 70 °C for 10 min. Elongation reactions were purified initially using Mini Quick Spin Oligo Columns (Roche) and then using P6̄ Micro Bio Spin Columns (BioRad). The Roche columns retain all synthesized products; the initiation products 7−10 nt on the ssDNA segment of the substrate oligonucleotide are purified and quantified with elongation products. The BioRad spin columns have an exclusion limit of 6 kDa, or approximately 20 bases, thus eliminating short initiation products from the quantified/purified mixture; this separation allows for comparison of truncated (30−35 nt) products and elongated products (60 nt) in the elongation assays.

Results

Human DNA Primase Redox Activity on DNA.

We first sought to investigate whether human primase participates in redox signaling when bound to DNA. Using multiplexed DNA-modified electrodes, we electrochemically monitored the redox activity of WT human DNA primase (p48/p58) using cyclic voltammetry

(CV) (Figure 4.1, Figure 4.2). Using a 36-mer duplex DNA substrate with a 9-nt, 5′-ssDNA overhang (Table 4.1) to accommodate the DNA footprint of primase[150], we initially observed

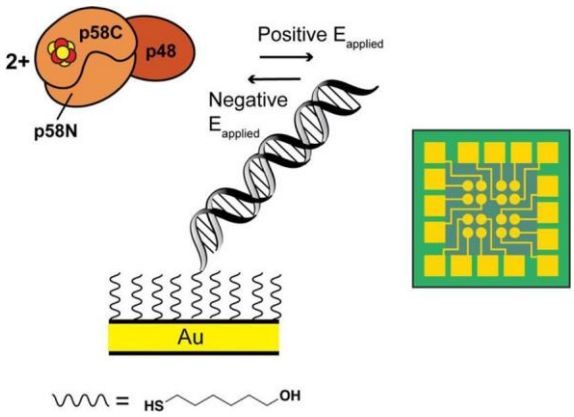

Figure 4.1**:** Electrochemical oxidation and reduction of human DNA primase. (Left) Scheme for the electrochemistry of p48/p58 in the presence of a DNA substrate. Bulk electrolysis is used to oxidize or reduce the [4Fe4S] cluster in DNA primase, applying positive or negative potentials for oxidation and reduction, respectively. Subsequent cyclic voltammetry scanning, in a strictly anaerobic environment, illuminates the electrochemical behavior of primase in each oxidation state. (Right) Primase electrochemistry is performed on a multiplex DNA electrode platform, with sixteen individually addressable electrodes separated into four quadrants on a single surface. The Au electrodes (circles, center) serve as the working electrode in a three-electrode cell, with a Ag/AgCl reference and a Pt counter electrode. Electrochemistry performed by Dr. E. O'Brien.

that electrochemically unaltered WT primase, which is largely in the $[4Fe4S]^{2+}$ redox state [76], does not participate in DNA-mediated redox signaling (Figure 4.2). This behavior is similar to electrochemically unaltered human and yeast p58C [76, 77] on DNA, confirming that the isolated, $[4Fe4S]^{2+}$ primase enzyme is redox-inert. When we scan the unaltered primase enzyme using square wave voltammetry (SWV), a more sensitive electrochemical technique that minimizes background current, however, an irreversible cathodic peak at −64 ± 7 mV vs NHE is observed. Oxidation of [4Fe4S] proteins, like primase, from the resting $[4Fe4S]^{2+}$ state to the $[4Fe4S]^{3+}$ state can lead to further oxidation with degradation of the oxidized cluster to the $[3Fe4S]^{+}$ degradation product [138]. We have, moreover, observed the $[3Fe4S]^{+}$ species on the DNA electrodes for mutants of both yeast p58C [77] and a human base excision repair enzyme MUTYH [180]. The samples of p48/p58 were exposed to atmospheric oxygen during purification and preparation for electrochemistry, and this peak potential is consistent with values expected

for the irreversible $[3Fe4S]^{+/0}$ reduction reaction [180], so we assign the signal to trace amounts of $[3Fe4S]^{+}$ product formed in the primase protein sample (Figure 4.2).

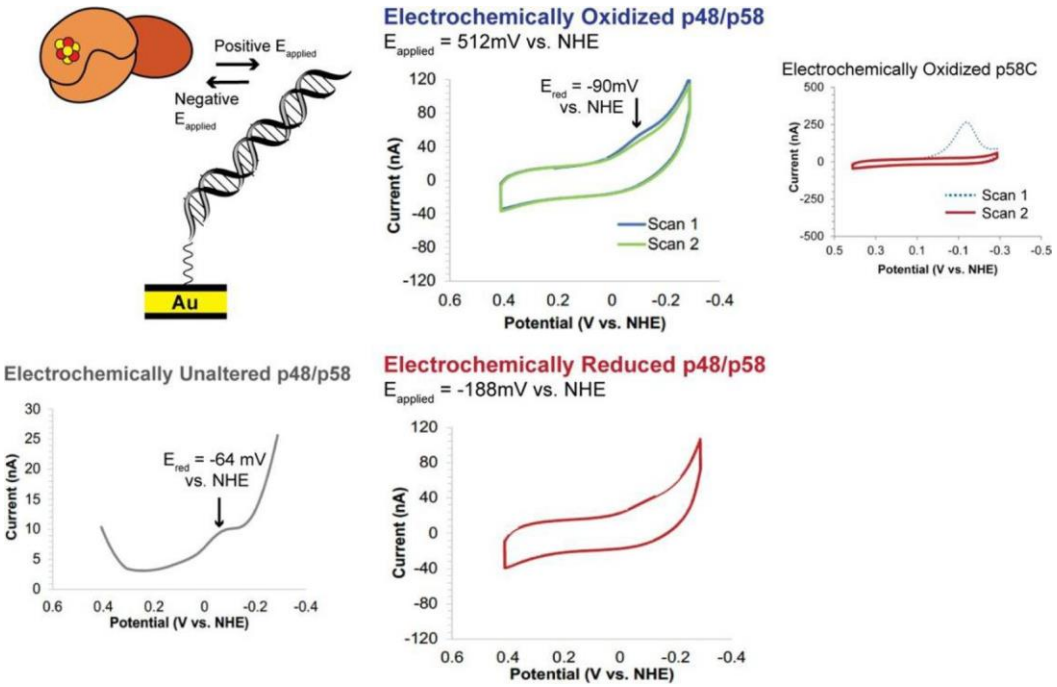

Figure 4.2: Electrochemical characterization of human p48/p58 in the presence of DNA. The electrochemically unaltered primase protein contains a small amount of $[3Fe4S]^{+}$ cluster degradation product, as observed in the square wave voltammetry (SWV) reductive sweep of the electrochemically unaltered protein (left, grey trace). This peak is distinct from the peak observed upon primase electrochemical oxidation at an applied potential of 512 mV vs. NHE, which is small for the p48/p58 enzyme and disappears after a single scan to reducing potentials. (above center, green and blue traces). The electrochemically reduced sample (below center, red trace) has a similar CV profile. The redox signal for electrochemically oxidized human p58C (inset, right) is much larger, as the isolated domain is not affected by the configuration of the other primase domains, notably the RNA polymerase domain in the p48 subunit. The distance between the RNA polymerase domain and the p58C domain likely inhibits coupling of the [4Fe4S] cluster to DNA under these conditions. Electrochemical scans were measured in anaerobic conditions, with 7.5 µM [4Fe4S] p48/p58 in 20 mM HEPES, pH 7.2, 150 mM NaCl, 5% glycerol. CV scans were measured at 100 mV/s scan rate, and SWV scans were measured at 15 Hz frequency, 25 mV amplitude. Electrochemistry performed by Dr. E. O'Brien.

While we observe a residual amount of $[3Fe4S]^{+}$ protein from oxidative damage during aerobic protein preparation, we do not assign this to an electrochemically induced effect. In the absence of oxygen, wild-type

[4Fe4S] primase, similarly to p58C, DNA polymerase δ, human MUTYH, and Endonuclease III [63, 76, 77, 98, 180], is stable and can be electrochemically cycled within this mild, physiological potential regime repeatedly during cyclic voltammetry.

We next electrochemically oxidized ($E_{applied}$ = 512 mV vs NHE) or electrochemically reduced ($E_{applied}$ = −188 mV vs NHE) a sample of 7.5 μM [4Fe4S] DNA primase on an electrode surface using bulk electrolysis. Strict anaerobic conditions ensured full control over the redox state of the protein [139]. Subsequent cyclic voltammetry (CV) scans over physiological potentials (Figure 4.2) show a small reductive peak on the order of ∼1 nC charge transport near −90 mV vs NHE in the oxidized sample. This peak essentially disappears after the first scan to negative, reducing potentials. Interestingly, this small redox signal is also observed in electrochemically reduced primase, though it is smaller than the signal in the initial scan of oxidized primase. In contrast, the CV of the p58C domain indicates a large reductive peak in the oxidized sample, but no measurable redox activity in the reduced sample (Figure 4.2). Hence, only the primase heterodimer is capable of supporting complete redox cycles. Because the reductive peak in the oxidized primase sample disappears after one scan to reductive potentials and is at a different redox potential, it is not indicative of the cluster degradation product $[3Fe4S]^{+}$ and its subsequent reduction to the $[3Fe4S]^{0}$ species. Thus, human primase can participate in redox signaling to some degree in the presence of DNA only, but additional factors are necessary to observe robust redox switching between $[4Fe4S]^{2+}$ and $[4Fe4S]^{3+}$ oxidation states.

DNA-Mediated, NTP-Dependent Redox Signaling in Human Primase.

The relatively small redox signal for oxidized $[4Fe4S]^{3+}$ primase generated on a DNA electrode (Figure 4.2), relative to that observed for the isolated p58C domain, indicates that their environments are distinctly different. One important point is that the primase heterodimer binds

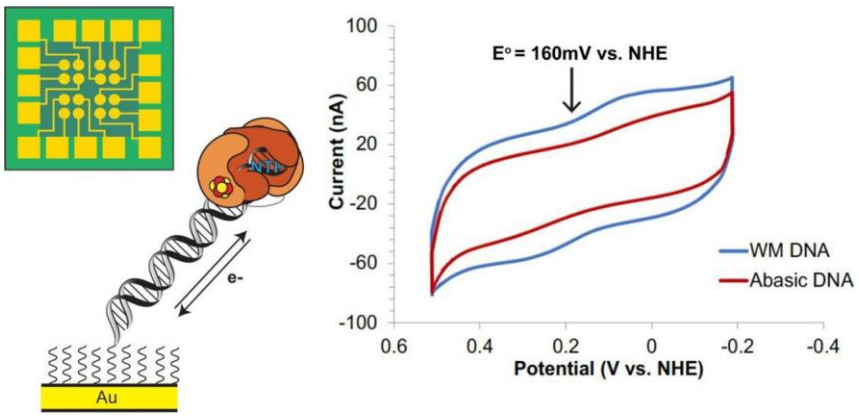

Figure 4.3: Semi-reversible, NTP-dependent redox signaling in p48/p58. In the absence of NTPs, p48/p58 is redox-inert on DNA. Upon addition of 3.3 mM [ATP+CTP] to the multiplexed DNA electrode surface (right, blue), reversible redox switching between the $[4Fe4S]^{3+}$ and $[4Fe4S]^{2+}$ oxidation states is observed. This signal is centered at 160 mV vs. NHE, within the physiological range, as well as the range for signaling with other DNA- processing, [4Fe4S] enzymes. In the presence of a DNA substrate containing an abasic site in the duplex segment of the substrate, the redox signal is attenuated (red), suggesting that the signal is DNA-mediated. This redox chemistry observed in WT p48/p58 suggests that the active form of primase, bound to both DNA and NTPs, is able to participate in redox signaling driven by the [4Fe4S] cluster. Electrochemical scans were measured in anaerobic conditions, with 5 μM [4Fe4S] p48/p58 in 20 mM HEPES, pH 7.2, 150 mM NaCl, 5% glycerol, in the presence of 3.3 mM [ATP + CTP]. CV scans were measured at 100 mV/s scan rate. Electrochemistry performed by Dr. E. O'Brien.

DNA more tightly than either p48 or p58C in both human [76, 84] (Figure 4.3) and yeast [72] primase. To verify that this is the case for our preparations, we measured DNA binding of human primase and isolated p58C using fluorescence anisotropy, and found that reduced full-length primase (p48/ p58) binds DNA with K_D = 0.30 ± 0.03 μM, whereas reduced p58C binds ~20-fold more weakly with K_D = 5.5 ± 0.5 μM [76]. We next investigated whether binding of NTPs in addition to DNA would promote redox signaling. An NTP pool present on the electrode surface allows sampling of catalytically relevant configurations by primase, while the absence of catalytic metals prevents polymerization. Divalent Mg^{2+} ions in millimolar concentrations moreover can coat the DNA on the electrode surface and occlude primase binding and redox signal generation. Upon incubating 5 μM p48/p58 on a DNA electrode with 3.3 mM [ATP+CTP], to promote NTP binding at the ss/dsDNA junction of the substrate conjugated to the Au surface, we observe that primase consistently displays a robust, semireversible redox signal. (Figure 4.3) The NTP-dependent CV signal for human DNA primase is attenuated in the presence of an abasic site in the DNA duplex (14 ± 2 nC charge transfer in the cathodic peak for well-matched

DNA versus 9 ± 4 nC charge transfer in the cathodic peak for abasic site-containing DNA), consistent with our previous results showing the signal is DNA-mediated [76]. (Figure 4.3) In our HEPES electrochemistry buffer (20 mM HEPES, pH 7.2, 150 mM NaCl, 5% glycerol), the signal is centered near 160 mV vs NHE. This signal is within the range expected for DNA processing [4Fe4S] enzymes cycling between the $[4Fe4S]^{2+}$ and $[4Fe4S]^{3+}$ states, [56, 58, 63, 67, 76, 77, 98, 138] and is similar to the reported values for human and yeast p58C [76, 77] in the presence of DNA and NTPs. The midpoint potential of primase in the presence of DNA and NTPs (160 ± 4 mV vs NHE) is slightly higher than the midpoint potentials observed for human and yeast p58C in the presence of DNA and NTPs, which is near 150 mV vs NHE [76, 77]. This shift may be due to an increased amount of insulating protein matrix surrounding full-length primase as compared to p58C, which promotes a higher reduction potential [179]. Binding of the DNA polyanion and negatively charged NTPs, importantly, still shifts the cluster potential of full-length primase into the physiological range for signaling activity. This result suggests that unlike p58C, the redox switch allows primase to cycle between the $[4Fe4S]^{3+}$ state and the $[4Fe4S]^{2+}$ state, presumably because primase remains associated with both DNA and NTPs. In the enzymatically competent form, primase readily participates in DNA-mediated redox signaling. The NTP-dependent electrochemical signal observed for p48/p58 demonstrates that primase can readily undergo a redox switch driven by the [4Fe4S] cluster cofactor upon forming an initiation complex with bound DNA and NTPs. Structural and biochemical evidence [34, 38, 84] suggest that this redox switch is accompanied by a realignment of the subunits within the p48/p58 heterodimer. The X-ray crystal structure of free primase in the absence of substrates shows it adopts an “open” conformation [34], with the RNA polymerase domain and the p58C domain ~60 Å apart. However, both the p48 and p58C domains of DNA primase contribute to binding of the DNA and two NTPs necessary to form the initiation complex [38, 81, 84, 181]. The primase heterodimer must therefore undergo a configurational reorientation so that the p58C domain is positioned over the DNA template and the p48 catalytic site in order for priming

to occur. The shift from the open configuration of DNA primase may be critical to both proper alignment of critical domains, NTPs and DNA template, and also the change in the electrostatic environment of the cluster in p58C.

Effects of NTP and DNA on Initiation and Elongation.

To further assess the effect of DNA template and NTP binding on initiation and elongation activity, we preloaded p48/p58 with either DNA or NTPs under anaerobic conditions, then measured polymerase activity during *in vitro* primer initiation and elongation. WT p48/p58 was first preincubated with template DNA (ssDNA for initiation, dsRNA/DNA for elongation, Table 4.1) or NTPs for 30 min in an anaerobic chamber at ambient temperature. Reactions were then begun by adding the remaining necessary substrates for activity to each sample and incubating the mixtures at 37 °C. All preincubation samples contained the same concentration of primase in the same total volume (15 µL). The final initiation reaction conditions were 400 nM [4Fe4S] p48/p58, 112 µM CTP, 188 µM UTP, 1 µM α-^{32}P ATP, 250 nM ssDNA (initiation substrate in Table 4.1) in 50 mM Tris, pH 8.0, 5 mM $MgCl_2$, and the final elongation reaction conditions were 320 nM p48/p58, 500 nM primed DNA (elongation substrate in Table 4.1), 180 µM [UTP], 120 µM [CTP], 1 µM α-32P ATP in 50 mM Tris, pH 8.0, 5 mM $MgCl_2$. We measured the products synthesized after quenching reaction mixtures at t = 1, 3, 5, 10, and 30 min.

We observe that preloading of primase with template DNA or NTPs does not enhance de novo primer synthesis on ssDNA (Figure 4.4). Both total products and primer-length (7−10 nt) products were quantified and normalized to primase-only incubation conditions. Levels of primer synthesis were indistinguishable across all preincubation conditions; loading primase with ssDNA or NTPs before the priming reaction did not confer any advantage. These data contrast, interestingly, with the previously observed effect reported by Sheaff et al., who observed no activity when DNA primase is incubated aerobically on a poly(dT) substrate with ATP [82]. We suspect that the presence of atmospheric oxygen may have nonspecifically oxidized ATP-bound p48/p58, thereby inhibiting initiation activity that is promoted by the redox switch. As NTP

binding appears electrochemically to promote primase accessing the $[4Fe4S]^{3+}$ redox state, it is expected that NTP-bound primase would be more susceptible to oxidation to the $[4Fe4S]^{3+}$ state, and subsequent degradation to the $[3Fe4S]^{+}$ species in aerobic conditions [138, 180].

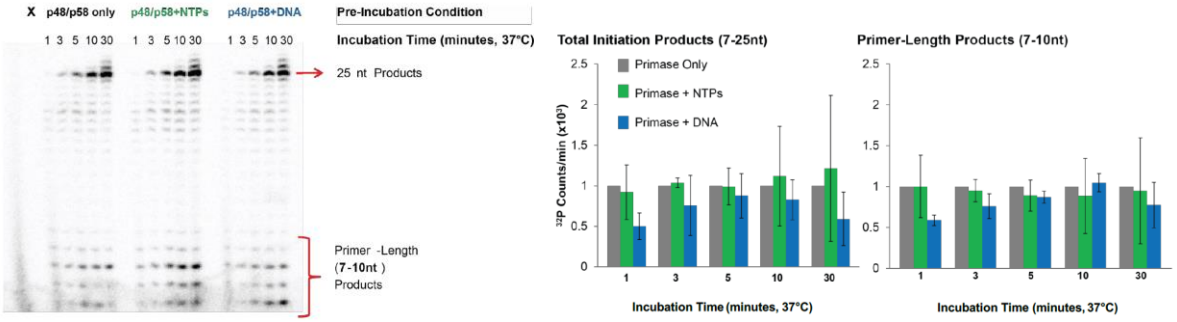

Figure 4.4: Substrate Binding Order Does not Affect Primase Initiation. Left: Gel separation of products for three primase initiation reactions. Primase alone (p48/p58 only, grey), primase pre-incubated with NTPs was added to DNA (p48/p58 + NTPs, green), or primase preincubated with DNA was added to NTPs (p48/p58 + DNA, blue) to start the reaction. Preincubation times were 30 minutes in anaerobic conditions; all pre-incubation volumes were equal. All experiments were performed in anaerobic conditions, with 400 nM p48/p58, 250nM primed DNA, 188μM [UTP], 112μM [CTP], 1μM α-^{32}P ATP in 50mM Tris, pH 8.0, 3mM $MgCl_2$, 37°C. Right: Quantification of primase initiation products in the pre-incubation assay. Total products (left) and primer-length (7-10nt) products (right) do not differ within error for the majority of time points assayed in the pre-incubation reaction under anaerobic conditions. This similarity suggests that substrate binding alone does not drive primase initiation, though it appears to drive elongation activity. All measurements are mean +/- S.D. for n= 3 trials. Biochemistry performed by Dr. E. O'Brien.

Primase elongation, in contrast, is aided by preincubation with NTPs or, to a lesser extent, a primed DNA substrate (Figure 4.5). Incubation with NTPs increases the number of total products synthesized on primed DNA 1.5−3-fold compared to primase not preloaded with substrates. Incubation with template DNA increases catalytic activity by a modest degree; t = 1 min showed no difference in products under these conditions, and t = 30 min showed the largest

increase, synthesizing 187% of the products formed when primase was incubated without any substrates. These numbers increase slightly (Figure 4.5) when only elongation products (32−60 nt) are quantified and compared to primase only preincubation conditions. We also conducted these assays under aerobic conditions and saw the same general pattern with more error, likely due to nonspecific oxidation of the primase cluster over time [139].

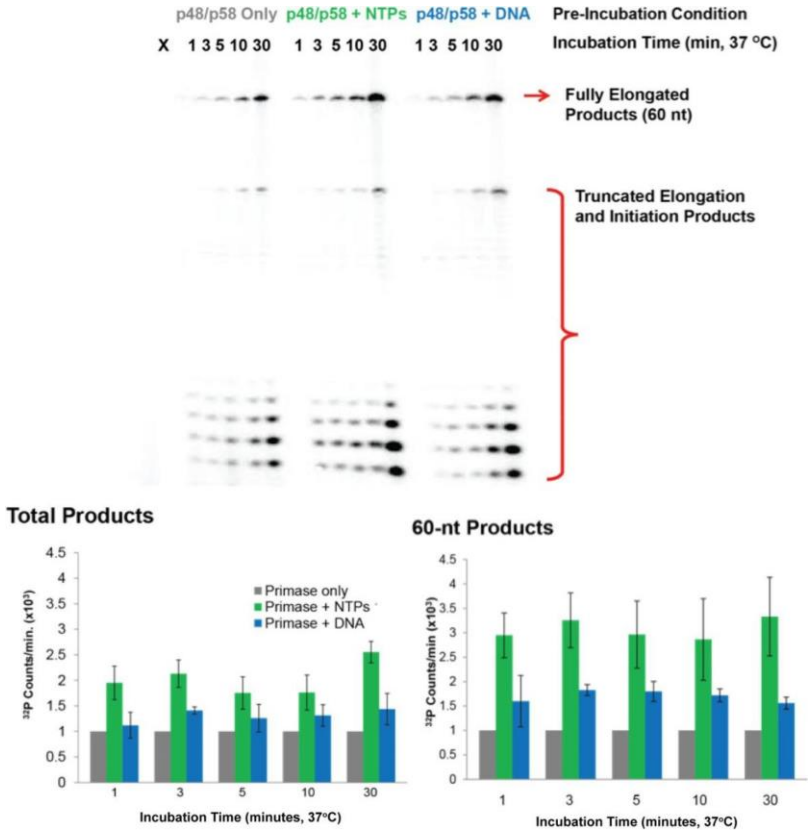

Figure 4.5: Primase pre-loading with DNA and NTPs enhances elongation activity. Primase pre-incubation with DNA and NTPs increases elongation product synthesis. Catalytic activity, as measured by elongation products, is most enhanced on average by pre-incubation with NTPs, but pre-incubation with DNA also enhances product formation. A representative gel for the pre-incubation conditions is shown above. Quantifications for the total elongation products synthesized (bottom left) and full elongation products (bottom right) are also shown. All experiments were performed under anaerobic conditions, with 320 nM p48/p58, 500 nM primed DNA, 180 μM [UTP], 120 μM [CTP], 1 μM α-^{32}P ATP in 50 mM Tris, pH 8.0, 5 mM $MgCl_2$. Quantifications are the mean +/- s.d. of n= 3 trials. Biochemistry performed by Dr. E. O'Brien.

Discussion

The dynamic interdomain movement and interactions of the heterodimeric DNA primase enzyme (p48/p58) are distinct from the isolated catalytic domain in the p48 subunit and the [4Fe4S] domain in the p58 subunit. Here we show that the [4Fe4S] cluster in p58C participates

in DNA-mediated redox signaling in the context of the full p48/p58 heterodimer. Comparison of the electrochemical behavior of the primase dimer versus p58C is highly informative because the [4Fe4S] domain acts in concert with the catalytic p48 subunit to regulate priming. In isolation, the oxidized and reduced p58C domain exhibit very different electrochemical properties [76]. Remarkably, electrochemically oxidized and reduced p48/p58 behave similarly in the presence of a DNA template. We attribute this effect to the alignment of p58C in close proximity to the p48 subunit, which is promoted by the interaction of both subunits with the polyanionic DNA [181]. We postulate the alignment of the two domains of the heterodimer may also affect the coupling of the cluster to the DNA bases.

Thus, the primase heterodimer readily participates in robust, semi-reversible electrochemical activity only in the presence of both DNA and NTPs. NTP binding has been demonstrated previously to enhance redox activity of [4Fe4S] enzymes on DNA, as in the case of DNA repair helicase XPD. The [4Fe4S] cluster in XPD, an ATP-dependent enzyme, is better coupled into the DNA bases in the presence of ATP and thus may signal other [4Fe4S] repair enzymes on DNA when it is active [140]. The concurrent switches to enhanced redox signaling and enzymatic activity may indicate a general linkage between catalytic and regulatory functions of DNA-processing, [4Fe4S] enzymes. We also observe that preloading of primase with NTPs or primed DNA enhances catalytic activity. The p48/p58 complex may sample more configurations that promote primer synthesis when loaded with one of the required substrates for catalysis, resulting in more complete and efficient elongation.

It is reasonable to conclude that electrostatic interactions with the primase [4Fe4S] cluster drive the substrate-dependent change in primase redox behavior. These clusters are tunable cofactors, with redox potentials influenced by factors such as solvent exposure and electrostatic environment [179]. DNA and NTPs both carry multiple negative charges, and binding to DNA has previously been demonstrated to alter redox properties of [4Fe4S] DNA repair proteins such as base excision repair glycoslyases MutY and Endonuclease III in

Escherichia coli [63, 182]. Binding of DNA shifts the redox potential of the cluster negative, stabilizing the oxidized $[4Fe4S]^{3+}$ protein. Electrochemically oxidized $[4Fe4S]^{3+}$ Endonuclease III was moreover directly demonstrated to bind 500-fold more tightly to DNA than reduced $[4Fe4S]^{2+}$ Endonuclease III using microscale thermophoresis [63]. Upon modeling the addition of negative charges from DNA into the Endonuclease III cluster environment, the change in potential could be calculated by summing the electrostatic interactions between negative charges on bound DNA and the positively charged [4Fe4S] cofactor. This model predicted the potential shifts of both MutY and Endonuclease III upon DNA binding, and it is interesting to think about expanding the model to consider DNA-binding, NTP-binding [4Fe4S] enzymes like primase. The electrostatic maps of the isolated p48 subunit, and the DNA-bound p58C subunit (Figure 4.6) illustrate the two electrostatic surfaces we predict are aligned during substrate binding and primase activity.

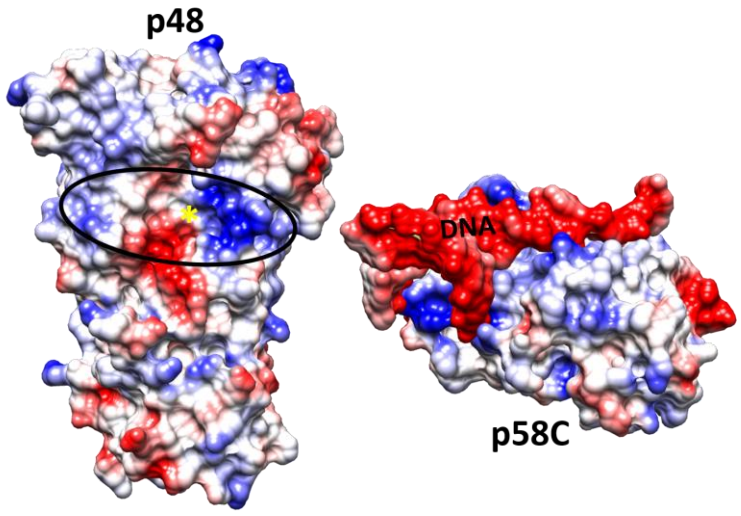

Figure 4.6: Electrostatic fields at the surface of p48 and p58C with a DNA substrate bound. The p48 catalytic site is indicated by a yellow asterisk. The black ring on p48 indicates where the DNA substrate and p58C need to be positioned for the initiation of priming. Coordinates used: p48 (4LIL); p58C-substate (5F0Q). Figure was generated using the MSMS package in UCSF Chimera. Analysis performed by L. E. Salay

We predict from these structures that the p58C [4Fe4S] cluster is approximately 25−30 Å from the bound DNA substrate during primer synthesis. The lack of structural data on NTP-bound

primase/p58C poses a challenge for predicting the distance between the [4Fe4S] cluster and bound NTPs during activity, but based on the changes in primase electrochemistry upon NTP binding, as well as the observed electrostatic effects on the [4Fe4S] cluster potentials of MutY and EndoIII [58, 182], we propose that NTPs are also within at least 20−30 Å of the cluster, possibly as close as 10 Å from the cofactor. As structural data become available on substrate-bound DNA polymerases, this electrostatic model for predicting potential shifts will become a useful tool for predicting and analyzing the properties of substrate-bound replication proteins that contain [4Fe4S] clusters.

Structures of substrate-bound primase will moreover elucidate important details of the configurational realignment for p48/p58 to initiate and extend the initial RNA primer. Our results show that primase elongation on RNA-primed template DNA is enhanced by preloading NTPs onto the p48/p58 heterodimer. This result illuminates an important effect, connected with the observed configurational realignment of the primase heterodimer during replication [38, 84, 181].

Conclusions

Redox switching driven by a change in [4Fe4S] oxidation state has now been demonstrated to modulate the DNA binding affinity of several DNA-processing [4Fe4S] enzymes in a manner that regulates activity [56, 67, 76, 98, 140, 182]. The primase heterodimer is regulated by a redox switch in the [4Fe4S] cluster; upon NTP binding the primase cluster can cycle readily between the $[4Fe4S]^{2+}$ and $[4Fe4S]^{3+}$ oxidation states, the p58C domain binding more tightly once oxidized. The electrostatic interaction of polyanionic DNA and NTPs with the primase cluster, in concert with the configurational alignment required for catalytic activity, may allow for efficient and regulated primer synthesis and handoff to DNA polymerase α (Figure 4.7). Structural analysis and modeling performed on polymerase α has suggested that this enzyme also undergoes significant configurational rearrangements during priming [26, 44]. The lagging strand polymerase, DNA polymerase δ, which contains a redox-active [4Fe4S]

cluster [79, 98] also adopts different configurations bound to and dissociated from DNA, which are related to polymerase δ interactions with the proliferating cell nuclear antigen (PCNA)

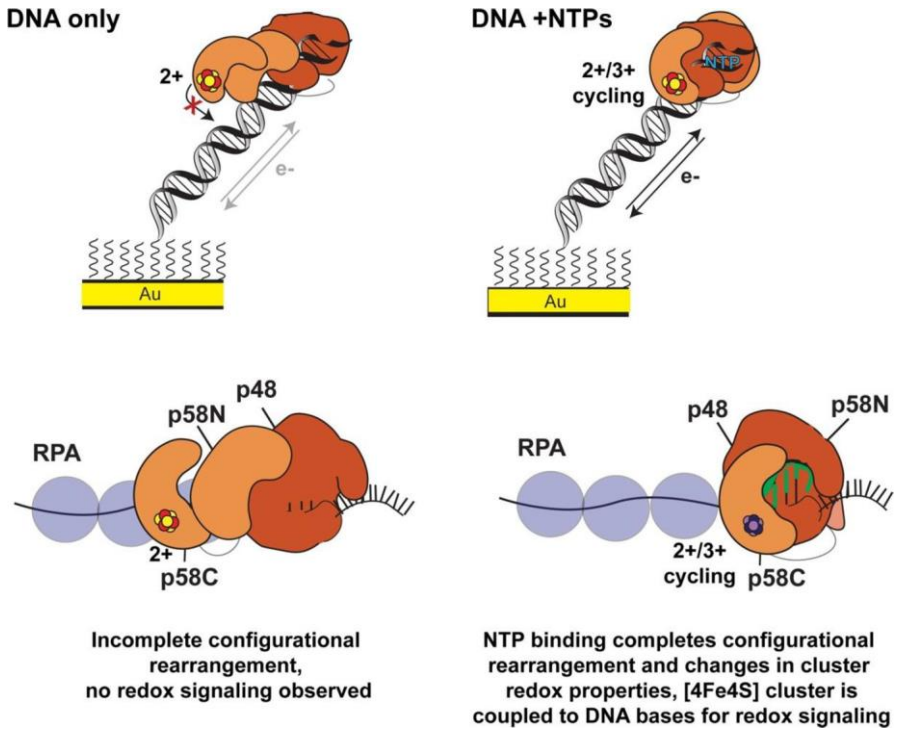

Figure 4.7**:** Model for the effect of substrate binding and configurational realignment on primase redox signaling and activity. When primase is bound only to DNA (top left), the [4Fe4S] cluster domain is not coupled into the DNA bases and only a small amount of redox signaling is observed. When primase is bound to both DNA and NTPs (top right), the protein participates in robust, semi-reversible redox cycling between the $[4Fe4S]^{3+}$ and $[4Fe4S]^{2+}$ redox states, favoring the tightly bound $[4Fe4S]^{3+}$ state. We propose (below) that the redox switch induced by the electrostatic effect on [4Fe4S] cluster environment, as well as the configurational realignment of primase domains for activity, regulate primer synthesis, which terminates with handoff to polymerase δ. Binding of polyanionic DNA and NTPs affects the [4Fe4S] cluster reduction potential, enabling the cofactor to participate in redox signaling under physiological conditions. In the heterodimeric primase enzyme, the configurational alignment to form the initiation complex, in which both the p48 and p58C domains contact the nascent primer, additionally contributes to positioning the [4Fe4S] cofactor in an orientation coupled with the DNA bases to perform redox signaling during replication.

processivity clamp [183], and here too activity is regulated by the oxidation state of the [4Fe4S] cluster. The [4Fe4S] enzymes central to DNA replication often contain many subunits and domains with flexible tethers, which interact with one another over the trajectory of a step such as priming and require careful coordination. Replication polymerases known to contain [4Fe4S] clusters [69, 70, 79] bind DNA, NTPs and dNTPs, anionic substrates that alter the

electrostatic environment of the cluster. Both the charged substrates bound to the [4Fe4S] enzyme and the configuration of the polymerase subunits during the reactions are crucial elements determining when and how the proteins participate in redox signaling on DNA. Understanding configurational realignment of subunits and domains, as well as the redox properties of isolated [4Fe4S] domains versus the corresponding intact proteins, will facilitate more accurate and thorough construction of [4Fe4S] protein redox signaling networks in replication, and other pathways containing dynamic, multi-subunit [4Fe4S] enzymes.

CHAPTER 5

YEAST REQUIRE REDOX SWITCHING IN DNA PRIMASE[6]

Introduction

DNA replication requires the coordinated activity of several polymerase enzymes [156]. DNA primase begins replication on the ssDNA template, synthesizing a short (8–12 nt) RNA primer before handing off the primed template to DNA polymerase α. Primase contains an RNA polymerase subunit (p48) and a regulatory subunit (p58) [124]. Primase [69, 70] and many other, if not all, replicative polymerases contain at least one [4Fe4S] cluster [45, 79], a metal cofactor associated with biological redox chemistry [119]. Given the high metabolic expense associated with incorporation of a cluster into one of these proteins [120], this cofactor is presumed to play a functional role. Interestingly, the clusters in human DNA primase and yeast DNA polymerase δ have been demonstrated to perform DNA-mediated redox chemistry [76, 98].

The [4Fe4S] cluster in eukaryotic primases is essential for primer synthesis on the ssDNA template *in vitro* [69, 70] and in cells [74]. The cluster is located in the C-terminal domain of the regulatory subunit, p58C, which is flexibly tethered to the N-terminal domain [38, 44] and can bind DNA independently of the rest of the primase enzyme [72, 73]. In human DNA primase, the cluster acts as a redox switch, modulating the interaction of p58C with its substrate. Binding of the DNA polyanion shifts the [4Fe4S] cluster redox potential, so that the $[4Fe4S]^{3+}$ protein is bound tightly, while the $[4Fe4S]^{2+}$ protein is bound more loosely [76]. Endonuclease III in *Escherichia coli* similarly undergoes an ~500-fold increase in DNA binding

[6] This chapter was published as O'Brien E*, Salay LE*, Epum, EA, Friedman, KL, Chazin WJ, Barton JK., Yeast Require Redox Switching in DNA Primase., Proc Natl Acad Sci USA, 2018. 115 (52) pp 13186-13191 (*Equal contribution)

affinity upon oxidation to the $[4Fe4S]^{3+}$ state from the resting $[4Fe4S]^{2+}$ state [61, 138]. We have proposed that the redox switch in human primase may facilitate binding and substrate handoff, through DNA-mediated charge transport [76]. In our model, active primase is in the $[4Fe4S]^{3+}$ state, coupled into the π-stacked bases for redox signaling. The p48 RNA polymerase domain and the p58C [4Fe4S] cluster domain are in contact with the nascent RNA/DNA. When the RNA primer reaches the appropriate length (8–14 nt), we propose that polymerase α, in the $[4Fe4S]^{2+}$state, contacts the RNA/DNA, becoming activated toward oxidation. Polymerase α sends an electron through the RNA/DNA duplex to reduce primase to the $[4Fe4S]^{2+}$ state, and in so doing is converted to the $[4Fe4S]^{3+}$ state. Primase dissociates, and polymerase α is now tightly bound, effectively executing a primer handoff.

During handoff in the redox-switching model, charge must travel through duplex RNA/DNA and protein matrix [61, 76, 138]. Biochemical and structural evidence shows that p58C contacts DNA through basic arginine and lysine residues [38, 84, 144, 181, 184], positioning the cluster 25–30 Å from the substrate. Charge must travel from the DNA to the cluster, through a pathway within p58C. Charge transfer pathways in proteins often comprise aromatic residues, which have comparatively low ionization energies and can transfer charge [144, 184] through single-step tunneling or electron hopping. In human primase, for example, the redox switch is mediated by conserved tyrosine residues, Y309, Y345, and Y347 in the p58C domain. Substitution of these residues with phenylalanine produces redox-deficient mutants, defective for initiation of primer synthesis. Redox pathways through several proteins [185, 186] have been characterized using Tyr → Phe mutations to perturb sites along the electron-hopping pathway. In yeast (*Saccharomyces cerevisiae*) primase, residues Y395 and Y397 are conserved and orthologous to Y345 and Y347 in human primase [76]. Although positioned differently than their human orthologs within the respective p58C crystal structures, they are spaced ~10–15 Å apart, and could feasibly comprise a redox pathway [144, 184]. We hypothesized that yeast and human p58C have similar redox-switch mechanisms, despite their

different tyrosine constellations. Establishing that a yeast primase redox pathway exists also provides an opportunity to assay the viability of yeast cells expressing redox-deficient primase variants.

Methods

Protein Expression and Purification.

Protein expression and purification was performed by L. E. Salay. Yeast p58C (Pri2) residues 316-512 were cloned into pBG100 using the BamHI and NotI restriction sites. This plasmid was transformed into Rosetta DE3 cells. The cells were grown to an OD600 of 1.0 at 37 °C. They were then induced with 1 mM isopropyl β-D-1-thiogalactopyranoside (IPTG) and transferred to 20 °C for 16 hr. The cells were harvested and stored at -80 °C.

For purification, the cells pellets were thawed and resuspended in 50 mM NaH2PO4 (pH 7.8), 500 mM NaCl, 10 mM imidazole. DNasin and lysozyme were added at 2 mg/g of cells. Protease inhibitor tablets (Roche) were added to the suspension. The suspension was homogenized using a Dounce homogenizer and then sonicated on ice for 10 min. The solution was spun at 50,000 rcf for 20 min at 4 °C. The supernatant was filtered and passed over a Ni-NTA column (GE Healthcare). The column was washed with 3 column volumes of 50 mM NaH2PO4 (pH 7.8), 500 mM NaCl, 20 mM imidazole. The protein was eluted with 50 mM NaH2PO4 (pH 7.8), 500 mM NaCl, 250 mM imidazole. The eluent was dialyzed overnight at 4 °C into 50 mM NaH2PO4 (pH 7.8), 500 mM NaCl, 10 mM imidazole and the 6xHis tag was cleaved using H3C protease. The dialyzed protein was repassed over the Ni-NTA column as in the previous step. The flow-through and wash fractions were collected. These fractions were dialyzed into 20 mM HEPES (pH 7.2), 50 mM NaCl, 2 mM dithiothreitol (DTT) (Heparin Buffer A), then was filtered and passed over a 5 ml Hi-Trap HP heparin column (GE Healthcare) that had been pre-equilibrated with Heparin Buffer A. The protein was eluted in Heparin Buffer B (20 mM HEPES (pH 7.2), 1 M NaCl, 2 mM DTT) using a linear gradient of 0 to 100% over 40 column volumes. The protein typically eluted at ~20% Heparin Buffer B (250 mM NaCl). The

protein was dialyzed into 20 mM HEPES (pH 6.8), 2 mM DTT, and 200 mM NaCl, then flash frozen in N_2, and stored at -80 °C.

Site Directed Mutagenesis.

Site directed mutagenesis for single-site and multi-site variants was performed by L. E. Salay using a Q5 mutagenesis kit (New England Biolabs). The primers to create the mutations are listed in Table 5.1. The same reverse primer was used for all mutations. The annealing temperature for amplification was 58 °C.

Table 5.1: Site directed mutagenesis primers

Mutation	Primer
Y395F	5'GAGAAGTTCAATAAAGAATTCCGTTACAGCTTCAGGC
Y397L	5'GAGAAGTTCAATAAAGAACTGCGTTACAGCTTCAGGC
Y397F	5'GAGAAGTTCAATAAAGAATACCGTTTCAGCTTCAGGC
Y397L	5'GAGAAGTTCAATAAAGAATACCGTCTGAGCTTCAGGC
Reverse primer	5'CATTGTCATGTTCCCATTTCTTGTAAATGC

Mutant Selection and Design.

Mutations in the p58C domain of human DNA primase were designed based on previously determined structural data and bioinformatics compiled for conserved residues in this domain [38, 71-73]. Chimera software e[130] was used to analyze the relevant residues in the 1.54 Å resolution structure of yeast p58C (PDB 3LGB) [72]. Distances between tyrosine residues were measured between centroids.

Circular Dichroism.

Near-UV circular dichroism was performed by L.E. Salay as described in [163].

Fluorescence anisotropy.

Fluorescence anisotropy was performed by L.E. Salay as described in [76, 163]. Yeast p58C and the related mutants were assayed in a buffer containing 20 mM HEPES (pH 6.8), 2 mM DTT, and 75 mM NaCl.

Table 5.2: Electrochemistry and fluorescence anisotropy substrates	
p58C Electrochemistry Substrates	5'-SH-GTCGTGCAACGTGTCTGCGC-3' 3'-CAGCACGTTGCACAGACGCGTAC-5'
p58C Fluorescence Anisotropy Substrate	3’-GAGAGTTT-5′ 5’-[Flc]-TCTCTCTCTCAAA-3′

Oligonucleotide preparation for electrochemistry experiments.

Oligonucleotides were prepared by Dr. E. O’Brien. All standard or modified phosphoramidites and DNA synthesis reagents were purchased from Glen Research. Unmodified DNA oligonucleotides for electrochemical experiments were purchased from Integrated DNA Technologies, Inc. DNA sequences for electrochemistry assays are shown in Table 5.1. Thiol-modified DNA strands for electrochemistry were made on an Applied Biosystems 3400 DNA synthesizer, with a C6 S-S phosphoramidite incorporated at the 5’-terminus. Single-stranded DNA was purified using standard procedures as described previously [118]. High pressure liquid chromatography (HPLC) using a reverse-phase PLRP-S column (Agilent) was used, and oligonucleotide mass confirmed using MALDI-TOF Mass Spectrometry. Thiol-modified strands were reduced after the initial HPLC purification with 100 mM dithiothreitol (Sigma) for 2-3 h in 50 mM Tris-HCl, pH 8.4, 50 mM NaCl. Reduced thiol-modified DNA was purified by size exclusion chromatography (Nap5 Sephadex G-25, GE Healthcare) and subsequent reverse-phase HPLC. Single-stranded oligonucleotides were then desalted using ethanol precipitation and stored in low salt buffer (5 mM Phosphate, pH 7.0, 50 mM NaCl). Duplex DNA for electrochemistry was prepared by quantification of the complementary single-stranded oligonucleotides by UV-Visible spectroscopy, followed by annealing at 90 °C. A mixture of equimolar complementary single-stranded DNA (50 µM) was prepared in low salt buffer. Thiol-modified duplex DNA substrates were then deoxygenated by bubbling argon gas through the solution for 90-180 s. Duplex DNA was annealed on a thermocycler (Beckman Instruments) by initial heating to 90 °C, followed by slow cooling to 4 °C over 90 minutes. DNA was quantified using absorbance at 260 nm, with extinction coefficients at 260 nm for DNA

obtained using Integrated DNA Technologies online OligoAnalyzer tool. Single-stranded DNA substrates were quantified using UV-Visible spectroscopy and stored in low salt buffer at a stock concentration for activity assays.

Multiplexed Chip Fabrication.

Multiplexed electrode platforms were prepared by Dr. E. O'Brien using standard photolithography techniques, adapted from established protocols [76, 118, 128]. Nine 1 in. by 1 in. chips were patterned on 525 um thick silicon wafers (SiliconQuest). A thermal oxide layer roughly 4000 Å thick was grown on the silicon wafers using a Tytan tube furnace (Tystar). S1813 photoresist (2 µm layer) was deposited onto the wafers for patterning of the chips before metal deposition. Electron beam evaporation (CHA Industries) was then used to deposit a 3 nm titanium adhesion layer followed by a 100nm gold layer, without breaking vacuum between depositions. Metal lift-off using Remover PG (MicroChem) was performed overnight (10-12 h) at room temperature. Wafers were subsequently dried with a nitrogen gun and dehydrated at 140 °C for 10 minutes. A 3 µm layer of insulating SU-8 photoresist was deposited and patterned onto the wafer as described previously [76, 118, 128] with connective wires between contact pads on the edges of the chips and working electrodes in the center were covered but the contact pads and working electrodes left exposed. This ensured a fixed working electrode surface area of 2 mM^2. SU-8 photoresist was cured (150 °C, 15 minutes) and wafers cleaved into individual chips using a Dynatex Scriber/Breaker or broken manually after scoring with a diamond tip scriber.

DNA-Modified Electrode Assembly/Preparation.

Chips were prepared by Dr. E. O'Brien. They were dried thoroughly using argon gas and ozone-cleaned for 20 minutes at 20 mW using a Uvo brand ozone cleaner. Clean chips were assembled onto polycarbonate holders with acrylic clamp and Buna-N rubber gasket according to previous protocols, with four quadrants in the chip separated by fastened gasket and clamp[118]. Duplex DNA substrates, with a thiol modifier at the 5'- end, (25 µM) were deposited

in a 20 µL volume onto each quadrant of the multiplex chip. Substrates incubated for 18-24 hours on the gold surface to allow formation of self-assembled DNA monolayer. DNA monolayers were washed with phosphate buffer (5 mM phosphate, pH 7.0, 50 mM NaCl, 5% glycerol) and subsequently backfilled with 1 mM 6-mercaptohexanol (Sigma) in phosphate buffer for 45 minutes. Monolayers are then washed 10 times per quadrant with phosphate buffer and twice per quadrant with TBP buffer (5 mM phosphate, pH 7.0, 50 mM NaCl, 4 mM $MgCl_2$, 4 mM spermidine) to aid in formation of a monolayer with termini accessible for p58C binding.

Sample preparation for electrochemistry.

All electrochemistry was performed by Dr. E. O'Brien. Wild type and mutant p58C samples were stored prior to experiments in p58C storage buffer (20 mM Tris, pH 7.2, 75 mM NaCl) or crystallography buffer (20 mM HEPES, pH 6.8, 200 mM NaCl, 2 mM DTT). All p58C variants were transferred to HEPES electrochemistry buffer (20 mM HEPES, pH 7.2, 75 mM NaCl) using Amicon ultra centrifugal filters (0.5 mL, 3MWCO) (Millipore Sigma). Protein was applied in a 90-140 µL volume to the filter and centrifuged for 15 minutes at 14000 x g at 4 °C. After centrifugation, 400 µL of HEPES electrochemistry buffer was applied to the filter and centrifuged at 14000 x g for 20 minutes. This was repeated four times to exchange the p58C protein into HEPES electrochemistry buffer. After buffer exchange and recovery of sample by centrifugation (2 minutes, 1000 x g), concentrations of [4Fe4S] cluster-containing p58C or mutants were measured using UV-Visible spectroscopy, by absorbance of the [4Fe4S] cluster at 410 nm (extinction coefficient = 17000 M-1 cm-1) [135]. Recovered samples (approx. 100-150 µL volume) were deoxygenated for 2-3 minutes with argon. Samples were then transferred into the anaerobic chamber (Coy Laboratory products). Before deposition onto the gold electrode surface, p58C/mutant samples were diluted to a molar concentration of 30 µM or 57 µM [4Fe4S] p58C variant with previously deoxygenated HEPES electrochemistry buffer.

DNA Electrochemistry Measurements of p58C Variants.

All electrochemistry was performed by Dr. E. O'Brien using a CHI620D potentiostat and 16-channel multiplexer (CH Instruments), in an anaerobic glove chamber. Multiplex gold electrodes were part of a three-electrode system with an external Ag/AgCl reference electrode (Bioanalytical Systems) and platinum counter electrode. Initial cyclic voltammetry scans of the monolayers in p58C buffer were performed to ensure monolayer formation on each electrode. All washes were performed with 20 µL buffer volumes on each quadrant. Before scanning, a 200 µL volume was deposited over the chip surface, a bulk solution well for completion of a three-electrode circuit with an external reference and counter electrode. Cyclic voltammetry scans were performed at 100 mV/s scan rates, over a potential range of +0.412 V to -0.288 V vs. NHE or +512 mV to – 188 mV vs NHE. Bulk electrolysis on DNA was performed at an applied potential of +0.412 V vs. NHE or +512mV vs. NHE for all electrochemical oxidation reactions and -0.188 V vs. NHE for all electrochemical reduction reactions. The oxidizing potential was applied for at least 8.33 minutes for single oxidation reactions on a surface, and 6.67 minutes for the iterative oxidation cycles of p58C variants. The reducing potential was applied for 8.33 minutes in all electrochemical reduction reactions. All bulk electrolysis and cyclic voltammetry were performed in previously deoxygenated p58C storage buffer (20 mM HEPES, pH 7.2, 75 mM NaCl). Charge transfer (nC) in the cathodic peak of oxidized samples CV scans was assessed using the area under the current wave of the reduction signal. Variants of p58C were compared for charge transfer proficiency using at least three trials of oxidation at +0.412 V vs. NHE or +512 mV vs. NHE, after at least 8.33 minutes of oxidation at the applied potential. Charge transfer was measured for oxidized samples using CHI software, assessing the area under the reductive peak in CV after electrochemical oxidation. Yields for bulk electrolysis were assessed by subtracting the total charge reported in Coulombs from the product of the electrolysis time (s) and the final current value (A). NTP-dependence of electrochemical signals were measured by pipetting a small volume (1-3 µL) of 0.1 M ATP stock

solution into each quadrant of the multiplexed chip setup. These stocks should be added by quadrant, rather than into the bulk solution. Divide the NTP stock into quarters and pipet ¼ of the total solution onto a quadrant. Samples were added by quadrant, as physical barriers in the setup prevent diffusion of NTPs between electrode quadrants. After the volume of ATP stock was deposited onto the electrode quadrant, resulting in a 2.5 mM or 5 mM concentration of ATP in the quadrant, CV scans were measured at a 100 mV/s scan rate. Square wave voltammetry in both reductive and oxidative sweeps was measured using a symmetric square wave form (25 mV amplitude), superimposed on a staircase (E_{step} = 4 mV). Scans were performed at 15 Hz frequency, 60 mV/s scan rate. Charge transfer was assessed using CHI software; charge values were determined by calculation of the area under the reductive and oxidative peak curves. Midpoint potentials of NTP-dependent redox signals were assessed using the peak selection function in CHI software.

X-Ray Crystallography.

Crystallography was performed by L.E. Salay. Crystals were grown at 16 °C by mixing 1:1 yeast p58C variants (~5 mg/ml) and mother liquor (100 mM TRIS (pH 8.5), 40-65% MPD) using hanging drop vapor diffusion. Crystals formed after 2 days. They were then looped, transferred to a cryo-protectant containing the mother liquor and 20% glycerol.

Data collection for yeast p58C Y397F was performed at 100 K using an in-house Bruker Microstar rotating anode x-ray generator with a Bruker Proteum PT135 CCD area detector at a wavelength of 1.54 Å. Sulfur single anomalous dispersion (SAD) was used to phase this data set with the program suite HKL2MAP [187]. The model was built using arp/Warp in the CCP4 suite of programs [188] followed by iterative rounds of refinement using Phenix [116] and *Coot* [114].

Crystallographic data for the remaining variants were collected at the Advanced Photon Source (Argonne National Laboratory, Chicago, IL) on Life Sciences Collaborative Access Team beamlines. Data were indexed and scaled using HKL2000 [132]. Molecular replacement

using Phaser [134] with the model of the yeast p58C variant Y397F was used to solve the phases of the remaining mutants. The models were refined iteratively using Phenix [116] and *Coot* [114]. Access to these programs was provided by SBGrid [166]. Collection and refinement statistics are shown in Table 5.3.

Yeast Strain Construction.

Yeast strains were constructed by Dr. E. Epum, Dr. K.L. Friedman, and L.E. Salay. PRI2 mutations were introduced into haploid strain YKF201 (MATa trp1 leu2 ura3 his7) by two-step gene replacement [189]. Integration plasmids were constructed by subcloning a PRI2 C-terminal domain (CTD) fragment of plasmid PRI2-3HA [74, 190] into the pRS406 vector [191] and mutations were created using overlap-extension PCR [192]. Silent nucleotide changes were included to create restriction site polymorphisms tightly linked to each mutation. Plasmids linearized with AgeI-HF (NEB) were transformed into YKF201 and Ura+ transformants were subsequently plated on media containing 5-fluoroorotic acid. Chromosomal integration of all mutations was verified by restriction digestion and sequencing (cells losing the URA3 marker by recombination also lost the 3HA tag). To test for viability of the pri2-Y395L allele, strain YKF201 was transformed with the complementing plasmid pRS416-PRI2, containing a 3.1kb fragment amplified from yeast genomic DNA inserted at the BamHI and EcoRI sites of pRS416. PRI2-3HA plasmids (either WT or containing the Y397F or Y497L alleles) were linearized with AgeI-HF (NEB) and integrated at the PRI2 locus with selection on media lacking uracil and tryptophan. Individual transformants were verified by PCR and sequencing, then restreaked on media lacking uracil and tryptophan to confirm growth and on media lacking tryptophan and containing 5-fluoroorotic acid (5-FOA) to select for loss of the complementing plasmid.

For inducible overexpression of PRI2 alleles, the open reading frame of PRI2 was cloned into plasmid p416-Gal1 at the BamHI and XbaI sites [193]. The Y397L mutation was incorporated by subcloning from the integration plasmid described above. All plasmids were verified by sequencing. Overexpression plasmids were transformed into haploid strain YKF1675

(MATa::DEL.HOcs::HisG ura3 trp1 leu2::KAN hml::hisG HMRa-stk; isogenic to strain CL11-7) [194] with selection on media lacking uracil. Individual transformants were restreaked on media lacking uracil and containing 2% glucose or galactose.

Table 5.3: Crystallographic data collection and refinement statistics

	WT	Y395F	Y395L	Y397F	Y397L
Data Collection					
Wavelength	1.07807	0.98782	0.97856	1.54184	1.078
Space group	P 21 21 21	P 21 21 21	P 21 21 21	P 21 21 21	P 21 21 21
Resolution range	30.32 - 1.39 (1.44 - 1.39)	24.48 - 1.12 (1.16 - 1.12)	29.26 - 1.82 (1.88 - 1.82)	22.12 - 1.36 (1.41 - 1.36)	31.90 - 1.32 (1.37 - 1.32)
Cell dimensions					
a, b, c (Å)	41.09, 50.77, 89.83	40.99, 50.87, 89.91,	38.46, 50.83, 90.18	40.81, 50.81, 90.04	40.95, 50.87, 89.62
α, β, γ (°)	90, 90, 90	90, 90, 90	90, 90, 90	90, 90, 90	90, 90, 90
Reflections					
Total	73655 (6688)	143868 (12902)	31456 (2754)	77970 (7012)	88564 (8503)
Unique	37491 (3464)	72515 (6689)	16031 (1494)	40483 (3945)	44430 (4291)
Completeness (%)	96.80 (91.44)	98.52 (91.89)	96.80 (92.26)	98.68 (97.87)	99.53 (98.19)
R_{merge}	0.0313 (0.1033)	0.0253 (0.2132)	0.0253 (0.1956)	0.0458 (0.3282)	0.0275 (0.0822)
R_{meas}	0.0442 (0.146)	0.0358 (0.302)	0.0357 (0.277)	0.0648 (0.464)	0.0389 (0.116)
$CC_{1/2}$	0.997 (0.968)	0.999 (0.911)	0.997 (0.946)	0.998 (0.796)	0.997 (0.981)
Multiplicity	2.0 (1.9)	2.0 (1.9)	2.0 (1.8)	1.9 (1.8)	2.0 (2.0)
Mean I/σ (I)	11.59 (5.34)	12.18 (3.15)	7.54 (3.64)	12.72 (2.21)	19.43 (6.73)
Refinement					
No. of non-H atoms	1816	1794	1465	1756	1800
	1609	1590	1431	1563	1574
Macromolecules					
Ligands	24	24	32	32	24
Solvent	183	180	2	161	202
R_{work}/R_{free}	0.125/0.146 (0.109/0.158)	0.128/0.139 (0.197/0.194)	0.272/0.318 (0.424/0.427)	0.156/0.178 (0.232/0.257)	0.122/0.144 (0.119/0.150)
RMSD (bonds, Å)	0.011	0.018	0.018	0.012	0.014
RMSD (angles, °)	1.32	1.71	1.08	1.45	1.49
Ramachandran					
Favored (%)	98.88	98.89	96.55	98.33	97.77
Allowed (%)	1.12	1.11	3.45	1.67	2.23
Outliers (%)	0	0	0	0	0
Rotamer outliers (%)	0.57	0.57	0	0.59	0.57
Clashscore	1.53	3.1	5.25	0.95	5.01
Wilson B-factor ($Å^2$)	10.75	12.1	30.16	9.31	11.26
Average B-factor (Å)	16.04	18.91	60.07	15.1	17.6
	14.24	17.59	60.09	13.9	15.96
Macromolecules					
Ligands	25.41	22.22	58.66	24.55	23.14
Solvent	30.63	30.13	68.61	24.84	29.66
PDB Code	6DI6	6DTV	6DU0	6DTZ	6DI2

Results

Redox Switch Through a Tyrosine Pathway in Yeast p58C.

Human and yeast p58C have similar overall structures (Figure 5.1) with a backbone root mean squared deviation (rmsd) of only 0.82 Å. Both proteins bind DNA with micromolar affinity [72, 73]. Yeast and human p58C each contain a [4Fe4S] cluster buried within the protein, ~25 Å from the DNA binding interface (Figure 5. 1).

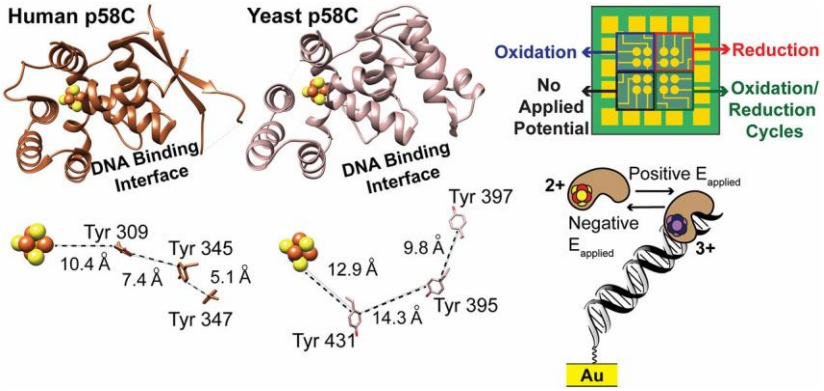

Figure 5.1: The structures of yeast and human p58C can support a common redox switch when bound to DNA. A) Comparison of p58C structures and conserved tyrosine residues near the [4Fe4S] cluster for yeast p58C (light brown) and human p58C (dark brown). Both proteins contain a [4Fe4S] cluster cofactor and several conserved tyrosine residues positioned between the DNA binding interface of p58C and the [4Fe4S] cluster that are within feasible distance for charge transfer. (24,25) Conserved tyrosine residues in each protein are shown below the respective p58C structures. Structures rendered using human p58C (PDBID 3L9Q) (20) and the yeast p58C structure from this study (PDBID 6DI6). B) Cartoon depicting the change in DNA binding and activity associated with [4Fe4S] cluster redox. (Below) Diagram of the multiplexed, sixteen-electrode DNA electrochemistry platform used for observation of electrochemistry under different conditions with replicates on a single surface.

Despite having only 40% identical sequences, yeast and human p58C both have multiple conserved tyrosines between the cluster and the DNA binding interface. In human p58C, these tyrosines shuttle charge through the protein to mediate the redox switch (Figure 5.1) [76]. We sought to determine whether the yeast p58C [4Fe4S] cluster has a redox-switching capability similar to that of human p58C. We identified several tyrosine residues conserved in yeast p58C, which are within feasible charge-transport distance of the yeast p58C cluster or DNA-binding interface, as possible mediators of a redox switch. Residues Y395 and Y397 in yeast p58C (Figure 5.1), orthologous to Y345 and Y347, respectively, in the human p58C redox pathway,

are prime candidates for a redox role [76]. Distances between tyrosine centroids are larger on average in the yeast protein crystal structure (12.9–15.3 Å) than in the human protein crystal structure (5.1–10.4 Å) [73], but fall securely within the distance for feasible microsecond electron transfer.

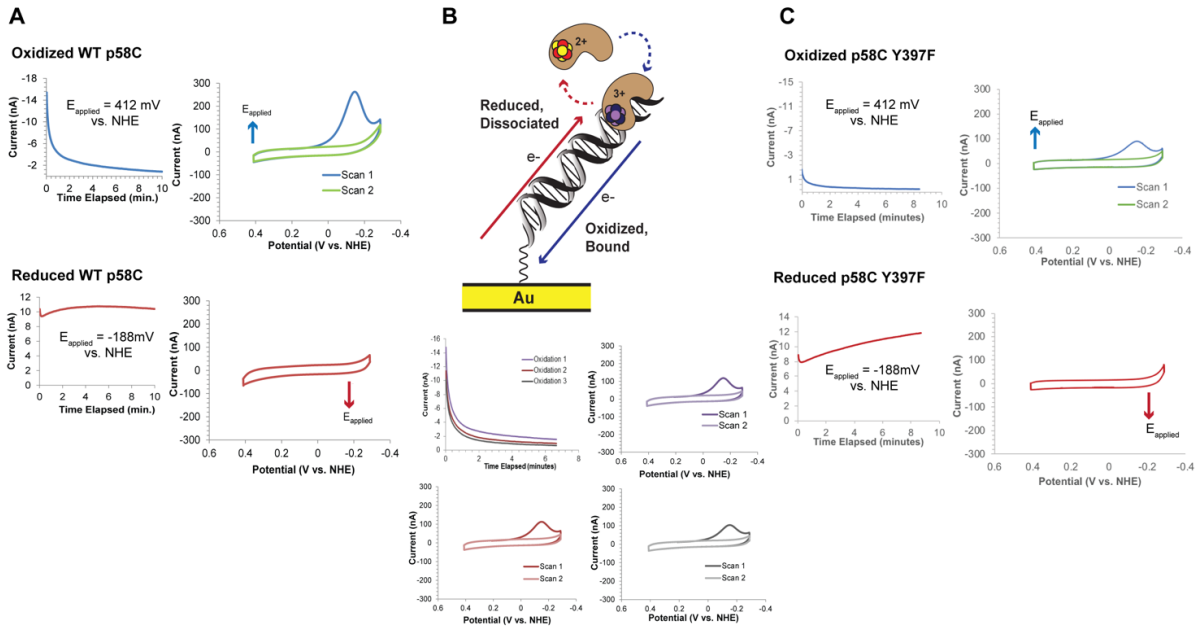

Figure 5.2: A redox switch in yeast p58C is mediated by the pathway of conserved tyrosine residues. A) Electrochemical oxidation and subsequent CV scans of yeast wild type p58C. A large reductive peak is observed in the initial scan of the oxidized protein but disappears after a single scan to negative potentials. The reduced p58C is electrochemically inactive on a DNA-modified surface. B) Cartoon (above) illustrates the electrochemically reversible switch between the oxidized, electrochemically active p58C in the $[4Fe4S]^{3+}$ state with tighter binding to the DNA substrate and the reduced electrochemically inactive p58C in the $[4Fe4S]^{2+}$ state with weaker DNA binding affinity. Iterative electrochemical oxidation and CV after each oxidation on a single DNA-modified surface. The p58C signal is regenerated upon oxidation at a positive applied potential. C) Electrochemically oxidized and reduced p58C Y397F. Y397F (Y347 ortholog in human p58C) and Y395F (Figure S3, Y345F ortholog in human p58C) were electrochemically oxidized and reduced, then scanned using CV on a DNA electrode. Both mutants showed similar behavior to WT p58C, with decreased charge transfer activity. The electrochemically reduced protein was not electrochemically active after electrochemical reduction. All scans were performed in anaerobic conditions, on 30 μM [4Fe4S] p58C (WT, Y395F, or Y397F), 20 mM Tris, pH 7.2, 75 mM NaCl. All CV was performed at 100 mV/s scan rate. Electrochemistry performed by Dr. E. O'Brien.

As the distance between centroids, rather than the relative positions of tyrosines, is the primary factor determining the feasibility of charge transfer through protein [184], we predicted that both pathways could mediate redox switching. To test whether a change in the oxidation state of the [4Fe4S] cluster in yeast p58C affects DNA binding, we compared anaerobically the

electrochemical behavior of oxidized $[4Fe4S]^{3+}$ p58C and reduced $[4Fe4S]^{2+}$ p58C on multiplexed DNA electrodes (Figure 5.1), modified with a 20-nt DNA duplex substrate containing a 3-nt, 5′- ssDNA overhang identical to the substrate used to study human p58C [76]. Purified WT yeast p58C, in the absence of an applied potential, displays no redox signal in cyclic voltammetry (CV) (Figure 5.2). This form of the protein is thus not coupled to the DNA base pairs for redox signaling. WT p58C was then electrochemically oxidized by applying a positive potential (412 or 512 mV vs. normal hydrogen electrode (NHE); Table 5.4) or electrochemically reduced by applying a negative potential (−188 mV vs. NHE) to the electrode surface.

Table 5.4: Summary of electrochemical oxidation conditions for yeast p58C mutant assays on DNA-modified electrodes

p58C mutant	Buffer	Concentration (μM)	E_{ox} (mV vs. NHE)	Q_{CV} (nC)
WT	Tris	30	412	145 ± 41
Y395F	Tris	30	412	9.03 ± 5.3
Y397F	Tris	30	412	44.9 ± 13
WT	HEPES	57	512	2.19 ± 0.33
Y395L	HEPES	57	512	0.266 ± 0.17
Y397L	HEPES	57	512	0.732 ± 0.15

Table 5.4: Summary of electrochemical oxidation conditions for yeast p58C variant assays on DNA-modified electrodes. Buffer conditions are 20 mM Tris, pH 7.2, 75 mM NaCl (Tris in table) or 20 mM HEPES, pH 7.2, 75 mM NaCl (HEPES in table). In HEPES buffer, protein samples were generally less redox-active than in Tris, which is likely due to some loss of [4Fe4S] cluster after buffer exchange. The charge transferred during CV (QCV) after bulk electrolysis is reported for each variant. WT moreover displayed greater QCV than variants tested at comparable conditions, suggesting that yeast p58C is less redox-proficient than human p58C but the redox activity depends on tunneling of charge through conserved tyrosines. Values reported are mean +/- S.D. for n≥ 3 trials. Electrochemistry performed by Dr. E. O'Brien.

Bulk electrolysis was performed on individual electrodes for a total of 8.3 min, to optimize the yield of electrochemically converted protein. Oxidized or reduced p58C samples were scanned by CV immediately after bulk electrolysis. The electrochemically oxidized sample displays a large cathodic peak near −130 to −150 mV vs.NHE in Tris storage buffer (20 mM Tris, pH 7.2, 75 mM NaCl). After a single scan to negative, reducing potentials, the signal disappears, indicating a loss of coupling between the [4Fe4S] cluster and the DNA bases. (Figure 5.2).

Electrochemically reduced p58C, conversely, does not display any signal after bulk electrolysis. This result suggests that oxidized $[4Fe4S]^{3+}$ yeast p58C is tightly bound to DNA and electronically coupled into the bases for redox signaling, but reduced $[4Fe4S]^{2+}$ yeast p58C is loosely associated and not coupled to the DNA for signaling. Human p58C can be electrochemically converted from the oxidized, tightly bound state to the reduced, loosely associated state [76]. Iterative oxidations on a DNA electrode indicate a similar behavior in yeast p58C (Figure 5.2). Oxidation of yeast p58C to the $[4Fe4S]^{3+}$ state produces a large, reductive CV signal, indicating conversion to the resting $[4Fe4S]^{2+}$ state [69, 70]. The signal disappears in the second CV scan, but a second oxidation regenerates the reductive peak. A single electron transfer reaction thus facilitates conversion between two forms of p58C with dramatically different DNA-binding and redox-signaling properties. We next investigated whether the observed yeast p58C redox switch is dependent on a pathway of conserved tyrosine residues, as in the human protein. We constructed yeast p58C variants with mutations at Y395 or Y397. As these residues are conserved orthologs to components of the human primase redox pathway, they were prime candidates for the yeast primase redox pathway. All generated p58C variants (Y395F, Y397F, Y395L, and Y397L) load the [4Fe4S] cluster comparably to WT, as assessed by the ratio of absorption at 410 nm/280 nm in UV-visible spectroscopy (Figure 5.3).

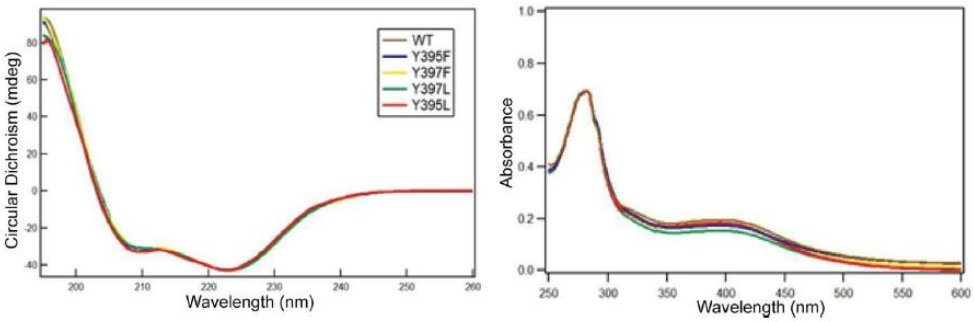

Figure 5.3: WT and mutant yeast p58C biophysical characterization. left) Circular dichroism (CD) spectroscopy of WT and mutant p58C indicate the mutations do not perturb any of the elements of secondary structure. All spectra normalized to WT at 222 nm. right) UV-Visible spectroscopy of WT and mutant p58C shows similar 280 nm/410 nm absorbance ratios, indicating similar degrees of [4Fe4S] cluster cofactor loading in all variants. All spectra normalized to WT at 410 nm. CD and UV-VIS spectroscopy by L.E. Salay.

Fluorescence anisotropy assays on WT and mutant p58C (Figure 5.4) show that all variants bind the substrate with virtually the same low micromolar affinity. This result suggests that the same number of p58C molecules are bound to the DNA on the electrode surface before electrochemical oxidation, when the sample is present largely in the $[4Fe4S]^{2+}$ state. Since the redox pathway through p58C is the conduit through which cluster oxidation occurs, we expect that fewer mutants versus WT are bound tightly to DNA in the $[4Fe4S]^{3+}$ state after bulk oxidation, if these tyrosines mediate the redox switch in yeast primase. Analysis of charge transfer in the reductive peak (QCV, Table 5.3) for WT yeast p58C, p58C Y395F, Y397F, Y397L, and Y395L, demonstrates that the mutants are consistently redox-deficient relative to WT p58C (Table 5.3). It is interesting to observe however that the p58C variants, particularly the Tyr → Phe mutants, retain partial redox-switching ability. Phenylalanine residues are generally less capable of mediating electron transfer through protein than tyrosines, due to their higher ionization energy[144] and inability to form discrete cation radicals; phenylalanines, however, can mediate electron transfer, although less efficiently through tunneling[185], partially inhibiting charge transfer in some protein systems [186, 195].

Tyrosine Mutations Do Not Change Yeast p58C Structure.

X-ray crystal structures of the WT and mutant yeast p58C demonstrate that no changes in the overall structure of the protein are caused by the tyrosine mutations (Figure 5.4, Table 5.3). Overlays of WT yeast p58C and p58C Y395F, Y397F, Y395L, and Y397L, all of which have an RMSD less than 0.5 Å from the WT, underscore the structural similarity. The F395 and F397 aromatic rings in Y395F and Y397F, respectively, are oriented in almost exactly the same position as the aromatic rings in the tyrosines of the WT protein, as had been seen previously with human p58C Y345F and Y347F mutants [76]. Notably, the more drastic substitution of the tyrosine aromatic ring with the leucine aliphatic chain also has very little effect on the structure, including the orientation of side chains.

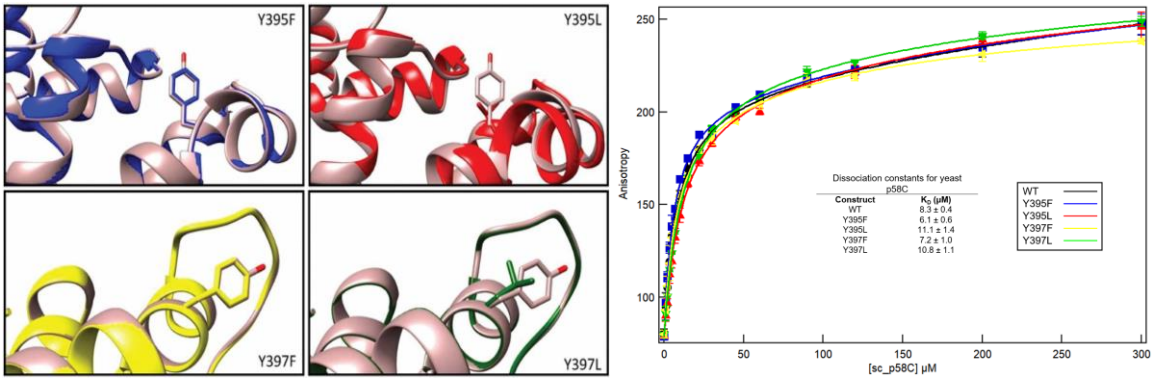

Figure 5.4: DNA binding and structure are preserved upon mutation of conserved tyrosine residues Y395 and Y397 in yeast p58C. Left: Crystal structures of WT and yeast p58C tyrosine mutants show minimal structural perturbation of the overall protein structure with redox pathway mutations. The WT yeast p58C (green) crystal structure is overlaid with each redox-deficient mutant. Mutation of tyrosines to either aromatic phenylalanine or aliphatic leucine do not produce significant changes in the structure. Right: DNA binding of yeast p58C variants measured using fluorescence anisotropy. WT yeast p58C and tyrosine mutants bind substrate with similar affinities, suggesting that differences in electrochemical signals are due to differences in redox proficiency rather than differences in ability to bind DNA. Crystallography and DNA binding analysis performed by L.E. Salay

The similar WT and mutant yeast p58C structures and substrate affinities corroborate that the difference in redox signal between WT and mutant p58C is a result of differences in the redox-switching ability and not the ability to interact with a DNA substrate. All p58C variants were

crystallized, moreover, with high [4Fe4S] cluster loading in the protein sample, supported by the UV-visible spectra (Figure 5.3). Overall, we observe that the p58C mutant proteins are less effective in participating in redox signaling on DNA relative to WT, when equal amounts of [4Fe4S] protein (determined spectroscopically) are initially deposited on the Au electrode. Different electrochemical behavior of these variants is thus a consequence of different chemical/electronic properties.

Reversible, Nucleotide Triphosphate-Dependent Redox Activity in Yeast p58C.

Yeast p58C displays a semi-reversible, nucleotide triphosphate (NTP)-dependent redox signal on DNA under anaerobic conditions, centered at 149 ± 14 mV vs. NHE, in the presence of 1.25 mM ATP. This potential is within the biological redox potential range [182] and comparable to the potential values observed for other DNA-processing [4Fe4S] proteins, suggesting that active primase may signal other DNA-bound [4Fe4S] proteins during replication [56, 67, 98, 140]. The signal observed in CV is 71 ± 10% reversible, displaying an average charge-transfer value of 8.7 ± 4 nC in the reductive peak and 5.8 ± 2 nC in the oxidative peak. The larger cathodic wave in CV is consistent with the oxidized $[4Fe4S]^{3+}$ protein having a higher binding affinity and being more strongly coupled to the DNA bases for redox activity than the reduced $[4Fe4S]^{2+}$ protein. The reductive peak corresponds to the electrochemical conversion of $[4Fe4S]^{3+}$ p58C to $[4Fe4S]^{2+}$ p58C, and the oxidative peak is a measurement of the reverse process. The primase redox-switch model predicts that more oxidized $[4Fe4S]^{3+}$ protein is bound in the p58C:DNA:NTP complex than reduced $[4Fe4S]^{2+}$ protein. The data corroborate this model and suggest that NTP binding induces redox switching in yeast p58C.

To assess whether this reversible signal depends on the p58C charge-transfer pathway, we measured the NTP-dependent signals of yeast p58C Y395 and Y397 mutants. Unlike WT yeast p58C, no mutants generated a signal detectable by CV in the presence of 1.25 mM ATP.

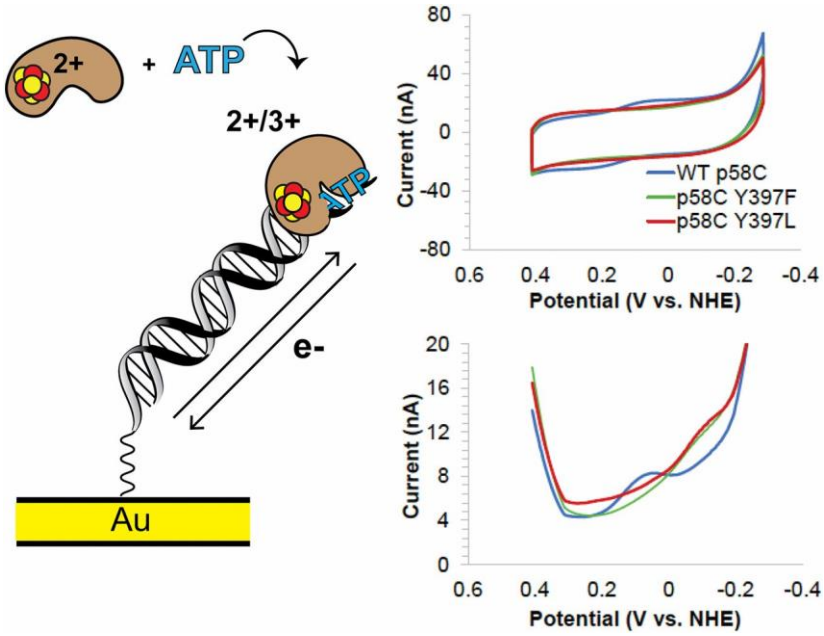

Figure 5.5: NTP binding promotes a reversible redox switch in yeast p58C. A) Cartoon depicts redox activity of yeast p58C bound to DNA and a nucleotide triphosphate (NTP). The protein can reversibly cycle between the $[4Fe4S]^{3+}$ and $[4Fe4S]^{2+}$ state when bound to all substrates essential for primase activity. B) CV scans of WT yeast p58C (blue trace), p58C Y397F (green trace), and p58C Y397L (red trace) in the presence of 1.25 mM ATP (WT). Both proteins show reversible redox signals centered at 149 ± 14 mV vs. NHE (WT). The WT protein signal is 70 ± 10% reversible. Mutant p58C does not have a measurable signal centered near 150mV vs. NHE, suggesting that the redox pathway is important for redox switching in the presence of all native primase substrates. Square Wave Voltammetry (Reduction sweep, left; oxidation sweep, right) of WT and tyrosine mutant p58C. Square Wave voltammetry in the reductive sweep show a small signal for the Y397F and Y397L variants near -80 mV vs. NHE, which is attributed to a $[3Fe4S]^{+}$ degradation product. These data suggest that the tyrosine pathway and reversible redox switching is integral for activity and cluster stability. All scans were performed in anaerobic conditions, on 57 µM [4Fe4S] p58C variant and 1.25 mM ATP in 20 mM HEPES, pH 7.2, 75 mM NaCl. All CV was performed at 100 mV/s scan rate. Square Wave voltammetry was performed at 15 Hz frequency. Potentials reported are mean values +/- s.d. of at least three trials. Electrochemistry performed by Dr. E. O'Brien.

We therefore used square-wave voltammetry (SWV), an electrochemical technique which can reliably detect smaller signals[196] to aid in characterizing mutant NTP-dependent redox activity. We observe a single reductive peak in SWV at −86 ± 13 mV vs. NHE and −90 ± 4 mV vs. NHE, for Y397F and Y397L, respectively, on a DNA electrode in the presence of 1.25 mM ATP (Figure 5.5). This signal appears at a potential distinct in SWV from the semi-reversible signal for the WT p58C (+85 ± 9 mV vs. NHE), reflecting the presence of a different species.

We next tested whether the p58C mutants displayed any redox activity in the presence of 2.5 mM ATP. The Y395L mutant displayed no measurable redox signal in the presence of

1.25 or 2.5 mM ATP (Figure 5.6, left). The Y395F variant displays some reversible charge transport centered at 162 ± 6 mV vs. NHE in the presence of 2.5 mM ATP (Figure 5.6 right), although the charge transport (3 ± 1 nC in the cathodic peak, 2 ± 0.6 nC in the anodic peak) is diminished relative to WT with 1.25 mM ATP (Figure 5.6, middle). In the presence of 2.5 mM ATP, Y397F displays an irreversible peak at a similar potential to the peak observed with 1.25 mM ATP (Figure 5.5) in some but not all scans. The Y397L variant displays minimal reversible redox activity in CV (Figure 5.5) centered at 140 ± 17 mV vs. NHE, with charge-transport values of 1.7 ± 1 nC in the cathodic peak and 1.5 ± 1 nC in the anodic peak. The NTP-dependent redox activity of the tyrosine mutants is thus consistently diminished relative to WT p58C, suggesting the primary redox pathway through Y395 and Y397 is important for redox signaling when bound to all necessary substrates for primer synthesis.

This irreversible reductive peak between −80 and −90 mV vs. NHE likely corresponds to the $[3Fe4S]^{+}$ degradation product of the [4Fe4S] cofactor [139]. This irreversible secondary reductive peak is actually observed in WT yeast p58C, alongside the primary wave, in the presence of a large excess of ATP (Figure 5.6, middle). A signal in the reductive wave at comparable potentials was recently observed electrochemically and spectroscopically in a cancer-causing variant of human base excision repair protein MUTYH, when exposed to atmospheric oxygen[180]. The $[3Fe4S]^{+}$ degradation product is a consequence of oxidation from the resting $[4Fe4S]^{2+}$ state to the $[4Fe4S]^{3+}$ state [56, 180] in a mutant with a destabilized metal cofactor. The $[3Fe4S]^{+}$ product can also occur as a result of oxidation in an aerobic atmosphere during purification or sample preparation [56, 79]. Since the $[3Fe4S]^{+/0}$ reduction peak occurs in p58C Y397F/Y397L in the presence of NTPs and in the absence of oxygen, however, these mutants likely undergo some electron transfer when bound to DNA and NTPs, anionic substrates expected to shift the potential of the [4Fe4S] cluster [63, 182]. Since the compromised redox pathway inhibits reversible cycling between the $[4Fe4S]^{2+}$ and $[4Fe4S]^{3+}$ states, redox signaling in these p58C variants can lead to a “trapped” high-energy $[4Fe4S]^{3+}$

species which cannot easily be reduced back to the $[4Fe4S]^{2+}$ state; the cluster then becomes unstable and degrades. Efficient redox switching is essential for regulation of activity, as well as [4Fe4S] cluster stability.

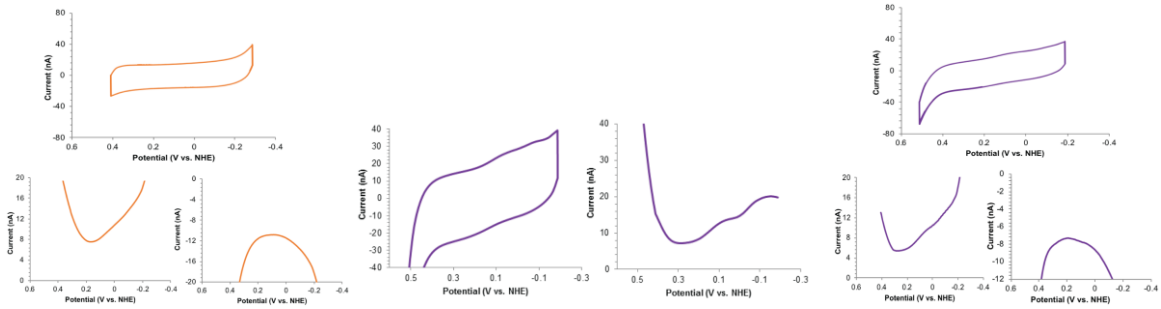

Figure 5.6 cyclic and square wave voltammetry of Y395L (left) and Y395F (right) compared to wildtype (middle)

Left: Electrochemistry of yeast p58C Y395L in the presence of 1.25mM ATP. above) CV scans show no redox signaling activity for p58C Y395L in the presence of DNA and NTPs. below) SWV of yeast p58C Y395L in the presence of 1.25mM ATP. Reductive (left) and oxidative (right) scans show no measurable redox signaling activity in this variant. All scans performed in anaerobic conditions on 57μM [4Fe4S] p58C Y395L and 1.25mM ATP, in 20mM HEPES, pH 7.2, 75mM NaCl, at a 100mV/s scan rate for CV or a 15 Hz frequency for SQWV.

Middle: Electrochemistry of WT yeast p58C in the presence of 5mM ATP. left) CV scans show a small peak in the reductive wave near -80mV vs. NHE, likely a $[3Fe4S]^{+}$ oxidative degradation product. right) SWV of yeast p58C in the presence of 5mM ATP. All scans performed in anaerobic conditions on 40μM [4Fe4S] p58C and 5mM ATP, in 20mM HEPES, pH 7.2, 75mM NaCl, at a 100mV/s scan rate for CV or a 15 Hz frequency for SQWV.

Right: Electrochemistry of yeast p58C Y395F in the presence of 2.5mM ATP. above) CV scans show some redox signaling activity in the presence of DNA and NTPs. Even in the presence of a higher concentration of ATP, this variant displays diminished redox signaling relative to WT. below) SWV of yeast p58C Y395F in the presence of 2.5mM ATP. Reductive (left) and oxidative (right) scans show no measurable redox signaling activity in this variant. All scans performed in anaerobic conditions on 40μM [4Fe4S] p58C Y395F and 2.5mM ATP, in 20mM HEPES, pH 7.2, 75mM NaCl, at a 100mV/s scan rate for CV or a 15 Hz frequency for SQWV. Figure by Dr. E. O'Brien.

The Yeast p58C Redox Switch Is Necessary for Viability.

After characterizing the redox switch in yeast DNA primase, we sought to investigate the consequences of this chemistry in yeast cells. Both subunits of yeast primase are essential; partially defective alleles compromise DNA synthesis and cell growth [197, 198]. Liu and Huang [74] additionally have shown that mutations of the cysteine residues ligating the p58C [4Fe4S] cluster cause growth defects in cells, suggesting the importance of the primase cluster for viability. We have shown that mutations at p58 residues Y395 or Y397 along the redox pathway

impair the Fe–S redox switch *in vitro* and hypothesized that these mutations would compromise cell growth. Since we observe the formation of a putative $[3Fe4S]^{+}$ species in the presence of DNA and NTPs electrochemically for the Y397 mutants, we were interested in potential differences between Y395 and Y397 tyrosine pathway mutants. Single-site mutations were introduced into the chromosomal gene encoding the p58 subunit of *S. cerevisiae* DNA primase (PRI2) at positions Y395 and Y397 under control of the endogenous promoter [197]. We incorporated Y395F, Y395L, Y397F, or Y397L mutations into the yeast genome to investigate the biological effects of both mutations at different loci along the charge-transfer pathway and mutations to aromatic phenylalanine versus aliphatic leucine. As these redox-pathway mutations do not affect [4Fe4S] cluster loading or DNA binding of p58C *in vitro*, we could specifically assess the effects of the cluster redox switch on cellular fitness.

We investigated whether the Y395F and Y397F mutations in p58C, which retain some redox switching on DNA electrochemically (Figure 5.2, Figure 5.6), affect cellular fitness.

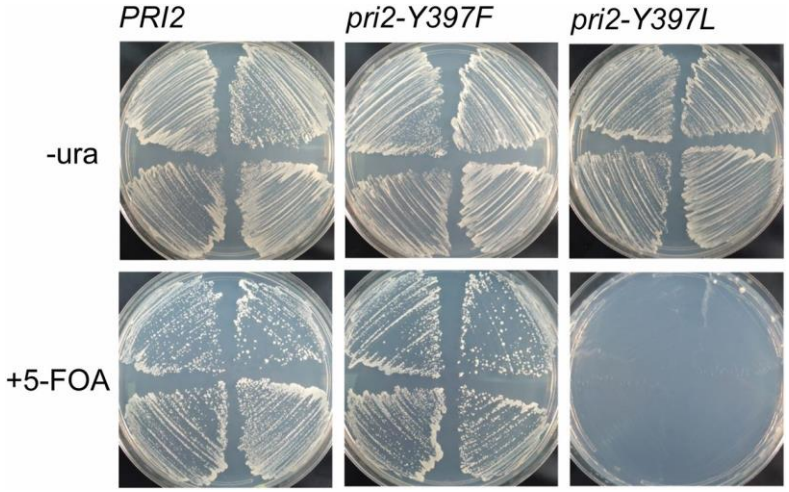

Figure 5.7: The p58Y397L mutation is lethal in yeast. To assess whether the Y397L mutation caused the lethal phenotype observed in the *pri2-Y397L* strain, we performed sporulation and subsequent tetrad analysis. Using the pop-in, pop-out method with a *URA3* marker gene, we integrated Y397F and Y397L mutations into the *PRI2* gene. Strains containing the integrated mutations have lost the *URA3* marker gene, which prohibits cell growth in the presence of 5'-fluoroorotic acid (5'-FOA). Mutant strains are thus viable in the presence of 5'-FOA, unless the integrated mutation causes growth defects. The single-atom *pri2-Y397F* mutation exhibits WT growth in the presence of 5'-FOA, consistent with the partially retained electron transfer in this p58C variant. The Y397L mutation abrogates the aromatic pathway, however, and confers lethality in yeast. Yeast experiments performed by Prof. K. L. Friedman.

Haploid strains expressing the pri2Y395F and pri2Y397F alleles were viable at 30 °C and grew comparably to the parental PRI2 strain. The Tyr → Phe mutants retain some redox-switching activity in the electrochemical scans, and the viability of cells is consistent with a partially but not completely inhibited redox pathway in these variants. Phenylalanine has an aromatic side chain, and although the ionization energy of this residue is higher than that of tyrosine [188], phenylalanine is still found disproportionately in oxidoreductase enzymes, suggesting that it can aid in redox pathways through protein [184].

We next investigated the effects of the pri2Y395L and pri2Y397L mutations on yeast viability. As aliphatic leucine more strongly abrogates the redox pathway through p58C (Table 5.4), we expected to observe more severe phenotypes with Tyr → Leu mutations in PRI2 than with Tyr → Phe mutations. We constructed a haploid pri2Y395L strain and observed, as with the Tyr → Phe variants, no growth defect relative to WT PRI2 strains. In contrast, we were unable to construct a haploid strain containing the pri2Y397L allele. To confirm lethality of pri2Y397L, we transformed the WT haploid strain with a URA3-marked PRI2 complementing plasmid and subsequently integrated either WT or mutant PRI2 alleles at the endogenous locus. Complemented strains expressing WT PRI2, pri2Y397F, or pri2Y397L grew well on media lacking uracil, as expected. However, when plated on media containing 5-fluoroorotic acid (5-FOA), only the pri2Y397L strain failed to generate colonies (Figure 5.7). Since the protein product of the URA3 gene converts 5-FOA to toxic 5-fluorouracil, this result confirms that cells expressing the lethal pri2Y397L allele cannot tolerate loss of the URA3-marked PRI2 complementing plasmid. Phenotypes of the pri2Y395L and pri2Y397L mutants were confirmed by tetrad analysis (Figure 5.8).

While the pri2Y397L mutation has no discernible effect on the protein structure *in vitro* (Figure 5.4), we wanted to confirm that the mutant is expressed and associates with the primase complex in yeast. If so, we would predict that the Y397L mutation in PRI2 impairs yeast growth when overexpressed in an otherwise WT background, competing with the normal protein for

incorporation into the primase complex. Conditional overexpression of the Y397L variant, but not of WT PRI2, causes severe growth defects (Figure 5.8). The Y397L mutation thus generates a p58 protein that can associate with primase, but is severely impaired *in vivo*.

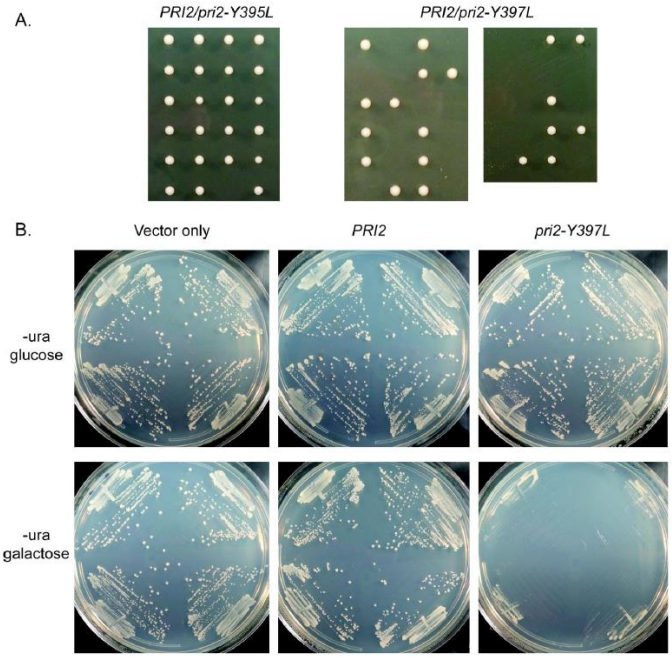

Figure 5.8: The non-viable *pri2-Y397L* allele causes synthetic lethality when over-expressed. A) Mutation of Tyr397 (but not Tyr395) to leucine results in lethality. *Pri2* mutations were generated by two-step integration (Materials and Methods) in diploid strain DKF206 (*MATa/MATα trp1/trp1 leu2/leu2 ura3/ura3 his7/his7*). DKF206 is isogenic with YKF201 (23). Diploid strains heterozygous for *pri2-Y395L* or *pri2-Y397L* were verified by sequencing, sporulated, and tetrads were dissected by standard methods. All surviving segregants of the *pri2-Y397L* strain were confirmed to carry the wild-type *PRI2* allele. B) Overexpression of *pri2-Y397L* inhibits cell growth. Empty vector (p416-Gal1) or p416-Gal1 containing wild-type *PRI2* or the *pri2-Y397L* allele were transformed into yeast and individual transformants were plated on media lacking uracil and containing glucose (top row, no induction) or galactose (bottom row, induction). Tetrad analysis and overexpression performed by Prof. K. L. Friedman and Dr. Esther Epum.

The severe phenotype in the pri2Y397L strain is consistent with the effect of the Y397L mutation on p58C redox signaling activity (Table 5.3). This mutant displays minimal redox switching on DNA, and the signal in the presence of DNA and NTPs suggests that redox signaling leads to oxidative degradation of the cluster in p58C Y397L. Small-molecule reactive oxygen species such as hydrogen peroxide can damage the [4Fe4S] cluster directly, causing degradation to the $[3Fe4S]^{+}$ form [139], or indirectly through DNA charge transport. We have observed, for example, that guanine radicals in oxidized duplex DNA induce redox switching in

a bound [4Fe4S] Endonuclease III protein [199]. WT p58C can more easily cycle between the $[4Fe4S]^{2+}$ and $[4Fe4S]^{3+}$ states than the tyrosine mutants when bound to both DNA and NTPs, mimicking the active primase. Y395F and Y395L variants appear to lose redox-switching activity, but are not oxidatively degrading on the DNA electrode. The Y397F and Y397L mutants, conversely, appear to be oxidized from the $[4Fe4S]^{2+}$ state to the $[4Fe4S]^{3+}$ state, but they are not easily reduced back to the $[4Fe4S]^{2+}$ state, causing the reductive peak likely associated with the irreversible $[3Fe4S]^{+/0}$ couple on DNA[180] to appear. We observe therefore that the combination of greater redox attenuation overall in Tyr → Leu variants, and the oxidative degradation observed in Y397F/L variants, dysregulate primase activity to a point for which cellular machinery cannot compensate.

Discussion

Reversible, redox-driven switches control DNA binding affinity in [4Fe4S] repair and replication enzymes, facilitating rapid binding and dissociation [63, 76, 98]. The oxidized $[4Fe4S]^{3+}$ bacterial glycosylase Endonuclease III, for example, binds the DNA polyanion 550-fold more tightly than the reduced $[4Fe4S]^{2+}$ Endonuclease III. Reversible cluster oxidation and reduction facilitates DNA-mediated redox signaling between Endonuclease III and other [4Fe4S] repair proteins in the first steps of locating oxidative DNA damage [63]. The [4Fe4S] enzyme yeast DNA polymerase δ is DNA-bound and active in the $[4Fe4S]^{2+}$ state, when associated with proliferating cell nuclear antigen (PCNA) [200]. When oxidized to the $[4Fe4S]^{3+}$ state, however, PCNA-associated polymerase δ binds DNA even more tightly, stalling replication [98]. This change in binding may allow polymerase δ to sense and respond to oxidative stress. Similar redox switching chemistry thus regulates diverse, specialized DNA-processing [4Fe4S] enzymes.

Here we establish a redox switch, driven by a change in [4Fe4S] cluster oxidation state, that regulates DNA binding and redox signaling in eukaryotic DNA primase. This switch regulates primer synthesis, but not catalytic activity, in human primase [76]. Structural and

biochemical evidence suggests that primase adopts a compact configuration during activity, with both the p48 (RNA polymerase) subunit and the p58C [4Fe4S] domain contacting the ~8–14-nt RNA/DNA duplex substrate [38, 84, 181]. Redox pathways comprising conserved tyrosines spaced 10–15 Å apart, shuttle charge approximately ~25–30 Å from the DNA binding interface to the [4Fe4S] cluster. Aromatic tyrosines spaced ≤15 Å apart can facilitate microsecond electron transfer [144, 184] in protein, possibly through formation of hopping intermediates. Despite previous arguments that structural differences in yeast and human primase preclude a general redox role for these residues [153, 154], the electrochemical and biological data unequivocally demonstrate that the electron-transfer pathway is conserved. Electrochemical attenuation of the p58C redox signal on DNA and lethality in yeast due to a single-residue redox-pathway mutation suggest a more significant role than the contributions of these tyrosines to any network of p58C/substrate hydrogen bonds [38].

The primary redox pathway affecting the yeast p58C [4Fe4S] cluster redox switch likely involves Y395 and Y397. When these conserved residues are mutated, two possible events may occur. First, the mutant residue at position 395 or 397 may transfer charge through single-step tunneling, as opposed to electron hopping onto the tyrosine. Additionally, the mutation may route the electron through another primary hopping pathway, less efficient than the WT, within p58C. Multiple potential pathways through p58C, involving conserved residues Y431 and Y352 for example, are available to transfer charge between bound DNA and the cluster.

Our model for redox-driven primer handoff is compatible with the time scale of primer synthesis. Studies of calf thymus primase [82] suggest that primer synthesis is quite slow, with a first-order rate constant of 0.0027 s^{-1}. Picosecond DNA-mediated electron transfer [152], microsecond electron transfer through primase/polymerase-α protein matrix [184], and microsecond/millisecond conformational changes in the polymerase-α active site [26] would all occur securely within this time. The aerobically measured binding constants of eukaryotic DNA primase and polymerase α (~100 nM–1 μM) [72, 76, 89] interestingly correspond to the upper

limit of the estimated primase/polymerase-α concentration in the yeast nucleus, based on protein copy number [201] and yeast cell volume [175] estimates. Tighter protein-DNA binding than these numbers indicate, which redox switching provides a means to access, may be necessary to efficiently execute replication.

Redox signaling in eukaryotic DNA primase is mediated by an aromatic pathway in the primase [4Fe4S] domain. Mutation of a conserved aromatic tyrosine at position 395 attenuates redox switching activity driven by the primase [4Fe4S] cluster. Mutation of conserved tyrosine 397 attenuates redox switching and leads to oxidative degradation during redox signaling on DNA. The Y397L mutation abrogates the aromatic pathway and leads to cluster degradation during the redox switch, conferring lethality in yeast. Tyrosines 395 and 397 are not located near the primase catalytic site, yet a mutation at a position between the [4Fe4S] cluster and DNA-binding domain affects the regulatory redox switch and can prohibit cell growth. These observations support our proposal that the conserved redox chemistry of the [4Fe4S] cluster in DNA primase plays a central role in coordinating the initial steps of eukaryotic DNA priming.

CHAPTER 6

INTERROGATING THE CHARGE TRANSPORT PATHWAY IN YEAST P58C

Introduction

Accurate, efficient DNA replication is essential for all organisms and relies on the concerted function of several key enzymes. Replicative DNA polymerases, such as polymerases δ or ε, synthesize daughter strands in the 5' to 3' direction but require a pre-existing 3'-OH for addition of a nucleotide [156]. To satisfy this requirement, a DNA-dependent RNA polymerase, DNA primase, generates a 7-12 nucleotide RNA primer *de novo* [202]. DNA primase then hands off the RNA primer to DNA polymerase α (pol α) to extend the RNA primer by approximately 20 nucleotides before hand-off to the more processive polymerases, δ or ε [203, 204]. In eukaryotes, DNA primase forms a heterotetramer with DNA polymerase α termed pol-prim [202]. Although absolutely required for successful priming of the template DNA, the mechanism of hand-off between DNA primase and DNA polymerase α is currently unknown.

Previous studies have attempted to provide insight into the mechanism of pol-prim hand-off, such as exploration of p58 N- and C-terminal domain linker length [34, 85] or proposed conformational flexibility [71] as potential primase counting mechanisms. However, these hypotheses have been disproven or lack functional validation. It is clear, however, that the ability to properly initiate and count is associated with the C-terminal domain of p58 regulatory subunit (p58C) [24, 82].

The p58C domain has been identified as a [4Fe4S] cluster-containing protein in both human and *Saccharomyces cerevisiae* (yeast) [69, 70, 72, 73]. Previous research, detailed in this dissertation, implies that in human and yeast p58C, the redox state of the cluster governs DNA binding affinity of human and yeast p58C [76-78, 86].

The p58C DNA binding surface and [4Fe4S] cluster are approximately 25 Å apart, a distance too far for direct electron transfer from DNA or a neighboring protein to the p58C cluster [76, 142]. Instead, amino acid side chains such as tyrosine or tryptophan act as intermediate donors and acceptors to facilitate electron hopping of distances ranging between 10-15 Å through the protein to reduce or oxidize an Fe-S cluster [143, 144, 205]. Investigation of human p58C has revealed that mutation of any one of three conserved tyrosine residues Y309, Y345, or Y347, to a residue less efficient at electron transfer such as phenylalanine [144], is sufficient to disrupt charge transport between the DNA binding surface and the [4Fe4S] cluster, thus inhibiting redox switching (Figure 6.1, red residues) [38, 73, 76, 84, 181].Furthermore, in *in vitro* studies with human primase, regulation of primer initiation and termination can be disrupted by such mutations in human p58C [76, 78]. These previous studies have led to the hypothesis that pol-prim hand-off is mediated in part by 4Fe-4S cluster redox-dependent regulation of the DNA binding affinity of pol-prim subunits.

Interestingly, though the property of redox switching is conserved from human to yeast, yeast p58C is surprisingly divergent from human in sequence, with only ~40% identity, as determined by BLAST local alignment tool [206]. Furthermore, human Y309, an essential residue in mediating redox switching, is not conserved in yeast. In yeast, the homologous residue is a leucine and cannot participate in electron transfer. In a previous study of yeast p58C, two conserved tyrosine residues Y395, Y397, and one conserved tyrosine positioned nearby, Y431 were identified as a potential electron transfer pathway in p58C (Figure 6.1B, red residues). These observations suggest that the electron hopping path that mediates redox switching may differ from human to yeast.

Accordingly, mutation of a single tyrosine to phenylalanine within the predicted electron path of yeast p58C is insufficient to abrogate redox switching, reducing the charge transferred by ~3 fold [77] compared to the human ~10 fold [76]. Moreover, incorporation of single tyrosine to phenylalanine mutations along the predicted electron hopping pathway do not decrease cell

viability in yeast, even under various stressors. The one exception occurs in a yeast strain where PRI2 Y397 is mutated to leucine and confers lethality [77]. This protein mutant seems to be more susceptible to oxidative degradation *in vitro* [77], though if this truly confers lethality remains to be seen.

Using the available structures of yeast p58C, we discovered that there were several additional residues that could potentially mediate CT (shown for reference in Figure 6.1), suggesting that there could be significant residual CT through alternate electron hopping pathways. Moreover, it implies that mutation of multiple tyrosine residues in yeast 58C may be required to significantly disrupt charge transport sufficiently and prevent efficient redox switching of the [4Fe4S] cluster.

To address the possibility that multiple pathways may facilitate charge transport through yeast p58C, mutants were constructed with multiple tyrosine to phenylalanine mutations. There are six possible tyrosines and a tryptophan that may participate in electron transfer pathways between the substrate binding interface and the 4Fe-4S cluster (Figure 6.1B). These yeast

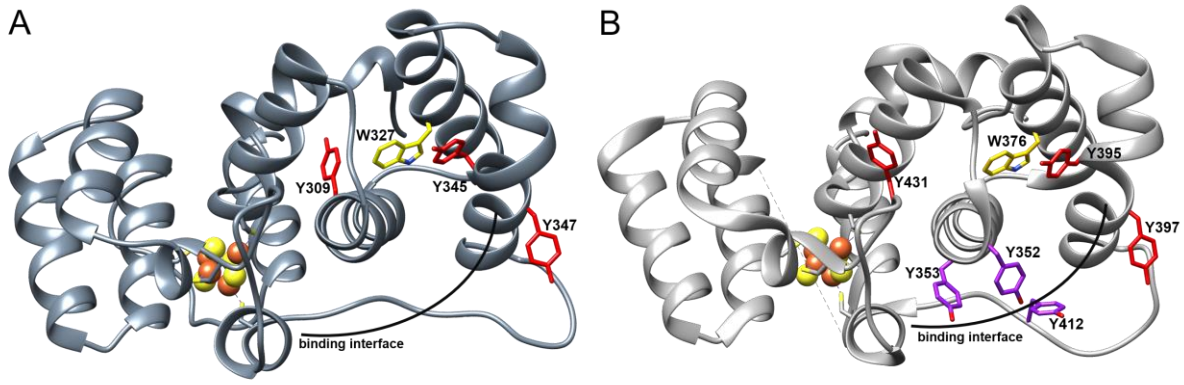

Figure 6.1: Comparison of conserved tyrosine residues in human and yeast p58C. *A*, Conserved tyrosine residues in the human p58C domain (PDB 5F0Q), highlighted in purple. Conserved tryptophan highlighted in yellow. Substrate binding interface is approximated by the curved black line. *B*, Conserved tyrosine residues in yeast p58C domain (PDB 6DI6), highlighted in red. Conserved tryptophan residue highlighted in yellow. Three additional tyrosine candidates that may participate in electron hopping pathways are highlighted in purple. Substrate binding interface is approximated by the curved black line.

p58C “multi-mutants” can be used to test if mutation of all possible electron hopping pathways suppresses electron transfer/redox switching to a larger extent than single site mutations. Furthermore, pending promising electrochemical results, these multi-mutants can be used in biochemical and cell-based assays to better understand the role of redox switching in primase.

Methods

Protein Expression and Purification.

Protein production was performed in collaboration with Dr. Alexandra Blee, Dr. Huiqing Chen, and Andy Dorfeuille. An expression vector pBG100 containing yeast p58C (Pri2) residues 316-512 and a N-terminal 6xHis tag inserted into the BamHI and NotI restriction sites as published in [207] was obtained from the Chazin laboratory. Rosetta DE3 cells were transformed with the plasmid and grown overnight at 37 °C in Terrific Broth. At OD_{600} 1.0, cells were induced with 1 mM isopropyl-β-D-thiogalactoside (IPTG) and cultured at 20 °C for 16 hours. Cells were pelleted and stored at -80 °C until use.

Wild-type (WT) or multi-tyrosine mutant p58C was purified as described [207]. Cell pellets were thawed and resuspended in 50 mM NaH_2PO_4 (pH 7.8), 500 mM NaCl, 10 mM imidazole (lysis buffer) with 2 mg/g pellet of lysozyme and Roche protease inhibitor tablets. The suspension was Dounce homogenized and sonicated on ice for 10 minutes. The solution was spun at 20,000 rpm for 25 minutes at 4 °C, and the supernatant was filtered and passed over a Ni-NTA column (GE Healthcare) pre-equilibrated with lysis buffer. The column was washed with 3 column volumes 50 mM NaH_2PO_4 (pH 7.8), 500 mM NaCl, 20 mM imidazole. The protein was eluted with 50 mM NaH_2PO_4 (pH 7.8), 500 mM NaCl, 250 mM imidazole and dialyzed overnight at 4 °C into 50 mM NaH_2PO_4 (pH 7.8), 500 mM NaCl, 10 mM imidazole. The 6xHis tag was cleaved using H3C protease. Dialyzed, cleaved protein was repassed over the Ni-NTA column as in the previous step, and flow-through and wash fractions were collected and dialyzed into Heparin Buffer A: 20 mM HEPES (pH 6.8), 50 mM NaCl, 2 mM dithiothreitol (DTT). Dialyzed

protein was filtered and passed over a 5 mL Hi-Trap HP heparin column (GE Healthcare) pre-equilibrated with Heparin Buffer A. Protein was typically eluted at ~25% Heparin Buffer B: 20 mM HEPES (pH 6.8), 1 M NaCl, 2 mM DTT, achieved using a linear gradient of 0 to 100% Buffer B over 40 column volumes. Fractions with eluted protein were dialyzed into 20 mM HEPES (pH 6.8), 200 mM NaCl, 2 mM DTT, flash frozen in liquid N_2, and stored at -80 °C until use.

Table 6.1: Site-Directed Mutagenesis Primer Pairs

Mutation	Forward	Reverse
Y352/353F	5'-CCATCATTTGAGGTTTTTTGGGAGACAACAAC	5'-GTTGTTGTCTCCCAAAAAACCTCAAATGATGG
Y395F	5'-GAGAAGTTCAATAAAGAATTCCGTTACAGCTTCAGGC	5'-CATTGTCATGTTCCCATTTCTTGTAAATGC
Y397F	5'-GAGAAGTTCAATAAAGAATACCGTTTCAGCTTCAGGC	5'-CATTGTCATGTTCCCATTTCTTGTAAATGC
Y412F	5'-AACAGAATCAACTTCAAACCATGGGAC	5'-ACCTTCAAGACCGTAATTATGC
Y431F	5'-TGGGCGCGGAGATTTTCATGGATGC	5'-GGTCTGGGCTTGGAAAGGATAGTGTG

Mutant Selection and Design.

Mutations in the yeast p58C domain were designed based on previous study of human and yeast p58C [76, 78, 86, 207], sequence conservation analysis using Clustal Omega [208], and analysis of tyrosine residues between the DNA binding surface and [4Fe4s] cluster in the 1.39 Å resolution structure of yeast p58C [207] using Chimera software [130].

Site-Directed Mutagenesis*.*

Mutagenesis was performed in collaboration with Dr. Alexandra Blee, Dr. Huiqing Chen, and Andy Dorfeuille. Site-directed mutagenesis for multi-tyrosine mutants was performed using a Q5 mutagenesis kit (New England Biolabs), using the primers listed in Table 6.1 with annealing temperatures of 58-60 °C.

Circular Dichroism Spectroscopy.

CD spectra were collected in collaboration with Dr. Alexandra Blee, Dr. Huiqing Chen, and Andy Dorfeuille. Prior to analysis, WT or mutant p58C protein samples were stored in 20 mM HEPES (pH 6.8), 200 mM NaCl, 2 mM DTT at -80 °C. Protein was thawed and transferred

to 10 mM KH_2PO_4 (pH 7.2) using Amicon ultra centrifugal filters. Circular dichroism spectroscopy was performed as described [163]. Briefly, dialyzed and filtered p58C was diluted to 0.5-1 mg/mL. The far-UV spectrum was measured from 260 – 190 nm in increments of 0.5 nm at a rate of 50 nm/min with a response time of 2 s and a bandwidth of 1 nm, using a Jasco J-810 Spectropolarimeter and quartz cuvette. A buffer blank was collected prior to the protein spectra. Three spectra were averaged and smoothed for each protein.

Preliminary thermal denaturation circular dichroism spectroscopy was performed as previously described [105, 163]. Briefly, the protein was dialyzed into 10 mM KH_2PO_4 (pH 7.2) using Amicon ultra centrifugal filters. The circular dichroism was monitored at every half degree at 222 nm as the temperature was increased from 20° to 80° C over 90 minutes. The apparent T_M was determined by taking the first derivative of the resulting curve.

Fluorescence Polarization Anisotropy.

Fluorescence polarization anisotropy assays were performed by Dr. Alexandra Blee. Optimization was attempted by Kateryna Nabukhotna, with guidance from L.E. Salay and Dr. Alexandra Blee. Prior to analysis, WT or mutant p58C protein samples were stored in 20 mM HEPES (pH 6.8), 200 mM NaCl, 2 mM DTT at -80 °C. Protein was thawed and transferred to 20 mM HEPES (pH 6.8), 75 mM NaCl, 2 mM DTT using Amicon ultra centrifugal filters. Fluorescence polarization anisotropy was performed as described [76]. Briefly, the 6-carboxyfluorescein labeled DNA substrate was annealed by adding both substrates (below) together in equimolar amounts and heating at 95 °C for 10 minutes. After annealing and cooling, an increasing concentration of protein was added to a solution containing 50 nm DNA substrate, and loaded onto a black 384-well plate. Polarized fluorescence intensities were measured using excitation and emission wavelengths of 485 nm and 520 nm using a Synergy H1 Hybrid Reader. 5’-[6FAM]-TCTCTCTCTCAAA-3’and 5’-TTTGAGAG-3’

Data represents the average of three replicates normalized to anisotropy at 0 µM protein. Final apparent K_d values were calculated using the one-site total binding equation in GraphPad Prism 8 and represent the mean ± one standard deviation.

X-Ray Crystallography.

Crystallization was performed in collaboration with Dr. Alexandra Blee, Dr. Huiqing Chen, and Andy Dorfeuille. Prior to crystallization, mutant p58C protein samples were stored in 20 mM HEPES (pH 6.8), 200 mM NaCl, 2 mM DTT at -80 °C. Protein was thawed and transferred to 20 mM HEPES (pH 6.8), 75 mM NaCl, 2 mM DTT using Amicon ultra centrifugal filters. Crystals of multi-tyrosine mutant p58C were grown by hanging drop vapor diffusion at 18 °C from a drop composed of equal volumes of p58C mutant (~5.5 mg/mL) and reservoir solution containing 100 mM TRIS (pH 8.5), 55-70% MPD. Crystals formed after 2 days, and were then looped and transferred to a cryo-protectant containing reservoir solution and 20% glycerol. Looped crystals were flash frozen in liquid N_2. X-ray data were collected at Sector 21 (Life Sciences Collaborative Access Team) of the Advanced Photon Source at Argonne National Laboratory. All data were indexed and scaled using HKL2000 [132]. Phasing of the diffraction data was done by molecular replacement using Phaser [209] and yeast p58C Y397F from [207] as the search model. The models were refined iteratively using Phenix [116] and *Coot* [114]. Backbone RMSD compared to WT was calculated for each mutant using *Coot* LSQ Superpose for backbone atoms. Access to these programs was provided by SBGrid [166].

Table 6.2: Crystallographic data collection and refinement statistics

	5YF412	**5YF431**	**6YF**
Data collection			
Wavelength	0.97872	0.97857	0.97857
Space group	P 21 21 21	P 21 21 21	P 21 21 21
Resolution range	26.02 – 1.53	30.36 – 2.07	29.61 – 1.80
	(1.58 – 1.53)	(2.12 – 2.05)	1.86 – 1.80
Cell dimensions			
a, b, c (Å)	40.62, 51.87, 89.48	41.04, 51.10, 90.22	39.52, 51.49, 90.03
α, β, γ (°)	90, 90, 90	90, 90, 90	90, 90, 90
Reflections			
Total	29195 (13278)	11684 (2866)	16950 (7180)
Unique	3387	1751	2173
Completeness (%)	99.56 (99.2)	96.22 (89.3)	96.72 (94.7)
R_{merge}	0.04	0.15	0.09
R_{meas}	0.043 (0.392)	0.166 (0.549)	0.095 (0.381)
R_{pim}	0.018 (0.169)	0.078 (0.272)	0.041 (0.172)
$CC_{1/2}$	0.997 (0.945)	0.969 (0.887)	0.982 (0.965)
CC*	0.999 (0.986)	0.992 (0.970)	0.995 (0.991)
Multiplicity	3.1 (2.7)	2.7 (2.0)	2.9 (2.4)
Mean $I/\sigma(I)$	39.03 (4.29)	8.59 (2.69)	12.02 (4.49)
Refinement			
No. of non-H atoms	1686	1546	1535
Macromolecules	1555	1503	1482
Ligands	8	8	8
Solvent	123	35	45
R_{work}/R_{free}	0.1516/0.1680	0.2356/0.2767	0.1962/0.2140
	(0.1810/0.2011)	(0.2919/0.3792)	(0.2332/0.2508)
RMSD (bonds, Å)	0.014	0.0034	0.016
RMSD (angles, °)	1.207	0.494	1.253
Ramachandran			
Favored (%)	97.78	98.89	96.67
Allowed (%)	2.22	1.11	3.33
Outliers (%)	0	0	0
Rotamer outliers (%)	1.18	1.9	0
Clashscore	1.89	4.7	3.09
Wilson B-factor ($Å^2$)	17.06	30.63	22.63
Average B-factor (Å)	26.99	42.77	40.53
Macromolecules	26.25	42.68	40.62
Ligands	37.33	49.48	32.69
Solvent	35.06	41.9	40.24
RMSD vs WT (6DI6)	0.42	0.24	0.47

Results

Structure-based design of charge transport-deficient yeast p58C mutations.

Structural analysis of yeast p58C revealed 6 tyrosine and 1 tryptophan residue bridging the DNA binding surface and [4Fe4S] cluster of yeast p58C. Four tyrosines (Y395, Y397, Y412, and Y431) and the tryptophan (Figure 6.1) are conserved between the two proteins. Two additional tyrosines, Y352 and Y353 are positioned close to the 4Fe-4S cluster and the DNA binding site and could be involved in 4Fe-4S to DNA electron transfer [210, 211]. All seven of these residues of interest are within feasible distances (10 – 15 Å) to contribute to a network of possible electron transfer chains within the protein, as measured by the distances between centroids of the residues in PDB 6DI6 (Table 6.3). These additional residues not may contribute to redundant electron transfer pathways through the protein.

In order to investigate the roles of these residues in electron transport, multiple site mutations in yeast p58C were prepared with the goal of completely suppressing the conduit through the protein between the 4Fe-4S cluster and the DNA binding site. Three multiple tyrosine mutants were generated: Y352F/Y353F/Y395F/ Y397F/Y412F/Y431F (6YF),

Table 6.3: Distances between residues of interest

Residue pair	Distance (Å)
Fe-S to Y431	14.1
Fe-S to Y353	14.2
Y353 to Y352	5.8
Y352 to W376	12.1
Y352 to Y412	9.4
Y431 to W376	13.0
Y431 to Y395	15.1
W376 to Y395	9.3
Y395 to Y397	11.6
Y352 to Y412	9.4
W376 to Y397	14.6

Y352F/Y353F/Y395F/Y397F/Y412F (5YF412), and Y352F/Y353F/Y395F/Y397F/Y431F (5FY431). The two yeast p58C mutants that contained five mutations, leaving out Y431 or Y412, were designed because of their apparent strategic role in setting up two divergent electron hopping pathways away from the 4Fe-4S cluster (Figure 6.1B, red vs purple residues). We surmised that selectively altering one pathway versus the other might give insight into the relative efficiency of the two apparent charge transfer pathways. This information in turn could be useful for cell-based assays to probe the ability to tune redox switching in p58C.

W376 likely plays a role in maintaining structural stability.

Given the evidence that W376 is conserved and that it is a residue able to mediate charge transport, one may ask why this residue was not included in the multi-site mutant designs.

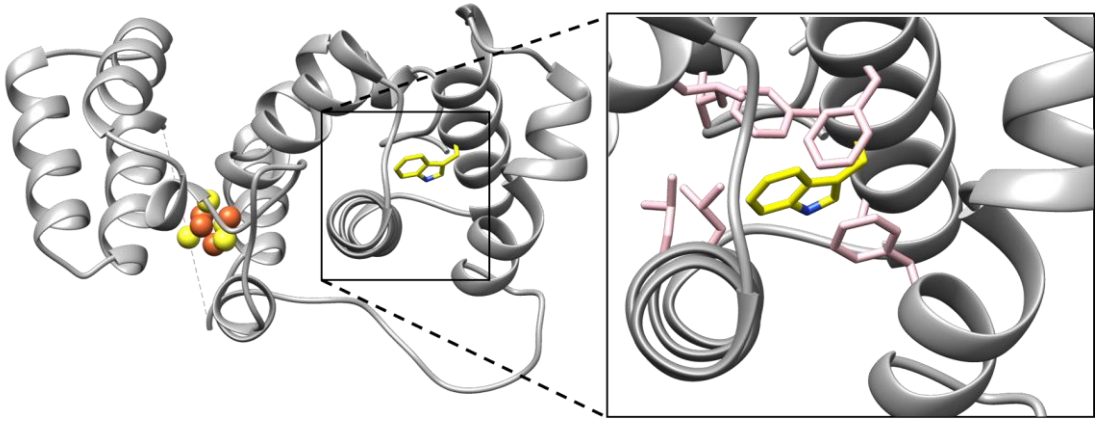

Figure 6.2: Hydrophobic residues surrounding W376. Crystal structure of yeast p58C (grey, 6DI6). W376 is depicted in yellow. Note that it extends into the space between several alpha-helices. Inset: Hydrophobic residues (light pink) surround W376.

We were able to produce the single-site W376F mutant, but when this mutation was included in along with additional Tyr mutations, the resultant protein was unstable, precluding further analysis. Interestingly, preliminary thermal denaturation curves show that the apparent T_M of the single W376F p58C mutant is 54°C, a full 13° lower than the wildtype protein (T_M = 67 °C), whereas the value for other multiple-site Tyr mutants have apparent T_M values of 63 ± 1°C. The disparity in thermal stability is likely due to the large number of hydrophobic contacts with the

conserved tryptophan in the hydrophobic core. Thus, W367 seems to play a critical role in maintaining the structural integrity of the protein (Figure 6.2).

Multi-Tyr mutants do not alter the structure or biophysical properties of yeast p58C.

While the Tyr residues are more peripheral to the hydrophobic core of yeast p58C and the substitution is more conservative than Trp to Phe, the combination of so many mutations risks causing significant perturbations of the protein. Importantly, in order for accurate electrochemical characterization, the mutant proteins must bind nucleic acid substrates similarly to the wild-type protein. Furthermore, structural destabilization may lead to spurious results in electrochemistry by altering distances between residues key to the electron hopping pathway. Structural perturbations might also complicate biochemical or cellular properties. In order to address these concerns, each mutant was subjected three assays and the results compared to each other and the wild type protein. CD spectroscopy was used to assess the distribution of secondary structural elements in solution and X-ray crystal structures were determined to determine if the tertiary structure was altered. Fluorescence anisotropy assays were then performed to determine if the affinity for DNA was perturbed.

The CD spectra of the three multi-tyrosine mutants revealed they all have similar global secondary structure distribution relative to the wild-type (WT) protein, with a high population of helical secondary structure elements (Figure 6.3A). The variants were then crystallized under the same conditions as the WT protein [77], and x-ray crystal structures were determined at 1.53 Å, 2.05 Å, and 1.80 Å for 5YF412, 5YF431, and 6YF, respectively (Table 6.2). These structures show that multiple tyrosine to phenylalanine mutations do not significantly alter the structure of p58C, as reflected for example in the very small backbone root-mean-square deviations (RMSD) compared to WT of 0.42 Å, 0.24 Å, and 0.47 Å for 5YF412, 5YF431, and

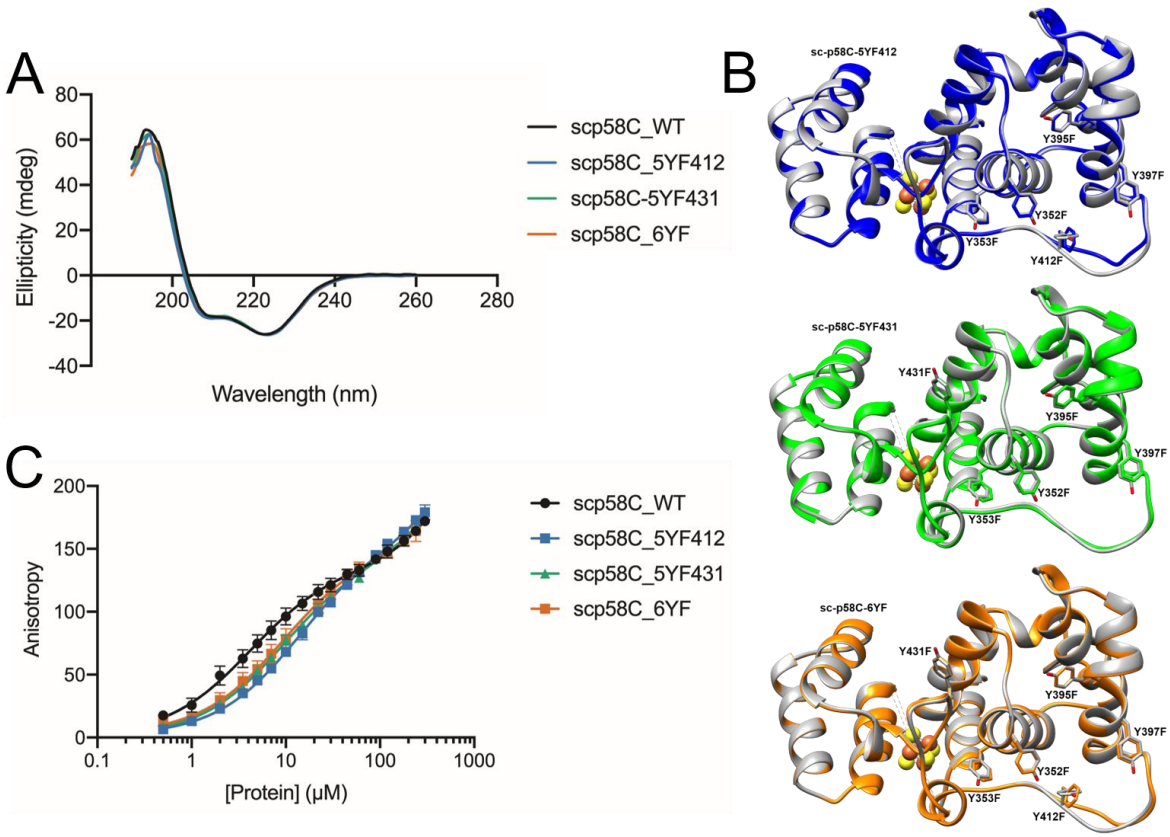

Figure 6.3: Multiple tyrosine to phenylalanine mutations do not significantly disrupt yeast p58C structure or DNA binding. *A*, Circular dichroism spectroscopy of yeast p58C wild-type (WT) and tyrosine to phenylalanine mutants (5YF412, 5YF431, and 6YF) measured at 20 °C). Each curve represents the average of three smoothed measurements. Ellipticity for buffer and cuvette alone were subtracted from each data point. Data were scaled to the WT spectrum. *B*, X-ray crystal structures of yeast 5YF412, 5YF431, and 6YF multi-tyrosine to phenylalanine p58C mutants (color) overlaid with WT p58C (grey, PDB ID code 6DI6). Mutated residue side chains shown. Structure for yeast 5YF412 determined at 1.53 Å, yeast 5YF431 at 2.05 Å, and yeast 6YF at 1.80 Å. Detailed data collection and refinement statistics in Table 6.3 *C*, Fluorescence polarization anisotropy (FA) of yeast p58C WT and tyrosine to phenylalanine mutants 5YF412, 5YF431, and 6YF, measured at room temperature (19-21 °C). An 8 base pair duplex fluorescent substrate that contains a single-stranded/double-stranded DNA junction was used. CD spectroscopy, fluorescence anisotropy, and crystallography performed by Dr. A.M. Blee with assistance from Dr. H. Chen, A.J. Dorfeuille, and L. E. Salay.

6YF, respectively (Figure 6.3B, Table 6.3). Interestingly, both mutants that contain the mutation Y412F vary subtly in in the loop region near residue 412 (Figure 6.3B). Inspection of the crystal structure reveals that a hydrogen bond is lost between H401 and Y412, which presumably correlates with the subtle perturbation with respect to the wild-type structure (Figure 6.4). It is possible that the effect on the structure in the crystal is suppressed and may be significantly

larger in solution, as the subsequent turn and alpha helix is stabilized by crystal packing interactions.

Fluoresce polarization anisotropy assays were carried out using a standard FITC labelled substrate as described in [76, 77, 163]. Each mutant binds slightly less well than the wild-type protein. The apparent K_D of each 4.0 ± 0.6 µM, 13 ± 1.3 µM, 8.9 ± 0.76 µM, and 8.9 ± 1.6 µM for wild-type, 5FY412, 5YF431, and 6YF, respectively. Although the DNA binding affinity of each multi-tyrosine mutant was slightly decreased compared to wild-type in aerobic conditions with a reduced 4Fe-4S cluster, (Figure 6.3C), the proteins still bind DNA in the same, low micromolar regime and thus can be used for further characterization.

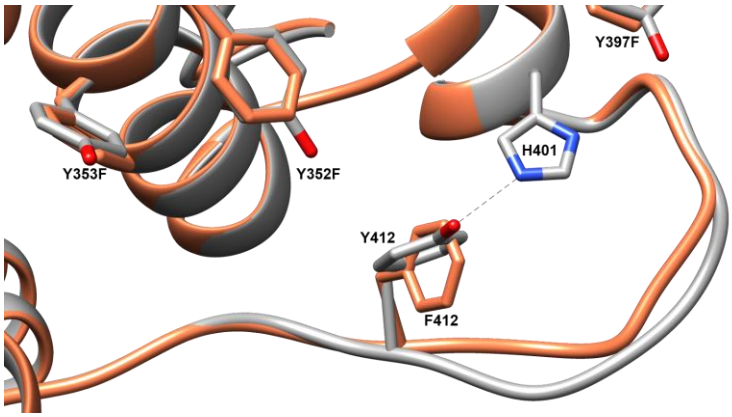

Figure 6.4: Comparison of the yeast p58C WT structure (grey, 6DI6) and the 6YF structure (orange). The hydrogen bond between H410 and Y412 in the WT structure is depicted by a dotted line.

While the data are satisfactory for preliminary analysis and the assays demonstrate that the proteins interact with the fluorescent DNA probe similarly, it is worth noting that the plot of anisotropy versus the log[protein] in Figure 6.3C suggests a complex binding phenomenon. In an ideal binding assay, the protein of interest would interact with a fixed amount of fluorescent probe in a single, specific way. This would result in an S-shaped curve with a distinct inflection point and a plateau when viewed on a plot of anisotropy versus log[protein]. A plateau denotes that the binding reaction is saturated, i.e. that all fluorescent probe molecules are bound. Instead, the curves in Figure 6.3C do not saturate and are multimodal, suggesting that multiple

equilibria are being measured, i.e. that the protein of interest interacts with the fluorescent probe in multiple ways, each with a different dissociation constant. In the assay detailed above, there seem to be at least two binding interactions—one in the low micromolar range, presumably the protein and its preferred DNA junction substrate [73], and a second in the hundreds of micromolar range. The second interaction, presumably a non-specific binding event between the protein and the fluorescent probe, is not saturated by the end of the assay. This complicates calculation of the true dissociation constant.

To address this, various modifications have been attempted, including using higher concentrations of protein to improve saturation and different substrates to promote a specific binding mode. Higher concentrations of protein simply exacerbates the problem and causes significant quenching of the fluorophore. We then sought to improve the substrate by providing a highly stable GC-rich duplex with a highly favorable p58C binding site, according to the literature[85, 86]. However, none of these variations offered any improvement, indicating that the common feature, the fluorophore, is likely the problem. Optimization is ongoing with a different fluorophore to generate quantitative data from which an accurate K_D can be measured.

Discussion

4Fe-4S cluster redox is important in human primase. Yeast p58C can also engage in redox switching, though to a lesser extent than the human protein. Inspection of the structure of yeast p58C reveals that multiple electron hopping pathways may exist. It is possible that these redundant electron hopping pathways between the 4Fe-4S cluster contribute to redox switching in yeast p58C. To test this, yeast p58C with mutations of multiple residues to more fully abrogate charge transfer between the protein surface and the 4Fe-4S cluster were generated.

These mutants are remarkably stable, similar to wild-type protein structurally and in their ability to bind DNA, given that ≥5 mutations were incorporated. Though at least five hydroxyl groups were removed, only three hydrogen bonds were lost upon mutation (Figure 6.5). Furthermore, only one tyrosine, Y353, makes a crystal contact with an adjacent molecule; this

interaction is hydrophobic in nature and the hydroxyl group on the tyrosine does not interact with either the backbone or sidechains. The remaining Tyr residues of interest are peripheral to the hydrophobic core of the protein, near the protein surface and the approximate DNA binding site (Figure 6.1B). These Tyr may aid in stabilizing aromatic nucleobases during substrate binding.

Characterization of the protein via electrochemical assays is ongoing. These mutants are expected to have significantly lower efficiency of charge transfer compared to the wild-type protein, causing a defect in redox switching. If the electrochemistry assays confirm that mutating multiple residues is an efficient way to more completely knockdown charge transfer in yeast p58C, these mutations can be incorporated into yeast pol-prim for biochemical assays.

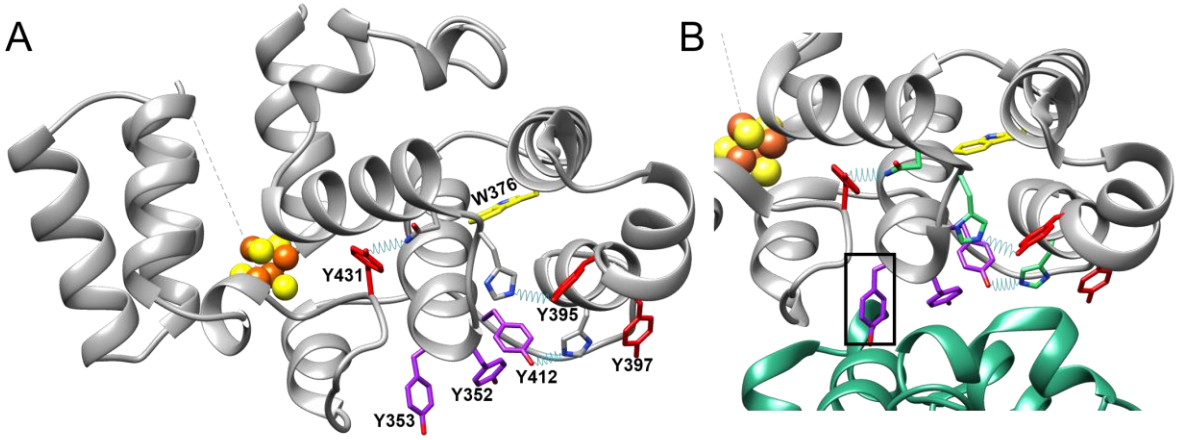

Figure 6.5: Hydrogen bonds and crystal contacts in yeast p58C WT (6DI6). A: Three of the six tyrosine residues (Y395, Y412, Y431) form intramolecular hydrogen bonds (blue springs). B: Tyr 353 (boxed) forms a crystal contact with the adjacent molecule (teal).

Interestingly, preliminary priming initiation assays performed by Dr. Elizabeth O'Brien with yeast primase containing single tyrosine mutations exhibit altered biochemical activity (Figure 6.6). In this assay, single Tyr primase mutants were incubated with single-stranded DNA and radiolabeled nucleotides. The product abundance and length were measured over time. The single Tyr to Leu mutant primase has decreased overall activity. The single Tyr to Phe mutant primase has an intermediate amount of activity. The extent of altered activity correlates with the efficiency of redox switching in the yeast p58C single mutants described in [77].

An alternative explanation of the biochemical results could be that primase is not efficient *in vitro*, generating a significant number of abortive products [24, 82]. Based on structural and biochemical data from collaborators in the Chazin lab, it is hypothesized that remodeling of primase subunits into a productive configuration during primer initiation is transient, requiring a large network of weak interactions. It is possible that minor mutations disrupt this network of interactions that facilitate primer initiation. Such an effect would be masked in DNA binding assays as the substrate binding and productive conformations are two putatively different binding modes. Thus, disruption of this network could have a large effect on priming activity *in vitro*. Kinetic experiments, such as those described in [39] could aid in understanding the extent by which the mutations affect priming independent of the ability to engage in redox switching.

Furthermore, if the putative defect in redox switching is associated with a defect in primase activity, similar to the human protein, then the activity of redox switch deficient primase can be examined in replisome reconstitution studies. Such a study would be useful to assess if polymerase activity or dynamics are different, compared to assays with the redox switch proficient primase[33, 96]. This information could guide further yeast phenotypic analysis and provide insight into the functional relevance of redox-switching in priming activity.

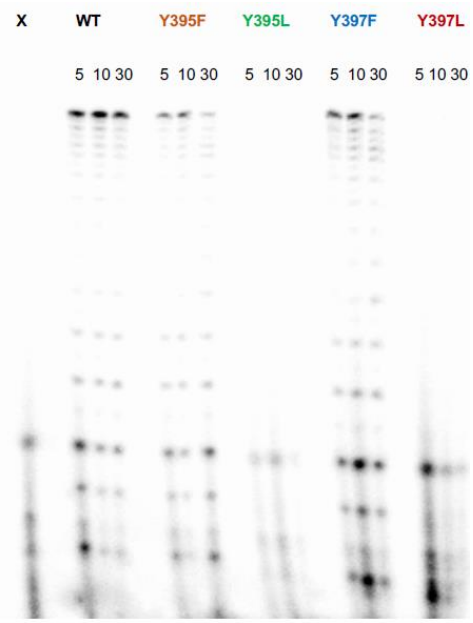

Figure 6.6: Priming initiation assay performed by Dr. E. O'Brien as described in O'Brien E, Holt ME, Thompson MK, Salay LE, Ehlinger AC, Chazin WJ, Barton JK. The [4Fe4S] Cluster of Human DNA Primase Functions as a Redox Switch using DNA Charge Transport. Science, 2017. 335 (6327) with full-length wild-type primase and primase with a single tyrosine mutation.

It would be worthwhile to compare the putative phenotype of the yeast and the biochemical activity of the mutated yeast primase complex. A correlation between the two would support a larger role of primase redox switching at the replication fork and/or a functional role for redox switching in governing primase activity

Absence of a correlation, however, may indicate deficiency in the approach or that the biochemical effects observed *in vitro* are artifacts of the system. It is possible that the only role of the 4Fe-4S cluster in primase is related to cellular redox sensing or redox homeostasis. In this case, no biochemical effect would be readily evident but a phenotype may be more obvious. Furthermore, slight deficiencies in priming activity could be compensated for in a cellular context by additional factors that interact with primase at the replication fork, obscuring a potential phenotype.

The observation of a significant decrease in the ability of the multi-mutant protein to engage in redox switching would also support the hypothesis that there are multiple, redundant

electron transfer pathways through the protein. In a recent computational study [211], performed on human p58C, the effect of mutations in the proposed charge transfer pathway was examined. The results suggest that are multiple pathways in human p58C and that mutations in one of these pathways promotes the use of an alternative “route” through the protein [211]. Characterization of alternate electron pathways through the protein may reveal differences in efficiency of each pathway. Furthermore, this implies that the ability of the 4Fe-4S cluster to engage in redox switching may be able to be tuned by selectively mutating the residues of interest to residues that are more or less efficient at electron transfer than the native residue. If the ability to engage in redox switching does effect primer initiation and termination, it may then be possible to regulate primase activity in such a way. This could be a useful tool to investigate specific questions in replisome reconstitution studies or in in-cell assays.

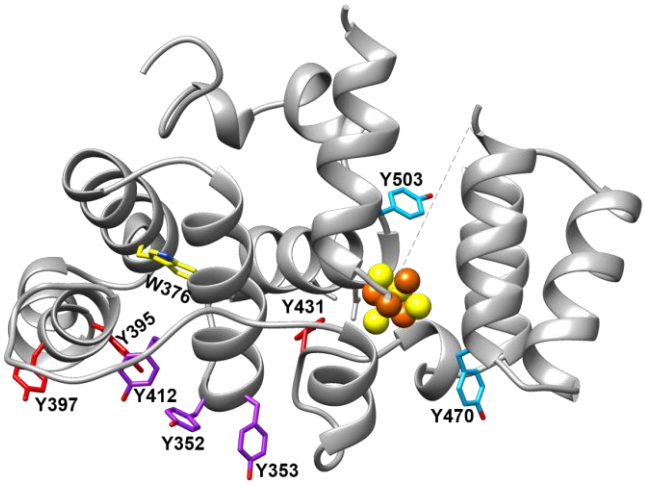

Figure 6.7: Tyr sidechains of interest in yeast p58C (6DI6). Residues characterized in this chapter are in red, purple, and yellow. Blue sidechains represent additional tyrosine residues that may mediate electron transfer directly to or away from the 4Fe-4S cluster.

Beyond the biological implications of the multiple electron transfer pathways in a replication protein, however, yeast p58C provides an opportunity to gain insight about intra-protein electron transfer. Specifically, computational studies can illuminate preferred electron hopping pathways and the role played by the mostly-insulating protein matrix in shuttling electrons from the 4Fe-4S cluster to the protein surface.

The above speculation relies on the observation that the yeast multi-mutants are deficient in charge transfer and redox switching. It is possible that the multi-mutants are not significantly more deficient in redox switching than the single mutants. In this case, the interrogated residues may not be a primary conduit from the 4Fe-4S cluster. In fact, there are two tyrosine residues that are much closer to the 4Fe-4S cluster than Y431 and Y353 (Figure 6.7). Y470 and Y503 are both within ~6 Å of the 4Fe-4S cluster and are peripheral to the hydrophobic core. These residues might mediate electron transfer in the opposite direction than the originally identified residues. The electrons would travel from the 4Fe-4S cluster to solvent. Furthermore, it is possible that the ability of the 4Fe-4S cluster to engage in redox switching is protective instead of functional; the electron transfer pathway might serve to allow electrons an escape to keep the 4Fe-4S cluster in a stable, reduced state. To investigate this, mutants of Y470 and Y503 should be investigated to assess if these residues contribute to the electron transfer pathway.

This study requires significant further investigation in order to clearly understand the possibilities and implications of charge transfer-mediated redox switches at the replication fork. Luckily these studies are underway and the field of DNA-protein redox chemistry is growing, positioning us in a favorable place for expanding our understanding of redox chemistry at the replication fork.

CHAPTER 7

THE SEARCH FOR THE SECOND IRON-SULFUR CLUSTER

Introduction

Generating complementary strands of DNA during replication begins with the synthesis of a primer. This primer is required for the replicative polymerases to carry out the bulk of DNA synthesis as proofreading polymerases (pols) can only elongate from an existing primer. Initial primer synthesis is carried out by the heterotetrameric complex of DNA primase and DNA polymerase α, pol-prim. Primase, a DNA-dependent RNA polymerase, initiates synthesis and builds the first seven to eleven ribonucleotides on the template. Primase then hands off the RNA-primed template intramolecularly to pol α. Pol α then extends this substrate and adds approximately twenty deoxyribonucleotides.

An open question in the field involves the mechanism behind the intramolecular handoff step from primase to pol α. This is in part because primase and pol α have been studied as two independent units; both primase and pol α can be generated separately and function independently *in vitro*. Studies with just primase or just pol α offered a simplified view the activity of the complex [23, 24, 34, 81, 85, 212]. These studies have been integral in defining the role of each subunit in generating the initial primer and in identifying unique aspects of pol-prim biochemistry but revealed nearly no information about the primer handoff step.

Notably, studies of primase and primase domains in isolation demonstrated a 4Fe-4S cluster exists as an integral part of human DNA primase [69, 70]. Subsequent studies, some detailed in this dissertation, revealed that the 4Fe-4S cluster is essential to primase function, that the redox state of the 4Fe-4S cluster can cycle between oxidized and reduced, and that the redox state of the 4Fe-4S cluster governs the substrate binding affinity of primase [74, 76-78]. This property of being able to cycle the redox state of the 4Fe-4S cluster is seemingly tied to the ability

of primase to appropriately initiate and terminate primers, an essential aspect of primer handoff. These studies imply that switching the redox state of the 4Fe-4S cluster may in part drive primer handoff.

This is an interesting insight, but not the full story. There is also evidence that the activity of primase is altered by pol α and vice versa [17, 25, 31, 82, 213]. Specifically, pol α acts as a molecular brake for primase by inhibiting synthesis after about seven to eleven nucleotides. This occurs even in the absence of pol α activity [31, 44, 89, 90]. Because pol α is an essential variable of the handoff equation, one wonders how does 4Fe-4S cluster redox in primase influence primer initiation and termination in the context of the pol-prim tetramer?

Adding to the complexity of this question, evidence for [4Fe-4S] clusters was found for the family B polymerases, including pol α [79]. As a constitutively bound partner to primase with a putative 4Fe-4S cluster, it is intriguing to speculate that pol α can possibly regulate of the redox state of the 4Fe-4S cluster in primase. In this model, the pol α 4Fe-4S cluster would exchange redox states with the primase oxidized 4Fe-4S cluster, reducing its affinity for its product, mediating primer counting and handoff. This implies that handoff between primase and pol α is chemically driven by redox switching.

However, the existence of the 4Fe-4S cluster is disputed. Evidence for the 4Fe-4S cluster in pol α was indirect and complicated by the presence of the 4Fe-4S cluster in primase[79]. The domain of pol α that purportedly binds a 4Fe-4S cluster, p180C, has two possible sites for its incorporation, CysA and CysB (Figure 7.1). In 2012, aerobic structural characterization of the domain of interest (p180C) revealed that both metal binding sites are filled with zinc ions [43, 121]. It was suggested that the evidence published by Netz et al [79] was a result of mis-incorporation of the cofactor [80]. This is contrary to the general wisdom of the field, which suggests that it is difficult to obtain a 4Fe-4S protein and that it is more common to mis-incorporate other metal ions (Zn^{2+} in particular) in recombinant systems [52-54, 214, 215].

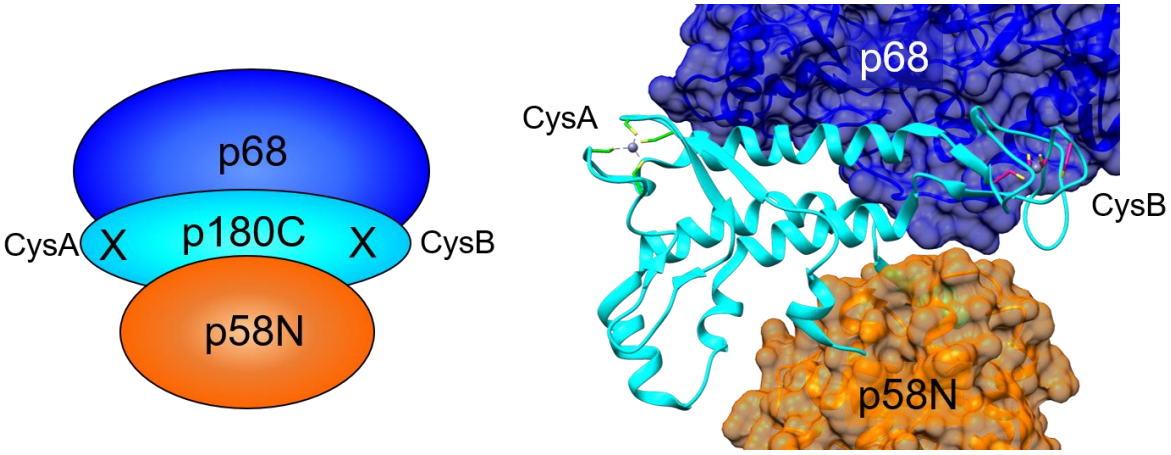

Figure 7.1: the p180C domain has two metal binding sites, CysA and CysB. Left: a cartoon representation of important domains and interactions near the two sites. Right: Crystal structure of pol-prim (5EXR), indicating the zinc-filled CysA and CysB sites, relative to the p68 and p58N subunits.

Thus, a controversy remains. The current evidence in the literature is insufficient to conclude that a [4Fe-4S] cluster is present in the native pol α protein. Additionally, all current pol-prim knowledge was obtained using protein that had zinc in both the CysA and CysB sites. However, as the existence of 4Fe-4S clusters have been confirmed in other family B pols δ [80, 216] and ε [97], the possibility of a 4Fe-4S cluster in pol α seems more likely. Resolving the controversy would further the understanding of pol-prim biochemistry and of 4Fe-4S clusters at the replication fork, so I set out to determine if pol α does indeed contain a 4Fe-4S cluster.

Methods

Endogenous pol-prim pull down

Endogenous pol-prim was isolated from yeast strains containing pol-prim alleles with C-terminal Tandem Affinity Purification tags (TAP) [217]. The TAP tag consisted of protein A – TEV cleavage site – calmodulin binding peptide, where the protein A motif interacts with IgG resin and the calmodulin binding peptide tag interacts with a calmodulin resin.

The yeast containing tagged pol-prim was grown in yeast-extract-peptone-dextrose (YPD) medium until an OD_{600} of 0.6. The cells were harvested by centrifugation and flash frozen in liquid nitrogen. The cells were lysed using a cryo-mill and resuspended in 10 mM sodium

phosphate pH 8.0, 1% NP-40, 150mM NaCl with Roche complete protease inhibitor tablets. Cell debris was separated from the soluble fraction by centrifugation prior to purification. The protein was then purified as described in [218]. The supernatant was filtered before application to an IgG resin (GE Healthcare). The supernatant and resin were incubated on a nutator at 4 °C for 2 hours. The supernatant and resin were spun down at 2000 x g for 6 min at 4 °C. The supernatant was removed and the resin was washed four times with 10 mM HEPES, pH 8.0, 150 mM NaCl, 1% NP-40. The resin was resuspended in 10 mM HEPES, pH 8.0, 150 mM NaCl, 1% NP-40, 1 mM DTT and 300 U of TEV protease. The resin was incubated at 4 °C overnight on a rotating shaker. The following morning, the resin was spun down and resuspended in 10 mM HEPES, 150 mM NaCl, 1 mM DTT, 1 mM $Mg(CH_3COO)_2$, 1 mM imidazole, 2 mM $CaCl_2$, 0.1% NP-40, and 2 mM DTT. The resin was transferred to a gravity column and the flow through was collected and 10 mM calcium chloride was added to the sample. The flow-through, containing the complex of interest, was then applied to calmodulin resin (GE Healthcare) and incubated on a rotating platform for 1 hour at 4°C. The resin was subsequently washed three times with 10 mM HEPES, pH 8.0, 150 mM NaCl, 1 mM $Mg(CH_3COO)_2$, 1 mM imidazole, 2 mM $CaCl_2$, 0.02% NP-40. The protein was then eluted with 5 ml of 10 mM HEPES pH 8.0, 150 mM NaCl, 0.02% NP-40, 1 mM $Mg(CH_3COO)_2$, 1 mM imidazole, 25 mM EGTA. The resulting eluate was then analyzed by SDS-PAGE, UV-Vis spectroscopy, and inductively coupled mass spectrometry (ICP-MS).

Expression and purification of p68dN-p180C

A duet plasmid containing His-p68dN-p180C was transformed into Rosetta PlySs cells. A single colony was picked and grown overnight in Luria Broth (LB) supplemented with ampicillin and chloramphenicol. The following morning a liter of Terrific Broth (TB), supplemented with ampicillin and chloramphenicol, was inoculated with the overnight culture. The TB culture was grown, with shaking, at 37° C until an OD_{600} of 1. The temperature was

subsequently lowered to 18° C and allowed to shake for approximately thirty minutes. Then, 0.5 mM phosphate buffered L-cysteine, pH 7.4, 50 µg/ml of ammonium iron citrate, 50 µg/ml of iron sulfate, and 0.2 mM IPTG were added to the culture. The culture was allowed to grow for about 8-12 hours with shaking before harvesting by centrifugation.

The cells were resuspended in 50 mM NaH_2PO_4 (pH 8.0), 500 mM NaCl, 10 mM imidazole, 10% glycerol, 1 mM TCEP. Cells were lysed by sonication, using a 5 s on 15 s off cycle at an amplitude of 50% for 10 minutes. Purification was performed using a three-step protocol: IMAC, ion exchange, and size exclusion chromatography as described in [43]. Briefly, the sample was passed over a Ni-NTA column before His-tag cleavage with TEV protease. The sample was diluted ten-fold and passed over a MonoQ ion exchange column. Finally, the sample was concentrated and passed over an S200 size exclusion chromatography column.

Expression and purification of the prim lobe

A co-lysis approach was undertaken to generate the biochemically active prim-lobe. Expression of primase was performed as in [163]. Expression of p68dN-p180C was performed as above. Two liters of primase was lysed for every three liters of p68dN-p180C. Cells were lysed by sonication, using a 5 s on, 15 s off cycle at an amplitude of 50% for 10 minutes. Purification was performed using a three-step protocol: IMAC, heparin affinity chromatography, and size exclusion chromatography as described in [43]. Briefly, the sample was passed over a Ni-NTA column before His-tag cleavage with H3C and TEV proteases. The sample was diluted ten-fold and passed over a heparin column. Finally, the sample was concentrated and passed over an S200 size exclusion chromatography column.

To adapt this protocol to be performed in an anaerobic environment, all buffers were deoxygenated by bubbling nitrogen through for 2 h / L of buffer. The buffer was then transferred to an anerobic environment and allowed to equilibrate with the atmosphere for 48 h before use[219]. The IMAC step was performed as in [163]. Following 6xHis tag cleavage, however, the protocols diverged. The sample is diluted to achieve a final salt concentration of ~150 mM

NaCl. This sample is loaded onto a pre-equilibrated 5 ml heparin column with a peristaltic pump and washed with 240 mM NaCl. Then, the sample is eluted with 385 mM NaCl in 5 mL fractions. Then, excess primase and other contaminants are eluted with 530 mM NaCl. The size exclusion chromatography step was omitted to prevent exposure to oxygen.

Biochemistry assays

Two types of biochemical assays were performed: initiation and elongation assays. For both assays, the buffer system was: 30 mM HEPES, pH 7.2, 10 mM NaCl, 10 mM $MgCl_2$, 1 mM $MnCl_2$, 1 mM TCEP. For initiation assays, 1 µM DNA template, 100 µM NTPs, and 0.5 µL γ-labelled ^{32}P-ATP were assembled in the reaction buffer on ice. For elongation assays, 1 µM RNA/DNA template, 100 µM NTPs, and 0.5 µL α-labelled ^{32}P-ATP were assembled on ice. The initiation assay reactions were transferred to 37 °C and elongation assay reactions were transferred to 20 °C. Both were allowed to incubate for 5 min prior to addition of 300 nM enzyme. Timepoints were taken according to experimental requirements and were quenched with 1:1 80%w/v formamide, 200 mM EDTA, 1 mg/ml bromophenol blue, 1 mg/ml xylene cyanol and incubated at 65 °C for 10 minutes. The timepoints were run on a 20% UREA-PAGE gel at 20 W for 8 hours. The gel was then exposed via storage phosphor and imaged using a Typhoon 9100 Imager.

Results and Discussion

Attempts to pull down endogenous pol-prim reveals the abundance is too low for this approach.

Most recombinant methods used to generate pol-prim require overexpression, which causes stress on the cell's protein and [4Fe-4S] cluster assembly machinery that can lead to incomplete incorporation of this co-factor. Moreover, purification is normally performed under aerobic conditions, which has been recorded to destabilize sensitive [4Fe-4S] clusters. One approach that circumvents the issue of over-expression is an endogenous pull-down and subsequent quantification of metal ion and protein concentration. Commercial yeast strains with

C-terminal TAP (tandem affinity purification) tags on pol-prim subunits offer a convenient way to quickly and relatively gently isolate small quantities of native pol-prim [217]. Using this approach, small amounts of heterotetrameric pol-prim complex were successfully isolated small amounts after optimizing the growth conditions and the purification. The complex is easily visualized on SDS-PAGE gels with Commassie stain, though degradation of the subunits of interest and some contaminants are evident (Figure 7.2).

Further characterization proved more difficult. Time of flight (TOF) mass spectrometry was unable to identify the polypeptides present in the solution, likely due to the low concentration of the sample. Quantification of the protein sample had too much uncertainty because of the divergence between different methods of quantification (Bradford assay vs UV-VIS spectrometry vs sulfur count in inductively coupled plasma mass spectrometry) and the ratio of impurities/degradation products to heterotetramer. Moreover, inductively coupled plasma mass spectrometry (ICP-MS) performed by Dr. Will Beavers of the Skaar lab revealed 2-5 moles of iron per mole of protein.

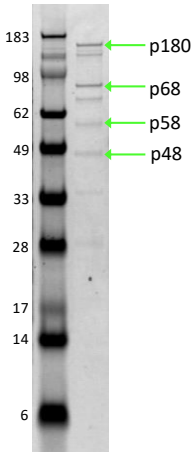

Figure 7.2: SDS-PAGE gel of a TAP purification of endogenous pol-prim. The left lane is a marker and the right lane contains the protein of interest. The green arrows show the subunits.

With the large variance in the amount of iron and the uncertainty in the concentration of the protein, the values obtained insufficient to reliably determine if a second cluster was present. There are several possible explanations. Typically, a 4Fe-4S cluster protein has about three

moles of iron per mole of protein, as determined experimentally by ICP-MS [70, 214, 215, 220]. This lower than expected value reportedly arises from oxidative degradation of some of the [4Fe-4S] clusters during the experiment, resulting in an average value of less than four. In the experiments with endogenous pol-prim, it is possible that both primase and pol α undergo varying degrees of [4Fe-4S] degradation and the resulting number is a combination of the two. Another possibility is that the [4Fe-4S] cluster in primase is more stable in the full heterotetrameric complex compared to the dimeric primase and the observed number of molecules is that of primase alone. While this seemed like a promising avenue, the low concentration of pol-prim obtained by the TAP tag approach proved to be an insurmountable obstacle.

Recombinant production of p180C.

I next turned to recombinant overexpression in *E. coli*. In 2014, the Aggarwal group reported the presence of an [4Fe-4S] cluster in pol ε using an E. coli over-expression system [97]. In 2017, the Tahirov group reported identification of an [Fe-S] cluster in the isolated C-terminal domain of pol ε also using an E. coli overexpression system [221]. These protocols were adapted to the small p180C domain to identify the putative [4Fe-4S] cluster. Expression and purification of the small p180C domain was performed with the help of a visiting professor, Dr. Huiqing Chen. Unfortunately, the yield and stability of the isolated p180C were not ideal. This domain interacts with the pol α regulatory subunit, p68. Co-expression of the structured part of p68 (p68dN; residues 155-598) has been documented to improve the stability of p180C [43]. Using a modified expression and anaerobic purification protocol, there is evidence of an iron-sulfur cluster in the sample (Figure 7.3).

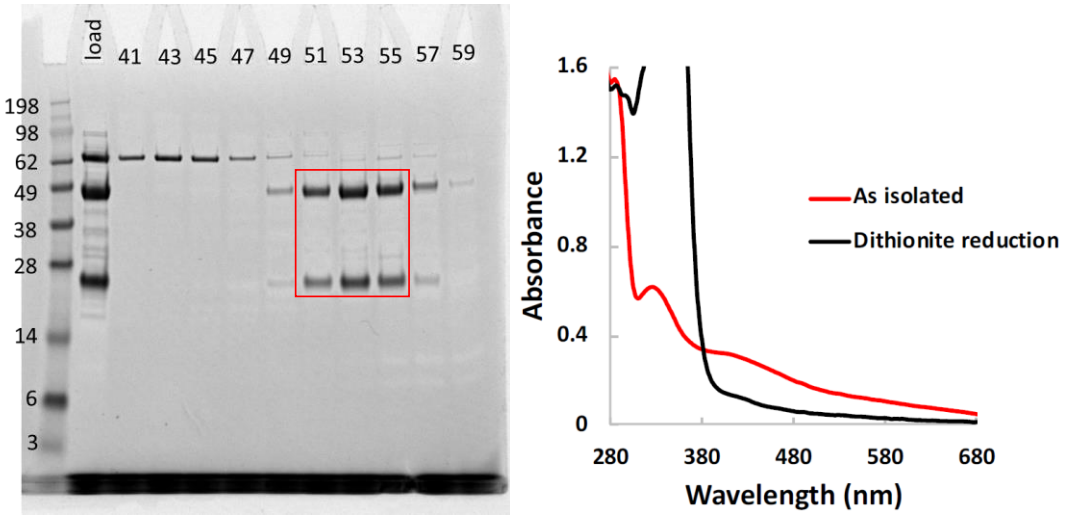

Figure 7.3: Purification of p68dN-p180C, Left: representative SDS-PAGE gel after size exclusion chromatography. The red box indicates p68dN (~49kDa) and p180C (~23 kDa). Purification and SDS-PAGE performed by L.E. Salay. Right: representative UV-VIS spectrum of the sample after purification (UV-Vis by Dr. Aoshu Zhong). Note the broad shoulder around 410 nm that is indicative of a 4Fe-4S cluster.

Most notably, the purified protein had a characteristic yellow-brown color and exhibited a broad peak around 410 nm in a UV-VIS spectrum. This peak disappeared upon disruption of the 4Fe-4S cluster with DTT or exposure to atmospheric oxygen for about ten hours.

Barton Lab collaborator Dr. Aoshu Zhong performed cyclic voltammetry (CV) experiments with a [4Fe-4S] cluster-containing this p68dN-p180C construct. A CV signal was apparent during the DNA-on-a-chip CV experiments, consistent with a 4Fe-4S protein that can engage in DNA-mediated redox state switching (Figure 7.4).

These observations strongly suggest that the p180C domain is able to accommodate an oxygen sensitive 4Fe-4S cluster. The electrochemical signal observed in the cyclic voltammetry experiments demonstrates that this 4Fe-4S cluster is able to engage in redox switching, similar to p58C, where the protein can be reduced and subsequently disengages from the substrate [76, 77]. This is especially interesting, as it shows that the redox switch may modify the ability of the protein to engage with a DNA substrate, as observed with primase and p58C.

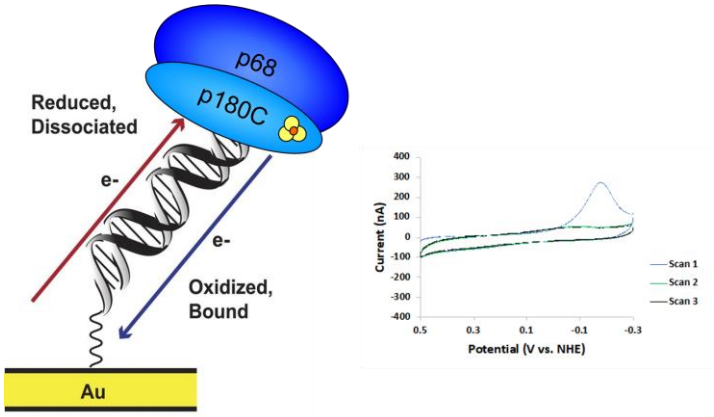

Figure 7.4: p180C can engage in redox switching. Left: DNA-on-a-chip technique where p68-p180C interacts with the DNA coupled to a gold electrode, Right: Cyclic voltammogram showing a reduction peak characteristic of Fe-S redox state switching. Electrochemistry performed by Dr. A. Zhong.

The electrochemistry of p58C and p180C are unique compared to other [4Fe-4S] clusters [56, 57, 60, 67, 98]. These observations support the hypothesis that redox switching is an important aspect of priming. To investigate this in detail, however, studies of the full complex are necessary.

Production of the prim complex

The p68dN-p180C complex does not have any biochemical activity. To investigate how it and the [4Fe-4S] cluster in p180C influence RNA priming by primase, it was necessary to generate a different complex that contained RNA priming activity. The prim complex has been previously produced and characterized [25, 44]. It contains the primase p48 and p58 subunits, in complex with p68dN-p180C. Importantly, this complex does not contain the p180cat domain, which precludes the interrogation of the DNA priming activity of the pol-prim complex. This simplifies biochemical analysis as the complex is only able to perform RNA priming. Furthermore, expression of this truncated construct allows for expression in *E. coli*.

The prim complex was generated by performing a co-lysis purification of cells expressing primase and cells expressing p68dN-p180C. The prim lobe was generated both aerobically, with zinc in the CysA and CysB sites, and anaerobically, hypothetically with at least one [4Fe-4S] cluster. Both the aerobic and anaerobic variants are important to be able to distinguish between

the possible effects of p180C containing a [4Fe-4S] cluster and the possible effects due to the presence of the p180C subunit. The samples were characterized by SDS-PAGE, UV-VIS, ICP-MS, ferene assay to quantify the iron and assess the quality of the sample (Figure 7.5).

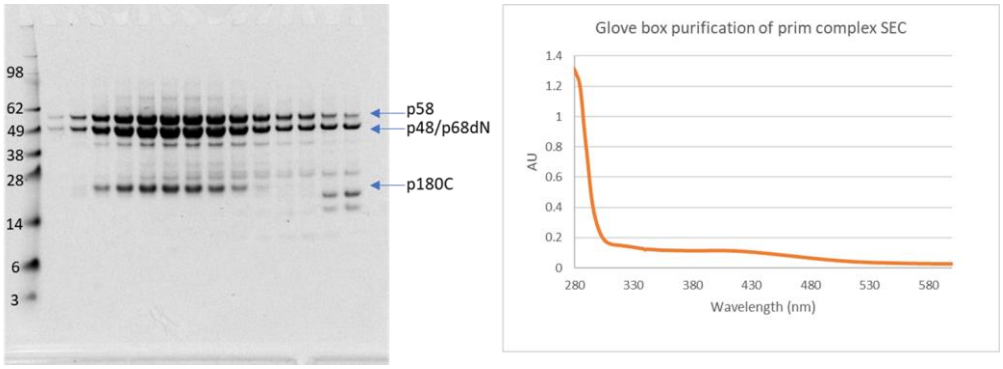

Figure 7.5: Recombinant production of the prim complex. Left: SDS-PAGE gel of the prim lobe. Arrows indicate bands around the expected molecular weight for each subunit. Right: UV-Vis spectrum of the prim lobe. Note the broad shoulder around 410 nm, suggesting the presence of a 4Fe-4S cluster. Purification and analysis performed by L. E. Salay.

ICP-MS revealed that the aerobic prim complex protein had approximately one [4Fe-4S] cluster per protein molecule. Purification of prim complex protein in an anaerobic environment revealed approximately two [4Fe-4S] clusters per molecule. Addition of iron and cysteine to the growth media during expression of p68dN-p180C resulted in even higher levels of iron, equivalent to roughly three 4Fe-4S clusters in the prim complex (Table 7.1).

Sample Name	Fe /protein
Aerobic prim lobe	4.14
Anaerobic prim lobe	7.69
Anaerobic prim lobe + Fe&Cys	12.7

Table 7.1: quantification of iron in proteins samples using ICP-MS

These results suggest that during normal (aerobic) expression and purification, the prim complex contains one [4Fe-4S] cluster, presumably that in primase. This is consistent with the observations in the literature [43]. After an anerobic purification, primase and the pol α subunits each presumably contain one [4Fe-4S cluster]. Under conditions that promote 4Fe-4S cluster

incorporation during protein expression, primase contains one [4Fe-4S] cluster and both metal binding sites in p180C are presumably filled with a [4Fe-4S] cluster.

The CysA and CysB question

The possibility of three [4Fe-4S] clusters, one in primase and one in each of the p180C metal binding sites is strange as no other pol had been documented to contain more than one 4Fe-4S cluster. Furthermore, cryo-electron microscopy of pol δ indicates that there is one 4Fe-4S cluster in the CysB site [222]. The incorporation of additional 4Fe-4S clusters in the prim complex may be physiologically relevant or, more likely, an artifact of the expression system. To address this, a plasmid that allowed for all four subunits to be co-expressed was developed. As a more relevant protein product, it is possible that additional protein interactions inherent in the prim complex will promote the proper insertion of the [4Fe-4S] cluster, which could clarify the location of the Fe-S cluster and the stoichiometry of clusters to p180C. CysA and CysB knockout mutations were incorporated into the plasmid as a control comparison and to aid in locating the [4Fe-4S] cluster in p180C.

The wildtype and mutant proteins were purified anaerobically. Interestingly, the knockout mutations gave rise to unexpected issues. Firstly, in an SDS-PAGE gel, a double band for p180C is usually apparent and is attributed to a degradation product of p180C. However, this degradation product is significantly more prevalent in the CysA and CysB knockout mutants compared to the wild-type protein. This is not too surprising as both the CysA and CysB sites are located in the heart of regions devoid of strong secondary structure (Figure 7.1, right) and are thus, more susceptible to proteolysis.

However, it is possible that either the degradation or the mutation of the metal binding site led to a weaker interaction with p58N, and dissociation of p68dN-p180C from p48-p58. In any case, the stoichiometry between the subunits is significantly different for the mutants

compared to the wild-type protein. This precluded accurate protein and iron quantitation.

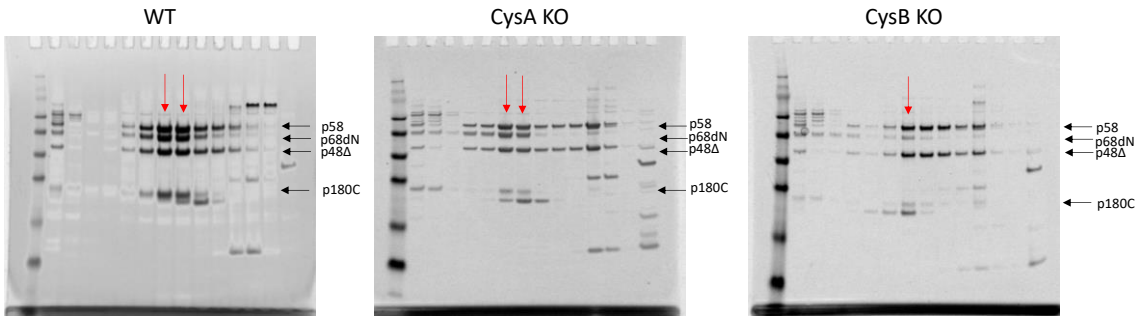

Figure 7.6: SDS-PAGE gel of the wild-type (WT), CysA knockout (KO), and CysB KO proteins. The red arrows indicate fractions used for preliminary quantification. Importantly, note the double bands representing the p180C subunit. Purification and analysis performed by L.E. Salay.

To obtain a rough estimate of cluster loading, the protein was subjected to a ferene assay. The average was significantly lower than previously observed in purifications of the prim lobe using the co-lysis method. The wild-type 4-gene prim lobe protein contained ~4.6 moles of iron per mole of protein. The CysA KO mutant protein contained ~3.6 moles of iron per mole of protein and the CysB KO mutant contained <3.2 moles of iron per mole of protein. The iron in the wild-type anaerobically purified protein does not reflect the consensus obtained by ICP-MS of the complex obtained by co-lysis methods (Table 7.1). Further experiments are necessary to investigate why there is a difference between the co-lysis and co-expression methods. One possibility is that the co-expression product is too complex to be properly processed by the bacterial 4Fe-4S cluster insertion machinery. Another possibility is that during the expression of p68dN-p180C, the equilibrium is shifted to favor abundant incorporation of [4Fe-4S] in all possible binding sites. To address this, mutations have been inserted into the construct that knock out both metal binding sites. Experiments to quantify the iron content in these mutants are ongoing.

The dependence of the existence of the 4Fe-4S cluster on expression and purification conditions is well-documented [55, 215]. However, it does not necessarily establish if a 4Fe-4S cluster exists in pol-prim in cells. In the face of the issues inherent to recombinant proteins, it would be useful to perform assays in cells, similar to what has been described for pol δ [223].

Biochemical characterization of the prim complex

Despite the open questions detailed above, there is enough evidence to support the hypothesis that p180C is able to accommodate a 4Fe-4S cluster and that the 4Fe-4S cluster in p180C does not prevent interactions with primase. Thus, biochemical activity assays can be performed to compare the activity of primase, the activity of aerobically purified prim complex, and the activity of anaerobically purified prim lobe.

These proteins were used in an initiation assay with a dT_{50} template with two different template: protein ratios (Figure 7.7).

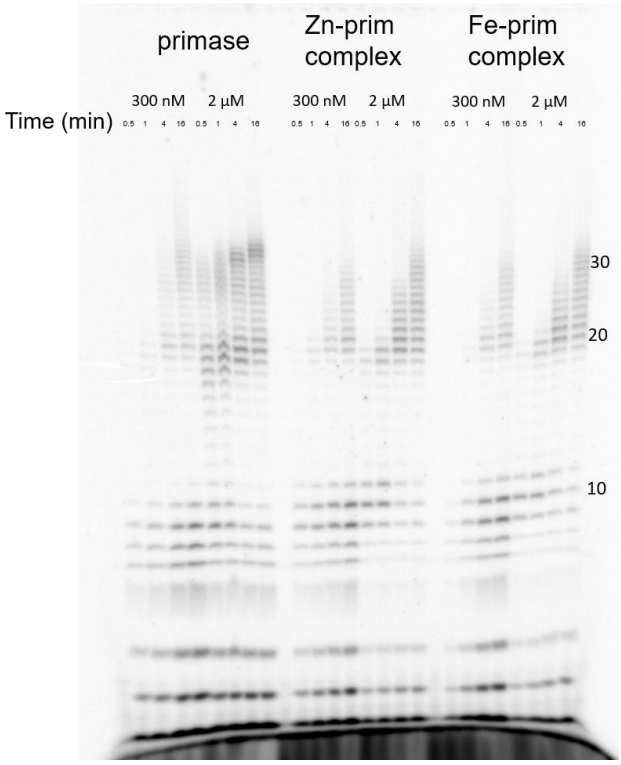

Figure 7.7: Urea-PAGE gel of initiation products generated by primase, the prim complex with zinc in p180C (Zn-prim complex) and the prim complex with a 4Fe-4S cluster in p180C (Fe-prim complex) at two different protein concentrations. In this assay, primase, Zn-prim complex and Fe-prim complex at 300 nM or 2 µM was incubated with 1 µM of $d(T)_{50}$, 10 µM ATP, and 0.5 µM γ-^{32}P-ATP. Product formation was monitored over time. The products were run on a denaturing PAGE gel and imaged as described in the Methods. Biochemistry performed by L.E. Salay.

This was to observe single hit conditions and to compare the same template:protein ratio used previously[76]. Between the two metal binding states of the prim lobe (aerobic (Zn) vs aerobic (4Fe-4S) in p180C), there are no significant differences observed. However, for both prim-

complex variants there is a shift in product distribution relative to isolated primase. The prim complex generates more primer length products (vs primer multimers and abortive products) compared to primase. This suggests that the p68dN-p180C subunits effect priming more than the identity of the metal in p180C. Moreover, high concentrations of the prim lobe seem to inhibit primer multimer formation compared to primase. This aligns with the literature suggesting that pol α may act as a molecular brake for primase, but does not align with the results reported in [25], which suggest that the p68dN and p180C subunits promote primase processivity.

The elongation activity of the proteins was also compared, using a 5-mer RNA oligo without a 5'-triphosphate and a complementary 58 nt template strand as the substrate:

CAGCGr-5'

5'AAGAGAAACCAGGACACACAGAAACAGAACACCAAGCACACAAACTGTCGCCAACCAA

This substrate was chosen in order to generate both unit-length products and multimers. The protein elongates off of the 5-mer with an α-^{32}P ATP, rapidly extending to primer length (~7-11) and subsequently generating primer multimers.

Unit length primers (10 nts) are the predominate product, followed by primer dimers 18-20 nts (Figure 7.8). These groups of products increase faster than primers products of intermediate length (intermediate means in between a unit length and primer dimer). Primase seems to be less effective at elongating a primer beyond a unit length primer in contrast to the prim complex, which very quickly elongates past a unit-length primer. This assay needs further optimization as it is too fast to truly observe proper counting or any difference between the two variants metal states of the prim lobe. Furthermore, there is some evidence in the literature that a 5'- triphosphate aids in primer length regulation [85]. Adding this 5'- triphosphate may improve

the assay and enhance differences between the two variants of the prim lobe.

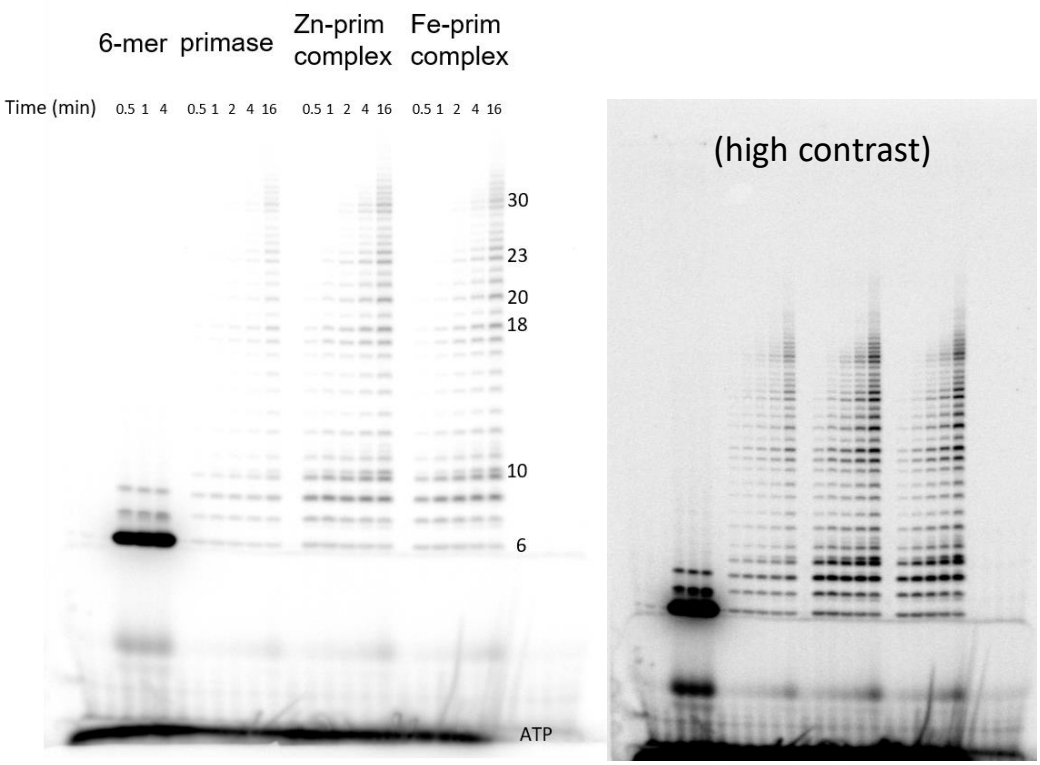

Figure 7.8: Elongation assay with primase, the prim complex with zinc in p180C (Zn-prim complex) and the prim complex with a 4Fe-4S cluster in p180C (Fe-prim complex). 6-mer is a product of primase + only radiolabelled ATP and no other nucleotides as a marker. Left: as imaged, right: high contrast image. In this assay, primase, Zn-prim complex and Fe-prim complex at 300 nM was incubated with 1 µM of annealed RNA:DNA duplex, 10 µM NTP mix, and 0.5 µM γ-^{32}P-ATP. Product formation was monitored over time. The products were run on a denaturing PAGE gel and imaged as described in the Methods. Biochemistry performed by L.E. Salay.

The similarities between the activity of aerobically vs anaerobically purified protein is surprising. A large conformational change was expected upon 4Fe-4S cluster binding in p180C, and that this change would disrupt either the association with primase or the activity of the protein [80]. Instead, these results imply that p180C can accommodate at least two different metal cofactors without compromising the activity of the complex and that if a significant structural change occurs, it does not have an effect on the association with primase. Furthermore, though these aerobically performed assays do not indicate a difference in the activity, the assays detailed above do not preclude a redox role for the [4Fe-4S] cluster in p180C. As both the 4Fe-4S cluster in primase and that in p180C is isolated in the reduced state,

it is unlikely that a redox event occurs between the two [4Fe-4S] clusters. To further investigate the possibility of a redox-mediated difference in activity, the assay needs to be repeated in the Barton lab with electrochemically generated oxidized and reduced primase + native pol αΔCAT (and vice versa) to understand the effect of redox state on priming initiation and counting.

Concluding Remarks

Here, we present evidence that the p180C subunit of pol α is able to accommodate at least one 4Fe-4S cluster. This 4Fe-4S cluster is oxygen sensitive and can engage in redox switching. There is no obvious effect of the 4Fe-4S cluster in p180C on RNA priming by primase, though the addition of p68dN-p180C improves the ability to of primase to properly count. There is a possibility that the number of 4Fe-4S clusters can be modulated by the conditions under which it is produced. Further experiments are necessary to understand if this manifests in a cellular context or is an artifact of recombinant protein production.

So far, there is no strong evidence that in a cellular context, p180C contains a 4Fe-4S cluster. However, as we report above that it is a possibility, it is intriguing to speculate as to its role during replication. *In vitro*, the 4Fe-4S cluster in pol δ seemingly plays a role in stalling DNA synthesis upon oxidation of the 4Fe-4S cluster [98]. If these observations translate to an in-cell environment, this could cause replication fork slowing or stalling. Following this line of reasoning, it is possible that in a cell, the 4Fe-4S cluster in pol α plays a similar, more obvious role in regulating priming by promoting primer handoff or in preventing replication during periods of intense oxidative stress.

With improvements in electrochemistry [63], in reconstituted replisome assays [91] and in live-cell imaging [224], the field is approaching a time where these questions can be readily investigated and the role of 4Fe-4S clusters and redox homeostasis at the replication fork can be understood.

CHAPTER 8

DISCUSSION AND FUTURE DIRECTIONS

Summary

Iron-sulfur clusters are fascinating cofactors, simultaneously incredibly simple and intriguingly complex. An ancient and versatile compound of just iron and sulfur, this metal cofactor is able to fill many roles, from participation in redox reactions and sensing to structural scaffolding and catalysis. With the identification of iron-sulfur clusters in an increasing number of DNA-associated proteins, the questions the field faces are: why do these proteins contain this electron-rich cofactor? Is there a functional role for the iron-sulfur cluster? The research detailed in this dissertation focused on these questions by elucidating a role for the iron-sulfur cluster in primase and identifying an iron-sulfur cluster in pol α. The main findings are summarized and discussed below.

The iron-sulfur cluster in primase functions as a redox switch.

Since the discovery of the iron-sulfur cluster in primase in 2007, the question of its purpose has been an area of significant research [69, 70]. Iron-sulfur clusters are important and typically functional because their incorporation is metabolically expensive. It is likely that this cluster has a structural role, as the cofactor is deeply buried in the protein and significant disruption of the cluster results in inviable cells and *in vitro*, insoluble protein [70, 73]. An additional yeast study demonstrates that disruption of the 4Fe-4S cluster in combination with a knockdown of proteins involved in redox homeostasis renders primase sensitive to the redox state of the cell [74]. This suggests that the iron-sulfur cluster may allow primase to respond to the redox state of the cell. However, no previous study has explored the direct role the iron-sulfur cluster in detail and how it directly relates to primase function.

Our understanding of the 4Fe-4S cluster in primase was advanced by collaborative studies performed with J. K. Barton's group at the California Institute of Technology. This group has pioneered the idea that DNA charge transport is used as a means to communicate between 4Fe-4S cluster proteins, primarily DNA repair proteins [225]. In their studies with [4Fe-4S] cluster containing glycosylases, they demonstrate that electrons can pass through duplex DNA from an electrode to an [4Fe-4S] cluster. Furthermore, the redox state of the 4Fe-4S cluster governs the strength of the association of the protein-DNA complex [63].

Together, we discovered that the iron-sulfur cluster domain of primase, p58C, can also engage in DNA charge transport and that the redox state of the 4Fe-4S cluster can be thus modulated (redox switching). Moreover, the data suggest that p58C is tightly associated with DNA when the 4Fe-4S cluster is oxidized and binds to the DNA much more weakly when reduced. Furthermore, the ability of p58C to perform redox switching can be altered by mutating a series of tyrosine residues (Y309, Y345, Y347) that bridge the 4Fe-4S cluster and the nucleic acid binding site. Mutating these residues individually does not have an effect on the extent of 4Fe-4S cluster loading, the fold of the protein, or how tightly the protein binds a nucleic acid substrate. However, these mutations significantly curtail the ability of the protein to engage in redox switching. When redox switching is inhibited, primase is unable to properly initiate or terminate primer synthesis in *in vitro* biochemical assays. These defects suggest that the ability of the protein to engage in redox switching is important for primase function. This is the first study to imply a chemical role for an iron-sulfur cluster in a polymerase [76].

Following publication of the above findings, two Technical Comments [153, 154] were published to criticize the results, suggesting that the electrochemical and biochemical results were artifacts, observed due to a misfolding of the p58C domain relative to a substrate-bound p58C domain. It was further posited that mutation of Y345 and Y347 disrupt interactions with the nucleic acid substrate.

These concerns were addressed in a Response to Technical Comments [162], reiterating that no difference in binding affinity was observed in solution-based binding assays. Furthermore, the biochemical and electrochemical results that show a defect in redox switching and priming initiation and termination are maintained upon examination of a third mutant, Y309F. This mutation is not involved in nucleic acid binding but also cannot efficiently engage in redox switching nor appropriate priming initiation or termination. This implied that the observations reported in the *Science* paper were not off-target effects of the Y345 and Y347 mutants.

The question of misfolding was further investigated in collaboration with Dr. Marilyn Holt. The misfolding in the Technical Comments was suggested to arise from omission of several N-terminal residues of the p58C domain used for electrochemical experiments ($p58C_{272-464}$). Dr. Holt added these residues to the domain and the resulting domain ($p58C_{266-464}$) was characterized in solution and *in crystallo*. Firstly, neither circular dichroism spectrometry nor nuclear magnetic resonance spectroscopy indicated a significant difference between the secondary structure distribution or overall fold of the p58C constructs. Secondly, solution-based binding assays showed no difference in the observed protein-nucleic acid affinity, suggesting that the $p58C_{272-464}$ construct is not limited in its interaction with DNA. Finally, the crystal structures of both constructs were compared. The two were nearly identical, though significantly different from the published structure of this domain with a substrate. However, analysis of these structures revealed that the differences arose from significantly divergent crystallization conditions [163]. These findings demonstrate an important reminder: a crystal structure is not inherently representative of the biomolecule in solution. It is necessary to validate functional differences using additional methods. Furthermore, these findings confirm the electrochemical results reported in the *Science* paper, validating that the results are not artifacts of the domain construct.

With advances in methodology, collaborator Dr. Liz O'Brien was able to demonstrate that the electrochemistry observed for the p58C domain was reproducible with the full primase heterodimer [78]. This implies that the observed redox switching is not an artifact of using the small 4Fe-4S cluster domain during electrochemical experiments. Moreover, electrochemistry experiments were performed in the presence of nucleotides, mimicking the substrates necessary for catalysis. Interestingly, the presence of nucleotides rendered the redox switching reversible. Thus, instead of undergoing a reduction event and disengaging completely from the DNA substrate, primase can rapidly engage and disengage with the substrates. This is likely a more physiological representation of the redox switch.

Yeast require redox switching in primase.

While the chemical basis for DNA charge transport and redox switching is supported by strong data from multiple labs, the relevance of this phenomenon in a cellular context is lacking. To address this, we collaborated with the Dr. K. Friedman group to use *S. cerevisiae* as a model system. We demonstrated that the [4Fe-4S] cluster domain of yeast primase is also able to perform redox switching, despite being significantly different in sequence to the human p58C [77]. While this is unsurprising, it demonstrates that this property is conserved between human and yeast primase. Furthermore, mutating tyrosine residues between the [4Fe-4S] cluster and the nucleic acid binding site result in a knockdown of the ability to engage in redox switching. Incorporating these mutations into the yeast genome revealed one mutation that conferred lethality, Y397L. Further electrochemical characterization of this yeast p58C mutant revealed that it is more susceptible to degradation of the 4Fe-4S cluster than the wild-type protein or other, more conservative mutations [77]. This suggests that the redox stability of the 4Fe-4S cluster is correlated to viability of the yeast, i.e. the ability to engage in reversible redox switching is important for survival.

The lethality of the Y397L mutations was confirmed by tetrad analysis. However, no yeast strains that contain other single-site mutations in p58C had an observable phenotype.

Since there are seven residues of interest between the [4Fe-4S] cluster and the nucleic acid binding site, it is possible that there is a threshold above which the ability to engage in redox switching is sufficient and/or there are redundant pathways by which the electron can travel through the DNA. To investigate this, we mutated each tyrosine residue to phenylalanine, resulting in yeast p58C mutants that contained multiple mutations and combinations of mutations. X-ray crystallography and CD spectroscopy indicate that these mutations do not cause significant structural perturbations. Fluorescence anisotropy DNA binding assays show that alterations in DNA binding affinity are minimal. Electrochemical characterization is ongoing. Pending promising results, the mutations can be incorporated into the yeast genome to assess phenotypes.

Evidence for an 4Fe-4S cluster in pol α.

Though primase is a useful construct to examine *in vitro*, it is not representative of the physiologically relevant pol-prim. Primase is constitutively bound to pol α and its activity is modulated by the presence of the pol α subunits [31]. Furthermore, in 2011, a closer look at eukaryotic polymerases suggested that pol α contains an [4Fe-4S] cluster in the C-terminal domain of the catalytic subunit, p180C [79]. Given our findings about the role of the [4Fe-4S] cluster in primase, we wanted to explore the possibility that the putative 4Fe-4S cluster in pol α influences primase activity or the ability to engage in redox switching.

Prior to this work, the existence of a [4Fe-4S] cluster in the C-terminal domain of the catalytic subunit of pol α, p180C, was controversial. X-ray crystal structures indicated that the domain does not contain any iron and all previous biochemical studies have been performed on aerobically produced protein [43]. [4Fe-4S] clusters are uniquely susceptible to oxidative degradation, often leading to incorporation of non-native metals in the binding site [53, 54, 215]. By adapting previously used protocols to an anaerobic environment, thus limiting oxidative degradation of the iron-sulfur cluster, it is readily possible to isolate protein with an iron-sulfur cluster in p180C. The presence of the iron-sulfur cluster was verified using UV-VIS

spectroscopy, inductively coupled mass spectrometry and a colorimetric iron quantitation assay. Furthermore, electrochemical investigation revealed that this iron-sulfur cluster can engage in redox switching, similar to p58C. Together, these observations provide evidence that the C-terminal domain of p180C can accommodate a [4Fe-4S] cluster.

To investigate if the iron-sulfur cluster in p180C affects priming in comparison to what has been published, a construct of full-length primase and a fragment of pol α that contains the [4Fe-4S] cluster was generated. The construct was purified both aerobically and anaerobically, allowing for the comparison between forms containing the [4Fe-4S] cluster-bound p180C and the literature standard p180C. Both variants were stable over size-exclusion chromatography and active in biochemistry assays, indicating that the 4Fe-4S cluster in p180C does not inhibit complex formation or render the protein inactive. The priming initiation and elongation activities of this construct were tested. Studies are ongoing but preliminary results show that there are no significant differences observed between the two metal binding variants, although in order to properly test this in an *in vitro* setting, it will be necessary to compare the activity of oxidized versus reduced protein, which requires electrochemical modification.

Because these experiments were performed in bacterial cells, the issue of whether or not the domain contains a cluster in eukaryotic cells remains an open question. Ideally, this problem could have been solved with our strategy of isolating pol-prim directly from yeast cells. Given the challenges faced, it will be necessary to find an alternative approach either to generate a larger amount of protein per cell or to more efficiently capture the pol-prim present. One idea for this would be to CRISPR a biotin tag into pol-prim to enable direct capture with streptavidin from cell lysate.

Discussion

Once considered a quirk of primase biology, the iron-sulfur cluster in primase seems to play a fundamental role in governing primase function. The discovery that its binding partner, pol α, can accommodate a [4Fe-4S] cluster opens the question further: do iron-sulfur clusters

play a larger role at the replication fork? The implications for priming and general replication are discussed below.

Redox switching in primase: implications for primase function

Primase is a unique, essential protein. Though it is arguably one of the most important proteins at the replication fork, given that it is the only replicative polymerase that can start a strand, major aspects of primase remain undefined. Notably, the ability of primase to generate products of a specific length (counting) is enigmatic; multiple hypotheses have been examined and been found wanting. Furthermore, the iron-sulfur cluster in primase plays an essential role in primase function, even if only the structural scaffolding aspects are considered. However, the iron-sulfur cluster escaped all meaningful characterization for over forty years. This cofactor does not seem to influence catalysis of primase products, but has been tied to the ability to properly initiate and count products in early biochemical studies. A direct relation between these phenomena had never been posited until recently.

In the 2017 *Science* paper, we proposed that the ability of the 4Fe-4S cluster to engage in redox switching, and thus the affinity for a product, is coupled to the ability of primase to initiate and count. This implies that a direct change in affinity between the primase and its product is instrumental in bringing about primer initiation and termination. We posit that primase with an oxidized 4Fe-4S cluster associates with a single-stranded DNA template and begins synthesis of the primer. When the primer reaches the proper length, a reduction event occurs. This causes primase to release the primer, allowing access for other pols to continue generating the product.

The biochemistry assays in the Science paper were performed with only primase, suggesting that another molecule of primase is able to cause such a reduction event (Figure 8.1), as long as the DNA and tyrosine “pathway” remains accessible. Indeed, to show such an effect, the biochemistry studies were performed with a large excess of primase to the template

DNA. This is very clearly not representative of physiological conditions, where at the replisome, only one or two molecules of primase seem to be associated[96, 226].

Furthermore, the evidence of a redox switch causing a shift in the affinity of primase for its product is indirect, with only electrochemical observations to support this hypothesis. It is clear from the electrochemistry that something happens to uncouple the 4Fe-4S cluster from the electrode and that this coupling is recyclable after treatment to oxidize the 4Fe-4S cluster. Interestingly, with the full-length primase protein and its relevant substrates, this is reversible. However, the exact nature of this electrochemical coupling is not defined.

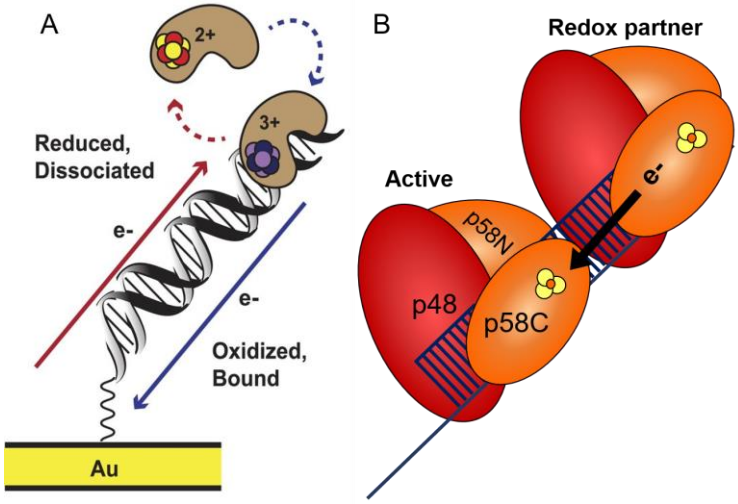

Figure 8.1: Primase can engage in redox switching, where the redox state of the p58C 4Fe-4S cluster can be cycled to an oxidized and a reduced state. A.) Our observations suggest that an oxidized 4Fe-4S cluster causes p58C bind to the DNA substrate tightly and a reduced 4Fe-4S cluster causes p58C to bind the DNA substrate weakly/dissociate from the substrate. B.) Model of 2 molecules of primase interacting to cause reduction and primer termination.

In the literature, one observation that may support this is that binding affinities of primase for its substrates vary by ~100-fold using different quantification measurements. In solution, using aerobically purified p58C domain binds substrates with a modest affinity of 2 μM [76, 86]. This contrasts with binding affinities measured by electrophoretic mobility shift assays that report affinities of approximately 30 nM [85]. It is documented that the conditions of electrophoretic mobility shift assays can cause oxidation of the protein sample [63] and this may

be the cause of the differences observed in affinities. In order to resolve this discrepancy, it is necessary to perform additional studies to validate that the reduced and oxidized protein associate differently with the substrate.

Furthermore, I note that computational studies have been published based on our observations. One theoretical study suggests that it is not energetically favorable for the [4Fe-4S] cluster in primase to both donate and receive an electron in the process of redox switching [65]. The authors go on to imply that additional factors are necessary for 4Fe-4S redox switching to occur. This prediction is logical, as primase exists is within a crowded environment during replication and many additional factors are present that may facilitate or even mediate redox switching, such as pol a, pol δ, Dna2, or even an oxidized guanine.

However, the predictions from this study do not preclude the possibility that redox switching may regulate primer synthesis. While we were limited by the conditions under which we could perform biochemical assays, much progress has been made since that time and the contribution of redox switching to regulating priming can be further investigated using a reconstituted replisome with redox-switching impaired primase.

Our studies with the yeast p58C protein add a further layer of complexity. Firstly, we were able to demonstrate that the ability to engage in redox switching is conserved from human to *S. cerevisiae*. However, the human and yeast proteins are significantly more divergent than anticipated. While in human p58C/primase proteins, a single tyrosine mutation was sufficient to significantly abrogate the ability of p58C to engage in redox switching, a homologous mutation in yeast was only able to slightly knock-down redox switching [76, 77].
Furthermore, the yeast protein was less efficient at redox switching compared to the human protein, exhibiting a maximum charge transfer of ~145 nC for yeast at 30 μM compared to ~300 nC for human at 16 μM [76, 77]. One possible reason for this might be the larger number of tyrosine residues involved and the existence of multiple “pathways” that bridge the iron-sulfur cluster and the nucleic acid binding site (Figure 8.2).

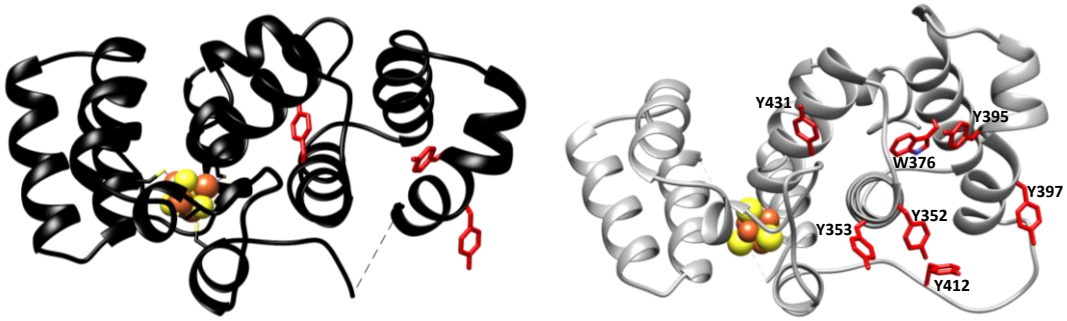

Figure 8.2: Crystal structures of human (left, 3Q36) and yeast (right, 6DI6) p58C. Residues that may be involved in mediating redox switching are highlighted in red. There are twice as many Tyr residues in the yeast protein (right) as in the human protein (left). I hypothesize that this difference is the origin of the observations of less efficient charge transfer in yeast p58C.

Interestingly, a recent study suggests that mutating specific residues does not inhibit redox switching, only changes the timescale by which redox switching occurs and the pathway of the electron through the protein [211]. This may be exacerbated in the yeast protein, with many possible routes, including to the surface of the protein where the electron can be neutralized by the solvent. To assess this, we have mutated nearly all the residues of interest and anxiously await the results of electrochemical characterization. Another test of this concept would be to perform electrochemical and biochemical assays in the presence of a radical scavenger, such as ascorbic acid. If the radical scavenger is able to inhibit redox switching as well as one of the documented mutations, this would indicate that the electron pathway through the protein is not as direct as we expect. A pathway from the DNA to the surface of the protein might be more commonly used. This would aid in understanding electron pathway use through the p58C protein.

Redox switching in primase: speculation for in cell studies

The larger number of electron transport-capable residues in the yeast protein may also explain why there is no observable phenotype for single-site mutations. The strain containing PRI2Y397L allele conferred lethality. However, no other mutation had an effect on the accumulation of mutations over generations (canavanine mutation assay), temperature

sensitivity, sensitivity to ultraviolet light, sensitivity to replication stress (hydroxyurea), sensitivity

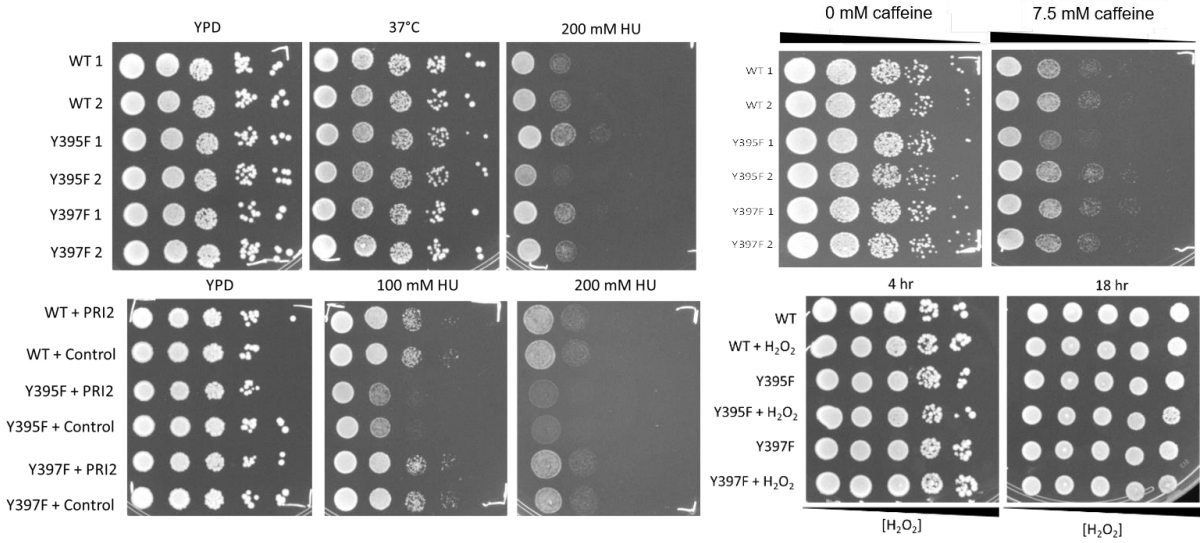

Figure 8.3: Spot assays showing tested phenotypes and non-complementation. Importantly, the inconsistencies between assays precluded any meaningful analysis.

to oxidative stress (hydrogen peroxide and methylene blue), or sensitivity to an ATR inhibitor (caffeine). As discussed above, there may be a biological threshold above which redox switching is sufficient for proper replication.

Mutating an essential gene to alter its function is not trivial. Though we were very careful to incorporate the mutations properly, even generating mutants by sporulating diploid cells into haploids to obtain some strains, we always observed a significant number of off-target effects and reversions. This resulted in varying phenotypes of strains containing the same mutations (Figure 8.3). The observed phenotypes were invariably not complemented by adding the wild-type protein in a plasmid. It is possible that this variety of off-target effects is itself a phenotype. However, whole genome analysis of several clones would be necessary to understand what is happening in this situation.

While yeast is a convenient model system, it is very divergent from mammalian cells, particularly with regard to DNA priming. Notably, in *S. cerevisiae*, RNaseH2 is dispensable [227]. Since primase generates RNA primers and inhibition of redox switching *in vitro* leads to dysregulation of primer length, a reasonable expectation is that in redox switching-deficient

cells, primase will generate significantly longer primers than in wild-type cells. This would leave more ribonucleotides in the cell that need to be dealt with through ribonucleotide repair pathways. This would cause significantly more stress, and theoretically, a more obvious phenotype in mammalian cells.

Primase creates redundant products. During Okazaki fragment maturation, pol δ replaces a significant portion of the primer generated by pol-prim, typically removing all of the RNA portion and nearly the entire DNA portion [228]. This obscures the effect of primase dysregulation. It is not feasible to observe the results of primase dysregulation in wild-type cells. Instead, it may be worth performing these experiments in cells that are deficient in Okazaki fragment maturation.

I would be remiss not to acknowledge the possibility that there is simply no functional relevance to inhibiting redox switching or that these mutations do not confer the desired effect in a cellular context. Why, then, does the ability to switch redox states occur and do the residues involved in mediating this *in vitro* have a function in a cellular context?

One possibility is that the iron-sulfur cluster exists to sense the redox state of the cell. This aligns with the 2015 study illustrating that disruption of the [4Fe-4S] cluster combined with a deletion of superoxide dismutase inhibits replication [74]. Increased reactive oxygen species in the nucleus may cause oxidative degradation of the iron-sulfur cluster, thereby inhibiting replication until redox homeostasis can be re-established. Alternatively, the residues involved in redox switching may protect the iron-sulfur cluster from direct oxidation or reduction by reactive oxygen species [229, 230]. These residues may shuttle electrons away from the iron-sulfur cluster to encourage stress tolerance. To test this, incorporating mutations that are involved in redox switching *in vitro* could be incorporated into redox-sensitive cells and assessing phenotypes in this context. However, until the issues inherent to yeast and Okazaki fragment maturation are addressed, it is impossible to conclude if there is or is not a functional role for redox switching in a cellular context.

An iron-sulfur cluster in pol α: implications for pol-prim function.

We have established that the redox switching property of primase is important for its activity *in vitro*. With the discovery of the 4Fe-4S cluster in pol ε and evidence for a functional role of the [4Fe-4S] cluster in pol δ, it is logical that the 4Fe-4S cluster in pol α may also be functionally important. Since the prim lobe is active *in vitro* whether it binds a zinc ion or a [4Fe-4S] cluster, it is not essential for the catalytic activity of pol α. More likely, it is involved in regulating primer length, either for primase, pol α or both.

Because the redox state of the primase [4Fe-4S] cluster governs its substrate binding affinity and possibly in part drives primer handoff, there must be some redox communication between primase and another element. The most obvious regulator to investigate is pol α. The pol α [4Fe-4S] cluster could exchange redox states with the primase oxidized [4Fe-4S] cluster, reducing its affinity for its product, mediating primer counting and handoff.

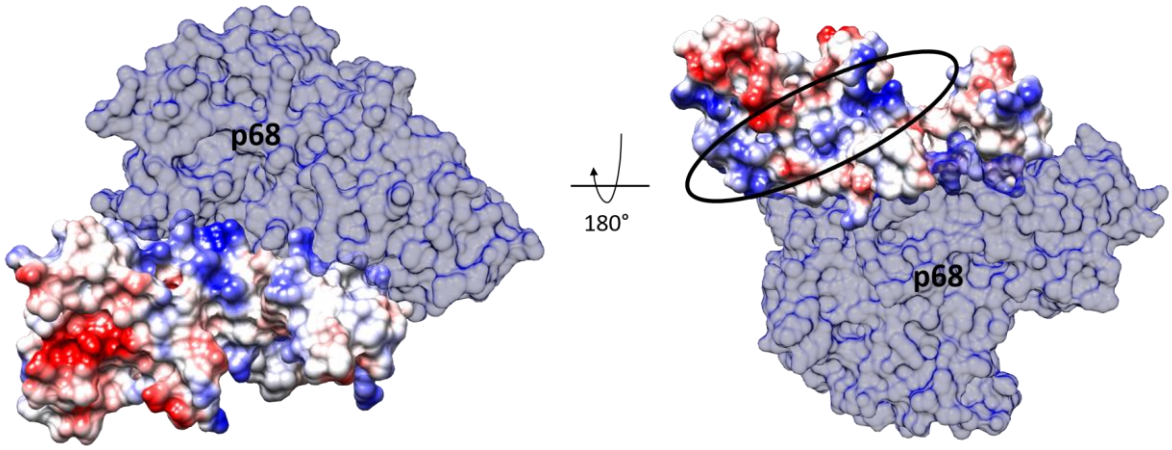

Figure 8.4: surface representation of p180C (residues 1256-1462) in complex with p68 (blue). p180C is colored by surface charge where blue represents basic surface areas and red represents acidic areas. The DNA polyanion would likely bind in a basic patch, indicated by a circle in the right panel.

So far, we have hypothesized that this redox switch must be through DNA, mediated by tyrosine residues that span from the substrate binding surface to the [4Fe-4S] cluster. However, there is no direct evidence in the literature that p180C binds DNA, which has been a red flag from the beginning. We have obtained some preliminary data that suggests that the p180C

complex can engage in DNA-mediated charge transfer. From the available crystal structures of p180C-p68, there are some basic patches in p180CTD that have the potential to bind DNA (Figure 8.4). There is a large area of positive charge on p180C forms an interaction with p68 (Figure 8.4, right). There is a secondary basic cleft that could be involved in nucleic acid binding (Figure 8.4, circled). I hypothesize that this cleft is what interacts with the DNA in the electrochemistry experiments.

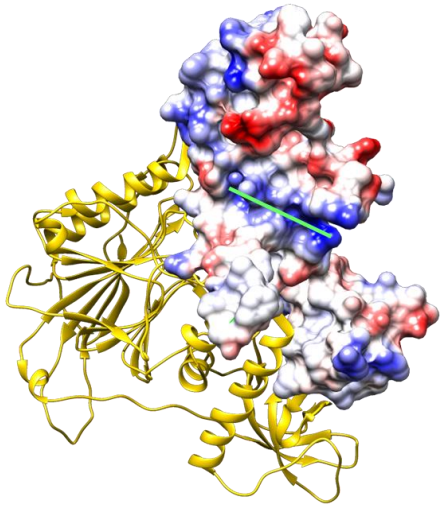

Figure 8.5: surface representation of p180C in complex with p68 (yellow) and p58N (light blue). The accessible basic cleft in the p68dN-p180C is marked with a green line. It is occluded when in complex with p58N.

However, this basic cleft is occluded by p58N in the pol-prim complex (Figure 8.5). While we don't know how the Fe-S cluster-loaded p180C is different than the zinc-loaded protein, the likelihood of this drastically changing the interactions with the additional subunits and creating a new nucleic acid binding interface is low, especially given that the putative cluster-binding CysB motif is in a solvent-exposed loop region that is fairly distal to the core of the protein.

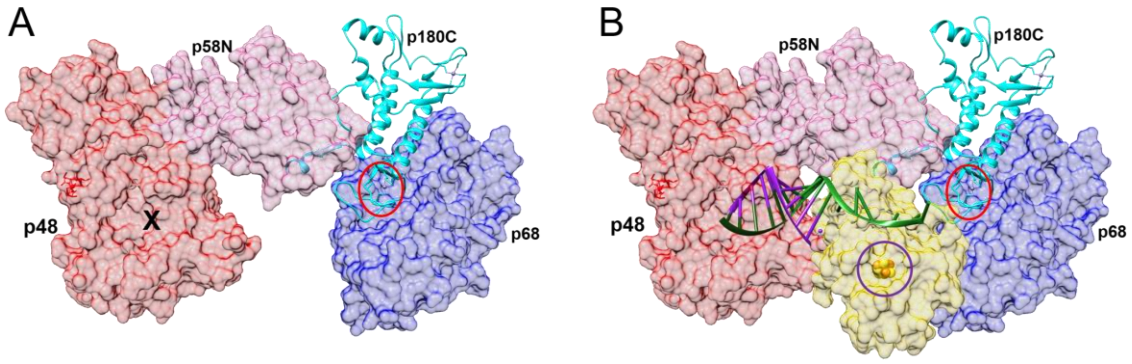

Figure 8.6: Model depicting how redox communication may occur in the prim lobe. A.) the prim lobe, with p58C absent. p48 is in red, p58N is in light blue, p180C is in green, p68 is in yellow. The catalytic site is marked with an X, the probable Fe-S site (predicted by homology with pol δ) is marked with a red circle. B.) Model of the prim lobe + p58C during priming. p48 is in red, p58N is in pink, p58C is in yellow, p180C is in cyan, p68 is in blue. The primed substrate is in purple and green. The Fe-S in p58C is indicated by a purple circle and the putative Fe-S site in p180C is marked with a red circle.

The binding of p180CTD to DNA also poses a steric problem—how is the DNA passed between three domains (p58C, p180C, and p180CAT)? Does p180C bind to the 3' end of the primer to facilitate DNA-mediated reduction of p58C's Fe-S cluster? However, interaction of p180C with the 3' end of the primer is inconsistent with all available crystal structures.

I propose a different mechanism. We know that the primase catalytic subunit p48 synthesizes the RNA primer. p58C binds the 5' triphosphate and p48 adds the 3' nucleotides. We expect p58C to participate in priming by initially sitting over the p48 active site, then moving towards p58N as the primer is synthesized. Importantly, it is p58N that binds p180C (Figure 8.6, left). This suggests that the Fe-S cluster of p180C is close to p58C as the primer reaches 8-12 nts (Figure 8.6, right). Due to their potentially close proximity, it is possible that electron transfer occurs directly between p180C and p58C. Redox exchange would reduce the oxidized Fe-S cluster in p58C, lower its affinity for the substrate, and oxidize p180CAT Fe-S cluster, which in turn would increase its affinity for the substrate and facilitate extending the primer.

In order to test this, it would be important to perform experiments with stably oxidized or stably reduced primase and pol α. Due to recent advances in electrochemistry, it is possible to

oxidize or reduce a protein of interest and subsequently use that protein in a biochemical assay without altering the redox state [63]. This type of assay is necessary to assess how redox communication may be involved in regulating priming.

Additional useful information could be obtained using structural techniques. Although structures will not provide direct evidence for communication between the 4Fe-4S clusters in p180C and p58C, having a global picture of the 3D architecture of pol-prim during the catalytic cycle will reveal the relative positioning of the subunits, allowing for more informed hypotheses about how redox exchange occurs. Structural information will also provide critical insight into the molecular basis for primer initiation and primer handoff between the primase active site and the pol α active site.

Iron-sulfur clusters at the replication fork.

Polymerase dynamics at the replication fork have always been a subject of intense study, especially on the lagging strand where pol-prim and pol δ collaborate to generate thousands of short Okazaki fragments. The identification of [4Fe-4S] clusters in all replicative polymerases offers an additional layer of complexity. While a functional role for the [4Fe-4S] cluster in pol ε has yet to be identified, functional roles have already been identified for pol δ and pol-prim, with the [4Fe-4S] cluster in pol δ serving to stall replication in the presence of oxidative stress [98] and the [4Fe-4S] clusters in pol-prim serving a role in regulation of priming [76-78]. Understanding of the roles of [4Fe-4S] clusters in polymerases continues to rapidly advance and it is well possible that redox homeostasis has a larger role in replisome dynamics than previously thought.

Interestingly, there is a strong link between mitochondrial dysfunction and genome instability [47, 48]. This is due to the necessity of a proper mitochondrial environment in transporting sulfide compounds out of the mitochondria to be used in cytosolic Fe-S assembly [231], a process by which most nuclear Fe-S cluster proteins are generated, including primase [232]. Interestingly, some yeast cells (ρ^0) are able to survive without an actively respiring

mitochondrion, but not without the mitochondrion itself [48]. It is possible that these mitochondria are impaired in normal processes but are able to perform some basal level of Fe-S biogenesis. This is supported by the fact that downregulation of Fe-S cluster proteins in the ρ^0 is able to rescue the genome instability phenotype [48]. This suggests that while mitochondrial respiration is an important function of the mitochondria in yeast, a more essential function involves Fe-S assembly. This is unsurprising given the ubiquity of Fe-4 clusters in basic cellular functions as well as in DNA replication and repair. In the nucleus, DNA replication and repair Fe-S cluster proteins could function as important regulators, coupling overall cell function to DNA replication and repair. In times of extreme stress, disrupted Fe-S assembly could cause stalling of replication and repair, allowing the cell to focus resources on regaining homeostasis or triggering apoptosis.

Despite the importance of Fe-S clusters in many DNA replication and repair proteins, some of the most fascinating work has been done using replisome reconstitution systems. All of these proteins are generated aerobically, likely precluding the incorporation of the 4Fe-4S cluster in pol α and pol ε. During assays, pol-prim is able to synthesize long tracts of daughter strand DNA in the absence of pol δ; in some cases, pol-prim can synthesize up to 3000 bases [33, 91]. This is significantly more than the ~30 nucleotide primers that pol-prim is assumed to make *in vitro*. In fact, in some reconstitution assays, only SV40 T-antigen, RPA, and a single replicative polymerase, pol-prim, is necessary for replication [1]. The observation of [4Fe-4S] clusters in polymerases may be the key to reconciling the observations *in vitro* with observations *in vivo*. If [4Fe-4S] cluster-containing pol α were used in these assays, would the SV40 T-antigen + RPA + pol-prim system still function as previously observed [1]? Would pol-prim still be able to synthesize long tracts of DNA if primase and pol α contain a [4Fe-4S] cluster? A recent study investigating the residence times of pols at the replication fork in live cells suggests that the residence time of pol-prim is much shorter than other pols [224]. Is this because the native pol-prim contains a 4Fe-4S cluster in both primase and in pol α? Do the observations of

[4Fe-4S] cluster redox hold *in vivo* and facilitate primer handoff as we hypothesize? Now that we have the tools to assess replisome behavior *in vitro*, it is possible to take a closer look at how redox switching plays a role in regulating replication.

Concluding Remarks

Replication is a fascinating subject. It is theoretically simple and yet despite 80 years of study, there are unanswered questions. The work presented here detailed a fundamentally new idea for how priming might be regulated by the redox state of [4Fe-4S] clusters. Future work will continue to assess how the [4Fe-4S] cluster in pol α influences priming and to put iron-sulfur clusters in proper context at the replication fork.

References

1. Fairman, M., et al., *Identification of cellular components required for SV40 DNA replication in vitro.* Biochim Biophys Acta, 1988. **951**(2-3): p. 382-7.
2. Spadari, S. and A. Weissbach, *RNA-primed DNA synthesis: specific catalysis by HeLa cell DNA polymerase alpha.* Proc Natl Acad Sci U S A, 1975. **72**(2): p. 503-7.
3. Tsurimoto, T., M.P. Fairman, and B. Stillman, *Simian virus 40 DNA replication in vitro: identification of multiple stages of initiation.* Mol Cell Biol, 1989. **9**(9): p. 3839-49.
4. Tsurimoto, T. and B. Stillman, *Multiple replication factors augment DNA synthesis by the two eukaryotic DNA polymerases, alpha and delta.* EMBO J, 1989. **8**(12): p. 3883-9.
5. Pavlov, Y.I., et al., *Evidence that errors made by DNA polymerase alpha are corrected by DNA polymerase delta.* Curr Biol, 2006. **16**(2): p. 202-7.
6. Tsurimoto, T., T. Melendy, and B. Stillman, *Sequential initiation of lagging and leading strand synthesis by two different polymerase complexes at the SV40 DNA replication origin.* Nature, 1990. **346**(6284): p. 534-9.
7. Koc, K.N., et al., *Regulation of yeast DNA polymerase delta-mediated strand displacement synthesis by 5'-flaps.* Nucleic Acids Res, 2015. **43**(8): p. 4179-90.
8. Maga, G., et al., *Okazaki fragment processing: modulation of the strand displacement activity of DNA polymerase delta by the concerted action of replication protein A, proliferating cell nuclear antigen, and flap endonuclease-1.* Proc Natl Acad Sci U S A, 2001. **98**(25): p. 14298-303.
9. Stith, C.M., et al., *Flexibility of eukaryotic Okazaki fragment maturation through regulated strand displacement synthesis.* J Biol Chem, 2008. **283**(49): p. 34129-40.
10. Kilkenny, M.L., et al., *The human CTF4-orthologue AND-1 interacts with DNA polymerase alpha/primase via its unique C-terminal HMG box.* Open Biol, 2017. **7**(11).
11. Simon, A.C., et al., *A Ctf4 trimer couples the CMG helicase to DNA polymerase alpha in the eukaryotic replisome.* Nature, 2014. **510**(7504): p. 293-297.
12. Ricke, R.M. and A.K. Bielinsky, *Mcm10 regulates the stability and chromatin association of DNA polymerase-alpha.* Mol Cell, 2004. **16**(2): p. 173-85.
13. Warren, E.M., et al., *Physical interactions between Mcm10, DNA, and DNA polymerase alpha.* J Biol Chem, 2009. **284**(36): p. 24662-72.
14. Cho, W.H., et al., *Human Tim-Tipin complex affects the biochemical properties of the replicative DNA helicase and DNA polymerases.* Proc Natl Acad Sci U S A, 2013. **110**(7): p. 2523-7.
15. De Falco, M., et al., *The human GINS complex binds to and specifically stimulates human DNA polymerase alpha-primase.* EMBO Rep, 2007. **8**(1): p. 99-103.
16. Errico, A., et al., *Tipin/Tim1/And1 protein complex promotes Pol alpha chromatin binding and sister chromatid cohesion.* EMBO J, 2009. **28**(23): p. 3681-92.
17. Dornreiter, I., et al., *Interaction of DNA polymerase alpha-primase with cellular replication protein A and SV40 T antigen.* EMBO J, 1992. **11**(2): p. 769-76.
18. Maga, G., et al., *Replication protein A as a "fidelity clamp" for DNA polymerase alpha.* J Biol Chem, 2001. **276**(21): p. 18235-42.
19. Maga, G., et al., *DNA polymerase switching: I. Replication factor C displaces DNA polymerase alpha prior to PCNA loading.* J Mol Biol, 2000. **295**(4): p. 791-801.
20. Tsurimoto, T. and B. Stillman, *Functions of replication factor C and proliferating-cell nuclear antigen: functional similarity of DNA polymerase accessory proteins from human cells and bacteriophage T4.* Proc Natl Acad Sci U S A, 1990. **87**(3): p. 1023-7.
21. Giannattasio, M. and D. Branzei, *DNA Replication Through Strand Displacement During Lagging Strand DNA Synthesis in Saccharomyces cerevisiae.* Genes (Basel), 2019. **10**(2).

22. Plevani, P., et al., *The yeast DNA polymerase-primase complex: genes and proteins.* Biochim Biophys Acta, 1988. **951**(2-3): p. 268-73.
23. Grosse, F. and G. Krauss, *The primase activity of DNA polymerase alpha from calf thymus.* J Biol Chem, 1985. **260**(3): p. 1881-8.
24. Zerbe, L.K. and R.D. Kuchta, *The p58 subunit of human DNA primase is important for primer initiation, elongation, and counting.* Biochemistry, 2002. **41**(15): p. 4891-900.
25. Zhang, Y., et al., *The C-terminal domain of the DNA polymerase catalytic subunit regulates the primase and polymerase activities of the human DNA polymerase alpha-primase complex.* J Biol Chem, 2014. **289**(32): p. 22021-34.
26. Perera, R.L., et al., *Mechanism for priming DNA synthesis by yeast DNA polymerase alpha.* Elife, 2013. **2**: p. e00482.
27. Zhang, Y., et al., *Divalent ions attenuate DNA synthesis by human DNA polymerase alpha by changing the structure of the template/primer or by perturbing the polymerase reaction.* DNA Repair (Amst), 2016. **43**: p. 24-33.
28. Voitenleitner, C., et al., *Cell cycle-dependent regulation of human DNA polymerase alpha-primase activity by phosphorylation.* Mol Cell Biol, 1999. **19**(1): p. 646-56.
29. Collins, K.L., et al., *The role of the 70 kDa subunit of human DNA polymerase alpha in DNA replication.* EMBO J, 1993. **12**(12): p. 4555-66.
30. Kuchta, R.D., B. Reid, and L.M. Chang, *DNA primase. Processivity and the primase to polymerase alpha activity switch.* J Biol Chem, 1990. **265**(27): p. 16158-65.
31. Sheaff, R.J., R.D. Kuchta, and D. Ilsley, *Calf thymus DNA polymerase alpha-primase: "communication" and primer-template movement between the two active sites.* Biochemistry, 1994. **33**(8): p. 2247-54.
32. Singh, H., et al., *Yeast DNA primase and DNA polymerase activities. An analysis of RNA priming and its coupling to DNA synthesis.* J Biol Chem, 1986. **261**(18): p. 8564-9.
33. Georgescu, R.E., et al., *Reconstitution of a eukaryotic replisome reveals suppression mechanisms that define leading/lagging strand operation.* Elife, 2015. **4**: p. e04988.
34. Baranovskiy, A.G., et al., *Crystal structure of the human primase.* J Biol Chem, 2015. **290**(9): p. 5635-46.
35. Vaithiyalingam, S., et al., *Insights into eukaryotic primer synthesis from structures of the p48 subunit of human DNA primase.* J Mol Biol, 2014. **426**(3): p. 558-69.
36. Kilkenny, M.L., et al., *Structures of human primase reveal design of nucleotide elongation site and mode of Pol alpha tethering.* Proc Natl Acad Sci U S A, 2013. **110**(40): p. 15961-6.
37. Holzer, S., et al., *Structural Basis for Inhibition of Human Primase by Arabinofuranosyl Nucleoside Analogues Fludarabine and Vidarabine.* ACS Chem Biol, 2019. **14**(9): p. 1904-1912.
38. Baranovskiy, A.G., et al., *Mechanism of Concerted RNA-DNA Primer Synthesis by the Human Primosome.* J Biol Chem, 2016. **291**(19): p. 10006-20.
39. Baranovskiy, A.G., et al., *Activity and fidelity of human DNA polymerase alpha depend on primer structure.* J Biol Chem, 2018. **293**(18): p. 6824-6843.
40. Coloma, J., et al., *Human DNA polymerase alpha in binary complex with a DNA:DNA template-primer.* Sci Rep, 2016. **6**: p. 23784.
41. Baranovskiy, A.G., et al., *Structural basis for inhibition of DNA replication by aphidicolin.* Nucleic Acids Res, 2014. **42**(22): p. 14013-21.
42. Klinge, S., et al., *3D architecture of DNA Pol alpha reveals the functional core of multi-subunit replicative polymerases.* EMBO J, 2009. **28**(13): p. 1978-87.
43. Suwa, Y., et al., *Crystal Structure of the Human Pol alpha B Subunit in Complex with the C-terminal Domain of the Catalytic Subunit.* J Biol Chem, 2015. **290**(23): p. 14328-37.
44. Nunez-Ramirez, R., et al., *Flexible tethering of primase and DNA Pol alpha in the eukaryotic primosome.* Nucleic Acids Res, 2011. **39**(18): p. 8187-99.

45. Fuss, J.O., et al., *Emerging critical roles of Fe-S clusters in DNA replication and repair.* Biochim Biophys Acta, 2015. **1853**(6): p. 1253-71.
46. Ye, H. and T.A. Rouault, *Human iron-sulfur cluster assembly, cellular iron homeostasis, and disease.* Biochemistry, 2010. **49**(24): p. 4945-56.
47. Lill, R., V. Srinivasan, and U. Muhlenhoff, *The role of mitochondria in cytosolic-nuclear iron-sulfur protein biogenesis and in cellular iron regulation.* Curr Opin Microbiol, 2014. **22**: p. 111-9.
48. Veatch, J.R., et al., *Mitochondrial dysfunction leads to nuclear genome instability via an iron-sulfur cluster defect.* Cell, 2009. **137**(7): p. 1247-58.
49. Lill, R. and U. Muhlenhoff, *Iron-sulfur-protein biogenesis in eukaryotes.* Trends Biochem Sci, 2005. **30**(3): p. 133-41.
50. McCarthy, E.L. and S.J. Booker, *Bridging a gap in iron-sulfur cluster assembly.* Elife, 2015. **4**.
51. Lill, R. and U. Muhlenhoff, *Iron-sulfur protein biogenesis in eukaryotes: components and mechanisms.* Annu Rev Cell Dev Biol, 2006. **22**: p. 457-86.
52. Bowman, S.E., J. Bridwell-Rabb, and C.L. Drennan, *Metalloprotein Crystallography: More than a Structure.* Acc Chem Res, 2016. **49**(4): p. 695-702.
53. Imlay, J.A., *Iron-sulphur clusters and the problem with oxygen.* Molecular Microbiology, 2006. **59**(4): p. 1073-1082.
54. Rouault, T.A., *Iron-sulfur proteins hiding in plain sight.* Nat Chem Biol, 2015. **11**(7): p. 442-5.
55. Silva, R.M.B., M.A. Grodick, and J.K. Barton, *UvrC Coordinates an O2-Sensitive [4Fe4S] Cofactor.* J Am Chem Soc, 2020. **142**(25): p. 10964-10977.
56. Boal, A.K., et al., *Redox signaling between DNA repair proteins for efficient lesion detection.* Proc Natl Acad Sci U S A, 2009. **106**(36): p. 15237-42.
57. Boon, E.M., et al., *DNA-mediated charge transport as a probe of MutY/DNA interaction.* Biochemistry, 2002. **41**(26): p. 8464-70.
58. Gorodetsky, A.A., A.K. Boal, and J.K. Barton, *Direct electrochemistry of endonuclease III in the presence and absence of DNA.* J Am Chem Soc, 2006. **128**(37): p. 12082-3.
59. Lee, P.E., B. Demple, and J.K. Barton, *DNA-mediated redox signaling for transcriptional activation of SoxR.* Proc Natl Acad Sci U S A, 2009. **106**(32): p. 13164-8.
60. Romano, C.A., P.A. Sontz, and J.K. Barton, *Mutants of the base excision repair glycosylase, endonuclease III: DNA charge transport as a first step in lesion detection.* Biochemistry, 2011. **50**(27): p. 6133-45.
61. Sontz, P.A., et al., *DNA charge transport as a first step in coordinating the detection of lesions by repair proteins.* Proc Natl Acad Sci U S A, 2012. **109**(6): p. 1856-61.
62. Boon, E.M. and J.K. Barton, *Charge transport in DNA.* Curr Opin Struct Biol, 2002. **12**(3): p. 320-9.
63. Tse, E.C.M., T.J. Zwang, and J.K. Barton, *The Oxidation State of [4Fe4S] Clusters Modulates the DNA-Binding Affinity of DNA Repair Proteins.* J Am Chem Soc, 2017. **139**(36): p. 12784-12792.
64. Xiang, L., et al., *Intermediate tunnelling-hopping regime in DNA charge transport.* Nat Chem, 2015. **7**(3): p. 221-6.
65. Teo, R.D., et al., *Charge Transfer between [4Fe4S] Proteins and DNA Is Unidirectional: Implications for Biomolecular Signaling.* Chem, 2019. **5**(1): p. 122-137.
66. Genereux, J.C., A.K. Boal, and J.K. Barton, *DNA-mediated charge transport in redox sensing and signaling.* J Am Chem Soc, 2010. **132**(3): p. 891-905.
67. Grodick, M.A., et al., *DNA-mediated signaling by proteins with 4Fe-4S clusters is necessary for genomic integrity.* J Am Chem Soc, 2014. **136**(17): p. 6470-8.
68. Yavin, E., et al., *Electron trap for DNA-bound repair enzymes: a strategy for DNA-mediated signaling.* Proc Natl Acad Sci U S A, 2006. **103**(10): p. 3610-4.

69. Klinge, S., et al., *An iron-sulfur domain of the eukaryotic primase is essential for RNA primer synthesis.* Nat Struct Mol Biol, 2007. **14**(9): p. 875-7.
70. Weiner, B.E., et al., *An iron-sulfur cluster in the C-terminal domain of the p58 subunit of human DNA primase.* J Biol Chem, 2007. **282**(46): p. 33444-51.
71. Agarkar, V.B., et al., *Crystal structure of the C-terminal domain of human DNA primase large subunit: implications for the mechanism of the primase-polymerase alpha switch.* Cell Cycle, 2011. **10**(6): p. 926-31.
72. Sauguet, L., et al., *Shared active site architecture between the large subunit of eukaryotic primase and DNA photolyase.* PLoS One, 2010. **5**(4): p. e10083.
73. Vaithiyalingam, S., et al., *Insights into eukaryotic DNA priming from the structure and functional interactions of the 4Fe-4S cluster domain of human DNA primase.* Proc Natl Acad Sci U S A, 2010. **107**(31): p. 13684-9.
74. Liu, L. and M. Huang, *Essential role of the iron-sulfur cluster binding domain of the primase regulatory subunit Pri2 in DNA replication initiation.* Protein Cell, 2015. **6**(3): p. 194-210.
75. Somyajit, K., et al., *Redox-sensitive alteration of replisome architecture safeguards genome integrity.* Science, 2017. **358**(6364): p. 797-802.
76. O'Brien, E., et al., *The [4Fe4S] cluster of human DNA primase functions as a redox switch using DNA charge transport.* Science, 2017. **355**(6327).
77. O'Brien, E., et al., *Yeast require redox switching in DNA primase.* Proc Natl Acad Sci U S A, 2018. **115**(52): p. 13186-13191.
78. O'Brien, E., et al., *Substrate Binding Regulates Redox Signaling in Human DNA Primase.* J Am Chem Soc, 2018. **140**(49): p. 17153-17162.
79. Netz, D.J., et al., *Eukaryotic DNA polymerases require an iron-sulfur cluster for the formation of active complexes.* Nat Chem Biol, 2011. **8**(1): p. 125-32.
80. Baranovskiy, A.G., et al., *DNA polymerase delta and zeta switch by sharing accessory subunits of DNA polymerase delta.* J Biol Chem, 2012. **287**(21): p. 17281-7.
81. Copeland, W.C. and T.S. Wang, *Enzymatic characterization of the individual mammalian primase subunits reveals a biphasic mechanism for initiation of DNA replication.* J Biol Chem, 1993. **268**(35): p. 26179-89.
82. Sheaff, R.J. and R.D. Kuchta, *Mechanism of calf thymus DNA primase: slow initiation, rapid polymerization, and intelligent termination.* Biochemistry, 1993. **32**(12): p. 3027-37.
83. Iyer, L.M., et al., *Origin and evolution of the archaeo-eukaryotic primase superfamily and related palm-domain proteins: structural insights and new members.* Nucleic Acids Res, 2005. **33**(12): p. 3875-96.
84. Arezi, B., et al., *Interactions of DNA with human DNA primase monitored with photoactivatable cross-linking agents: implications for the role of the p58 subunit.* Biochemistry, 1999. **38**(39): p. 12899-907.
85. Baranovskiy, A.G., et al., *Insight into the Human DNA Primase Interaction with Template-Primer.* J Biol Chem, 2016. **291**(9): p. 4793-802.
86. Holt, M.E., et al., *Functional and structural similarity of human DNA primase [4Fe4S] cluster domain constructs.* PLoS One, 2018. **13**(12): p. e0209345.
87. Thompson, H.C., R.J. Sheaff, and R.D. Kuchta, *Interactions of calf thymus DNA polymerase alpha with primer/templates.* Nucleic Acids Res, 1995. **23**(20): p. 4109-15.
88. Tsurimoto, T. and B. Stillman, *Replication factors required for SV40 DNA replication in vitro. I. DNA structure-specific recognition of a primer-template junction by eukaryotic DNA polymerases and their accessory proteins.* J Biol Chem, 1991. **266**(3): p. 1950-60.
89. Sheaff, R., D. Ilsley, and R. Kuchta, *Mechanism of DNA polymerase alpha inhibition by aphidicolin.* Biochemistry, 1991. **30**(35): p. 8590-7.
90. Holmes, A.M., et al., *Initiation of DNA synthesis by the calf thymus DNA polymerase-primase complex.* J Biol Chem, 1985. **260**(19): p. 10840-6.

91. Aria, V. and J.T.P. Yeeles, *Mechanism of Bidirectional Leading-Strand Synthesis Establishment at Eukaryotic DNA Replication Origins.* Mol Cell, 2018.
92. Kurat, C.F., et al., *Chromatin Controls DNA Replication Origin Selection, Lagging-Strand Synthesis, and Replication Fork Rates.* Mol Cell, 2017. **65**(1): p. 117-130.
93. Yeeles, J.T., et al., *How the Eukaryotic Replisome Achieves Rapid and Efficient DNA Replication.* Mol Cell, 2017. **65**(1): p. 105-116.
94. Mossi, R., et al., *DNA polymerase switching: II. Replication factor C abrogates primer synthesis by DNA polymerase alpha at a critical length.* J Mol Biol, 2000. **295**(4): p. 803-14.
95. Tsurimoto, T. and B. Stillman, *Replication factors required for SV40 DNA replication in vitro. II. Switching of DNA polymerase alpha and delta during initiation of leading and lagging strand synthesis.* J Biol Chem, 1991. **266**(3): p. 1961-8.
96. Lewis, J.S., et al., *Tunability of DNA Polymerase Stability during Eukaryotic DNA Replication.* Mol Cell, 2020. **77**(1): p. 17-25 e5.
97. Jain, R., et al., *An iron-sulfur cluster in the polymerase domain of yeast DNA polymerase epsilon.* J Mol Biol, 2014. **426**(2): p. 301-8.
98. Bartels, P.L., et al., *A Redox Role for the [4Fe4S] Cluster of Yeast DNA Polymerase delta.* J Am Chem Soc, 2017. **139**(50): p. 18339-18348.
99. Schmid, F.-X., *Biological Macromolecules: UV-visible Spectrophotometry.* eLS, 2001.
100. Freibert, S.A., et al., *Biochemical Reconstitution and Spectroscopic Analysis of Iron-Sulfur Proteins.* Methods Enzymol, 2018. **599**: p. 197-226.
101. Smith, F.E., et al., *Serum iron determination using ferene triazine.* Clin Biochem, 1984. **17**(5): p. 306-10.
102. Greenfield, N.J., *Using circular dichroism spectra to estimate protein secondary structure.* Nat Protoc, 2006. **1**(6): p. 2876-90.
103. Kypr, J., et al., *Circular dichroism and conformational polymorphism of DNA.* Nucleic Acids Res, 2009. **37**(6): p. 1713-25.
104. Greenfield, N.J., *Determination of the folding of proteins as a function of denaturants, osmolytes or ligands using circular dichroism.* Nat Protoc, 2006. **1**(6): p. 2733-41.
105. Greenfield, N.J., *Using circular dichroism collected as a function of temperature to determine the thermodynamics of protein unfolding and binding interactions.* Nat Protoc, 2006. **1**(6): p. 2527-35.
106. Rossi, A.M. and C.W. Taylor, *Analysis of protein-ligand interactions by fluorescence polarization.* Nat Protoc, 2011. **6**(3): p. 365-87.
107. Wlodawer, A., et al., *Protein crystallography for non-crystallographers, or how to get the best (but not more) from published macromolecular structures.* FEBS J, 2008. **275**(1): p. 1-21.
108. Wlodawer, A., et al., *Protein crystallography for aspiring crystallographers or how to avoid pitfalls and traps in macromolecular structure determination.* FEBS J, 2013. **280**(22): p. 5705-36.
109. Russo Krauss, I., et al., *An overview of biological macromolecule crystallization.* Int J Mol Sci, 2013. **14**(6): p. 11643-91.
110. Vekilov, P.G., et al., *Solvent entropy contribution to the free energy of protein crystallization.* Acta Crystallogr D Biol Crystallogr, 2002. **58**(Pt 10 Pt 1): p. 1611-6.
111. Stura, E.A. and I.A. Wilson, *Applications of the streak seeding technique in protein crystallization.* Journal of Crystal Growth, 1991. **110**(1): p. 270-282.
112. Scapin, G., *Molecular replacement then and now.* Acta Crystallogr D Biol Crystallogr, 2013. **69**(Pt 11): p. 2266-75.
113. Evans, P. and A. McCoy, *An introduction to molecular replacement.* Acta Crystallogr D Biol Crystallogr, 2008. **64**(Pt 1): p. 1-10.

114. Emsley, P., et al., *Features and development of Coot.* Acta Crystallogr D Biol Crystallogr, 2010. **66**(Pt 4): p. 486-501.
115. Murshudov, G.N., et al., *REFMAC5 for the refinement of macromolecular crystal structures.* Acta Crystallogr D Biol Crystallogr, 2011. **67**(Pt 4): p. 355-67.
116. Adams, P.D., et al., *PHENIX: a comprehensive Python-based system for macromolecular structure solution.* Acta Crystallogr D Biol Crystallogr, 2010. **66**(Pt 2): p. 213-21.
117. Grodick, M.A., N.B. Muren, and J.K. Barton, *DNA charge transport within the cell.* Biochemistry, 2015. **54**(4): p. 962-73.
118. Pheeney, C.G., et al., *Multiplexed electrochemistry of DNA-bound metalloproteins.* J Am Chem Soc, 2013. **135**(32): p. 11869-78.
119. Rees, D.C. and J.B. Howard, *The Interface Between the Biological and Inorganic Worlds: Iron-Sulfur Metalloclusters.* Science, 2003. **300**(5621): p. 929.
120. Rouault, T.A., *Mammalian iron-sulphur proteins: novel insights into biogenesis and function.* Nat Rev Mol Cell Biol, 2015. **16**(1): p. 45-55.
121. Kilkenny, M.L., et al., *A conserved motif in the C-terminal tail of DNA polymerase alpha tethers primase to the eukaryotic replisome.* J Biol Chem, 2012. **287**(28): p. 23740-7.
122. Arezi, B. and R.D. Kuchta, *Eukaryotic DNA primase.* Trends Biochem Sci, 2000. **25**(11): p. 572-6.
123. Frick, D.N. and C.C. Richardson, *DNA primases.* Annu Rev Biochem, 2001. **70**: p. 39-80.
124. Kuchta, R.D. and G. Stengel, *Mechanism and evolution of DNA primases.* Biochim Biophys Acta, 2010. **1804**(5): p. 1180-9.
125. O'Donnell, M., L. Langston, and B. Stillman, *Principles and concepts of DNA replication in bacteria, archaea, and eukarya.* Cold Spring Harb Perspect Biol, 2013. **5**(7).
126. Lue, N.F., et al., *The CDC13-STN1-TEN1 complex stimulates Pol alpha activity by promoting RNA priming and primase-to-polymerase switch.* Nat Commun, 2014. **5**: p. 5762.
127. Garg, P. and P.M.J. Burgers, *DNA Polymerases that Propagate the Eukaryotic DNA Replication Fork.* Critical Reviews in Biochemistry and Molecular Biology, 2005. **40**(2): p. 115-128.
128. Slinker, J.D., et al., *Multiplexed DNA-modified electrodes.* J Am Chem Soc, 2010. **132**(8): p. 2769-74.
129. Slinker, J.D., et al., *DNA charge transport over 34 nm.* Nat Chem, 2011. **3**(3): p. 228-33.
130. Pettersen, E.F., et al., *UCSF chimera - A visualization system for exploratory research and analysis.* Journal of Computational Chemistry, 2004. **25**(13): p. 1605-1612.
131. Forbes, S.A., et al., *COSMIC: mining complete cancer genomes in the Catalogue of Somatic Mutations in Cancer.* Nucleic Acids Res, 2011. **39**(Database issue): p. D945-50.
132. Otwinowski, Z. and W. Minor, *Processing of X-ray diffraction data collected in oscillation mode.* Methods Enzymol, 1997. **276**: p. 307-26.
133. Winn, M.D., et al., *Overview of the CCP4 suite and current developments.* Acta Crystallogr D Biol Crystallogr, 2011. **67**(Pt 4): p. 235-42.
134. Mccoy, A.J., et al., *Phaser crystallographic software.* Journal of Applied Crystallography, 2007. **40**: p. 658-674.
135. Cunningham, R.P., et al., *Endonuclease III is an iron-sulfur protein.* Biochemistry, 1989. **28**(10): p. 4450-5.
136. Kirk, B.W., et al., *Eucaryotic DNA primase does not prefer to synthesize primers at pyrimidine rich DNA sequences when nucleoside triphosphates are present at concentrations found in whole cells.* Biochemistry, 1997. **36**(22): p. 6725-31.

137. Kirk, B.W. and R.D. Kuchta, *Human DNA primase: anion inhibition, manganese stimulation, and their effects on in vitro start-site selection.* Biochemistry, 1999. **38**(31): p. 10126-34.
138. Boal, A.K., et al., *DNA-bound redox activity of DNA repair glycosylases containing [4Fe-4S] clusters.* Biochemistry, 2005. **44**(23): p. 8397-407.
139. Imlay, J.A., *Iron-sulphur clusters and the problem with oxygen.* Mol Microbiol, 2006. **59**(4): p. 1073-82.
140. Mui, T.P., et al., *ATP-stimulated, DNA-mediated redox signaling by XPD, a DNA repair and transcription helicase.* J Am Chem Soc, 2011. **133**(41): p. 16378-81.
141. Gray, H.B. and J.R. Winkler, *Electron flow through metalloproteins.* Biochimica et Biophysica Acta (BBA) - Bioenergetics, 2010. **1797**(9): p. 1563-1572.
142. Winkler, J.R. and H.B. Gray, *Long-range electron tunneling.* J Am Chem Soc, 2014. **136**(8): p. 2930-9.
143. Shih, C., et al., *Tryptophan-accelerated electron flow through proteins.* Science, 2008. **320**(5884): p. 1760-2.
144. Plekan, O., et al., *Valence photoionization and photofragmentation of aromatic amino acids.* Molecular Physics, 2008. **106**(9-10): p. 1143-1153.
145. Stubbe, J., et al., *Radical initiation in the class I ribonucleotide reductase: long-range proton-coupled electron transfer?* Chem Rev, 2003. **103**(6): p. 2167-201.
146. Stubbe, J. and W.A. van Der Donk, *Protein Radicals in Enzyme Catalysis.* Chem Rev, 1998. **98**(2): p. 705-762.
147. Sheaff, R.J. and R.D. Kuchta, *Misincorporation of nucleotides by calf thymus DNA primase and elongation of primers containing multiple noncognate nucleotides by DNA polymerase alpha.* J Biol Chem, 1994. **269**(30): p. 19225-31.
148. Boon, E.M. and J.K. Barton, *DNA electrochemistry as a probe of base pair stacking in A-, B-, and Z-form DNA.* Bioconjug Chem, 2003. **14**(6): p. 1140-7.
149. O'Neill, M.A. and J.K. Barton, *2-Aminopurine: a probe of structural dynamics and charge transfer in DNA and DNA:RNA hybrids.* J Am Chem Soc, 2002. **124**(44): p. 13053-66.
150. Garcia-Diaz, M., et al., *Role of the catalytic metal during polymerization by DNA polymerase lambda.* DNA Repair (Amst), 2007. **6**(9): p. 1333-40.
151. O'Neill, M.A. and J.K. Barton, *DNA-mediated charge transport requires conformational motion of the DNA bases: elimination of charge transport in rigid glasses at 77 K.* J Am Chem Soc, 2004. **126**(41): p. 13234-5.
152. O'Neill, M.A., et al., *Ultrafast dynamics in DNA-mediated electron transfer: base gating and the role of temperature.* Angew Chem Int Ed Engl, 2003. **42**(47): p. 5896-900.
153. Baranovskiy, A.G., et al., *Comment on "The [4Fe4S] cluster of human DNA primase functions as a redox switch using DNA charge transport".* Science, 2017. **357**(6348).
154. Pellegrini, L., *Comment on "The [4Fe4S] cluster of human DNA primase functions as a redox switch using DNA charge transport".* Science, 2017. **357**(6348).
155. Stodola, J.L. and P.M. Burgers, *Mechanism of Lagging-Strand DNA Replication in Eukaryotes.* Adv Exp Med Biol, 2017. **1042**: p. 117-133.
156. Burgers, P.M.J. and T.A. Kunkel, *Eukaryotic DNA Replication Fork.* Annu Rev Biochem, 2017. **86**: p. 417-438.
157. Yao, N. and M. O'Donnell, *Bacterial and Eukaryotic Replisome Machines.* JSM Biochem Mol Biol, 2016. **3**(1).
158. Yeeles, J.T.P., et al., *How the Eukaryotic Replisome Achieves Rapid and Efficient DNA Replication.* Mol Cell, 2017. **65**(1): p. 105-116.
159. Baranovskiy, A.G. and T.H. Tahirov, *Elaborated Action of the Human Primosome.* Genes (Basel), 2017. **8**(2).
160. Pellegrini, L. and A. Costa, *New Insights into the Mechanism of DNA Duplication by the Eukaryotic Replisome.* Trends Biochem Sci, 2016. **41**(10): p. 859-871.

161. Holzer, S., et al., *Primer synthesis by a eukaryotic-like archaeal primase is independent of its Fe-S cluster.* Nat Commun, 2017. **8**(1): p. 1718.
162. O'Brien, E., et al., *Response to Comments on "The [4Fe4S] cluster of human DNA primase functions as a redox switch using DNA charge transport".* Science, 2017. **357**(6348).
163. Holt, M.E., L.E. Salay, and W.J. Chazin, *A Polymerase With Potential: The Fe-S Cluster in Human DNA Primase.* Methods Enzymol, 2017. **595**: p. 361-390.
164. Afonine, P.V., et al., *Towards automated crystallographic structure refinement with phenix.refine.* Acta Crystallogr D Biol Crystallogr, 2012. **68**(Pt 4): p. 352-67.
165. Pettersen, E.F., et al., *UCSF Chimera--a visualization system for exploratory research and analysis.* J Comput Chem, 2004. **25**(13): p. 1605-12.
166. Morin, A., et al., *Collaboration gets the most out of software.* Elife, 2013. **2**: p. e01456.
167. Guillerez, J., et al., *A mutation in T7 RNA polymerase that facilitates promoter clearance.* Proc Natl Acad Sci U S A, 2005. **102**(17): p. 5958-63.
168. Linke, P., et al., *An Automated Microscale Thermophoresis Screening Approach for Fragment-Based Lead Discovery.* Journal of Biomolecular Screening, 2016. **21**(4): p. 414-421.
169. Bertini, I., et al., *NMR Spectroscopy of Paramagnetic Metalloproteins.* ChemBioChem, 2005. **6**(9): p. 1536-1549.
170. Eyal, E., et al., *The limit of accuracy of protein modeling: influence of crystal packing on protein structure.* J Mol Biol, 2005. **351**(2): p. 431-42.
171. Diener, J.L., *Complex conformations and crystal contacts.* Nat Struct Biol, 2003. **10**(7): p. 494; author reply 494-5.
172. Layten, M., V. Hornak, and C. Simmerling, *The open structure of a multi-drug-resistant HIV-1 protease is stabilized by crystal packing contacts.* J Am Chem Soc, 2006. **128**(41): p. 13360-1.
173. Taylor, P., et al., *Two structures of cyclophilin 40: folding and fidelity in the TPR domains.* Structure, 2001. **9**(5): p. 431-8.
174. Arunkumar, A.I., et al., *Independent and coordinated functions of replication protein A tandem high affinity single-stranded DNA binding domains.* J Biol Chem, 2003. **278**(42): p. 41077-82.
175. Moran, U., R. Phillips, and R. Milo, *SnapShot: key numbers in biology.* Cell, 2010. **141**(7): p. 1262-1262 e1.
176. Beinert, H., R.H. Holm, and E. Munck, *Iron-sulfur clusters: nature's modular, multipurpose structures.* Science, 1997. **277**(5326): p. 653-9.
177. Kelley, S.O., et al., *Single-base mismatch detection based on charge transduction through DNA.* Nucleic Acids Res, 1999. **27**(24): p. 4830-7.
178. Nunez, M.E., D.B. Hall, and J.K. Barton, *Long-range oxidative damage to DNA: effects of distance and sequence.* Chem Biol, 1999. **6**(2): p. 85-97.
179. Dey, A., et al., *Solvent tuning of electrochemical potentials in the active sites of HiPIP versus ferredoxin.* Science, 2007. **318**(5855): p. 1464-8.
180. McDonnell, K.J., et al., *A human MUTYH variant linking colonic polyposis to redox degradation of the [4Fe4S](2+) cluster.* Nat Chem, 2018. **10**(8): p. 873-880.
181. Kirk, B.W. and R.D. Kuchta, *Arg304 of human DNA primase is a key contributor to catalysis and NTP binding: primase and the family X polymerases share significant sequence homology.* Biochemistry, 1999. **38**(24): p. 7727-36.
182. Bartels, P.L., et al., *Electrochemistry of the [4Fe4S] Cluster in Base Excision Repair Proteins: Tuning the Redox Potential with DNA.* Langmuir, 2017. **33**(10): p. 2523-2530.
183. Johansson, E., P. Garg, and P.M. Burgers, *The Pol32 subunit of DNA polymerase delta contains separable domains for processive replication and proliferating cell nuclear antigen (PCNA) binding.* J Biol Chem, 2004. **279**(3): p. 1907-15.

184. Winkler, J.R. and H.B. Gray, *Electron Flow through Metalloproteins.* Chemical Reviews, 2014. **114**(7): p. 3369-3380.
185. Liang, N., et al., *Yeast cytochrome c with phenylalanine or tyrosine at position 87 transfers electrons to (zinc cytochrome c peroxidase)+ at a rate ten thousand times that of the serine-87 or glycine-87 variants.* Proc Natl Acad Sci U S A, 1987. **84**(5): p. 1249-52.
186. Lukacs, A., et al., *Electron hopping through the 15 A triple tryptophan molecular wire in DNA photolyase occurs within 30 ps.* J Am Chem Soc, 2008. **130**(44): p. 14394-5.
187. Pape, T. and T.R. Schneider, *HKL2MAP: a graphical user interface for macromolecular phasing with SHELX programs.* Journal of Applied Crystallography, 2004. **37**: p. 843-844.
188. Perrakis, A., et al., *wARP: Improvement and extension of crystallographic phases by weighted averaging of multiple-refined dummy atomic models.* Acta Crystallographica Section D-Biological Crystallography, 1997. **53**: p. 448-455.
189. Ji, H., et al., *Regulation of telomere length by an N-terminal region of the yeast telomerase reverse transcriptase.* Mol Cell Biol, 2005. **25**(20): p. 9103-14.
190. Ricke, R.M. and A.K. Bielinsky, *A conserved Hsp10-like domain in Mcm10 is required to stabilize the catalytic subunit of DNA polymerase-alpha in budding yeast.* J Biol Chem, 2006. **281**(27): p. 18414-25.
191. Sikorski, R.S. and P. Hieter, *A system of shuttle vectors and yeast host strains designed for efficient manipulation of DNA in Saccharomyces cerevisiae.* Genetics, 1989. **122**(1): p. 19-27.
192. Warrens, A.N., M.D. Jones, and R.I. Lechler, *Splicing by overlap extension by PCR using asymmetric amplification: an improved technique for the generation of hybrid proteins of immunological interest.* Gene, 1997. **186**(1): p. 29-35.
193. Mumberg, D., R. Muller, and M. Funk, *Regulatable promoters of Saccharomyces cerevisiae: comparison of transcriptional activity and their use for heterologous expression.* Nucleic Acids Res, 1994. **22**(25): p. 5767-8.
194. Lydeard, J.R., et al., *Break-induced replication and telomerase-independent telomere maintenance require Pol32.* Nature, 2007. **448**(7155): p. 820-3.
195. Guergova-Kuras, M., et al., *Evidence for two active branches for electron transfer in photosystem I.* Proc Natl Acad Sci U S A, 2001. **98**(8): p. 4437-42.
196. Osteryoung, J.G. and R.A. Osteryoung, *Square wave voltammetry.* Analytical Chemistry, 1985. **57**(1): p. 101-110.
197. Foiani, M., et al., *A single essential gene, PRI2, encodes the large subunit of DNA primase in Saccharomyces cerevisiae.* Mol Cell Biol, 1989. **9**(7): p. 3081-7.
198. Francesconi, S., et al., *Mutations in conserved yeast DNA primase domains impair DNA replication in vivo.* Proc Natl Acad Sci U S A, 1991. **88**(9): p. 3877-81.
199. Yavin, E., et al., *Protein-DNA charge transport: redox activation of a DNA repair protein by guanine radical.* Proc Natl Acad Sci U S A, 2005. **102**(10): p. 3546-51.
200. Johansson, E., J. Majka, and P.M. Burgers, *Structure of DNA polymerase delta from Saccharomyces cerevisiae.* J Biol Chem, 2001. **276**(47): p. 43824-8.
201. Kulak, N.A., et al., *Minimal, encapsulated proteomic-sample processing applied to copy-number estimation in eukaryotic cells.* Nat Methods, 2014. **11**(3): p. 319-24.
202. Waga, S. and B. Stillman, *The DNA replication fork in eukaryotic cells.* Annu Rev Biochem, 1998. **67**: p. 721-51.
203. Bullock, P.A., Y.S. Seo, and J. Hurwitz, *Initiation of simian virus 40 DNA synthesis in vitro.* Mol Cell Biol, 1991. **11**(5): p. 2350-61.
204. Nethanel, T., et al., *An Okazaki piece of simian virus 40 may be synthesized by ligation of shorter precursor chains.* J Virol, 1988. **62**(8): p. 2867-73.

205. Gray, H.B. and J.R. Winkler, *Electron flow through metalloproteins.* Biochim Biophys Acta, 2010. **1797**(9): p. 1563-72.
206. Altschul, S.F., et al., *Gapped BLAST and PSI-BLAST: a new generation of protein database search programs.* Nucleic Acids Res, 1997. **25**(17): p. 3389-402.
207. O'Brien, E., et al., *Yeast require redox switching in DNA primase.* Proc Natl Acad Sci U S A, 2018.
208. Sievers, F., et al., *Fast, scalable generation of high-quality protein multiple sequence alignments using Clustal Omega.* Mol Syst Biol, 2011. **7**: p. 539.
209. McCoy, A.J., et al., *Phaser crystallographic software.* J Appl Crystallogr, 2007. **40**(Pt 4): p. 658-674.
210. Aubert, C., et al., *Intraprotein electron transfer between tyrosine and tryptophan in DNA photolyase from Anacystis nidulans.* Proc Natl Acad Sci U S A, 1999. **96**(10): p. 5423-7.
211. Teo, R.D., A. Migliore, and D.N. Beratan, *Mutation effects on charge transport through the p58c iron–sulfur protein.* Chemical Science, 2020. **11**(27): p. 7076-7085.
212. Copeland, W.C., *Expression, purification, and characterization of the two human primase subunits and truncated complexes from Escherichia coli.* Protein Expr Purif, 1997. **9**(1): p. 1-9.
213. Harrington, C. and F.W. Perrino, *Initiation of RNA-primed DNA synthesis in vitro by DNA polymerase alpha-primase.* Nucleic Acids Res, 1995. **23**(6): p. 1003-9.
214. Cardenas-Rodriguez, M., A. Chatzi, and K. Tokatlidis, *Iron-sulfur clusters: from metals through mitochondria biogenesis to disease.* J Biol Inorg Chem, 2018. **23**(4): p. 509-520.
215. Crack, J.C., et al., *Techniques for the production, isolation, and analysis of iron-sulfur proteins.* Methods Mol Biol, 2014. **1122**: p. 33-48.
216. Jain, R., et al., *Cryo-EM structure and dynamics of eukaryotic DNA polymerase delta holoenzyme.* Nat Struct Mol Biol, 2019. **26**(10): p. 955-962.
217. Ghaemmaghami, S., et al., *Global analysis of protein expression in yeast.* Nature, 2003. **425**(6959): p. 737-41.
218. Puig, O., et al., *The Tandem Affinity Purification (TAP) Method: A General Procedure of Protein Complex Purification.* Methods, 2001. **24**(3): p. 218-229.
219. Butler, I.B., M.A. Schoonen, and D.T. Rickard, *Removal of dissolved oxygen from water: A comparison of four common techniques.* Talanta, 1994. **41**(2): p. 211-5.
220. Yamaguchi, M. and H. Fujisawa, *Reconstitution of iron-sulfur cluster of NADH-cytochrome c reductase, a component of benzoate 1,2-dioxygenase system from Pseudomonas arvilla C-1.* J Biol Chem, 1981. **256**(13): p. 6783-7.
221. Baranovskiy, A.G., et al., *Crystal structure of the human Pol B-subunit in complex with the C-terminal domain of the catalytic subunit.* J Biol Chem, 2017.
222. Lancey, C., et al., *Structure of the processive human Pol delta holoenzyme.* Nat Commun, 2020. **11**(1): p. 1109.
223. Jozwiakowski, S.K., S. Kummer, and K. Gari, *Human DNA polymerase delta requires an iron-sulfur cluster for high-fidelity DNA synthesis.* Life Sci Alliance, 2019. **2**(4).
224. Kapadia, N., et al., *Processive Activity of Replicative DNA Polymerases in the Replisome of Live Eukaryotic Cells.* Mol Cell, 2020. **80**(1): p. 114-126 e8.
225. Barton, J.K., R.M.B. Silva, and E. O'Brien, *Redox Chemistry in the Genome: Emergence of the [4Fe4S] Cofactor in Repair and Replication.* Annu Rev Biochem, 2019. **88**: p. 163-190.
226. Yuan, Z., et al., *Ctf4 organizes sister replisomes and Pol alpha into a replication factory.* Elife, 2019. **8**.
227. Williams, J.S., S.A. Lujan, and T.A. Kunkel, *Processing ribonucleotides incorporated during eukaryotic DNA replication.* Nat Rev Mol Cell Biol, 2016. **17**(6): p. 350-63.
228. Reijns, M.A.M., et al., *Lagging-strand replication shapes the mutational landscape of the genome.* Nature, 2015. **518**(7540): p. 502-506.

229. Winkler, J.R. and H.B. Gray, *Electron flow through biological molecules: does hole hopping protect proteins from oxidative damage?* Q Rev Biophys, 2015. **48**(4): p. 411-20.
230. Gray, H.B. and J.R. Winkler, *Hole hopping through tyrosine/tryptophan chains protects proteins from oxidative damage.* Proc Natl Acad Sci U S A, 2015. **112**(35): p. 10920-5.
231. Netz, D.J., et al., *Maturation of cytosolic and nuclear iron-sulfur proteins.* Trends Cell Biol, 2014. **24**(5): p. 303-12.
232. Kassube, S.A. and N.H. Thoma, *Structural insights into Fe-S protein biogenesis by the CIA targeting complex.* Nat Struct Mol Biol, 2020. **27**(8): p. 735-742.